universität wien

DISSERTATION/DOCTORAL THESIS

Titel der Dissertation/Title of the Doctoral Thesis

Uncertainty Quantification with Applications in Nanotechnology

verfasst von/submitted by

Amirreza Khodadadian

angestrebter akademischer Grad/in partial fulfilment of the requirements for the degree of

Doktor der Naturwissenschaften (Dr. rer. nat.)

Wien, 2017/Vienna 2017

Studienkennzahl lt. Studienblatt/ degree programme code as it appears on the student record sheet:	A 796 605 405
Dissertationsgebiet lt. Studienblatt/ field of study as it appears on the student record sheet:	Mathematik
Betreut von / Supervisor:	Assoc. Prof. DI. Dr. Clemens Heitzinger

Zusammenfassung

In den letzten Jahren haben nanotechnologische Vorrichtungen, z.B. Silizium-Nanodraht-Sensoren, Feldeffekttransistoren sowie Nanoporen, auf natürliche Weise zu Mehrskalenproblemen geführt. Experimentell wurde gezeigt, dass Silizium-Nanodrahtsensoren winzige Konzentrationen von Biomolekülen wie DNA-Oligomeren, Tumormarkern, toxischen Gasmolekülen wie Kohlenmonoxid und die Diffusion von Ionen durch Transmembranproteine detektieren können. Feldeffekttransistoren (FETs) sind zu einem weit verbreiteten Bauteil in der Elektronikindustrie geworden. Diese Bauteile basieren auf modernsten Technologien und sind zugleich ein interessantes Modellsystem für stochastische PDEs.

Verschiedene Quellen von Rauschen und Schwankungen werden hier in die Modellgleichungen inkludiert. Die Dotierung von Halbleitern is inhärent zufällig und führt zu einer zufälligen Anzahl von Verunreinigungsatomen, die an zufälligen Positionen platziert werden und von denen sich die Ladungskonzentrationen und Mobilität an den Standorten ändert. Die hier entwickelten Simulationswerkzeuge sind allgemein genug, um viele Situationen mit einzuschließen, wo der Ladungstransport in einer zufälligen Umgebung auftritt. Diese Effekte aufgrund der zufälligen Lage von Dotierstoffen sind von zunehmender Bedeutung, da die Geräte in die Nanometer-Skala geschrumpft sind und Milliarden von ihnen trotz der unvermeidlicher Prozessvariationen zusammen arbeiten müssen. In Feldeffektsensoren binden Zielmoleküle an zufällig platzierte Rezeptormolekülen in einem stochastischen Prozess, so dass der Detektionsmechanismus auch inhärent stochastisch ist. Die Brownsche Bewegung der Zielmoleküle führt auch zu Änderungen der Ladungskonzentration und der Permittivität. Die Zufälligkeit an der Sensoroberfläche breitet sich durch die selbstkonsistenten Transportgleichungen aus und führt schließlich zum Rauschen im Sensorausgang.

Diese Überlegungen motivieren die Entwicklung fortgeschrittener stochastischer numerischer Methoden, um die Unsicherheit in nanoelektronischen Geräten zu modellieren. Wir addressieren die numerische Herausforderung durch Verwendung von State-of-the-Art-Methoden, wie z.B., der Multi-Level Monte-Carlo-Methode (MLMC) und verbessern sie indem wir die Diskretisierungsparameter im numerischen Ansatz so bestimmen, dass die Rechenarbeit für einen vorgeschriebenen Gesamtfehler minimiert wird. Auf diese Weise werden die verschiedenen Fehlerquellen optimal ausgeglichen.

Abstract

In recent years, nanoscale devices such as silicon nanowire sensors, field-effect transistors (FETs), and nanopores have been promising devices in medicine and engineering. Silicon nanowire sensors have been used to detect minute concentrations of biomolecules e.g., DNA oligomers, tumor markers, toxic gases and diffusion of ions through transmembrane proteins. FETs have become a very widely used device within the electronics industry. These devices are cutting-edge technologies and, at the same time, an interesting model system for stochastic partial differential equations (PDEs).

Various sources of noise and fluctuations are included in the model equations here. Doping of semiconductor devices is inherently random and results in a random number of impurity atoms placed at random positions. These effects due to the random location of dopants are of increasing importance, as the devices have been shrunk into the nanometer scale and billions of them are required to work together despite the unavoidable process variations. In field-effect sensors, target molecules bind to randomly placed probe molecules in a stochastic process so that the detection mechanism is inherently stochastic. The Brownian motion of the target molecules also results in changes in charge concentration and permittivity which propagates through the self-consistent transport equations and finally results in noise in the sensor output.

These considerations motivate the development of advanced stochastic numerical methods to model the uncertainty in nanoelectronic devices. We develop stochastic drift-diffusion-Poisson system of equation to model the effect of randomness on charge transport. To that end, existence and local-uniqueness theorems for weak solutions of the are presented and for the stochastic PDE an efficient computational technique (Scharfetter-Gummel iteration) is used to solve it. In order to calculate the ionic currents through various transmembrane proteins a transport equation for confined structures is employed. The computational significance of this continuum model is that the $(6 + 1)$-dimensional Boltzmann equation is reduced to a $(2 + 1)$-dimensional diffusion-type equation and ionic currents through confined structures can be calculated immediately.

We address the numerical challenge by using state-of-the-art methods, such as multilevel Monte Carlo method, and improve on it by determining the discretization parameters in the numerical approach such that the computational work is minimized for a prescribed total error. In this way, the various sources of error are balanced optimally. To further improve the computational efficiency, a randomized low-discrepancy sequence such as a randomly shifted rank-1 lattice are applied.

Acknowledgements

I would like to appreciate the people who helped me during the study period in the department of mathematics of the University of Vienna as well as working at Institute for Analysis and Scientific Computing TU Vienna.
First and foremost of all, I would like to express my special appreciation and thanks to my advisor Associate Prof. Dr. Clemens Heitzinger, he has been a tremendous mentor for me. He gave me opportunities to take part in several accredited scientific conferences and gave me insight into how one carries out research in applied mathematics and mathematical modeling.
I would also like to thank my committee members, Professor Luca Selmi (University of Udine) and Professor Christian Ringhofer (Arizona State University) for serving as my committee members. I also want to thank them for the brilliant comments and suggestions. I am also grateful to all staffs of Vienna University of Technology, AIT Austrian Institute of Technology and the University of Vienna for their kind support.
I want to show my kind appreciation for my research team, who kindly supported me and allowed me to grow up as a research scientist. I thank my friends, Dr. Gerhard Tulzer, Dr. Jose A. Morales Escalante, Mrs. Leila Taghizadeh and Mr. Gregor Mitscha-Baude who helped kindly during my PhD program and gave very useful comments for writing this dissertation.
The work has been supported financially by two Austrian agencies. For the first year of my program, I was paid by a project by the Viennese Science and Technology Fund (WWTF) and for the rest of my PhD period, I joined to START prize project No. Y660 *PDE Models for Nanotechnology* and I acknowledge them significantly for their support.
I should thank my Iranian friends in SHEZAN company, Dr. Reza Kalantarinejad, Mr. Kiarash Hosseini, Mr. Ali Manzour-ol-Ajdad and Mrs. Marjan Hedayati who nicely collaborated with me to design troponin-sensitive sensors.
Last, but certainly not least, my special thanks to my family. Words cannot express how grateful I am to my mother, father and my brother, for all of the sacrifices that you have made on my behalf. I would also like to thank all of my Iranian and Austrian friends who supported me in my writing and motivated me to strive towards my goal.

Contents

Zusammenfassung ii

Abstract iii

Acknowledgements iv

Contents iv

1 Introduction 1
- 1.1 Silicon nanowire field-effect sensors . . . 3
  - 1.1.1 Biological noise in SiNW-FETs . . . 4
  - 1.1.2 Application of the biosensors in medicine . . . 7
- 1.2 Multi-Gate FETs and FinFETs . . . 9
  - 1.2.1 Random dopant fluctuation . . . 10
- 1.3 Ion channels . . . 12

2 Stochastic PDE models 14
- 2.1 Charge transport in nanoelectronic devices . . . 15
- 2.2 Stochastic drift-diffusion-Poisson system . . . 18
  - 2.2.1 Stochastic Poisson-Boltzmann equation . . . 18
  - 2.2.2 The stochastic drift-diffusion equations . . . 20
  - 2.2.3 Existence and local uniqueness . . . 23
  - 2.2.4 Weak solution of the model equations . . . 24
  - 2.2.5 Scharfetter-Gummel iteration . . . 25
  - 2.2.6 Existence and local uniqueness of the solution . . . 26
- 2.3 Transport equation for confined structure . . . 29
  - 2.3.1 Current calculation . . . 33
- 2.4 Stochastic Langevin equation . . . 33
  - 2.4.1 Interaction processes . . . 34
  - 2.4.2 The stochastic process at the functionalized surface . . . 35
- 2.5 Conclusions . . . 38

3 Stochastic numerical methods 39
- 3.1 Monte Carlo finite element method . . . 41
  - 3.1.1 Monte Carlo finite element approximation . . . 42
- 3.2 Multilevel Monte Carlo finite element method . . . 45

3.3 The optimal Monte Carlo methods . . . 47
3.3.1 The optimal Monte Carlo finite element method . . . 48
3.3.2 The optimal multilevel Monte Carlo finite element method . . . 50
3.3.3 A leading example . . . 51
3.4 Optimal multilevel randomized quasi-Monte Carlo . . . 56
3.4.1 Randomized quasi-Monte Carlo finite element methods . . . 59
3.4.2 Error bound for RQMC-FEM . . . 60
3.5 Multilevel randomized quasi-Monte Carlo finite element method (MLRQMC-FEM) . . . 61
3.5.1 Optimal multilevel randomized quasi-Monte Carlo . . . 64
3.6 Basis adaptation . . . 66
3.6.1 Polynomial chaos expansion (PCE) . . . 66
3.6.2 Application to the stochastic nonlinear Poisson-Boltzmann equation 68
3.7 Conclusions . . . 69

4 Application of UQ in nanotechnology 70
4.1 Silicon nanowire field-effect sensors . . . 71
4.1.1 Noise quantification in nanowire field-effect sensors . . . 71
4.1.2 Three-dimensional simulation of SiNW-FETs . . . 78
4.2 Cardiac troponin sensitive sensors . . . 85
4.2.1 The charge of biomolecules . . . 88
4.2.2 Troponin sensor response . . . 89
4.3 Current variation in FinFETs . . . 97
4.3.1 Three-dimensional simulation of SOI-FinFETs . . . 98
4.3.2 MLRQMC-FEM for FinFETs current variations . . . 100
4.4 Confined structure applied to the ion channels . . . 107
4.4.1 Determination of the confinement potential . . . 107
4.4.2 Simulation of phosphate specific OprP channels . . . 108
4.4.3 Simulation of Gramicidin A Channels . . . 109
4.4.4 Simulation of KcsA channels . . . 111
4.5 Conclusions . . . 116

5 Conclusions 120

List of Figures 122

Curriculum Vitae 142

Chapter 1

Introduction

Designing fully functional nanoscale devices with sensing, computing, and actuating capabilities has been a long-standing goal of science and engineering community. In the last few decades, the noticeable advances in nanotechnology such as the development of novel nanodevices like silicon nanowire sensors and multi-gate field-effect transistors are pronounced.

Generally, uncertainty quantification (UQ) is the process by which uncertainties in a system are characterized and propagated to a given Quantity of Interest (QoI). In fact, the UQ is a broad phrase used to describe methodologies for taking account of uncertainties when mathematical and computer models are used to describe real-world phenomena. This includes propagating uncertainty from unknown model inputs to model outputs, the study of uncertainty in the models themselves, developing approximation schemes that result in accurate computer models, robust design, model calibration, and other inverse problems, model bias, and discrepancy etc. In nanoelectronic devices, noise and fluctuations are of great importance, especially in nanometer-scale devices, as any random effect becomes proportionally more important as devices are shrunk. In this dissertation, we will focus on the UQ to model the complex systems which have complicated mathematical descriptions such as systems of partial differential equations. The developed stochastic models, on one hand, enable us to study the physical behavior of the semiconductor devices and model the noise and fluctuations due to their uncertainty. Also, they are useful to decrease the cost of calculation in the computer model and obtain the solution with lower computational effort. Furthermore, in order to verify the achieved results, several comparisons with the measurements will be drawn.

The main aim of this work is using uncertainty quantification to study the noise and fluctuations in the nanoelectronic devices. Their physical behavior can be modeled by using stochastic partial differential equations. The thesis is organized as follows.

- In Chapter 1, we first introduce three nanoelectronic devices, namely silicon nanowire sensors, multi-gate transistors and ion channels. Then, we explain their physical/biological significance and different sources of noise in these devices will be described in detail.

- In Chapter 2, we will present comprehensive PDE-based mathematical/physical systems to model the randomness in the explained devices. An important feature of the models used here is that the random coefficients in the stochastic equations are computed from additional physical models, so that there are essentially no free parameters or coefficient functions whose values are unknown or have to be estimated. The system of stochastic PDEs representing a full transport model and the additional models for the random coefficients together constitute the most comprehensive model for this general type of devices developed and implemented so far. Moreover, a transport equation for confined structures will be used to calculate the ionic currents through various transmembrane proteins. The computational importance of this model is that the (6+1)-dimensional Boltzmann equation is reduced to a (2 + 1)-dimensional diffusion-type equation that can be solved with small computational effort so that ionic currents through confined structures can be calculated quickly.

- In Chapter 3, we will develop the advanced stochastic numerical techniques to quantify noise and fluctuations in the devices. These methods will be compared with popular stochastic approaches, e.g., Monte Carlo to explain their efficiency. For the numerical approximation of the expected value of the solution of the system, we develop a multilevel Monte Carlo (MLMC) finite-element method (FEM) and we analyze its rate of convergence and its computational complexity. This allows to find the optimal choice of discretization parameters. Afterward, a multilevel quasi-Monte Carlo finite element method for a class of elliptic PDEs with random coefficients will be presented. It will be shown that the computational cost of the optimal multilevel randomized quasi-Monte Carlo method, which uses randomly shifted low-discrepancy sequences, is one order of magnitude smaller than that of the optimal multilevel Monte Carlo method and five orders of magnitude smaller than that the standard Monte Carlo method.

- In Chapter 4, we will concentrate on the application of uncertainty quantification in the introduced nanoelectronic devices. The stochastic drift-diffusion-Poisson system models a nanowire field-effect biosensor. This concrete model system serves two purposes. First, it is a much more complex model system than a semiconductor transistor and highlights the challenges of developing comprehensive models and efficient numerical methods. It includes many other applications as special cases, in particular, nanoscale transistors such as FinFETs. Second, it is a useful device with important applications whose fabrication has been demonstrated. We apply this approach to develop cardiac troponin sensors which have many utilities in early diagnosis of cardiovascular diseases. In ion channels, the transport equation will be used to calculate the ionic current through three different ion channels. The simulated currents are compared with measurements, and very good agreement is found in each case.

Finally, the conclusions will be drawn in Chapter 5.

1.1 Silicon nanowire field-effect sensors

Silicon nanowire (SiNW) field-effect biosensors [43, 86, 121, 122, 140, 141] (SiNW-FETs) and gas sensors [21, 91] have been demonstrated experimentally in recent years (see Figure 1.1). SiNW-FETs initially introduced in Lieber's group [69]. They have received substantial interests because they are ultrasensitive, selective, low-cost devices and they can be fabricated using commercial microfabrication technology. The devices are designed to detect and quantify biological species, e.g., cancer cells [92], tumor-initiating cells [58], DNA/miRNA [69, 168] and proteins [140]. Hence, SiNW-FETs are very promising candidates for the sensitive electrical detection of biomarkers since they are reliable, label-free, have rapid response and they are able to detect the subpicomolar concentration of target species [32].

Generally, biosensors are detection devices used to detect the presence or concentration of a biological analyte, such as biomolecules. A biosensor usually consists of sensing and electronic components where its uniqueness is that the components are integrated into one single sensor. In the device, biological parts are target molecules e.g., biomarkers and recognition elements e.g., antibodies or aptamers that act as the sensor. The transducer converts the signal generating from the interactions of the analytes into a measurable electrical signal i.e., a current or voltage. In order to improve the detection property of the sensor, bioreceptor molecules have to be immobilized in the vicinity of the transducer.

In general, electrical biosensors can be classified into two groups based on their recognition method: biocatalytic and affinity-based sensors. Biocatalytic recognition employs specific enzymes immobilized on a layer to detect the targets based on enzymatic reactions [159]. Affinity-based sensors are based on the selective binding of certain receptor-ligand pairs on the recognition layer [132]. Affinity-based sensors are feasible for a larger range of target molecules with higher sensitivity and selectivity. Moreover, affinity-based biorecognition is more convenient for the current molecular communication models which are mostly based on ligand-receptor binding, thus, provides an easier path to be adapted into the receiver models. Therefore, in this work, we only focus our attention into affinity-based electrical sensors.

In recent years, several types of biosensors are used to detect DNA molecules. Optical biosensors are advantageous detection and analysis device because they enable the direct, real-time and label-free detection of many biological species. Optical Surface plasmon resonance (SPR) biosensors are useful detection tools that have vast applications in medicine, biotechnology, medical diagnostics, healthcare, and pharmaceuticals. Fluorescence-based biosensors are frequently used to monitor environmentally hazardous gas molecules e.g., nitric oxide, hydrogen sulfide or metastatic cells and tissues. Electrochemiluminescence-based biosensors are developed to detect different human biomarkers e.g., cardiac troponin I [137]. At present, the most successful surface-based affinity biosensors are SPR sensors. However, these devices have a detection limit for small molecular weights (typically less than 2,000 $g\,\mathrm{mol}^{-1}$) and require integration with optical components, significantly increasing the cost of operation and causing difficulties in carrying out high-throughput analyses [50]. Moreover, other methods require labeling which increases detection time and complexity of the sensor device.

Using silicon nanowires has several advantages which some of them are listed here. First, the small size of nanowires allows us to fabricate devices with a parallel array of nanowires which improves noticeably the device performance. Different types of nanowires e.g., trapezoidal, rectangular, triangular and radial devices can be fabricated for different purposes [87]. Second, binding of molecules at the surface increases the accumulation of carriers and enhance the sensitivity. In fact, using longer nanowires increases the surface to volume ratio and therefore the response of the sensor to the biomolecule. Third, the dopant type and its concentration can be controlled and therefore the sensitivity is tuned in the absence of backgate voltages [42].

The sensor can directly translate the analyte–surface interaction into an electrical signal to provide real-time ultrasensitive high-throughput detection of the desired biomolecules, without the requirement for any labels. The specificity of the biosensor system is given by the immobilized biomolecules. In fact, the devices are fabricated by immobilizing biological receptor materials on the surface of a suitable transducer that converts the biochemical signal into a quantifiable electronic signal [126]. Biological species are charged in the electrolyte and they can be detected by the device when appropriate receptors are linked to the nanowire surface [120]. As target molecules bind to the immobilized probe molecules on the surface layer, the charge distribution changes and modulates the conductance of the semiconductor transducer. The transducer (Ω_{Si}) converts the molecular signal into an electric or digital signal that can be quantified, displayed and analyzed. As an example, a target molecule with negative charge results in the accumulation of hole carriers in a p-type SiNW-FET and, therefore, increase its conductivity [120].

Affinity-based sensors, in particular, the recently experimentally demonstrated nanowire field-effect sensors, pose demanding numerical problems because of a large number of stochastic dimensions. The longitudinal and vertical cross sections through the nanowire field-effect biosensor are illustrated in Figure 1.2 and Figure 4.1, respectively. The same principle also works for gas sensors. The sensors are affinity-based since the target molecules are only detected when they are sufficiently close to the sensor. The current through the semiconducting silicon nanowire, which is the actual transducer, is measured. The conductance of the nanowire is modulated by the electrostatic potential, which, in turn, is changed when charged target molecules bind to the probe molecules functionalized at the surface of the sensor. Furthermore, the target molecules are not marked in the field-effect sensors in contrast to the commonly used fluorescent or radioactive markers in other detection methods.

1.1.1 Biological noise in SiNW-FETs

There are various sources of noise and fluctuations in affinity-based sensors, where the biological noise is one of the most prominent. Its quantification is essential for understanding the signal-to-noise ratio [128] and the detection limit of the sensors. Noise sources can be mainly grouped into two important categories:

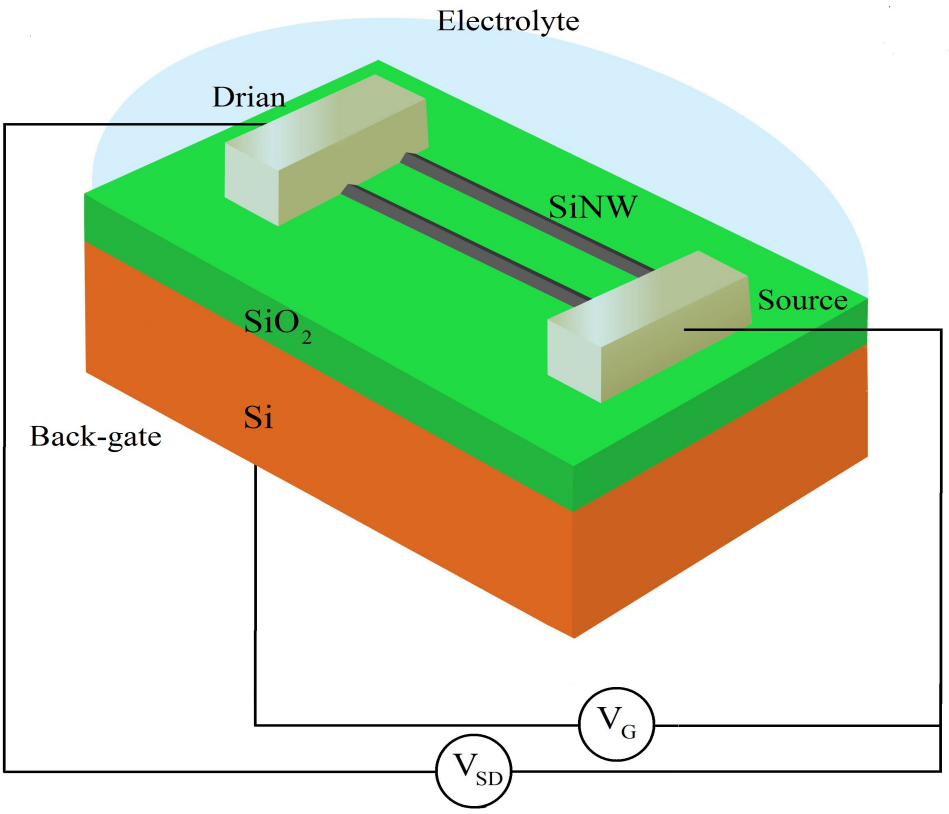


FIGURE 1.1: Schematic diagram of a nanowire field-effect sensor showing metal source and drain electrodes with the NW and contacts on the surface of SiO_2/Si substrate.

- **Biological noise** [86]: Target molecules in the electrolyte undergo random movement which is governed by Brownian motion, and stochastically binds to the receptors on the functionalized layer. The uncertainty in the location and the binding state of the molecules results in random fluctuations of the transduced signal and may severely hamper the instant detection of the concentration, and thus, the molecular messages. Since this type of noise is due to the biological interactions between target and probe molecules, it is called **biological noise**.

- **Thermal and flicker noise** [127]: Thermal noise results from thermal fluctuations of charge carriers on the bound ligands. On the other hand, $1/f$ noise is caused by the traps and defects in the semiconductor channel and could be effective at low frequencies. Hence, $1/f$ noise may dominate over other noise sources, and needs a careful investigation.

Regarding the modeling, the randomness due to the biological noise at the sensor surface affects the entire PDE model and finally yields the sensor output. In other words, the random distribution of target molecules (due to Brownian motion) and their stochastic binding to the immobilized receptors (probe molecules) gives rise to the randomness of movement and orientation. Here, the position of each molecule is independent of other molecules which guarantee the independence of input data. Randomness in the

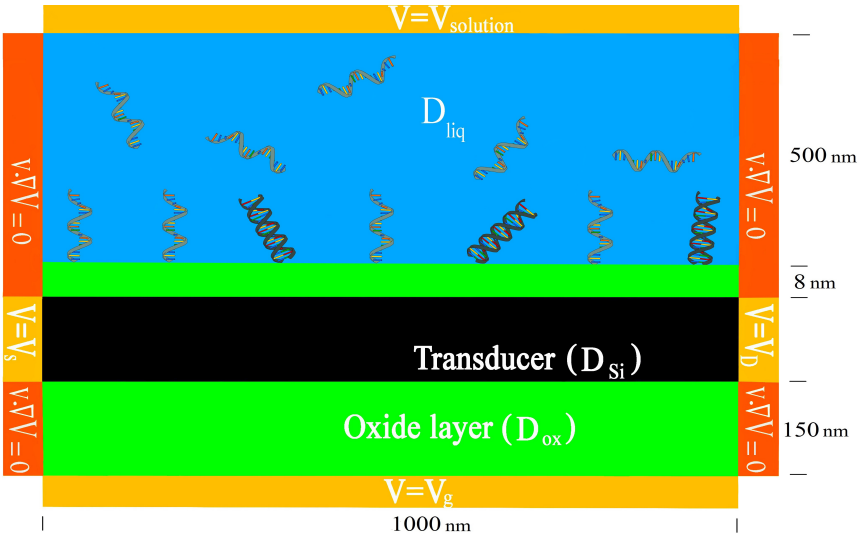


FIGURE 1.2: A longitudinal cross section of nanowire field effect sensor indicating the random binding of the target molecules to the receptors. Here, the Dirichlet boundary conditions (V_g, V_{solution}, V_S and V_D) and zeros Neumann boundary condition (on left and right) are depicted. The geometry of the device is shown additionally.

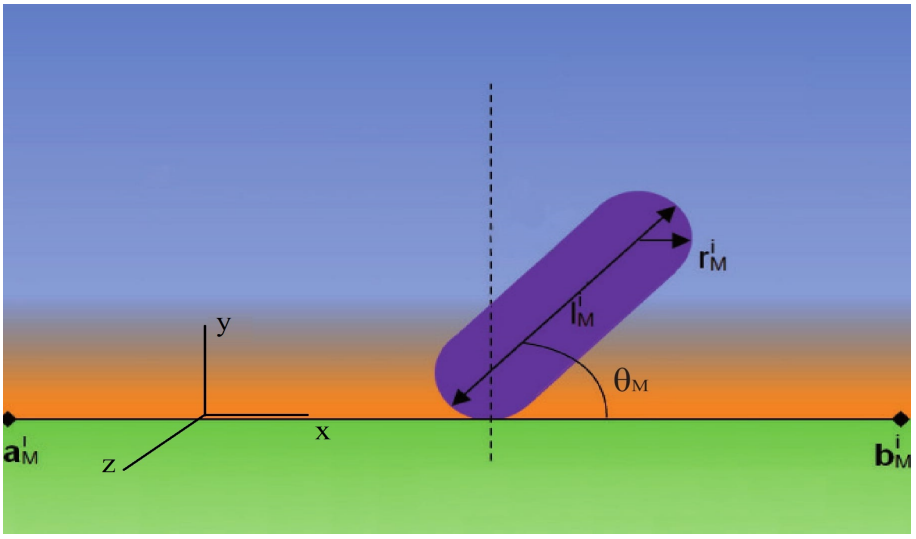


FIGURE 1.3: The orientation of a molecule in respect of oxide layer. The reference axes are shown additionally.

biological system can be characterized by the position x_M^i in the domain and θ_M^i the angle with respect to $y-$axis (Figure 1.3). For the ith molecule we have

$$x_M^i = (1-\alpha^i)a_M^i + \alpha^i b_M^i, \qquad \alpha^i \in [0,1], \tag{1.1a}$$

$$\theta_M^i = \alpha^{m+i}\frac{\pi}{2}, \qquad \alpha^{m+i} \in [0,1]. \tag{1.1b}$$

Here, each molecule has two degrees of freedom for its randomness i.e., position and orientation. In Section 2.2, we will develop a system of PDEs containing the stochastic Poisson-Boltzmann equation to model the electrostatic interaction of randomly distributed charged molecules at the surface. The system is also coupled with drift-diffusion equations to model the charge transport of carriers (holes/electrons) through the nanowire. In Section 4.1 we will use a real example of the random distribution of the DNA molecules. In this model, we will use the Boltzmann distribution to calculate the probability of the molecule orientations. Finally, considering the system of equations, we will obtain the electrical current due the modulation of the transducer.

In the nanowire field-effect sensors, the surface of a nanowire sensor is functionalized with probe molecules and surrounded by an aqueous solution containing the target molecules. In the case that number of molecules taking part in the association-dissociation or hybridization processes are sufficiently large, the binding process is deterministic. However, since we are interested in detection limits, it is essential to consider cases when only a few molecules are present in the system. Therefore, the number of target molecules bound to probes on the sensor (**PT**-complex) at the surface is random. In Section 2.4, we will introduce the stochastic Langevin equation and explain how analytically the expected value and the variance of the **PT**-complex can be calculated. Also, in 4.2.2 we will add this term of noise to random movement/orientation of molecules and will make a comprehensive stochastic model for biological noise.

1.1.2 Application of the biosensors in medicine

The sensors recently have shown their unavoidable importance in clinical diagnostics [19, 83, 90]. The devices are used in diverse range of diseases medical diagnosis. CA 15-3, for Carcinoma Antigen 15-3, is a tumor marker for many types of cancer, most notably breast cancer. Its main use is to monitor a person's response to breast cancer treatment and to help watch for breast cancer recurrence. The advantage of the using the device for the detection of breast cancer biomarker was studied in [155]. Prostate-specific antigen (PSA), is a protein produced by cells of the prostate gland. The blood level of PSA is often elevated in men with prostate cancer, and the PSA test was originally approved by the FDA in 1986 to monitor the progression of prostate cancer in men who had already been diagnosed with the disease.

In recent years, direct detection of proteins from whole blood has been demonstrated experimentally including the detection of PSA a short while ago. In fact, PSA antigen-antibody sensors consist of nanowires functionalized with antibodies at the surface [14]. CA125 is a protein that is found in blood. A small sample of blood will be taken from the arm and sent to a lab where a simple test will measure the level of CA125 in the blood sample. In most healthy women the level of CA125 is usually less than 25 U/mL [51]. However, some women do have a naturally high level of CA125 in their blood. The level of CA125 in the blood can rise for many reasons, which include endometriosis, menstruation, ovarian cysts, and sometimes ovarian cancer. Similar to the troponin sensitive sensors, for CA125 we can develop the sensors to detect the protein in the blood.

Troponin I and troponin T are proteins found in heart muscle and are released into the blood when there is damage to the heart. The interaction of troponin-C with troponin-I plays a central role in skeletal and cardiac muscle contraction [99]. Troponin tests are also sometimes used to evaluate people for heart injury due to causes other than a heart attack or to distinguish signs and symptoms such as chest pain that may be due to other causes. Testing may also be done to evaluate people with angina if their signs and symptoms worsen. In this thesis, we focus on the design strategy of troponin sensitive sensors. The main aim is the development of the most sensitive device in order to detect different cardiac troponin concentrations.

Cardiovascular diseases (CVDs) are the leading cause of morbidity and mortality for both men and women in developed and developing countries [6]. In the US, in 2010, the overall rate of death attributable to CVD was 235.5 per 100 000 [65]. Additionally, each year cardiovascular diseases cause over 4.3 million deaths (48%) in Europe and over 2.0 million deaths (42%) in the European Union [3]. Acute myocardial infarction (AMI), also known as heart attack, occurs when the flow of blood to the heart is blocked, most often by a build-up of fat, cholesterol, and other substances, which form a plaque in the arteries that feed the heart (coronary arteries). The interrupted blood flow can damage or destroy part of the heart muscle.

Rapid and accurate diagnosis of CVDs is extremely important since it increases patient survival and saves enormous costs for the health-care system. An electrocardiogram (ECG) is a traditional test that checks for problems with the heart electrical activity. However, ECG is a poor diagnostic test for AMI since more than half of the CVD patients who go to the Emergency Department show normal or no diagnostic electrocardiograms, which makes an early diagnosis of CVD more difficult [143, 160]. A range of biochemical markers is available for diagnosis of AMI of which the cardiac troponins, cardiac troponin T (cTnT), and cardiac troponin I (cTnI) are the newest and clinically the most interesting. The unique features of the cardiac troponins (cTn) are that they are highly sensitive and specific for myocardial damage and they are prognostic [9, 131]. In patients with suspected myocardial infarction or minor myocardial damage, the cTn was found in their blood. However, in the many cases, creatine kinase-MB (CK-MB) mass was not increased and the ECGs did not indicate any cardiac problem [10, 114]. Enzyme-linked immunosorbent assay (ELISA) [46] is one of the most popular techniques that may be used for cardiac biomarker detection since it ensures high diagnostic accuracy. However, the method has several drawbacks, such as long diagnostic time, which may range from hours to days due to laborious bio-analytical methodologies, or delay in transportation of samples [167]. Although the method requires highly skilled laboratory staff and considerable investment in resources and equipment, it is not often sensitive enough or fast for early diagnosis and treatment [32]. Furthermore, the technique is not able to allow for the label-free and highly targeted detection of sub 10 pg/mL concentration of troponin [32, 114].

Nowadays, several CVD marker detection sensors have been developed to overcome the disadvantages of ELISA. The surface plasma resonance (SPR) based biosensors [97], fluorescence-based sensors [130] and electrochemiluminescence-based biosensor [137] are a few of the biomarker detection methods. These methods require labeling, which leads

to increased detection time and complexity of the sensor device [90]. Therefore, the development of accurate, inexpensive, fast response and high sensitive diagnostic device to detect cTn in blood is necessary. Silicon nanowire (SiNW) field-effect transistors (FETs) [26, 29, 120] have shown high sensitivity and a noticeable capability to detect specific biological species.

The specificity of the biosensor system is given by the immobilized biomolecules. In fact, the devices are fabricated by immobilizing biological receptor materials (in this case the antibodies [32]) on the surface of a suitable transducer that converts the biochemical signal into a quantifiable electronic signal [126]. Proteins are charged in the electrolyte (in our case blood) and can be detected by the sensors when the suitable receptors are linked to the nanowire surface [120]. As target molecules (here cTn) bind to the immobilized probe molecules on the surface layer, the charge distribution changes and modulates the conductance of the semiconductor transducer, similarly to the effect that a change in gate voltage has on a MOSFET. In other words, the changes of the device conductivity is the response of the sensor to the specific binding of cardiac troponins to the anti-troponin probes [32] on the surface [87].

1.2 Multi-Gate FETs and FinFETs

The term metal–oxide–semiconductor field-effect transistor (MOSFET) [20, 34, 37, 144] stands for Metal Oxide Semiconductor Field Effect Transistor, and the name gives a clue to its construction. The devices had been known for several years but only became important in mid and late 1960s. Initially, semiconductor research had focused on developing the bipolar transistor, and problems had been experienced in fabricating MOSFETs because of process problems, particularly with the insulating oxide layers. Now this device is one of the most widely used semiconductor techniques, having become one of the principle elements in integrated circuits (ICs) today. Their performance has enabled power consumptions in ICs to be reduced. This has reduced the amount of heat being dissipated and enabled the large ICs we take for granted today to become a reality. As a result of this, the MOSFET is the most widely used form of transistors in existence today.

A MOSFET has four terminals which are, gate, source, drain, and the substrate. The MOS capacitance present in the device is the main part. The conduction and valence bands position relative to the Fermi level at the surface is a function of MOS capacitor voltage. Also, the oxide layer acts as the insulator of the state MOS capacitor. Between the drain and source terminal an inversion layer is formed and due to the flow of carriers in it, the current flows in MOSFET the inversion layer is controlled by the gate voltage.

Two basic types of MOSFET are n channel and p-channel MOSFETs. A P-channel MOSFET is a type of MOSFET in which the channel of the MOSFET is composed of a majority of holes as current carriers. When the MOSFET is activated and is on, the majority of the current flowing are holes moving through the channels. This is in contrast to the other type of MOSFET, which are N-channel MOSFETs, in which

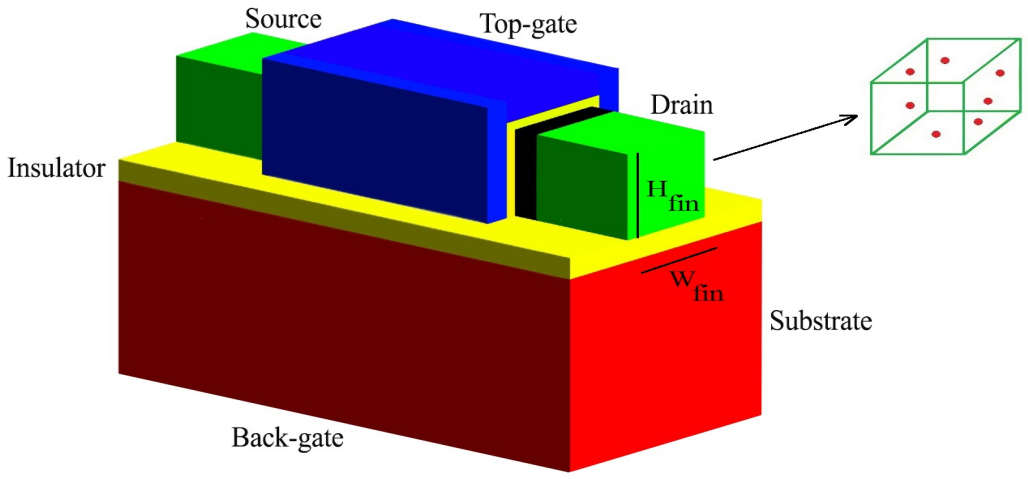


FIGURE 1.4: The 3D structure of the simulation geometry where the dopant atoms are distributed in source and drain regions.

the majority of current carriers are electrons. Together they are the building blocks of CMOS technology to fabricate integrated circuits.

In the past decades, the minimum transistor size has been down-scaled according to Moore's law and ITRS guidelines. However, scaling of conventional MOSFET devices is limited due to short channel effects, gate insulator tunneling and limited control of doping concentrations. FinFET, also known as Fin Field Effect Transistor [36, 124], is a type of non-planar or 3D MOS transistor used in the design of modern CMOS circuits to replace conventional transistors. The device is classified as a type of multi-gate MOSFETs. A 3D schematic of a silicon on insulator (SOI) FinFET indicating its different regions is shown in Figure 1.4. The characteristic of the FinFET is that the conducting channel is wrapped around a thin silicon "fin", which forms the body of the device. In the device, a gate wrapping around three sides of a narrow fin-shaped channel as well. FinFETs have several advantages like higher transconductance, fully depleted structure, reducing short-channel effects and lower power consumption. Due to the structure of the device, i.e., the surrounding gate, better control over the channel is obtained and therefore less channel doping is necessary. In other words, the threshold voltage is set by the metal instead of the channel doping.

1.2.1 Random dopant fluctuation

Generally, there are two types of semiconductors that carry electric current: intrinsic (pure semiconductor) and extrinsic (impure semiconductor). Intrinsic by definition means natural or inherent material and they do not have dopants or impurities. Silicon and germanium are the two most commonly used examples of intrinsic semiconductors, as they are elemental semiconductors. They were some of the first widely studied and used semiconductors. The electronic structure of semiconductors is the foundation of their unique properties. The mechanisms which make semiconductors their own class of material is based on the electrical structure, which dictates their core properties.

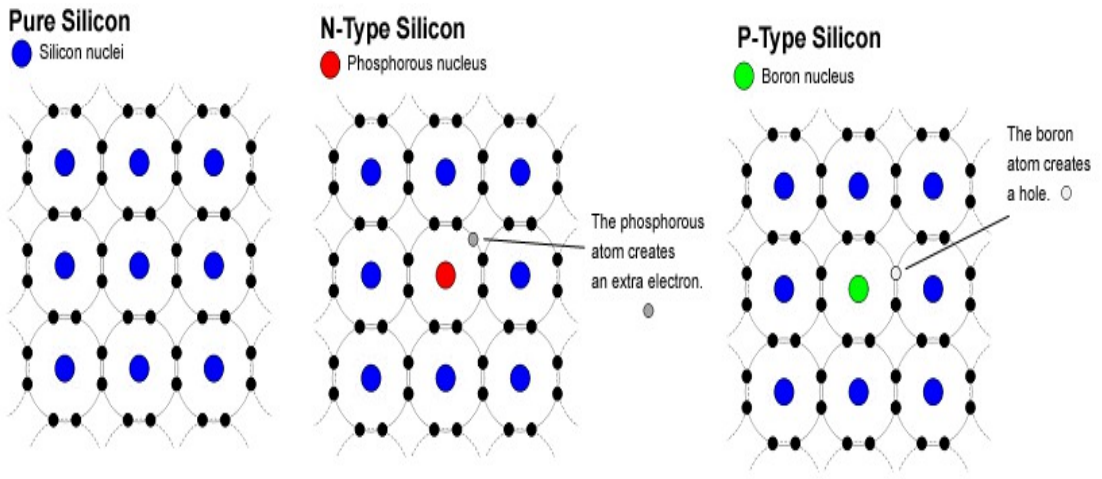


FIGURE 1.5: Schematic representation of the valence of silicon lattice where the phosphorous and boron atoms create an extra electron and hole, respectively.

Semiconductors are materials that possess the unique ability to control the flow of their charge carriers. An extrinsic semiconductor is a semiconductor with impurities (dopants) introduced into its crystal lattice. Doping is the process where semiconductors increase their electrical conductivity by introducing atoms of different elements into their lattice. A semiconductor can be doped e.g., by vapor phase epitaxy, where some concentration of impurities in their gaseous phase is contacted with the semiconductor wafer or, with the help of photolithography (microprocessing areas of a wafer), diffusion (gradient controlled particle motion), and ion implantation (utilizing an electric field to contact an ion with a solid) to increase the dopant concentration in certain parts of the wafer. Based on whether the added impurities are electron donors or acceptors, the semiconductor's Fermi level moves either up or down from its original position in the center of the energy band gap. Therefore, by adding a few amount of dopants e.g., boron, aluminum, indium or arsenic, we can control or modulate the electrical properties such as conductivity (Figure 1.5). In fact, even if the total number of impurity atoms is few (compared to that lot of atoms), they change the conductivity considerably. The corresponding fluctuation of device properties (known as RDF, random dopant fluctuation) is considerably important in modern technologies.
In this thesis, we thus consider the discrete dopant fluctuation effect [133]. In fact, instead of a continuum charge profile assumption, ionized impurities are treated discretely and randomly in silicon structure. The potential and carrier density profile fluctuation due to the discreteness and randomness of dopants are clearly captured. We will consider the doping density (number of dopant atoms-per-unit volume) [30] according to the dopant concentration of silicon. In Chapter 4, we will study the RDF effect on FinFETs and SiNW-FETs. In fact, in transistors, we will consider the random position of the dopants in source/drain regions (see Figure 1.4) and model the stochasticity by a multi-level numerical technique. Similarly, in SiNW-FETs, the randomness of the dopants in the transducer is considered with an advanced numerical method. The current variation due to the randomness of the discrete atoms will be shown in Chapter 4.

1.3 Ion channels

Ion channels are membrane protein complexes and their function is to facilitate the diffusion of ions across biological membranes. Ion channels are located in the membrane of most cells and of many intracellular organelles. They are often described as narrow, water-filled tunnels that allow only ions of a certain size and/or charge to pass through. Operation of cells in the nervous system, contraction of the heart and of skeletal muscle, and secretion in the pancreas are examples of physiological processes that require ion channels. In addition, ion channels in the membranes of intracellular organelles are important for regulating cytoplasmic calcium concentration and acidification of specific subcellular compartments (e.g., lysosomes).

Generally, ion channels allow ions to cross the hydrophobic barrier of the core membrane, guaranteeing to the cell a controlled exchange of ionized particles. When ions flux through the channels, they produce an electric current accompanied by changes of the membrane potential [85]. Ion permeation is crucial for a variety of biological functions such as nervous signal transmission and osmotic regulation. An important property of channel in the open state is given by their selective permeability [39]. This is defined as the ability to allow only a restricted class of ions to flow trough the channel pore in large amounts.

In spite of considerable advantages of popular approaches in current calculation of ion channels such as molecular dynamics (MD), Brownian dynamics or Monte Carlo they need lots of computational effort. The obvious advantage of MD over Monte Carlo is that it gives a route to dynamic properties, e.g., transport coefficients of the system. However, MD needs 3D simulation of molecular behavior (and in some cases an X-ray crystallography), which is computationally expensive in order to arrive at statistics that yield a reliable current value. In practice, the diffusion of ion through the channels is a random walk and in order to calculate the current precisely, stochastic numerical methods should be used. Computationally speaking, using these techniques as well as finite element method is prohibitive specifically for transmembrane proteins with complicated geometries. The computational models allows us to calculate the random movement of ions through the membrane and calculate the ionic current.

In this dissertation, due to the physiological importance of ion channels [106], the transport model for confined structure described in Section (2.3) will be applied to three transmembrane proteins here, namely the phosphate-specific channel OprP (an antibiotic), the Gramicidin A channel (another antibiotic), and the well-known KcsA ionic channel.

The outer membrane porin OprP of Pseudomonas aeruginosa forms a highly specific phosphate-selective channel. This channel is responsible for the high-affinity uptake of phosphate ions into the periplasmic space of the bacteria.

Gramicidin channels are mini-proteins composed of two tryptophan-rich subunits. Gramicidin A forms univalent cation-selective channels of $\approx$ 4Å diameter in phospholipid bilayer membranes. The transport of ions and water throughout most of the channel

length is by a single file process; that is, cations and water molecules cannot pass each other within the channel.

Potassium channels e.g. KcsA are a large subfamily of ionic channels. They possess the capability to be highly selective of K^+ over Na^+ ions and other ionized particles. The strong ability in selectivity is accompanied to speed and a high ionic throughput.

In all above-mentioned cases, the model will be validated by comparison with current measurements of various ions. Then we elucidate physiological properties of the channels. For example, the selectivity of potassium channels between sodium and potassium is its primary physiological function and therefore it is investigated in the simulations. The model reproduces selectivity as well. We also constructed virtual ion channels by changing the length of the selectivity filter in order to answer the question if and in which respect the natural KcsA channel is optimal.

Chapter 2

Stochastic PDE models

A stochastic partial differential equation (SPDE) is a partial differential equation containing a random (noise) term. SPDEs serve as fundamental models of physical systems subject to random inputs, interactions or environments. It is a particular challenge to develop tools to construct solutions, prove the robustness of approximation schemes, and study properties like ergodicity and fluctuation statistics for a wide variety of SPDEs. In Chapter 3, we will describe considerably the efficient numerical techniques to solve the SPDEs with the lower computational cost.

The Poisson-Boltzmann equation arising in the Debye-Hückel theory as a second order nonlinear partial differential equation describes the electrostatic potential. It is used for a wide range of applications, including the computation of the electrostatic potential at the solvent-accessible molecular surface, the computation of encounter rates between molecules in the solution, the computation of the free energy of association and its salt dependence, and the combination of classical molecular mechanics and dynamics. In this work, we extended the equation by adding the noise due to the stochasticity of position and orientation of biomolecules. As the next step, we couple the equation with drift-diffusion equations to obtain the electrical current and conductivity. It is obvious that because of the randomness, expected value and variance of the parameters should be considered. The existence and uniqueness of the solution were discussed in [13, 145]. In Chapter 3, we will consider these properties for the stochastic version of the coupled equations and will use the numerical methods to solve the nonlinear coupled system of equations. In Chapter 4, we will apply them to obtain electrical potential and current in field effect sensors and transistors.

The transport equation for confined structures is used to calculate the ionic currents through various transmembrane proteins [85]. The transport equation is a diffusion-type equation where the concentration of the particles depends on the one-dimensional position in the confined structure and on the local energy. The computational significance of this continuum model is that the $(6 + 1)$-dimensional Boltzmann equation is reduced to a $(2 + 1)$-dimensional diffusion-type equation that can be solved with small computational effort so that ionic currents through confined structures can be calculated quickly [74, 75]. In Chapter 4, we verify the obtained conductivity and current with experimental data for three ion channels, namely OprP, Gramicidin A, and KcsA.

In this chapter, we use a comprehensive model of the devices that provides physical and quantitative understanding. It is based on SPDEs coupled to a stochastic reaction model for the association/dissociation process, and it has been extended to a system of SPDEs in order make it possible to include noise and fluctuation [86]. The model consists of the Poisson-Boltzmann equation to model the electrolyte, the drift-diffusion-Poisson system to model the charge transport in the transducer, and a reaction equation to model the association of target molecules at the sensor surface and their dissociation [145]. The model enables us to calculate the sensitivity of the device with respect to the target molecules and the signal-to-noise ratio due to the biological noise. In Chapter 4, a realistic model for cardiac troponin sensors will be developed by using the system of equations.

This chapter is a summary of the mathematical theorems and model equations that are explained in [85, 86, 88, 145].

2.1 Charge transport in nanoelectronic devices

In drift-diffusion model, the current densities are expressed as a sum of two components: the drift component which is driven by the electric field and the diffusion component caused by the gradient of the electron concentration. In semiconductors, particles tend to spread out or redistribute from areas of high concentration to areas of lower concentration. Diffusion current is a current caused by the diffusion of charge carriers. By contrast, the drift current is due to charged particle motion in response to an electric field. Diffusion current can be in the same or opposite direction of a drift current. The diffusion current and drift current together are described by the drift–diffusion model.

In drift current, on average the population of holes move in the direction of the electric field (from + to − electrical potential) and electrons move in the opposite direction of the electric field (from − to +). Motion of individual particles is highly non-directional on a local scale, but has a net direction on a macroscopic scale. When an electric field E is applied across a piece of material, the electrons (holes) respond by moving with an average velocity called the drift velocity. The velocities are modeled at first order to be proportional to electrical field as

$$v_n = -\mu_n E,$$
$$v_p = \mu_p E.$$

Electrons (holes) mobility is almost always specified in units of $\mathrm{cm}^2/(\mathrm{Vs})$. This model is called linear transport regime which breaks down at large fields (short channel devices). However, in typical sensor applications long channel transistors are used at low chain bias so the linear model may still suffice. The densities of the currents are the products of the particle charges, the carrier concentration, and the average drift velocities. These relations are true in semiconductor device, however, in electrochemistry (the mobility is

defined as the ratio between velocity and force) are not true. Therefore, we have

$$J_n^{\text{drift}} = -qnv_n, \tag{2.1}$$
$$J_p^{\text{drift}} = qpv_p. \tag{2.2}$$

We should also note that drift current obeys Ohm's law, i.e., J_n is proportional to the electrical field (E), as the velocity model and the above relations. The random motion of carriers can lead to a net flux of carriers if one particular region has a higher concentration of carriers than another region (a concentration gradient between the high carrier concentration region and the low carrier concentration region). The net movement of carriers is therefore from areas of high concentration to low. Here, diffusion means particle movement (flux) in response to the concentration gradient. In fact, collisions between particles and medium (silicon crystal) send particles off in random directions. Ficks's first law describes diffusion with particle fluxes that are proportional to the gradient in concentrations. Here, the flux is the number of particles crossing a unit area per unit time [$\text{cm}^{-2}\text{s}^{-1}$]. Therefore, the fluxes are

$$F_n = -D_n \nabla n,$$
$$F_p = -D_p \nabla p.$$

The coefficients measure the ease of carrier diffusion in response to a concentration gradient and are limited by many sources of scattering among which the vibration of lattice atoms, surface roughness and ionized dopantsare often the dominant ones. The current densities of the diffusion process are given by multiplying the diffusion fluxes with the particle charges, i.e., with $-q$ for electrons and $+q$ for holes. This yields

$$J_n^{\text{diff}} = qD_n \nabla n, \tag{2.3}$$
$$J_p^{\text{diff}} = -qD_p \nabla p, \tag{2.4}$$

since the diffusion directions is opposite to the gradient concentration. In general, total current can flow by drift and diffusion separately. Total current density is given by

$$J_n = J_n^{\text{drift}} + J_n^{\text{diff}} = -qnv_n + qD_n \nabla n, \tag{2.5}$$
$$J_p = J_p^{\text{drift}} + J_p^{\text{diff}} = qpv_p - qD_p \nabla p. \tag{2.6}$$

The total current density is $J_n + J_p$. Finally, the electrical current is obtained by taking integral over a cross-section of the transducer.

Graded-channel approximation is a simplified model for current calculation and in most of the cases is advantageous. Solving the stochastic Poisson-Boltzmann equation yields the electrostatic potential on a cross section of the structure, from which the current through the sensor can be calculated by the graded-channel approximation as in [72]. The graded-channel approximation can be derived from the drift-diffusion equations, ((2.15)b)-((2.15)e). The concentration of electrons and holes are given by

Boltzmann distribution as

$$p(x,\omega) = n_i \exp\left(-\frac{qV(x,\omega) - \Phi_F}{k_B T}\right), \tag{2.7}$$

$$n(x,\omega) = n_i \exp\left(\frac{qV(x,\omega) - \Phi_F}{k_B T}\right). \tag{2.8}$$

For sake of simplicity, two assumptions are necessary for the graded-channel approximation. The first assumption is that only the drift current, and not the diffusion current, plays a role. This yields the current density as

$$J_n^{\text{drift}} + J_p^{\text{drift}} = -q\mu_n n \nabla u - q\mu_p p \nabla u.$$

The second assumption is that the electric field is constant along the z-axis of the sensor (in source-to-drain direction), i.e., $E = (u_1 - u_2)/Z$ holds, where $u_2 - u_1$ is the potential difference between the two contacts a distance Z apart. Since $E = -\partial_z u$, we hence find

$$J_n^{\text{drift}} + J_p^{\text{drift}} = eE(\mu_n n + \mu_p p).$$

Then, the conductivity due to electrons and holes can be calculated as

$$\sigma = \frac{J_n^{\text{drift}} + J_p^{\text{drift}}}{E} = e(\mu_n n + \mu_p p).$$

The total electrical current is now obtained by taking the integral

$$I = \int_{D_{\text{Si}}} (J_n^{\text{drift}} + J_p^{\text{drift}}) \mathrm{d}xy = qE \int_{D_{\text{Si}}} (\mu_n n(x,y) + \mu_p p(x,y)) \mathrm{d}xy \tag{2.9}$$

over a cross section D_{Si} of the semiconducting part of the sensor. As we have seen, the graded-channel approximation is a simplification of the drift-diffusion-Poisson equations and neglects diffusion. The MOSFET drain current model apparently neglects diffusion currents and as such it is not suited to describe the subthreshold region. However, the maximum transconductance-to-current ratio (g_m/I) and therefore the maximum sensitivity is often found exactly in that region. Hence, the full drift-diffusion is very well-suited for current investigations from weak inversion (subthreshold) to strong inversion (above-threshold) regime. Finally, we should note that in the international metric system, the units: $[n]$=$[p]$=$1/\text{m}^3$, $[\mu_n] = [\mu_p] = \text{m}^2/(\text{Vs})$, $[E] = \text{V/m}$.

In this dissertation, the main noise source for us is biological noise which represents an anticipated noise source for the biological applications. This is expected to be mostly due to the random motion of immobilized DNA probes within the electrolyte. This motion can couple to the semiconductor channel and cause random fluctuation in the carrier concentration or mobility. Furthermore, it is also expected that this noise source would depend on the potential across the DNA layer, since a higher potential could possibly further immobilize the probes and cause less noise. We define the **signal-to-noise**

ratio (SNR) as one of the most significant characteristics of a sensor as

$$\mathrm{SNR}(I) := \frac{\mathbb{E}[I]}{\sqrt{\mathbb{V}ar[I]}}. \tag{2.10}$$

The expected value of the current directly arises of the randomness of the solution, we consider it as the signal of current and consequently, corresponding standard deviation as the unavoidable noise. There are many device design and operating parameters which affect the noise in the system. We will study the effect of them on signal as well as noise and determine which one is the most effective in order to intensify SNR substantially.

2.2 Stochastic drift-diffusion-Poisson system

Semiconductors are one of the most important electrical materials and are the foundation of every solid-state electronic device which is in use today. They are substances that only conduct electricity under certain conditions and include silicon and germanium. There are semiconductors that occur naturally and do not require any sort of chemical doping and can often be recognized by characteristic crystal lattice structures that they form. The semiconductor device equations can be used to describe the whole simulation domain of a semiconductor device. They are applied to the bulk semiconductor, the doped regions such as source and drain, and to dielectric regions such as the gate dielectric.

2.2.1 Stochastic Poisson-Boltzmann equation

We consider D as the domain where $D \subseteq \mathbb{R}^d$ is bounded, convex and $d \leq 3$ with boundary ∂D. The domain $D \subseteq \mathbb{R}^3$ is partitioned into four subdomains with different physical properties. The first subdomain D_{Si} consists of the (silicon) nanowire and acts as the transducer of the sensor; in this subdomain, the Poisson-drift-diffusion equations are used to model charge transport and electrostatics. The semiconductor is coated with a dielectric layer (as an insulator) which comprises the second subdomain D_{ox}, where the Poisson equation holds. In D_{liq}, the aqueous solution (electrolyte e.g., salty water or blood) containing cations and anions; therefore, the Poisson-Boltzmann equation holds as well. The last subdomain is about the DNA molecules (D_{M}). In summary, the stochastic Poisson-Boltzmann equation can be summarized as

$$-\nabla \cdot (A(x,\omega)\nabla V(x,\omega)) = \begin{cases} q(C_{\mathrm{dop}}(x,\omega) + p(x,\omega) - n(x,\omega)) & \text{in } D_{\mathrm{Si}}, \\ 0 & \text{in } D_{\mathrm{ox}}, \\ \rho(x,\omega) & \text{in } D_{\mathrm{M}}, \\ -2\varphi(x,\omega)\sinh(\beta(V(x,\omega) - \Phi_F) & \text{in } D_{\mathrm{liq}}, \end{cases} \tag{2.11a}$$

where $A(x,\omega)$ (the permittivity function) is a random field with $x \in \mathbb{R}^d$ and a random parameter $\omega \in \Omega$ in a probability space $(\Omega, \mathbb{A}, \mathbb{P})$. Ω denotes the set of elementary events, i.e., the sample space, $\mathbb{A}$ the σ-algebra of all possible events, and $\mathbb{P}\colon \mathbb{A} \to [0,1]$ is a probability measure. φ is the ionic concentration (holds for a symmetric electrolyte of

monovalent ions), Φ_F is the Fermi level, $\rho(x,\omega)$ describes the fixed charges of molecules. C_{dop} is the doping concentration, i.e., the concentration of dopants and can be negative or positive. The relative permittivities of the subdomains are assumed constant and equal to $A_{\text{Si}} = 11.7$, $A_{\text{ox}} = 3.9$, $A_{\text{M}} = 3.7$ and $A_{\text{liq}} = 78.4$. In extrinsic semiconductors, the sillicon crystal is doped with different elements, e.g., boron or phosphorus which have their dielectric constants. Furthermore, the constant β is defined as $\beta := q/(k_B T)$ in terms of the Boltzmann constant k_B, the temperature T and the elementary charge $q > 0$.

At the interface Γ between the silicon oxide and the liquid, the charge concentration exhibits a rapidly oscillating spatial structure which leads to a multiscale problem [73]. The continuity conditions (2.12a) and (2.12b) are due to the jump in the permittivity A between two different materials. Here, $0+$ denotes the limit at the interface on the side of the liquid, while $0-$ is the limit on the side of the silicon oxide layer. The two interface condition mean that the rapidly oscillating charge concentration in the surface layer is described by the macroscopic dipole moment density α and the macroscopic surface-charge density γ.

$$V(0+,y,\omega) - V(0-,y,\omega) = \alpha(y,\omega) \quad \text{on } \Gamma, \tag{2.12a}$$

$$A(0+)\partial_x V(0+,y,\omega) - A(0-)\partial_x V(0-,y,\omega) = \gamma(y,\omega) \quad \text{on } \Gamma. \tag{2.12b}$$

The boundary conditions are Dirichlet boundary conditions (∂D_D) and Neumann boundary condition (∂D_N). For nanowire sensors, a voltage across the simulation domain in the vertical direction can be applied as well by an electrode in the liquid (solution voltage) and by a back-gate contact at the bottom of the structure (back-gate voltage). These are also part of ∂D. Zero Neumann boundary conditions hold on the Neumann part ∂D_N of the boundary. Figure 4.1 illustrates the boundary conditions. In FET devices, e.g., MOSFETs and FinFETs, contacts allow the current flow in and out of the device. Precisely, ohmic contacts where only voltages can be applied are source, drain and the gate. The Neumann boundary condition guarantees that the simulation domain is self-contained and there are no fluxes across the boundary. At Ohmic contacts and the interface between silicon and the insulators, Dirichlet boundary conditions are applied and Neumann boundary conditions are applied at all other boundaries of the solution domain.

We can also linearize the nonlinear term of (2.23) including an arbitrary Fermi level Φ_F. Taylor expansion of right-hand side (RHS) of the equation in $V(x,\omega)$ around an arbitrary potential Φ_0 yields

$$\text{RHS} = \alpha(x,\omega) - \gamma(x,\omega)V(x,\omega) + O((V(x,\omega) - \Phi_0)^2)$$

with

$$\alpha(x,\omega) := 2\varphi(x,\omega)\sinh\frac{q(\Phi_F - \Phi_0)}{k_B T} + \frac{2q\Phi_0\kappa(x,\omega)}{k_B T}\cosh\frac{q(\Phi_F - \Phi_0)}{k_B T}, \tag{2.13a}$$

$$\gamma(x,\omega) := \frac{2q\varphi(x,\omega)}{k_B T}\cosh\frac{q(\Phi_0 - \Phi_F)}{k_B T}, \tag{2.13b}$$

where again $\kappa(x,\omega)$ is the bulk concentration of the ions [72]. Hence, the linearized Poisson-Boltzmann equation for arbitrary Fermi level is the following equation

$$-\nabla\cdot(A(x,\omega)\nabla V(x,\omega))+\gamma(x)V(x,\omega)=f(x,\omega)+\alpha(x), \quad \text{in } U \tag{2.14a}$$

$$u=u_D \quad \text{on } \partial U \tag{2.14b}$$

An approach to the proof is to use the Leray-Schauder fixed-point theorem and can be found in [108]. In [72], the PDE is used to model the random movement (Brownian motion) of the biomolecules in the boundary layer, i.e., the various orientations of the molecules with respect to the surface. In this case, the solution (electrostatic potential) can be obtained immediately, therefore, the ease of implementation can be mentioned as the most important advantage of the model. However, due to using the Taylor expansion, the exactness of the equation compared with the nonlinear equation is not sufficient. In spite of this fact, since the Newton solver (for solving the PBE) needs a suitable initial guess, the solution of the linearized equation can be used (as the guess) to converge the solution more efficiently.

2.2.2 The stochastic drift-diffusion equations

In the subdomain D_{Si}, the stochastic drift-diffusion-Poisson equations [145]:

$$-\nabla\cdot(A(x,\omega)\nabla V(x,\omega))=q(C_{dop}(x,\omega)+p(x,\omega)-n(x,\omega)), \tag{2.15a}$$

$$\nabla\cdot J_n(x,\omega)=eR(n(x,\omega),p(x,\omega)), \tag{2.15b}$$

$$\nabla\cdot J_p(x,\omega)=-eR(n(x,\omega),p(x,\omega)), \tag{2.15c}$$

$$J_n(x,\omega)=e(D_n\nabla n(x,\omega)-\mu_n n(x,\omega)\nabla V(x,\omega)), \tag{2.15d}$$

$$J_p(x,\omega)=e(-D_p\nabla p(x,\omega)-\mu_p p(x,\omega)\nabla V(x,\omega)), \tag{2.15e}$$

are used to model charge transport. Here, $n(x,\omega)$ and $p(x,\omega)$ are the concentrations of electrons and holes, respectively, $J_n(x,\omega)$ and $J_p(x,\omega)$ are current densities of the carriers, D_n and D_p are diffusion coefficients, μ_n and μ_p are the mobilities and $R(n(x,\omega),p(x,\omega))$ is the recombination rate. We use the Shockley-Read-Hall (SRH) recombination rate which is defined as

$$R(n(x,\omega),p(x,\omega)):=\frac{n(x,\omega)p(x,\omega)-n_i^2}{\tau_p(n(x,\omega)+n_i)+\tau_n(p(x,\omega)+n_i)}, \tag{2.16}$$

where n_i $(1.5\times10^{10}\text{cm}^{-3})$ is the intrinsic charge density and and τ_n and τ_p are the lifetimes of the free carriers. In the Slotboom variables $u(x,\omega)$ and $v(x,\omega)$, which are defined by

$$n(x,\omega)=:n_i e^{V(x,\omega)/U_T}u(x,\omega), \tag{2.17a}$$

$$p(x,\omega)=:n_i e^{-V(x,\omega)/U_T}v(x,\omega), \tag{2.17b}$$

the system (2.15) becomes

$$-\nabla \cdot (A\nabla V(x,\omega)) = en_i(e^{-V(x,\omega)/U_T}v(x,\omega) - e^{V(x,\omega)/U_T}u(x,\omega)) + qC_{dop}(x,\omega), \tag{2.18a}$$

$$U_T n_i \nabla.(\mu_n e^{V(x,\omega)/U_T}\nabla u(x,\omega)) = n_i \frac{u(x,\omega)v(x,\omega) - 1}{\tau_p(e^{V(x,\omega)/U_T}u(x,\omega) + 1) + \tau_n(e^{-V(x,\omega)/U_T}v(x,\omega) + 1)}, \tag{2.18b}$$

$$U_T n_i \nabla.(\mu_p e^{-V(x,\omega)/U_T}\nabla v(x,\omega)) = n_i \frac{u(x,\omega)v(x,\omega) - 1}{\tau_p(e^{V(x,\omega)/U_T}u(x,\omega) + 1) + \tau_n(e^{-V(x,\omega)/U_T}v(x,\omega) + 1)}. \tag{2.18c}$$

The boundary ∂D_{Si} is partitioned into Dirichlet and Neumann boundaries. The Dirichlet conditions

$$V(x,\omega)|_{\partial D_D} = V_D(x), \quad u(x,\omega)|_{\partial D_{\mathrm{Si},D}} = u_D(x), \quad v(x,\omega)|_{\partial D_{\mathrm{Si},D}} = v_D(x),$$

hold on the $\partial D_{\mathrm{Si},D}$ (source and drain contacts of semiconductor). For details about the boundary conditions at the ohmic contacts the reader is referred to [108]. In the sensors, Also, the boundary values $u_D(x)$ and $v_D(x)$ are defined by

$$u_D(x) = n_i^{-1}e^{-V_D(x)/U_T}n_D(x),$$
$$v_D(x) = n_i^{-1}e^{V_D(x)/U_T}p_D(x),$$

where

$$n_D(x) = \frac{1}{2}\left(C_{dop} + \sqrt{C_{dop}^2 + 4n_i^2}\right),$$
$$p_D(x) = \frac{1}{2}\left(-C_{dop} + \sqrt{C_{dop}^2 + 4n_i^2}\right).$$

The zero Neumann conditions

$$\nabla_n V(x,\omega)|_{\partial D_N} = 0, \quad \nabla_n u(x,\omega)|_{\partial D_{\mathrm{Si},N}} = 0, \quad \nabla_n v(x,\omega)|_{\partial D_{\mathrm{Si},N}} = 0,$$

hold on the Neumann part $\partial D_{\mathrm{Si},N}$ of the boundary, as well.

At Ohmic contacts the space charge vanishes i.e., $C_{\mathrm{dop}} - p + n = 0$ on ∂D_D, and the system is in thermal eqilibrium i.e., $np = n_i^2$ on ∂D_D. Therefore, the quasi Fermi levels Φ_n and Φ_p are defined by

$$\Phi_n = E_c - U_T \ln \frac{n}{n_i}, \tag{2.21}$$

$$\Phi_p = E_v + U_T \ln \frac{p}{n_i}, \tag{2.22}$$

where and E_c and E_v are respectively conduction band and valance band in the semiconductor, U_T is the thermal voltage and n_i is again the intrinsic carrier concentration

of silicon. In crystals of pure silicon, the number density of electrons in the conduction band and of holes in the valence band are equal and therefore the Fermi level as a function of doping concentration can be calculated for electrons and holes as

$$\Phi_F = E_c + U_T \ln \frac{n}{n_i} = E_v - U_T \ln \frac{p}{n_i}.$$

In the subdomain D_{ox}, there are no charge carriers and the Poisson equation is simply

$$-\nabla \cdot (A \nabla V(x,\omega)) = 0.$$

In the subdomain D_{liq}, the nonlinear Poisson-Boltzmann equation

$$-\nabla \cdot (A(x,\omega)\nabla V(x,\omega)) + 2\varphi \sinh(\beta(V(x,\omega) - \Phi_F)) = 0$$

holds and models screening by free charges. Here φ is the ionic concentration, the constant β equals $\beta := q/(k_B T)$ in terms of the Boltzmann constant k_B and the temperature T, and Φ_F is the Fermi level.

In summary, for all $\omega \in \Omega$, the model equations are the boundary-value problem

$$\begin{aligned}
&-\nabla \cdot (A(x,\omega)\nabla V(x,\omega)) && && (2.23a)\\
&= qC_{\text{dop}}(x,\omega) - qn_i(\mathrm{e}^{V(x,\omega)/U_T}u(x,\omega) - \mathrm{e}^{-V(x,\omega)/U_T}v(x,\omega)) && \text{in } D_{\text{Si}}, &\\
&-\nabla \cdot (A(x,\omega)\nabla V(x,\omega)) = 0 && \text{in } D_{\text{ox}}, && (2.23b)\\
&-\nabla \cdot (A(x,\omega)\nabla V(x,\omega)) = -2\eta \sinh(\beta(V(x,\omega) - \Phi(x,\omega))) && \text{in } D_{\text{liq}}, && (2.23c)\\
&V(0+,y,\omega) - V(0-,y,\omega) = \alpha(y,\omega) && \text{on } \Gamma, && (2.23d)\\
&A(0+)\partial_x V(0+,y,\omega) - A(0-)\partial_x V(0-,y,\omega) = \gamma(y,\omega) && \text{on } \Gamma, && (2.23e)\\
&U_T \nabla \cdot (\mu_n \mathrm{e}^{V(x,\omega)/U_T}\nabla u(x,\omega)) && && (2.23f)\\
&= \frac{u(x,\omega)v(x,\omega) - 1}{\tau_p(\mathrm{e}^{V(x,\omega)/U_T}u(x,\omega) + 1) + \tau_n(\mathrm{e}^{-V(x,\omega)/U_T}v(x,\omega) + 1)} && \text{in } D_{\text{Si}}, &\\
&U_T \nabla \cdot (\mu_p \mathrm{e}^{-V(x,\omega)/U_T}\nabla v(x,\omega)) && && (2.23g)\\
&= \frac{u(x,\omega)v(x,\omega) - 1}{\tau_p(\mathrm{e}^{V(x,\omega)/U_T}u(x,\omega) + 1) + \tau_n(\mathrm{e}^{-V(x,\omega)/U_T}v(x,\omega) + 1)} && \text{in } D_{\text{Si}}, &\\
&\alpha(y,\omega) = M_\alpha(V(y,\omega)) && \text{in } \Gamma, && (2.23h)\\
&\gamma(y,\omega) = M_\gamma(V(y,\omega)) && \text{in } \Gamma, && (2.23i)\\
&V(x,\omega) = V_D(x) && \text{on } \partial D_D, && (2.23j)\\
&\mathbf{n} \cdot \nabla V(x,\omega) = 0 && \text{on } \partial D_N, && (2.23k)\\
&u(x,\omega) = u_D(x), \quad v(x,\omega) = v_D(x) && \text{on } \partial D_{D,\text{Si}}, && (2.23l)\\
&\mathbf{n} \cdot \nabla u(x,\omega) = 0, \quad \mathbf{n} \cdot \nabla v(x,\omega) = 0. && \text{on } \partial D_{N,\text{Si}}. && (2.23m)
\end{aligned}$$

The structure of the MOSFETs is much simpler. The device only consists of the silicon (channel and source/drain regions) and the insulator. Therefore, for the FETs the same system of equations can be applied neglecting the liquid (D_{liq}) and the molecule (D_{M}) subdomains. We should note that in the subsequent simulations, the molecule

subdomain (binding of target molecules to immobilized receptor molecules at the surface) is defined by assigning a finite volume of the electrolyte to molecules (volumetric molecules). Regarding the interface condition, we should note that the existence of a charge inside the insulator and at the semiconductor-insulator interface also induces a semiconductor charge at zero bias:

$$V(0+, y, \boldsymbol{\omega}) - V(0-, y, \boldsymbol{\omega}) = 0 \qquad \text{on } \Gamma, \tag{2.24}$$

$$A(0+)\partial_x V(0+, y, \boldsymbol{\omega}) - A(0-)\partial_x V(0-, y, \boldsymbol{\omega}) = 0 \qquad \text{on } \Gamma. \tag{2.25}$$

It is defined as $\Gamma = D_{\mathrm{Si}} \cap D_{\mathrm{ox}}$ where the jump of the permittivity function explains the jump of electric field. Here, $0+$ denotes the limit at the interface on the side of the silicon oxide, while $0-$ is the limit on the side of the channel.

2.2.3 Existence and local uniqueness

In order to state the main theoretical results, we first record the assumptions on the data of the system (2.23) [145]. The assumptions are moderate in the sense that similar ones are necessary for the deterministic system of equations. Then weak solutions and Bochner spaces are defined. Using the assumptions and definitions, existence and local uniqueness are shown.

The following assumptions are required:

1. The bounded domain $D \subset \mathbb{R}^3$ has a C^2 Dirichlet boundary ∂D_D, the Neumann boundary ∂D_N consists of C^2 segments, and the Lebesgue measure of the Dirichlet boundary ∂D_D is nonzero. The C^2 manifold $\Gamma \subset D$ splits the domain D into two nonempty domains D^+ and D^- so that $\Gamma \cap \partial D = 0$ and $\Gamma \cap \partial D \subset \partial D_N$ hold.

2. $(\Omega, \mathbb{A}, \mathbb{P})$ is a probability space, where Ω denotes the set of elementary events (sample space), $\mathbb{A}$ the σ-algebra of all possible events, and $\mathbb{P}\colon \mathbb{A} \to [0, 1]$ is a probability measure.

3. The diffusion coefficient $A(x, \omega)$ is assumed to be a strongly measurable mapping from Ω into $L^\infty(D)$. It is uniformly elliptic and bounded function of position $x \in D$ and the elementary event $\omega \in \Omega$, i.e., there exist constants $0 < A^- < A^+ < \infty$ such that

$$0 < A^- \leq \operatorname{ess\,inf}_{x \in D} A(x, \omega) \leq \|A(\cdot, \omega)\|_{L^\infty(D)} \leq A^+ < \infty \quad \forall \omega \in \Omega.$$

   Furthermore, $A(x, \omega)|_{D^+ \times \Omega} \in C^1(D^+ \times \Omega, \mathbb{R}^{3\times 3})$ and $A(x, \omega)|_{D^- \times \Omega} \in C^1(D^- \times \Omega, \mathbb{R}^{3\times 3})$.

4. The doping concentration $C_{\mathrm{dop}}(x, \omega)$ is bounded above and below with the bounds

$$\underline{C} := \inf_{x \in D} C_{\mathrm{dop}}(x, \omega) \leq C_{\mathrm{dop}}(x, \omega) \leq \sup_{x \in D} C_{\mathrm{dop}}(x, \omega) =: \overline{C} \quad \forall \omega \in \Omega.$$

5. There is a constant $\mathbb{R} \ni K \geq 1$ satisfying

$$\frac{1}{K} \leq u_D(x), v_D(x) \leq K \quad \forall x \in \partial D_{\mathrm{Si},D}.$$

6. The functionals $M_\alpha : L^2(\Omega; H^1(D)) \cap L^\infty(D \times \Omega) \to L^2(\Omega; H^{1/2}(\Gamma)) \cap L^\infty(\Gamma \times \Omega)$ and $M_\gamma : L^2(\Omega; H^1(D)) \cap L^\infty(D \times \Omega) \to L^\infty(\Gamma \times \Omega)$ are continuous.

7. The mobilities $\mu_n(x,\omega)$ and $\mu_p(x,\omega)$ are uniformly bounded functions of $x \in D$ and $\omega \in \Omega$, i.e.,

$$\begin{aligned} 0 < \mu_n^- \leq \mu_n(x,\omega) \leq \mu_n^+ < \infty \qquad & \forall x \in D, \quad \forall \omega \in \Omega, \\ 0 < \mu_p^- \leq \mu_p(x,\omega) \leq \mu_p^+ < \infty \qquad & \forall x \in D, \quad \forall \omega \in \Omega, \end{aligned}$$

   where $\mu_p(x,\omega), \mu_n(x,\omega) \in C^1(D_{\mathrm{Si}} \times \Omega, \mathbb{R}^{3\times 3})$.

   Furthermore, the inclusions $f(x,\omega) \in L^2(\Omega; L^2(D)) \cap L^\infty(D \times \Omega)$, $V_D(x) \in H^{1/2}(\partial D) \cap L^\infty(\Gamma)$, $u_D, v_D(x) \in H^{1/2}(\partial D_{\mathrm{Si}})$, $\alpha(x,\omega) \in L^2(\Omega; H^{1/2}(\Gamma))$, and $\gamma(x,\omega) \in L^2(\Omega; L^2(\Gamma))$ hold.

Assumptions (3) and (7) guarantee the uniform ellipticity of the Poisson and the continuity equations, respectively.

2.2.4 Weak solution of the model equations

In order to define the weak formulation of the stochastic boundary-value problem (2.23), it suffices to consider the semilinear boundary-value problem [145]

$$-\nabla \cdot (A^*(x,\omega)\nabla w(x,\omega)) + h(x, w(x,\omega)) = f(x,\omega) \quad \forall x \in D \setminus \Gamma \quad \forall \omega \in \Omega, \tag{2.26a}$$

$$w(x,\omega) = w_D(x) \quad \forall x \in \partial D_D \quad \forall \omega \in \Omega, \tag{2.26b}$$

$$\mathbf{n} \cdot \nabla w(x,\omega) = 0 \quad \forall x \in \partial D_N \quad \forall \omega \in \Omega, \tag{2.26c}$$

$$w(0+,y,\omega) - w(0-,y,\omega) = \alpha(y,\omega) \quad \forall x \in \Gamma \quad \forall \omega \in \Omega, \tag{2.26d}$$

$$A^*(0+)\partial_x w(0+,y,\omega) - A^*(0-)\partial_x w(0-,y,\omega) = \gamma(y,\omega) \quad \forall x \in \Gamma \quad \forall \omega \in \Omega, \tag{2.26e}$$

which is a semilinear Poisson equation with interface conditions. Here (2.26a) includes (2.23a)–(2.23c) if A^* is replaced by the permittivity A, and it includes (2.23f) and (2.23g) if A^* is replaced by $\mu_n \mathrm{e}^{V/U_T}$ and $\mu_p \mathrm{e}^{-V/U_T}$, respectively. Uniform ellipticity holds in each of these cases per Assumption (2.2.3).

For the weak formulation, we define the Hilbert space

$$X := H^1_g(D) = \{ w \in H^1(D) \mid Tw = g \} \tag{2.27}$$

as the solution space, where T is the trace operator defined such that $Tw = g$, where g is Dirichlet lift of $w_D := w|_{\partial D_D}$. The operator T is well-defined and continuous from

$H^1(D)$ onto $H^{1/2}(\partial D)$ for the Lipschitz domain D. For $g = 0$, we define the test space

$$X_0 := H_0^1(D) = \left\{ w \in H^1(D) \mid Tw = 0 \right\}. \tag{2.28}$$

Definition 2.1 (Bochner spaces)**.** Given a Banach space $(X, \|\cdot\|_X)$ and $1 \le p \le +\infty$, the *Bochner space* $L^p(\Omega; X)$ is defined to be the space of all measurable functions $w\colon \Omega \to X$ such that for every $\omega \in \Omega$ the norm

$$\|w\|_{L^p(\Omega;X)} := \begin{cases} \left(\int_\Omega \|w(\cdot,\omega)\|_X^p \mathrm{d}\mathbb{P}(\omega) \right)^{1/p} = \mathbb{E}\left[\|w(\cdot,\omega)\|_X^p \right]^{1/p} < \infty, & 1 \le p < \infty, \\ \operatorname{ess\,sup}_{\omega\in\Omega} \|w(\cdot,\omega)\|_X < \infty, & p = \infty \end{cases} \tag{2.29}$$

is finite.We should remind that the essential supremum of a function is the smallest number $a \in \bar{\mathbb{R}}$ for which the function only exceeds a on a set of measure zero.

To derive the variational formulation of our model (2.26), we fix the event $\omega \in \Omega$ at first, multiply ((2.26a)) by a test function $\phi \in L^2(\Omega; X_0)$, and integrate by parts in D to obtain the relation

$$\int_D A^* \nabla w \cdot \nabla \phi + \int_D h(w)\phi = \int_D f\phi + \int_\Gamma \gamma\phi \qquad \forall \phi \in L^2(\Omega; X_0).$$

Definition 2.2 (Weak solution on $D \times \Omega$)**.** Suppose that A^* satisfies Assumptions (2.2.3) and that $f(x,\omega) \in L^2(\Omega; L^2(D))$, $w_D(x) \in H^{1/2}(\partial D_D)$, and $\gamma(x,\omega) \in L^2(\Omega; L^2(\Gamma))$ holds. A function $w \in L^2(\Omega; X)$ is called a *weak solution* of the boundary-value problem ((2.26)), if it satisfies

$$a(w,\phi) = \ell(\phi) \qquad \forall \phi \in L^2(\Omega; X_0), \tag{2.30}$$

where $a\colon L^2(\Omega; X) \times L^2(\Omega; X_0) \to \mathbb{R}$ and $\ell\colon L^2(\Omega; X_0) \to \mathbb{R}$ are defined by

$$a(w,\phi) := \mathbb{E}\left[\int_D A^* \nabla w \cdot \nabla \phi \mathrm{d}x \right] + \mathbb{E}\left[\int_D h\left(w\right) \phi \mathrm{d}x \right]$$

and

$$\ell(\phi) := \mathbb{E}\left[\int_D f\phi \mathrm{d}x \right] + \mathbb{E}\left[\int_\Gamma \gamma\phi \mathrm{d}x \right].$$

2.2.5 Scharfetter-Gummel iteration

Newton's method is a coupled procedure which solves the equations (2.18) simultaneously, through a generalization of the Newton–Raphson method for determining the roots of an equation. We rewrite the problem in the following residual form

$$W_V(V,n,p) = 0, \quad W_n(V,n,p) = 0, \quad W_p(V,n,p) = 0. \tag{2.31}$$

Starting from an initial guess V_0, n_0, and p_0, the corrections δV , δn, and δp, are calculated from the Jacobian system

$$\begin{bmatrix} \frac{\partial W_V}{\partial V} & \frac{\partial W_V}{\partial n} & \frac{\partial W_V}{\partial p} \\ \frac{\partial W_n}{\partial V} & \frac{\partial W_p}{\partial n} & \frac{\partial W_n}{\partial p} \\ \frac{\partial W_p}{\partial V} & \frac{\partial W_p}{\partial n} & \frac{\partial W_p}{\partial p} \end{bmatrix} \begin{bmatrix} \partial V \\ \partial n \\ \partial p \end{bmatrix} = \begin{bmatrix} \partial W_V \\ \partial W_n \\ \partial W_p \end{bmatrix}, \tag{2.32}$$

which is obtained by Taylor expansion. The solutions are then updated according to the scheme

$$\begin{aligned} V_{k+1} &= V_k + \partial V_k \\ n_{k+1} &= n_k + \partial n_k \\ p_{k+1} &= p_k + \partial p_k \end{aligned}$$

where k indicates the iteration number. The system (2.32) has 3 equations for each mesh point on the grid. Denoting by N_{dof} the number of degrees of freedom (dofs), each block of (2.32) is an $N_{\text{dof}} \times N_{\text{dof}}$ matrix size. This indicates the main disadvantage of a full Newton iteration, related to the computational cost of matrix inversion (one may estimate that a $3N_{\text{dof}} \times 3N_{\text{dof}}$ matrix takes typically 20 times longer to invert than an analogous $N_{\text{dof}} \times N_{\text{dof}}$ matrix. Moreover, it is important to provide a very good initial guess vector (V_0, n_0, p_0). Because the problem variables have different orders of magnitude and the Jacobian matrix is often quite ill-conditioned, appropriate scaling and balancing techniques are needed in order to avoid problems associated with round-off error.

In 1964, H. K. Gummel proposed an original and alternative to (2.32) approach in order to solve the system (2.18) in a semiconductor device in one spatial dimension [68]. The main idea of the algorithm is to move the nonlinearity to the Poisson equation only, and once obtained the electric potential profile, both continuity equations are solved in linear form. This is possible if we consider the Maxwell-Boltzmann approximation for electrons and holes. However, we should note that there are some limitations in source/drain regions (since they are highly doped) and in the inversion layer.

2.2.6 Existence and local uniqueness of the solution

In the next step, we prove existence and local uniqueness of solutions of system of stochastic elliptic boundary-value problems with interface conditions (2.23) [145] using the Schauder fixed-point theorem and the implicit-function theorem similarly to [13, Theorem 2.2 and 5.2].

Theorem 2.3 (Existence)**.** *Under Assumptions* (2.2.3)*, for every* $f(x,\omega) \in L^2(\Omega; L^2(D))$ *and* $V_D, u_D, v_D \in H^{1/2}(\partial D)$*, there exists a weak solution*

$$\begin{aligned} (V(x,\omega), u(x,\omega), v(x,\omega), \alpha(x,\omega), \gamma(x,\omega)) \in \big(L^2(\Omega; H^1_{V_D}(D) \cap L^\infty(D \times \Omega)\big) \\ \times \big(L^2(\Omega; H^1_{u_D}(D_{\text{Si}})) \cap L^\infty(D_{\text{Si}} \times \Omega)\big) \times \big(L^2(\Omega; H^1_{v_D}(D_{\text{Si}})) \cap L^\infty(D_{\text{Si}} \times \Omega)\big) \\ \times \big(L^2(\Omega; H^1(\Gamma)) \cap L^\infty(\Gamma \times \Omega)\big)^2 \end{aligned}$$

of the stochastic boundary-value problem (2.23), and for every $\omega \in \Omega$ it satisfies the L^∞-estimate

$$\begin{aligned} \underline{V} \le V(x,\omega) \le \overline{V} \qquad & \text{in } D, \\ \frac{1}{K} \le u(x,\omega) \le K \qquad & \text{in } D_{\mathrm{Si}}, \\ \frac{1}{K} \le v(x,\omega) \le K \qquad & \text{in } D_{\mathrm{Si}}, \end{aligned}$$

where

$$\begin{aligned} \underline{V} &:= \min(\inf_{\partial D_D} V_D, \Phi - \sup_D V_L, U_T \ln(\frac{1}{2Kn_i}(\underline{C} + \sqrt{\underline{C}^2 + 4n_i^2})) - \sup_D V_L), \\ \overline{V} &:= \max(\sup_{\partial D_D} V_D, \Phi - \inf_D V_L, U_T \ln(\frac{K}{2n_i}(\overline{C} + \sqrt{\overline{C}^2 + 4n_i^2})) - \inf_D V_L). \end{aligned}$$

Here $V_L(x,\omega)$ is the solution of the linear problem (i.e., problem (2.26) with $h \equiv 0$), for which the estimate

$$\|V_L\|_{L^2(\Omega;H^1_{V_D}(D))} \le C \left(\|f\|_{L^2(\Omega;L^2(D))} + \|V_D\|_{H^{1/2}(\partial D_D)} + \|\alpha\|_{L^2(\Omega;H^{1/2}(\Gamma))} + \|\gamma\|_{L^2(\Omega;L^2(\Gamma))} \right)$$

holds, where C is a positive constant.

Proof. The existence of the solution is proved using the Schauder fixed-point theorem and the estimates are obtained from a maximum principle. First, we define a suitable space

$$\begin{aligned} N := \big\{ (V,u,v,\alpha,\gamma) \in L^2(\Omega;H^1(D)) \times L^2(\Omega;H^1(D_{\mathrm{Si}}))^2 \times L^2(\Omega;H^1(\Gamma))^2 \mid \\ \underline{V} \le V(x,\omega) \le \overline{V} \quad \text{a.e. in } D \times \Omega, \quad \frac{1}{K} \le u(x,\omega), v(x,\omega) \le K \quad \text{a.e. in } D_{\mathrm{Si}} \times \Omega, \\ \alpha, \gamma \text{ bounded a.e. on } \Gamma \times \Omega \big\}, \end{aligned}$$

which is closed and convex. Then we define a fixed-point map $F\colon N \to N$ by

$$F(V_0,u_0,v_0,\alpha_0,\gamma_0) := (V_1,u_1,v_1,\alpha_1,\gamma_1),$$

where the elements of the vector $(V_1,u_1,v_1,\alpha_1,\gamma_1)$ are the solutions of the following equations for given data $(V_0,u_0,v_0,\alpha_0,\gamma_0)$.

1. Solve the elliptic equation

$$\begin{aligned} -\nabla \cdot (A \nabla V_1) = qn_i(e^{-V_1/U_T} v_0 - e^{V_1/U_T} u_0) + qC_{\mathrm{dop}} \quad & \text{in } D, \\ \mathbf{n} \cdot \nabla V_1 = 0 \quad & \text{on } \partial D_N, \\ V_1 = V_D \quad & \text{on } \partial D_D \end{aligned}$$

   for V_1.

2. Solve the elliptic equation

$$\begin{aligned} U_T \nabla \cdot (\mu_n e^{V_1/U_T} \nabla u_1) \\ -\frac{u_1 v_0 - 1}{\tau_p(e^{V_1/U_T} u_0 + 1) + \tau_n(e^{-V_1/U_T} v_0 + 1)} &= 0 \quad \text{in } D_{\mathrm{Si}}, \\ \mathbf{n} \cdot \nabla u_1 &= 0 \quad \text{on } \partial D_{\mathrm{Si},N}, \\ u_1 &= u_D \text{ on } \partial D_{\mathrm{Si},D} \end{aligned}$$

for u_1.

3. Solve the elliptic equation

$$\begin{aligned} U_T \nabla \cdot (\mu_p e^{-V_1/U_T} \nabla v_1) \\ -\frac{u_0 v_1 - 1}{\tau_p(e^{V_1/U_T} u_0 + 1) + \tau_n(e^{-V_1/U_T} v_0 + 1)} &= 0 \quad \text{in } D_{\mathrm{Si}} \\ \mathbf{n} \cdot \nabla v_1 &= 0 \quad \text{on } \partial D_{\mathrm{Si},N}, \\ v_1 &= v_D \text{ on } \partial D_{\mathrm{Si},D}, \end{aligned}$$

for v_1.

4. Update the surface-charge density and dipole-moment density according to the microscopic model

$$\begin{aligned} \alpha_1(y,\omega) &:= M_\alpha(V_0), \\ \gamma_1(y,\omega) &:= M_\gamma(V_0). \end{aligned}$$

Using lemmata on the existence and uniqueness of solutions of elliptic boundary-value problems with interface conditions, every equation present in the model is uniquely solvable. Therefore the map F is well-defined. Furthermore, continuity and the self-mapping property of F as well as the precompactness of $F(N)$ can be shown similarly to [13, Theorem 2.2]. Therefore, applying the Schauder fixed-point theorem yields a fixed-point of F, which is a weak solution of (2.23). □

In general, the solution in Theorem (2.3) is not unique; uniqueness of the solution only holds in a neighborhood around thermal equilibrium. The following theorem yields local uniqueness of the solution of our system (2.23) of model equation. The proof is based on the implicit-function theorem.

Theorem 2.4 (Local uniqueness)**.** *Under Assumption* (2.2.3)*, for every* $f(x,\omega) \in L^2(\Omega; L^2(D))$*,* $V_D, u_D, v_D \in H^{1/2}(\partial D)$*,* $\alpha \in L^2(\Omega; H^{1/2}(\Gamma))$*, and* $\gamma \in L^2(\Omega; L^2(\Gamma))$*, there exists a sufficiently small* $\sigma \in \mathbb{R}$ *with* $|U| < \sigma$ *such that the stochastic problem in the existence theorem* (2.3) *has a locally unique solution*

$$\begin{aligned} \Big(V^*(U), u^*(U), v^*(U), \alpha^*(U), \gamma^*(U)\Big) &\in L^2(\Omega; H^2(D \setminus \Gamma)) \times L^2(\Omega; H^2(D_{\mathrm{Si}}))^2 \\ &\quad \times L^2(\Omega; H^{1/2}(\Gamma)) \times L^2(\Omega; L^2(\Gamma)). \end{aligned}$$

The solution satisfies

$$\Big(V^*(0), u^*(0), v^*(0), \alpha^*(0), \gamma^*(0)\Big) = (V_e, 1, 1, \alpha_e, \gamma_e)$$

and it depends continuously differentiably on U *as a map from* $\{U \in \mathbb{R}^k,\ |U| < \sigma\}$ *into* $L^2(\Omega; H^2(D \setminus \Gamma)) \times L^2(\Omega; H^2(D_{\mathrm{Si}}))^2 \times L^2(\Omega; H^{1/2}(\Gamma)) \times L^2(\Omega; L^2(\Gamma))$.

Proof. We call the equilibrium potential $V_e(x,\omega)$ and the equilibrium surface densities $\alpha_e(x,\omega)$ and $\gamma_e(x,\omega)$. $(V_e, 1, 1, \alpha_e, \gamma_e)$ is a solution of the stochastic equilibrium boundary-value problem, which has a unique solution due to the existence and uniqueness of solutions of stochastic semilinear elliptic boundary-value problems of the form

$$\begin{aligned}
-\nabla \cdot (A(x,\omega)\nabla V_e(x,\omega)) &= qC_{\mathrm{dop}}(x,\omega) - qn_i(e^{V_e(x,\omega)/U_T} - e^{-V_e(x,\omega)/U_T}) && \text{in } D_{\mathrm{Si}},\\
-\nabla \cdot (A(x,\omega)\nabla V_e(x,\omega)) &= 0 && \text{in } D_{\mathrm{ox}},\\
-\nabla \cdot (A(x,\omega)\nabla V_e(x,\omega)) &= -2\eta \sinh(\beta(V_e(x,\omega) - \Phi(x,\omega))) && \text{in } D_{\mathrm{liq}},\\
V_e(0+,y,\omega) - V_e(0-,y,\omega) &= \alpha_e(y,\omega) && \text{on } \Gamma,\\
A(0+)\partial_x V_e(0+,y,\omega) - A(0-)\partial_x V_e(0-,y,\omega) &= \gamma_e(y,\omega) && \text{on } \Gamma,\\
V_e(x,\omega) &= V_D(x) && \text{on } \partial D_D,\\
\mathbf{n} \cdot \nabla V_e(x,\omega) &= 0 && \text{on } \partial D_N.
\end{aligned}$$

To apply the implicit-function theorem, we define the map

$$\begin{aligned}
&G\colon B \times S_{\sigma_1(0)} \to L^2(\Omega; L^2(D)) \times L^2(\Omega; L^2(D_{\mathrm{Si}}))^2 \times L^2(\Omega; L^2(\Gamma))^2,\\
&G(V, u, v, \alpha, \gamma, U) = 0,
\end{aligned}$$

where G is given by the boundary-value problem (2.23) after substituting $\overline{V} := V - V_D(U)$, $\overline{u} := u - u_D(U)$, and $\overline{v} := v - v_D(U)$. B is an open subset of $L^2(\Omega; H^2_\partial(D)) \times L^2(\Omega; H^2_\partial(D_{\mathrm{Si}}))^2 \times L^2(\Omega; L^2(\Gamma))^2$ with

$$H^2_\partial(D) := \{\phi \in H^2(D) \mid \mathbf{n} \cdot \nabla\phi = 0 \text{ on } \partial D_N,\ \phi = 0 \text{ on } \partial D_D\},$$

and the sphere S_{σ_1} with radius σ_1 and center 0 is a subset of $\mathbb{R}^d$. The equilibrium solution $(V_e - V_D(0), 0, 0, \alpha_e, \gamma_e, 0)$ is a solution of the equation $G = 0$. One can show that the Fréchet derivative $D_{(V,u,v,\alpha,\gamma)}G(V_e - V_D(0), 0, 0, \alpha_e, \gamma_e, 0)$ has a bounded inverse (see, e.g., [13, Theorem 2.2]). Then the implicit-function theorem implies uniqueness of the solution of (2.23). □

2.3 Transport equation for confined structure

The fundamental transport equation for large-scale systems is the Boltzmann transport equation [74, 75]. Its independent variables are time, three space, and three momentum dimensions; therefore, calculating numerical approximations to its solutions is very computationally expensive. Popular stochastic approaches for the calculation of currents through ion channels such as Monte Carlo or Brownian dynamics [79, 161] and

molecular dynamics are valuable to elucidate various aspects, but also require a huge computational effort when currents are calculated. However, only currents are measured in experiments. In order to overcome this problem, we have derived a $(2+1)$-dimensional transport equation from the $(6+1)$-dimensional Boltzmann transport equation to simulate geometrically complicated structures and to decrease the computational cost of current calculations [74, 85].

Here confined structures are understood as long, narrow 3D geometries where the transport of the particles occurs in one space dimension, namely the longitudinal direction, due to the presence of potential wells in the two transverse dimensions. The potential wells responsible for the confinement can vary along the transport direction and are given as functions of position. The independent variables in the $(2+1)$-dimensional transport equation are position along the longitudinal direction, local particle energy, and time. In the case of harmonic confinement potentials, i.e., when they are quadratic functions of position, it was even possible to find explicit expressions for the transport coefficients [74].

This is an essential feature of the present model: the confinement potentials determine the local fluxes and hence the transport coefficients [75]. This is an important improvement compared to using bulk transport coefficients for the simulation of extremely small structures and it means that the physical properties of the channels and especially their selectivity filters are captured. Since the transport coefficients are given by explicit expressions, the numerical solution of the transport equation is as computationally expensive as the solution of a diffusion equation with constant transport coefficients so that currents are obtained with relatively small computational effort. Therefore this transport equation for confined structures is ideally suited for the simulation of ion channels.

Due to the physiological importance of ion channels [106], this transport model is applied to three transmembrane proteins here, namely the phosphate-specific channel OprP (an antibiotic), the Gramicidin A channel (another antibiotic), and the well-known KcsA ionic channel. In each case, the model is validated by comparison with current measurements of various ions. Then we elucidate physiological properties of the channels. For example, the selectivity of potassium channels between sodium and potassium is its primary physiological function and therefore it is investigated in the simulations. The model reproduces selectivity. We also constructed virtual ion channels by changing the length of the selectivity filter in order to answer the question if and in which respect the natural KcsA channel is optimal.

We recapitulate the transport equation and its relation to the given confinement potential in this Section. Throughout [74], the calculations were performed using dimensionless variables and the theoretical feasibility of this approach was demonstrated. In [75], the derivation of the transport equation was extended so that all variables have physical units and a complete discussion of all the units can be found there as well.

The starting point is the Boltzmann transport equation in the form

$$\partial_t f + \{\mathcal{E}, f\}_{XP} + \mathcal{Q}[f] = 0, \tag{2.33}$$

where the Poisson bracket is defined as

$$\{g, f\}_{XP} := \nabla_P g \cdot \nabla_X f - \nabla_X g \cdot \nabla_P f. \tag{2.34}$$

Here $f(X, P, t)$ is the kinetic particle density, $X \in \mathbb{R}^3$ is position, $P \in \mathbb{R}^3$ is momentum, t is time, $E(X, P)$ is the energy, and $\mathcal{Q}$ is the scattering operator. The energy is defined as

$$\mathcal{E}(X, P) := V(X) + \frac{|P|^2}{2m},$$

being the sum of the potential energy V of the confinement and the kinetic energy. m denotes the mass of a particle.

The spatial multiscale problem arises, since the structures are much narrower than long. We write the confinement potential as

$$V(x, y) = V_0(x) + V_1(x, y), \tag{2.35}$$

where V_0 is the applied potential, and we will rescale in (2.36a) below.

Here we consider 3D structures that are confined in two dimensions such that transport occurs in one dimension. Therefore we split position X and momentum P into

$$X = (x, y) = (x, y_1, y_2),$$
$$P = (p, q) = (p, q_1, q_2),$$

where x is the longitudinal direction of charge transport and y_1 and y_2 are the two transverse directions of confinement. Accordingly, p is the momentum in the longitudinal direction and q_1 and q_2 are the momenta in the transverse directions. We also split the energy $\mathbb{E}$ into two contributions $\mathbb{E}_x$ and $\mathbb{E}_y$ from the longitudinal and transverse directions, respectively, i.e.,

$$\mathbb{E}(X, P) = \mathbb{E}_x(x, p) + \mathbb{E}_y(x, y, q),$$
$$\mathbb{E}_x(x, p) := V_0(x) + \frac{|p|^2}{2m},$$
$$\mathbb{E}_y(x, y, q) := V_1(x, y) + \frac{|q|^2}{2m}.$$

The scattering operator $\mathcal{Q}$ is defined such that it describes the physical system correctly. In the transport (longitudinal) x-direction, it relaxes the density towards a Maxwellian distribution, whereas in the confinement (transverse) y-direction it conserves the local energy so that the particles do not lose or gain energy on average by colliding with the sidewalls of the structure, i.e., there is no net energy transfer between the particles and the sidewalls. The scattering operator is a relaxation operator and it has the form

$$\mathcal{Q}[f](x, y, p, q, t) := \frac{1}{\tau}\left(f - M(p)\frac{u_f(x, E_y(x, y, q), t)}{N(x, E_y(x, y, q))}\right).$$

The details of the operator can be found in [74, Section 2.1]. Then, in [74, Section 2.2], all variables were scaled and transformed into a dimensionless formulation. Here,

however, we only scale the confinement direction y and time t by setting

$$y_s := \frac{y}{\epsilon}, \tag{2.36a}$$

$$t_s := \epsilon t. \tag{2.36b}$$

We consider the limit $\epsilon \to 0$. Regarding the spatial multiscale problem, this means that the width $\epsilon \ll 1$ of the structure is very small corresponding to pores that are much longer than wide. Regarding the temporal multiscale problems, this scaling in conjunction with the scattering operators means that we are interested in time scales where diffusion is the dominant mechanism. We now simplify notation by using the same variable names as before the scaling; additionally, in order to be consistent with the notation in [74], we set $v := p$ and $w := q$, but note that v and w denote momenta.

Dramatic simplifications are possible when assumptions on the form of the confinement potential, and especially in the form of $V_1(x, y)$, are made. We assume that $V_1(x, y)$ has the quadratic form

$$V_1(x, y) = \frac{1}{2}\left(B_1(y_1 - b_1)^2 + B_2(y_2 - b_2)^2\right), \tag{2.37}$$

where $y, b \in \mathbb{R}^2$. In this case, the confinement potential is called harmonic. Of course, it is required that $B_1(x) > 0$ and $B_2(x) > 0$ for all x so that the particles are indeed confined.

Finally, a diffusion-type equation for transport through a confined structure can be found. Its coefficients are given by the coefficients of the confinement potential. The equation is the conservation law

$$\partial_t \rho(x, \eta, t) + \partial_x F^x(x, \eta, t) + \partial_\eta F^\eta(x, \eta, t) = 0, \tag{2.38}$$

where $\rho(x, \eta, t)$ is the charge concentration. Also, the three independent variables are x, the longitudinal position, η, the local energy in the transverse direction, and time t.

The two fluxes F^x and F^η are

$$F^x(x, \eta, t) = -\frac{4\pi^2 kT\tau\eta}{\sqrt{B_1 B_2}} T_1 - \frac{\pi^2 kT\tau\eta^2}{\sqrt{B_1 B_2}}\big(\partial_x(\ln B_1) + \partial_x(\ln B_2)\big) T_2 \tag{2.39}$$

and

$$\begin{aligned} F^\eta(x, \eta, t) = &-\frac{\pi^2 kT\tau\eta^2}{\sqrt{B_1 B_2}}\big(\partial_x(\ln B_1) + \partial_x(\ln B_2)\big) T_1 \\ &- \frac{\pi^2 kT\tau\eta^2}{6\sqrt{B_1 B_2}}\left(\frac{12mB_1(\partial_x b_1)^2}{m + \tau^2 B_1} + \frac{12mB_2(\partial_x b_2)^2}{m + \tau^2 B_2} + 2\eta\partial_x(\ln B_1)\partial_x(\ln B_2)\right. \\ &\left. + \frac{\eta(3m + 8\tau^2 B_1)(\partial_x(\ln B_1))^2}{m + 4\tau^2 B_1} + \frac{\eta(3m + 8\tau^2 B_2)(\partial_x(\ln B_2))^2}{m + 4\tau^2 B_2}\right) T_2, \end{aligned} \tag{2.40}$$

where

$$T_1 := \mathrm{e}^{-V_0/kT}\nabla_x\big(\mathrm{e}^{V_0/kT}\frac{\rho}{N}\big),$$
$$T_2 := \mathrm{e}^{-\eta/kT}\nabla_\eta\big(\mathrm{e}^{\eta/kT}\frac{\rho}{N}\big),$$

and τ is the relaxation time. Regarding the units, we have

$$[F^x] = \frac{\mathrm{s}}{\mathrm{kg}\cdot\mathrm{m}^2}, \qquad [F^\eta] = \frac{1}{\mathrm{m}\cdot\mathrm{s}}, \qquad [\tau] = s,$$

and therefore

$$[\partial_t\rho] = [\nabla_x \cdot F^x] = [\partial_\eta F^\eta] = \frac{\mathrm{s}}{\mathrm{kg}\cdot\mathrm{m}^3}.$$

The computational significance is that this $(2+1)$-dimensional equation can be solved fast numerically in contrast to the original $(6+1)$-dimensional problem. For the details of the derivation, the reader is referred to [74, 75].

2.3.1 Current calculation

Here the total current can immediately be found by integrating the flux F^x in the longitudinal direction over all local energies η, i.e., the total current I is

$$I = \int_{\eta=0}^{\infty} F^x(x_0,\eta)\mathrm{d}\eta,$$

which does not depend on the particular cross section given by x_0 and the ion charge is included (using the potential of mean force, PMF (see Section 4.4.1)). In Chapter 4, we apply this method to calculate the current due to the passage of different ions through three particular channels, namely OprP, Gramicidin A, and the well-known KcsA ionic channel.

2.4 Stochastic Langevin equation

The binding and unbinding events of target molecules are described as a stochastic process that occurs in the boundary layer [152, 154]. It is crucial for the understanding of the sensing principle of field-effect sensors devices. In the case of a DNA sensor, the binding and unbinding events are the hybridization and dehybridization of mobile single DNA strands to be detected with immobilized single DNA strands of known sequence to form a double-helix. The overall double-helix formation, which depends on the rate of DNA transport and on the rate of the hybridization reaction, has been studied by many research groups. In fact, the binding and unbinding depends on different effects including, e.g., specific and non-specific binding processes and the hybridization of mismatched and partially matched DNA strands. These processes, due to their stochastic

nature, result in a random signal fluctuation and hence in noise. The transport of target molecules in the analyte solution to the active sensor surface must be taken into account in order to calculate time-dependent simulations. The time until the number of probe-target complexes has reached its chemical equilibrium (or until at least a detectable quantity has bound to the probe molecules at the sensor surface) determines the response time of the sensor. The chemical equilibrium is understood as a balance between association and dissociation events [152].

In order to obtain a more realistic model of the sensing process, it is not sufficient to consider the hybridization/dissociation dynamics at the surface. Rather, it is crucial to take the limited transport of the DNA molecules through the liquid into account, as especially in the case of low target molecule concentrations, the hybridization characteristics are changed significantly by this process. A thorough investigation and a quantification of the resulting effects are the objectives of this dissertation. Here, we present a model describing the surface interactions as stochastic processes and including a transport model for the biomolecules in the liquid.

2.4.1 Interaction processes

The dynamic process of binding and unbinding of the respective species, or hybridization and dissociation, again changes the surface charge density and hence the electrical characteristics of the nanowire, which allows detection of the binding processes in measurements. The association and dissociation processes of target molecules at the surface can be described by the reaction equations

$$\mathbf{T} + \mathbf{P} \xrightarrow{r_a} \mathbf{PT}, \tag{2.41a}$$

$$\mathbf{PT} \xrightarrow{r_d} \mathbf{P} + \mathbf{T}. \tag{2.41b}$$

Equation (2.41a) describes the binding of target molecules $\mathbf{T}$ at time t (target-molecule concentration), to probe molecules $\mathbf{P}$ (target-molecule concentration), thus forming the probe-target complex $\mathbf{PT}$ (probe-target concentration). Furthermore, we should note that $[\mathbf{P}] = [\mathbf{PT}] = [\mathrm{cm}^{-2}]$ and $[\mathbf{T}] = M$.

Analogously, equation (2.41b) describes a dissociation processes, in which probes and target molecules are formed from a complex $\mathbf{PT}$. Moreover, the constants r_a and r_b are reaction constants regarding the association and dissociation constants respectively. The stochastic Langevin equation is the most widely known mathematical model for the phenomenon of Brownian motion. It is a first order differential equation (ODE) which contains a stochastic term corresponding to a random force. We can rewrite this equation in the form

$$\frac{\mathrm{d}\mathbf{PT}(t)}{\mathrm{d}t}(t) = r_a C_T (C_P - \mathbf{PT}(t)) - r_d \mathbf{PT}(t), \tag{2.42}$$

$$\mathbf{PT}(0) = 0. \tag{2.43}$$

where C_T and C_P are respectively probe concentration (at the surface, $[\mathrm{cm}^{-2}]$) and target concentration (in the liquid, [M] (molar)). The above initial condition indicates

that there are no probe-target complexes presents at the surface in the beginning. From that equation, the concentration at the surface can be computed at any time. This is a kind of partial differential equation which can be easily solved, yielding

$$\mathbf{PT}(t) = \frac{r_a C_P C_T}{r_a C_T + r_d}(1 - \exp^{-(r_a C_T + r_d)t}). \tag{2.44}$$

For more technical details about the introduced model we strongly recommend the interested reader to [64, 77].

2.4.2 The stochastic process at the functionalized surface

To make the system of equations more realistic a we consider (2.43) as a stochastic model. To this end, We consider a sensor surface that is immersed in an aqueous solution containing target molecules. We continue to use the notation **P** for probe molecules, **T** for target molecules, and **PT** for probe-target complexes. The reactive solid surface with area A is functionalized with C_P probe molecules per unit area, and the liquid contains target molecules with the unit of mole per liter, and the initial concentration of probe-target complexes at the surface is assumed to be zero. In order to quantify the biological noise of the system, we treat the reaction at the surface as a stochastic process, i.e., the binding of probe and target molecules occurs in an essentially random manner. Langevin equations for chemical reactions in a fixed volume have been discussed recently. Here we obtain the Langevin equation for an association/dissociation process at a surface [152]. We consider a system of n probe molecules at time $t = j\tau$, $j \in 0, 1, ...$ The variables ω_i^j, $j \in 1, 2, \ldots, n$, are independent random variables for the indicator function. Here $\omega_i^j := 1$ if the ith probe molecule is bound at time $t = j\tau$ and is zero otherwise. Using the indicator function, the number of probe-target complexes **PT** can be written as $\sum_{i=1}^{n} \omega_i^j$ and the number of probe molecules **PT** at time t can be written as $n - \sum_{i=1}^{n} \omega_i^j$. Now we define a new random variable

$$X_t := \frac{1}{A} \sum_{i=1}^{n} \omega_i^j. \tag{2.45}$$

Lemma 1. Let $d[B_1(t)]/[\mathrm{d}t]$ and $\mathrm{d}[B_2(t)]/[\mathrm{d}t]$ be statistically independent Gaussian white-noise processes describing the association and dissociation process, respectively. The evolution of X_t from a given initial state X_0 is governed by the stochastic process equation

$$\frac{\mathrm{d}X_t(t)}{\mathrm{d}t} = r_a(C_P - X_t)C_T - r_d X_t + \sqrt{r_a(C_P - X_t)C_T}\frac{\mathrm{d}B_1(t)}{\mathrm{d}t} - \sqrt{r_d X_t}\frac{\mathrm{d}B_1(t)}{\mathrm{d}t}, \tag{2.46}$$

where statistically independent Gaussian white noises are given by

$$\frac{\mathrm{d}B_1(t)}{\mathrm{d}t} = \frac{\mathcal{N}_a(0,1)}{\sqrt{\mathrm{d}t}}, \tag{2.47}$$

$$\frac{\mathrm{d}B_2(t)}{\mathrm{d}t} = \frac{\mathcal{N}_d(0,1)}{\sqrt{\mathrm{d}t}}. \tag{2.48}$$

Note that a sufficient number of events must occur during this time intervals of length τ. See [1] for more details.

To calculate the uncertainty of the system i.e., random binding and unbinding processes we should calculate *expected value* and *standard deviation* of X_t. More precisely speaking X_t is the number **PT** of probe-target complexes at time t.

First, we calculate the expectation. We use the Langevin equation (2.46) and take the expectation of both sides to find [152]

$$\mathrm{d}\mathbb{E}(X_t) = r_a C_T(C_P - \mathbb{E}(X_t))\mathrm{d}t - r_d\mathbb{E}(X_t)\mathrm{d}t + \mathbb{E}(\sqrt{r_a C_T(C_P - X_t)}\mathrm{d}B_1) - \mathbb{E}(\sqrt{r_d X_t}\mathrm{d}B_2) \tag{2.49}$$

To calculate the **expected value**, we take expectation of the above equation. As a result we have

$$\begin{aligned}\mathrm{d}\mathbb{E}(X_t) = r_a C_T(C_P - \mathbb{E}(X_t))\mathrm{d}t - r_a\mathbb{E}(X_t)\mathrm{d}t \\ + \underbrace{\mathbb{E}(\sqrt{r_a C_T(C_P - X_t)}\mathrm{d}B_1)}_{=0} \\ - \underbrace{\mathbb{E}(\sqrt{r_d X_t}\mathrm{d}B_2)}_{=0}\end{aligned}$$

simplifying to

$$\frac{\mathrm{d}\mathbb{E}[X_t]}{\mathrm{d}t} = -\mathbb{E}[X_t](r_d + r_a C_T) + r_a C_P C_T. \tag{2.50}$$

Using same procedure as (2.46), the solution is obtained by

$$\mathbb{E}[X_t] = \frac{r_a C_T C_P}{r_d + r_a C_T}(1 - \exp(-(r_a C_T + r_d)t)). \tag{2.51}$$

In addition to the initial condition $\mathbb{E}(X_t) = 0$.

Second, we calculate the **variance**. We define the variable $H(X_t) = X_t^2$ and we note that it does not explicitly depend on t. Applying Ito's formula, we have

$$\mathrm{d}H(X_t) = 2X_t\mathrm{d}X_t + \mathrm{d}X_t\mathrm{d}X_t. \tag{2.52}$$

Then, we obtain

$$\begin{aligned}\mathrm{d}(X_t^2) = (r_a C_T C_P + (2r_a C_T C_P - r_a C_T + r_d)X_t)\mathrm{d}t - 2(r_a C_T + r_d)X_t^2\mathrm{d}t \\ + 2X_t(\sqrt{r_a C_T(C_P - X_t)}\mathrm{d}B_1 - \sqrt{r_d X_t}\mathrm{d}B_2)\end{aligned}$$

and further the stochastic differential equation

$$\begin{aligned}\frac{\mathrm{d}(X_t)^2}{\mathrm{d}t} = X_t^2(-2r_a C_T - 2r_d) + X_t(r_a C_T(2C_P - 1) + r_d) + r_a C_T C_p \\ + \sqrt{4r_a(C_P - X_t)X_t^2 C_T}\frac{\mathrm{d}[B_1(t)]}{\mathrm{d}t} - \sqrt{4r_d X_t^3}\frac{\mathrm{d}[B_2(t)]}{\mathrm{d}t}.\end{aligned}$$

By taking the expectation, we have

$$\frac{\mathrm{d}\mathbb{E}[X_t^2]}{\mathrm{d}t} = -\mathbb{E}[X_t^2](2r_aC_T + 2r_d) + E[X_t](r_aC_T(2C_P - 1) + r_d) + r_aC_TC_P. \tag{2.53}$$

For sake of simplicity, we define two variables to make the formulas simpler

$$\alpha := r_aC_PC_T, \tag{2.54}$$
$$\beta := r_aC_T + r_d. \tag{2.55}$$

Then, (2.56) can be rewritten as

$$\frac{\mathrm{d}\mathbb{E}[X_t^2]}{\mathrm{d}t} = \alpha\mathrm{d}t + (2\alpha - r_aC_T + r_d)\mathbb{E}(X_t)\mathrm{d}t - 2\beta\mathbb{E}(X_t^2)\mathrm{d}t. \tag{2.56}$$

With the initial condition $\mathbb{E}(X_t^2) = 0$ we have (by solving above ODE)

$$\mathbb{E}[X_t^2] = \frac{\mathbb{E}[X_t](r_aC_T(2C_P - 1) + r_d) + r_aC_TC_P}{2(r_aC_T + r_d)}(1 - \exp(-2(r_aC_T + r_d)t)) \tag{2.57}$$

In summary, we have found the variance as $\mathbb{V}[X_t] := \mathbb{E}[X_t^2] - \mathbb{E}[X_t]^2$ which can be summarized using the defined notations

$$\mathbb{V}[X_t] = \frac{\alpha}{\beta^2}(1 - \exp\left(r_d + r_aC_T\exp(-\beta t)\right). \tag{2.58}$$

As mentioned before, we calculate the SNR arising from biological noise in this work. The expectation ($\mathbb{E}[X_t]$) of the binding events occurring at time t is considered as the signal and the standard deviation as the noise. We find

$$\mathrm{SNR}(t) := \frac{\mathbb{E}(X_t)}{\sqrt{\mathbb{V}(X_t)}} = \sqrt{\alpha}\frac{1 - \exp(-\beta t)}{(1 - \exp(-\beta t)(r_d + r_aC_T\exp(-\beta t)))}. \tag{2.59}$$

We define X_∞ as the number X_t of bound probe molecules when the system is in equilibrium. In fact, SNR is bounded in time by the inequality

$$0 < \mathrm{SNR}(t) < \sqrt{\frac{r_a}{r_d}C_PC_T}. \tag{2.60}$$

Therefore, we find that

$$\lim_{t\to\infty}\mathrm{SNR}(t) = \sqrt{\frac{r_a}{r_d}C_PC_T}. \tag{2.61}$$

Since $C_T < \infty$, the SNR is bounded in time by the inequality

$$0 < \mathrm{SNR}(t) < \sqrt{\frac{r_a}{r_d}C_PC_T} \qquad \forall t > 0. \tag{2.62}$$

Molecular binding is an attractive interaction between two molecules that results in a stable association in which the molecules are in close proximity to each other. The

binding efficiency (BE) of probe molecules at time t is the fraction of all probe molecules that are bound to target molecules at time t. We can calculate its expected value as

$$\mathbb{E}[\mathrm{BE}(t)] = \frac{r_a C_T}{r_d + r_a C_T}(1 - \exp(-(r_a C_T + r_d)t)), \tag{2.63}$$

as well as its value in equilibrium as

$$\lim_{t\to\infty} \mathbb{E}[\mathrm{BE}(t)] = \frac{r_a C_T}{r_d + r_a C_T}. \tag{2.64}$$

Furthermore, a lower bound for the limit of the standard deviation as $t \to \infty$ is given by

$$0 < \frac{\sqrt{r_a r_d C_P C_T}}{r_a C_T + r_d} \leq \sigma[X_\infty] = \sqrt{\mathbb{V}[X_\infty]}. \tag{2.65}$$

In Section (4.2.2) we will use the stochastic Langevin equation to model the random binding process of cardiac troponin target molecules to the receptors.

2.5 Conclusions

In this chapter, we considered the stochastic drift-diffusion-Poisson equations as the main model equation for describing transport in random environments with many applications. We presented existence and local uniqueness theorems for the weak solution of the system. The method can be used in several microelectronic devices. The model describes how various stochastic processes propagate through a PDE model and result in noise and fluctuations in a transport model. We explained the usefulness of the Scharfetter-Gummel iteration. Also, we described the current calculation in the introduced microelectronic devices in details.

We have used a continuum transport model for confined structures to investigate three kinds of transmembrane channels. The main feature of this diffusion-type transport equation is that the geometry of the confining protein directly determines the transport coefficients in the equation. Its great advantage as a continuum model is the fact that the currents are obtained immediately from the 2D numerical solution by integration over local energy; the numerical solutions of this 2D equation can be calculated quickly.

We have treated the binding and unbinding reactions in the surface layers of field-effect biosensors as a stochastic process and we have obtained the Langevin equation for the association and the dissociation processes at the surface. This allows us to derive explicit formulas for the expectation and the standard deviation of the number of probe-target complexes at the sensor surface and, therefore, the signal-to-noise ratio.

Chapter 3

Stochastic numerical methods

In this chapter, we develop the stochastic numerical method to quantify noise and fluctuation in nano-electronic devices. In many realistic situations, the probability space is highly dimensional. For example, each probe molecule, each target molecule, and each probe-target complex need to be modeled in sensors. In transistors, the number of impurities and their positions are random. The large number of dimensions favors the use of Monte Carlo methods because it is well-known that the convergence rate of standard MC methods is independent of the number of dimensions. On the other hand, it is inversely proportional to the square root of the number of evaluations and here each evaluation requires solving a two- or three-dimensional system of elliptic equations.

These considerations motivate the development of a multilevel Monte Carlo (MLMC) algorithm. In [61], after earlier work [71] on numerical quadrature, it was shown that a multilevel approach and a geometric sequence of timesteps can reduce the order of computational complexity of MC path simulations for estimating the expected value of the solution of a stochastic ordinary differential equation. This is done by reducing the variance and leaving the bias unchanged due to the Euler discretization used as the ODE solver. In [63], the Milstein scheme was used as the ODE solver to improve the convergence rate of the MLMC method for scalar stochastic ordinary differential equations and the method was made more efficient. The new method has the same weak order of convergence, but an improved first-order strong convergence, and it is the strong order of convergence which is central to the efficiency of MLMC methods. In [62], the MLMC method was combined with quasi-Monte Carlo (QMC) integration using a randomized rank-1 lattice rule and the asymptotic order of convergence of MLMC was improved and a lower computational cost was achieved as well.

In [11], an MLMC finite-element method was presented for elliptic partial differential equations with stochastic coefficients. In this problem, the source of randomness lies in the coefficients inside the operator and the coefficient fields are bounded uniformly from above and away from zero. The MLMC error and work estimates are given both for the mean of the solutions and for computation of higher moments. Also, in [33], the same problem was considered and numerical results indicate that the MLMC estimator is not limited to smooth problems. In [95], a multilevel quasi-Monte Carlo finite element

method for a class of elliptic PDEs with random coefficients was presented. The error analysis of QMC was generalized to a multilevel scheme with the number of QMC points dependent on the discretization level and with a level-dependent dimension truncation strategy.

In [27], uniform bounds on the finite-element error were shown in standard Bochner spaces. These new bounds can be used to perform a rigorous analysis of the MLMC method for elliptic problems, and a rigorous bound on the MLMC complexity in a more general case was found. In [147], the finite-element error analysis was extended for the same type of equations posed on non-smooth domains and with discontinuities in the coefficient. In [70], a general optimization of the parameters in the MLMC discretization hierarchy based on uniform discretization methods with general approximation orders and computational costs was developed. In this chapter, we define a global optimization problem which minimizes the computational complexity such that the error bound is less or equal to a given tolerance level. This approach will be applied to both randomly distributed point (Monte Carlo sampling) and quasi-random points.

To speed up the convergence of standard Monte Carlo method, one approach is to use methods which reduce the variance such as the multilevel Monte Carlo method which we applied to the stochastic drift-diffusion-Poisson system. Another approach is to change the choice of applied sequences, meaning that instead of using random sequences, we can replace them with quasi random sequences whose points have correlation and hence better uniformity. Therefore, the quasi-Monte Carlo as a low-discrepancy method leads to faster convergence than standard Monte Carlo method. On the other hand, the big disadvantage of the quasi-Monte Carlo method is that the low-discrepancy sequence applied in this method is deterministic due to correlation between points. Therefore, the quasi-Monte Carlo method is considered as a deterministic algorithm with an error bound which is difficult to estimate. To overcome this problem, one can randomize the method by randomizing the applied sequences using a random shift which is a uniformly distributed vector. The idea of random shifting was first introduced by Cranley and Patterson [40] in the context of good lattice rules. Later, Joe [81] applied the idea of general lattice rules. Then, Tuffin [150] elaborated on the shifted sequences and their discrepancy.

If we use randomized low-discrepancy sequences such as randomly shifted lattice rule, a new method is created which is called randomized quasi-Monte Carlo (RQMC) method. Using the idea of stratification, we can improve the single level RQMC to multilevel randomized quasi-Monte Carlo (MLRQMC) method which we are considering here. In this paper, our main goal is to develop the MLRQMC to an optimal method in solving the stochastic drift-diffusion-Poisson system which has many applications including modeling field-effect transistors. To this end, we define a work function for the MLRQMC method, which calculates the computational cost of solving the stochastic model using the aforementioned numerical method. We aim to minimize this work function such that the estimated error of this method to be less than a given error tolerance. By solving this optimization problem, optimal values such as optimal mesh size of discretization and optimal number of quasi-points are obtained in order to develop an optimized numerical method with the lowest cost of calculation. For this, we also need to calculate

the variance of the MLRQMC method as well as estimation of error for this numerical method in combination with the finite element as the discretization method.

A basis adaptation in homogeneous chaos expansions of random fields was introduced in [148]. The homogeneous Wiener chaos [162] representation of random processes has provided a convenient way to characterize solutions of systems of equations that describe physical phenomena as was demonstrated in [60] and further applied to a wide range of engineering problems. In 3.6.1, we introduce the polynomial chaos expansion (PCE). In this chapter we develop the basis adaptation approach (using the PCE) to quantify the biological noise in the field effect sensors. The numerical implementation and comparison of the results with classical Monte Carlo and the experiments will be given in 4.1.1.

Finally, this chapter is a summary of the advanced numerical models that are explained in [85, 86, 88, 89, 145].

3.1 Monte Carlo finite element method

In part, we first of all briefly recapitulate the Galerkin finite element approximation and fix some notation. It provides the foundation for the following section.

We suppose that the domain D can be partitioned into quasi-uniform triangles or tetrahedra such that sequences $\{\tau_{h_\ell}\}_{\ell=0}^{\infty}$ of regular meshes are obtained. For any $\ell \geq 0$, we denote the mesh size of τ_{h_ℓ} by

$$h_\ell := \max_{K \in \tau_{h_\ell}} \{\operatorname{diam} K\},$$

where for all $K \in \tau_{h_\ell}$, it indicates the radius of the largest ball that can be inscribed. To ensure that the mesh quality does not deteriorate as refinements are made, shape-regular meshes can be used.

Definition 3.1 (Shape regular mesh)**.** A sequence $\{\tau_{h_\ell}\}_{l=0}^{\infty}$ of meshes is *shape regular* if there exists a constant $\kappa < \infty$ independent of ℓ such that

$$\frac{h_K}{\rho_K} \leq \kappa \quad \forall K \in \tau_{h_\ell}.$$

Here ρ_K is the radius of the largest ball that can be inscribed into any $K \in \tau_{h_\ell}$.

Uniform refinement of the mesh can be achieved by regular subdivision. This results in the mesh size

$$h_\ell = r^{-\ell} h_0, \tag{3.1}$$

where h_0 denotes the mesh size of the coarsest triangulation and $r > 1$ is independent of ℓ. The nested family $\{\tau_{h_\ell}\}_{\ell=0}^{\infty}$ of regular triangulations obtained in this way is shape regular.

The Galerkin approximation is the discrete version of the weak formulation in (2.30) of the stochastic elliptic boundary-value problem (2.23). We consider finite element

discretizations with approximations $u_h \in X_{h_\ell}$ of $u \in X$. Given a mesh τ_{h_ℓ}, X is the solution space (2.27) and $X_{h_\ell} \subset X$ is the discretized space. For all $k \geq 1$, it is defined as

$$X_{h_\ell} := \mathbb{P}^k(\tau_{h_\ell}) := \{u \in X \mid u|_K \in \mathbb{P}^k(K) \ \forall K \in \tau_{h_\ell}\}, \tag{3.2}$$

where $\mathbb{P}^k(K) := \operatorname{span}\{x^\alpha \mid |\alpha| \leq k\}$ is the space of polynomials of total degree less equal k. The space X_0 is the space (2.28) of test functions. The discretized test space $X_{0h_\ell} \subset X_0$ is defined analogously to (3.2).

After introducing the finite element spaces, everything is ready to define the Galerkin approximation.

Definition 3.2 (Galerkin approximation)**.** Suppose $X_{h_\ell} \subset X$ and $X_{0h_\ell} \subset X_0$. The *Galerkin approximation* of (2.26) is the function

$$w_{h_\ell} \in L^2(\Omega; X_{h_\ell})$$

that satisfies

$$B(w_{h_\ell}, \phi_{h_\ell}) = F(\phi_{h_\ell}) \qquad \forall \phi_{h_\ell} \in L^2(\Omega; X_{0h_\ell}), \tag{3.3}$$

where B and F are defined in (2.30).

3.1.1 Monte Carlo finite element approximation

The straightforward Monte Carlo method for a stochastic PDE approximates the expectation $\mathbb{E}[u]$ of the solution u by the sample mean of a (large) number of evaluations. Since we use the same finite element mesh τ with the mesh size h for all samples, we drop the index ℓ in this subsection for the MC-FEM. We approximate $\mathbb{E}[u]$ by $\mathbb{E}[u_h]$, where u_h is again the FE approximation of u using a mesh of size h. The standard MC estimator E_{MC} for $\mathbb{E}[u_h]$ is the sample mean

$$\mathrm{E}_{\mathrm{MC}}[u_h] := \hat{u}_h := \frac{1}{M} \sum_{i=1}^{M} u_h^{(i)}, \tag{3.4}$$

where $u_h^{(i)} = u_h(x, \omega^{(i)})$ is the ith sample of the solution.

The following lemma shows the error of the MC estimator for a random variable u which is not discretized in space is of order $O(M^{-1/2})$.

Lemma 3.3. *For any number of samples $M \in \mathbb{N}$ and for a random variable $u \in L^2(\Omega; X)$, we have [145]*

$$\|\mathbb{E}[u] - \mathrm{E}_{\mathrm{MC}}[u]\|_{L^2(\Omega;X)} = M^{-1/2}\sigma[u] \tag{3.5}$$

holds for the MC error, where $\sigma[u] := \|\mathbb{E}[u] - u\|_{L^2(\Omega;X)}$.

Proof. The result follows from the calculation

$$\begin{aligned}\|\mathbb{E}[u] - \mathrm{E}_{\mathrm{MC}}[u]\|^2_{L^2(\Omega;X)} &= \mathbb{E}\Big[\Big\|\mathbb{E}[u] - \frac{1}{M}\sum_{i=1}^{M} u^{(i)}\Big\|_X^2\Big] \\ &= \frac{1}{M^2}\sum_{i=1}^{M}\mathbb{E}\Big[\|\mathbb{E}[u] - u^{(i)}\|_X^2\Big] \\ &= \frac{1}{M}\mathbb{E}\Big[\|\mathbb{E}[u] - u\|_X^2\Big] = M^{-1}\sigma^2[u].\end{aligned}$$

□

Therefore, the variance of the MC estimator is

$$\sigma^2[\mathrm{E}_{\mathrm{MC}}[u]] = \|\mathbb{E}[\mathrm{E}_{\mathrm{MC}}[u]] - \mathrm{E}_{\mathrm{MC}}[u]\|^2_{L^2(\Omega;X)} = M^{-1}\sigma^2[u]. \tag{3.6}$$

Next, we generalize the result to the finite element solution by using the MC estimator to approximate the expectation $\mathbb{E}[u]$ of a solution u of an SPDE, which is discretized in space by the finite element method. In other words, if u_h and $\hat{u}_h$ are the finite element and MC solutions of the SPDE, respectively, then we have

$$\mathbb{E}[u] \approx \mathbb{E}[u_h] \approx \hat{u}_h.$$

Therefore, the MC-FEM method involves two approximations and hence there are two sources of error.

Discretization error The approximation of $\mathbb{E}[u]$ by $\mathbb{E}[u_h]$ gives to the discretization error, which stems from the spatial discretization.

Statistical error The approximation of the expected value $\mathbb{E}[u_h]$ by the sample mean $\hat{u}_h$ gives rise to the statistical error, which is caused by the MC estimator.

Lemma (3.3) takes care of the statistical error. The order of the discretization error depends on the order of the finite element method.

Recalling that $\hat{u}_h = \mathrm{E}_{\mathrm{MC}}$, we first obtain the mean square error of the Monte Carlo FEM in the L^2-norm in the following proposition. Later we also show a theorem for the error in the H^1-norm.

Proposition 3.4. *Let $\hat{u}_h$ be the Monte Carlo estimator with M samples to approximate the expectation $\mathbb{E}[u]$ of a solution $u(\cdot,\omega) \in L^2(D)$ of an SPDE by using a FE solution $u_h(\cdot,\omega)$ with mesh size h. Then the mean square error of the Monte Carlo estimator satisfies [145]*

$$\|\hat{u}_h - \mathbb{E}[u]\|^2_{L^2(\Omega;L^2(D))} = M^{-1}\sigma^2[u_h] + \|\mathbb{E}[u_h] - \mathbb{E}[u]\|^2_{L^2(\Omega;L^2(D))}. \tag{3.7}$$

Proof. Starting from the mean square error, we calculate

$$\begin{aligned} \text{MSE} &:= \|\hat{u}_h - \mathbb{E}[u]\|^2_{L^2(\Omega;L^2(D))} \\ &= \mathbb{E}\Big[\|\hat{u}_h - \mathbb{E}[u]\|^2_{L^2(D)}\Big] = \mathbb{E}\Big[\int_D (\hat{u}_h - \mathbb{E}[u])^2 \mathrm{d}x\Big] \\ &= \int_D \mathbb{E}[(\hat{u}_h - \mathbb{E}[u])^2]\mathrm{d}x, \end{aligned} \tag{3.8}$$

where the last equation holds due to Fubini's Theorem. Add and subtracting the term $\mathbb{E}[\hat{u}_h]$, we find

$$\begin{aligned} \text{MSE} &= \int_D \mathbb{E}[(\hat{u}_h - \mathbb{E}[\hat{u}_h] + \mathbb{E}[\hat{u}_h] - \mathbb{E}[u])^2]\mathrm{d}x \\ &= \int_D \mathbb{E}[(\hat{u}_h - \mathbb{E}[\hat{u}_h])]\mathrm{d}x + \int_D \mathbb{E}[(\mathbb{E}[\hat{u}_h] - \mathbb{E}[u])^2]\mathrm{d}x \\ &= \|\hat{u}_h - \mathbb{E}[\hat{u}_h]\|^2_{L^2(\Omega;L^2(D))} + \|\mathbb{E}[u_h] - \mathbb{E}[u]\|^2_{L^2(\Omega;L^2(D))} \\ &= \sigma^2[\hat{u}_h] + \|\mathbb{E}[u_h] - \mathbb{E}[u]\|^2_{L^2(\Omega;L^2(D))} \\ &= M^{-1}\sigma^2[u_h] + \|\mathbb{E}[u_h] - \mathbb{E}[u]\|^2_{L^2(\Omega;L^2(D))}, \end{aligned} \tag{3.9}$$

where we used $\mathbb{E}[\hat{u}_h] = \mathbb{E}[u_h]$, because the Monte Carlo estimator is unbiased, and $\sigma^2[\hat{u}_h] = M^{-1}\sigma^2[u_h]$ due to equation (3.6). □

Now we extend this result to H^1. In the following theorems, the finite element space X is H^1 (see (2.27)).

Theorem 3.5. *Suppose $\alpha, C_0, C_1 \in \mathbb{R}^+$. Let $\hat{u}_h$ be the Monte Carlo estimator with M samples to approximate the expectation $\mathbb{E}[u]$ of a solution $u(\cdot,\omega) \in X$ of an SPDE by using a FE solution $u_h(\cdot,\omega) \in X_h$ with mesh size h [145]. Suppose that the discretization error converges with order α, i.e.,*

$$\|\mathbb{E}[u_h - u]\|_{L^2(\Omega;X)} \leq C_1 h^\alpha, \tag{3.10}$$

and that the estimate

$$\sigma^2[u_h] \leq C_0 \tag{3.11}$$

holds. Then the mean square error of the MC estimator satisfies

$$\|\hat{u}_h - \mathbb{E}[u]\|^2_{L^2(\Omega;X)} = O(h^{2\alpha}) + O(M^{-1}). \tag{3.12}$$

Proof. We use the mean square error and calculate

$$\begin{aligned}
\mathrm{MSE} &:= \|\hat{u}_h - \mathbb{E}[u]\|^2_{L^2(\Omega;X)} \\
&= \|\hat{u}_h - \mathbb{E}[u]\|^2_{L^2(\Omega;L^2(D))} + \|\nabla\hat{u}_h - \mathbb{E}[\nabla u]\|^2_{L^2(\Omega;L^2(D))} \\
&= \|\hat{u}_h - \mathbb{E}[\hat{u}_h]\|^2_{L^2(\Omega;L^2(D))} + \|\mathbb{E}[\hat{u}_h] - \mathbb{E}[u]\|^2_{L^2(\Omega;L^2(D))} \\
&\quad + \|\nabla\hat{u}_h - \mathbb{E}[\nabla\hat{u}_h]\|^2_{L^2(\Omega;L^2(D))} + \|\mathbb{E}[\nabla\hat{u}_h] - \mathbb{E}[\nabla u]\|^2_{L^2(\Omega;L^2(D))} \\
&= \|\hat{u}_h - \mathbb{E}[\hat{u}_h]\|^2_{L^2(\Omega;X)} + \|\mathbb{E}[\hat{u}_h] - \mathbb{E}[u]\|^2_{L^2(\Omega;X)} \\
&= \sigma^2[\hat{u}_h] + \|\mathbb{E}[\hat{u}_h] - \mathbb{E}[u]\|^2_{L^2(\Omega;X)} \\
&= M^{-1}\sigma^2[u_h] + \|\mathbb{E}[u_h] - \mathbb{E}[u]\|^2_{L^2(\Omega;X)}.
\end{aligned} \tag{3.13}$$

In the last expression, $\mathbb{E}[\hat{u}_h] = \mathbb{E}[u_h]$ holds again because the Monte Carlo estimator is unbiased, and $\sigma^2[\hat{u}_h] = M^{-1}\sigma^2[u_h]$ holds due to (3.6). Therefore, using the assumptions (3.10) and (3.11), we have

$$\mathrm{MSE} \leq C_0 M^{-1} + (C_1 h^\alpha)^2 = O(M^{-1}) + O(h^{2\alpha}), \tag{3.14}$$

which concludes the proof. □

3.2 Multilevel Monte Carlo finite element method

In this section, we first present the MLMC FE method and an its error. In this method, several levels of meshes are used and the MC estimator is employed to approximate the solution on each level independently. We start by discretizing the variational formulation (2.30) on the sequence

$$X_{h_0} \subset X_{h_1} \subset \cdots \subset X_{h_L} \subset X$$

of finite-dimensional subspaces, where $X_{h_\ell} := \mathbb{P}^1(\tau_{h_\ell})$ for all $\ell \in \{0, 1, 2, \ldots, L\}$ (see Section (3.1)). The finite element approximation at level L can be written as the telescopic sum

$$u_{h_L} = u_{h_0} + \sum_{\ell=1}^{L} (u_{h_\ell} - u_{h_{\ell-1}}),$$

where each u_{h_ℓ} is the solution on the mesh τ_{h_ℓ} at level ℓ. Therefore, the expected value of u_{h_L} is given by

$$\mathbb{E}[u_{h_L}] = \mathbb{E}[u_{h_0}] + \mathbb{E}\left[\sum_{\ell=1}^{L} (u_{h_\ell} - u_{h_{\ell-1}})\right] = \mathbb{E}[u_{h_0}] + \sum_{\ell=1}^{L} \mathbb{E}[u_{h_\ell} - u_{h_{\ell-1}}]. \tag{3.15}$$

In the MLMC FEM, we estimate $\mathbb{E}[u_{h_\ell} - u_{h_{\ell-1}}]$ by a level dependent number M_ℓ of samples. The MLMC estimator $\mathbb{E}[u]$ is defined as

$$\mathrm{E}_{\mathrm{MLMC}}[u] := \hat{u}_{h_L} := \mathrm{E}_{\mathrm{MC}}[u_{h_0}] + \sum_{\ell=1}^{L} \mathrm{E}_{\mathrm{MC}}[u_{h_\ell} - u_{h_{\ell-1}}], \tag{3.16}$$

where E_{MC} is the Monte Carlo estimator defined in (3.4). Therefore, we find

$$\hat{u}_{h_L} = \frac{1}{M_0}\sum_{i=1}^{M_0} u_{h_0}^{(i)} + \sum_{\ell=1}^{L}\frac{1}{M_\ell}\sum_{i=1}^{M_\ell}(u_{h_\ell}^{(i)} - u_{h_{\ell-1}}^{(i)}). \tag{3.17}$$

It is important to note that the approximate solutions $u_{h_\ell}^{(i)}$ and $u_{h_{\ell-1}}^{(i)}$ correspond to the same sample i, but are computed on different levels of the mesh, i.e., on the meshes M_ℓ and $M_{\ell-1}$, respectively.

Recalling the two sources of error constituting the MC-FE error, the following result holds for the MLMC-FEM error.

Theorem 3.6. *Suppose $\alpha, \beta, C_{00}, C_0, C_1 \in \mathbb{R}^+$. Let $\hat{u}_{h_L}$ be the multilevel Monte Carlo estimator to approximate the expectation $\mathbb{E}[u]$ of a solution $u(\cdot,\omega) \in X$ of an SPDE by using a FE solution $u_{h_\ell}(\cdot,\omega) \in X_{h_\ell}$ with M_ℓ samples in level ℓ, $\ell \in \{0,1,2,\dots,L\}$ and with mesh size h_ℓ. Suppose that the convergence order α for the discretization error, i.e.,*

$$\|\mathbb{E}[u_{h_\ell}] - \mathbb{E}[u]\|_{L^2(\Omega;X)} \leq C_1 h_\ell^\alpha, \tag{3.18}$$

the convergence order β for

$$\sigma^2[u_{h_\ell} - u_{h_{\ell-1}}] \leq C_0 h_{\ell-1}^\beta, \tag{3.19}$$

and assume that the estimate

$$\sigma^2[u_{h_0}] \leq C_{00} \tag{3.20}$$

holds. Then the mean-square error of the MLMC estimator satisfies

$$\|\mathbb{E}[u] - \hat{u}_{h_L}\|_{L^2(\Omega;X)}^2 = O(h_L^{2\alpha}) + O(M_0^{-1}) + \sum_{\ell=1}^{L} O(M_\ell^{-1})O(h_{\ell-1}^\beta). \tag{3.21}$$

Proof. Analogously to the MC case, the MSE is used to assess the accuracy of the MLMC FE estimator. We calculate

$$\begin{aligned}
\mathrm{MSE} &:= \|\hat{u}_{h_L} - \mathbb{E}[u]\|_{L^2(\Omega;X)}^2 \\
&= \|\hat{u}_{h_L} - \mathbb{E}[u]\|_{L^2(\Omega;L^2(D))}^2 + \|\nabla\hat{u}_{h_L} - \mathbb{E}[\nabla u]\|_{L^2(\Omega;L^2(D))}^2 \\
&= \|\hat{u}_{h_L} - \mathbb{E}[\hat{u}_{h_L}]\|_{L^2(\Omega;L^2(D))}^2 + \|\mathbb{E}[\hat{u}_{h_L}] - \mathbb{E}[u]\|_{L^2(\Omega;L^2(D))}^2 \\
&\quad + \|\nabla\hat{u}_{h_L} - \mathbb{E}[\nabla\hat{u}_{h_L}]\|_{L^2(\Omega;L^2(D))}^2 + \|\mathbb{E}[\nabla\hat{u}_{h_L}] - \mathbb{E}[\nabla u]\|_{L^2(\Omega;L^2(D))}^2 \\
&= \|\hat{u}_{h_L} - \mathbb{E}[\hat{u}_{h_L}]\|_{L^2(\Omega;X)}^2 + \|\mathbb{E}[\hat{u}_{h_L}] - \mathbb{E}[u]\|_{L^2(\Omega;X)}^2 \\
&= \sigma^2[\hat{u}_{h_L}] + \|\mathbb{E}[\hat{u}_{h_L}] - \mathbb{E}[u]\|_{L^2(\Omega;X)}^2.
\end{aligned} \tag{3.22}$$

Expanding as in (3.13), using the relation $\sigma^2[\hat{u}_{h_L}] = \sum_{\ell=0}^{L} M_\ell^{-1}\sigma^2[u_{h_\ell} - u_{h_{\ell-1}}]$ [33], and finally applying the assumptions (3.18)–(3.20), we obtain the asserted estimate by

observing that

$$\begin{aligned}\mathrm{MSE} &= M_0^{-1}\sigma^2[u_{h_0}] + \sum_{\ell=1}^{L} M_\ell^{-1}\sigma^2[u_{h_\ell} - u_{h_{\ell-1}}] + \|\mathbb{E}[u_{h_L}] - \mathbb{E}[u]\|^2_{L^2(\Omega;X)} \\ &\leq C_{00}M_0^{-1} + C_0 \sum_{\ell=1}^{L} M_\ell^{-1} h_{\ell-1}^{\beta} + (C_1 h_L^{\alpha})^2 \\ &= O(M_0^{-1}) + \sum_{\ell=1}^{L} O(M_\ell^{-1}) O(h_{\ell-1}^{\beta}) + O(h_L^{2\alpha}),\end{aligned} \tag{3.23}$$

which concludes the proof. □

3.3 The optimal Monte Carlo methods

In this section, we first estimate the computational cost of the MLMC FE method to achieve a given accuracy and compare it with the MC FE method. Based on these considerations, the computational work is then minimized for a given accuracy to be achieved in order to find the optimal number of samples and the optimal mesh size.

As the model equations (2.23) are a system of PDEs, the work estimate consists of the sum of the work for all equations, i.e., the Poisson equation for V and the two drift-diffusion equations for u and v. Therefore, the total computational work is given by

$$W := W_P + 2W_D = W_{P,a} + W_{P,s} + 2W_{D,a} + 2W_{D,s}, \tag{3.24}$$

where the index P indicates the Poisson equation, the index D indicates the two drift-diffusion equations, the index a denotes assembly of the system matrix, and the index s denotes solving the system matrix. We assume that the necessary number of fixed-point or Newton iterations to achieve numerical convergence is constant; this is supported by the numerical results. For each of these four parts the work per sample in level ℓ is given by

$$W_{\ell,P,a} = \mu_1 h_\ell^{-\gamma_1}, \tag{3.25a}$$
$$W_{\ell,P,s} = \mu_2 h_\ell^{-\gamma_2}, \tag{3.25b}$$
$$W_{\ell,D,a} = \mu_3 h_\ell^{-\gamma_3}, \tag{3.25c}$$
$$W_{\ell,D,s} = \mu_4 h_\ell^{-\gamma_4} \tag{3.25d}$$

with all $\mu_k > 0$ and $\gamma_k > 0$. Here M_ℓ is the number of samples used at level ℓ, and h_ℓ is the corresponding mesh size. Therefore the work per sample is given by

$$W_\ell = W_{\ell,P,a} + W_{\ell,P,s} + 2(W_{\ell,D,a} + W_{\ell,D,s}). \tag{3.26}$$

Analogously, in the case of the standard Monte Carlo method, the computational work is obtained without stratification, i.e., there is only one level. In this case, we will drop the index ℓ.

The exponents (and constants) in equations (3.25) are determined by the algorithm used for assembling the FE matrix in the case of $W_{P,a}$ and $W_{D,a}$ (see, e.g., [44] for an efficient algorithm) and by the order of the FE discretization in the case of $W_{P,s}$ and $W_{D,s}$ (see Section 3.1.1). The constants $\mu_i > 0$ depend on the implementation.

Each of the four parts of the computational work has the form $\mu_k h_\ell^{-\gamma_k}$, $k \in \{1, \dots, 4\}$, with $\mu_k > 0$ and $\gamma_k > 0$, which are multiplied by the number M_ℓ of samples at level ℓ. Hence, the total work W is

$$\begin{aligned} W &:= \sum_{\ell=0}^{L} M_\ell W_\ell \\ &= \sum_{\ell=0}^{L} M_\ell (W_{\ell,P,a} + W_{\ell,P,s} + 2W_{\ell,D,a} + 2W_{\ell,D,s}) \\ &= \sum_{\ell=0}^{L} M_\ell (\mu_1 h_\ell^{-\gamma_1} + \mu_2 h_\ell^{-\gamma_2} + \mu_3 h_\ell^{-\gamma_3} + \mu_4 h_\ell^{-\gamma_4}), \end{aligned} \tag{3.27}$$

where the exponents are determined by the algorithms and implementations used for assembling the finite-element matrix and by the order of the finite-element discretization. The typical values of the coefficients for the problems at hand are given in Chapter 4.

3.3.1 The optimal Monte Carlo finite element method

In the case of the Monte Carlo method, there is only one level so that the index ℓ will be dropped. We will choose the optimal M and h such that the total computational cost W is minimized given an error bound ϵ to be achieved. This optimization problem with inequality constraints can be solved using the Karush-Kuhn-Tucker (KKT) conditions, which are the generalization of Lagrange multipliers in the presence of inequality constraints.

In view of (3.25) and (3.13), the most general problem is the following. We minimize the computational work subject to the accuracy constraint $\text{MSE} \leq \varepsilon^2$ so that the root-mean-square error $\text{RMSE} \leq \varepsilon$. To this end, we solve the optimization problem

$$\begin{aligned} \underset{M,h}{\text{minimize}} \quad & f(M,h) := MW \\ \text{subject to} \quad & g(M,h) := \frac{C_0}{M} + (C_1 h^\alpha)^2 - \varepsilon^2 \leq 0, \end{aligned} \tag{3.28}$$

where the optimization is over $M > 1$ and $h > 0$. To simplify the problem, we introduce the new variable θ with $0 < \theta < 1$ such that

$$\frac{C_0}{M} = \theta \varepsilon^2 \qquad \text{and} \qquad (C_1 h^\alpha)^2 = (1-\theta)\varepsilon^2. \tag{3.29}$$

By viewing h and M as functions of θ, (3.28) becomes a one-dimensional convex optimization problem. Due to the exponents of h and M, it is a nonlinear constraint optimization problem. Our goal is to formulate the inequality constrained problem as

an equality constrained problem to which Newton's method can be applied. In order to solve the optimization problem, we use the interior-point method [57, 163].

For each $\mu > 0$, we replace the non-negativity constraints with logarithmic barrier terms in the objective function

$$\begin{aligned} \underset{\chi,s}{\text{minimize}} \quad & f_\mu(\chi, s) := f(\chi) - \mu \sum_i \ln(s_i) \\ \text{subject to} \quad & g(\chi) - s = 0. \end{aligned} \tag{3.30}$$

Here χ, a vector, denotes (M, h) and the vectors g and s represent the $g_i(x)$ and s_i, respectively. The s_i are restricted to be positive away from zero to ensure that the $\ln(s_i)$ are bounded. As μ decreases to zero, the minimum of f_μ approaches the minimum of f. After denoting the Lagrange multiplier for the system (3.30) by y, the system

$$\begin{aligned} \nabla f(\chi) - \nabla g(\chi)^T y &= 0, \\ SYe &= \mu e, \\ g(\chi) - s &= 0 \end{aligned}$$

is obtained, where S is a diagonal matrix with elements s_i, e is a vector of all ones, and ∇g denotes the Jacobian of the constraint g. Now we apply Newton's method to compute the search directions $\Delta\chi$, Δs, Δh via

$$\begin{pmatrix} H(\chi, y) & 0 & -A(\chi)^T \\ 0 & Y & S \\ A(x) & -I & 0 \end{pmatrix} \begin{pmatrix} \Delta\chi \\ \Delta s \\ \Delta h \end{pmatrix} = \begin{pmatrix} -\nabla f(\chi) + A(\chi)^T y \\ \mu e - SYe \\ -g(\chi) + s \end{pmatrix}. \tag{3.31}$$

The Hessian matrix is given by

$$H(\chi, y) = \nabla^2 f(\chi) - \sum_i y_i \nabla^2 g_i(\chi)$$

and $A(\chi)$ is the Jacobian matrix of the constraint (3.28). The second equation is used to calculate Δs. By substituting into the third equation, we obtain the reduced KKT system

$$\begin{pmatrix} -H(\chi, y) & A(\chi)^T \\ A(\chi) & SY^{-1} \end{pmatrix} \begin{pmatrix} \Delta\chi \\ \Delta s \end{pmatrix} = \begin{pmatrix} \nabla f(\chi) - A(\chi)^T y \\ -h(\chi) + \mu Y^{-1} e \end{pmatrix}. \tag{3.32}$$

Now we use iteration to update the solutions by

$$\begin{aligned} \chi^{(k+1)} &:= \chi^{(k)} + \alpha^{(k)} \Delta\chi^{(k)}, \\ s^{(k+1)} &:= s^{(k)} + \alpha^{(k)} \Delta s^{(k)}, \\ y^{(k+1)} &:= y^{(k)} + \alpha^{(k)} \Delta y^{(k)}, \end{aligned}$$

where $(\chi^{(0)}, s^{(0)}, y^{(0)})$ is the initial guess and $\alpha^{(k)}$ is chosen to ensure both that $s^{(k+1)} > 0$ and the objective function

$$\Psi_{\upsilon,\mu}(\chi, s) = f_\mu(\chi, s) + \frac{\upsilon}{2} \|g(\chi) - s\|,$$

is sufficiently reduced [16]. The parameter υ may increase with the iteration number to force the solution toward feasibility.

3.3.2 The optimal multilevel Monte Carlo finite element method

For an optimal multilevel Monte Carlo finite element method, our goal is to determine the optimal hierarchies $(L, \{M_\ell\}_{\ell=0}^{L}, h_0, r)$ which minimize the computational work subject to the given accuracy constraint MSE $\leq \varepsilon^2$. The optimal number L of levels is also unknown a priori. To this end, we solve the optimization problem

$$\begin{aligned} &\underset{M_\ell, h_0, r}{\text{minimize}} \quad f(M_\ell, h_0, r, L) := \sum_{\ell=0}^{L} M_\ell W_\ell \\ &\text{subject to} \quad g(M_\ell, h_0, r, L) := \frac{C_{00}}{M_0} + C_0 \sum_{\ell=1}^{L} \frac{h_{\ell-1}^{\beta}}{M_\ell} + (C_1 h_L^{\alpha})^2 \leq \varepsilon^2. \end{aligned} \tag{3.33}$$

Again, the problem is over $M_\ell > 1$, $h_0 > 0$, and $r > 1$. To obtain the optimal number M_ℓ of samples for $\ell \in \{0, \ldots, L\}$, we calculate

$$\frac{\partial}{\partial M_\ell}(f + \xi^2 g) = 0, \tag{3.34}$$

where ξ^2 is the Lagrange multiplier. This leads to

$$M_\ell = \xi \sqrt{V_\ell / W_\ell}, \tag{3.35}$$

where $V_0 = C_{00}$ and $V_\ell = C_0 h_{\ell-1}^{\beta}$. Similarly to (3.29), the equations

$$\frac{C_{00}}{M_0} + C_0 \sum_{\ell=1}^{L} \frac{h_{\ell-1}^{\beta}}{M_\ell} = \theta \varepsilon^2 \qquad \text{and} \qquad (C_1 h_L^{\alpha})^2 = (1-\theta)\varepsilon^2 \tag{3.36}$$

hold. Hence, the Lagrange multiplier is given by

$$\xi = \left(\theta \epsilon^2\right)^{-1} \sum_{\ell=0}^{L} \sqrt{V_\ell W_\ell}. \tag{3.37}$$

Additionally, according to (3.36), h_0 is calculated by

$$h_0 = \left(\frac{\sqrt{1-\theta}\ \varepsilon}{C_1} \right)^{1/\alpha} r^L. \tag{3.38}$$

Thus we arrive at a two-dimensional optimization problem for the unknowns θ and r. Similarly to the standard Monte Carlo case, we use the interior-point method to solve this nonlinear problem and optimize the hierarchies. In problems with two or three physical/spatial dimensions, the optimal determination of the mesh sizes h_ℓ is a crucial factor in the optimization problem specifically if the exponents γ_k are greater than 1.

There are two options: one is to choose the h_ℓ as a geometric progression according to (3.1). In this case, we solve the minimization problem (3.33). The other is to choose the mesh sizes h_ℓ freely such that they only satisfy the natural condition

$$h_0 \geq h_1 \geq h_2 \geq \cdots \geq h_L.$$

We will explore both options in Subsection 3.3.3.

In the second case, when the mesh sizes are freely chosen, we write them as

$$h_\ell := \frac{h_0}{r_\ell}, \qquad \ell = 1, \ldots, L,$$

where

$$r_\ell := \prod_{i=1}^{\ell} r_i \qquad \text{and} \qquad r_i \geq 1. \tag{3.39}$$

It is clear that $r_L \geq r_{L-1} \cdots \geq r_1 \geq 1$. Here the optimization problem is an $(L+1)$-dimensional problem for the unknowns θ and $r_1, \ldots, r_L$. The same procedure can be applied to solve the problem.

3.3.3 A leading example

Random dopant effects are also called discrete dopant fluctuation effects [86, 133, 156]. In nanoscale semiconductor devices, the charge profile of the dopant atoms cannot be validly modeled as a continuum anymore, but the random location of each dopant needs to be taken into account. This means that each device is a realization of a random process and corresponds to an event ω. In this manner, the potential and carrier density fluctuations due to the discreteness and randomness of the dopants are clearly captured.

Here the silicon lattice is doped with boron as the impurity atoms (red circles in Figure 3.1). The domain $D \subset \mathbb{R}^2$ is depicted in Figure 3.1. The thickness of the oxide layer is 8 nm, the thickness of the nanowire is 40 nm, its width is 60 nm and the nanowire length is 60 nm. Regarding the geometry, Dirichlet boundary conditions are used at the contacts with a back-gate voltage of -1 V (at the bottom of the device) and an electrode voltage of 0 V (at the top of the device). Zero Neumann boundary conditions are used everywhere else. The relative permittivities in the subdomains are $A_{\mathrm{Si}} = 11.7$, $A_{\mathrm{ox}} = 3.9$, $A_{\mathrm{liq}} = 78$, and $A_{\mathrm{dop}} = 4.2$. The number of dopants placed randomly in the device corresponds to a doping concentration of $4 \cdot 10^{16}\,\mathrm{cm}^{-3}$. According to its volume, the silicon subdomain hence contains 6 negative impurity atoms when $C_{\mathrm{dop}} = 5 \cdot 10^{15}\,\mathrm{cm}^{-3}$ and 600 dopants when $C_{\mathrm{dop}} = 5 \cdot 10^{17}\,\mathrm{cm}^{-3}$. In this numerical example, the source and drain regions are not included in the computational domain.

Regarding the doping concentration C_{dop}, the discrete dopants are approximated by Gaussian distributions

$$C_{\text{dop}}(x) := \sum_j \frac{C_j}{(2\pi\sigma^2)^{3/2}} \exp\left(-\frac{(x-x_j)^2}{2\sigma^2}\right),$$

where σ is the influence parameter, C_j is the charge of the j-th dopant atom, and x_j its position [80].

Figure 3.1 shows a cross section of the domain in the longitudinal direction. The longitudinal direction accounts for the transport of charge carriers through the nanowire (black meshes) connecting the source and drain contacts. At least two spatial dimensions are required for this type of problem: the potentials applied at the top and bottom require one dimension and the transport between the source and drain contacts requires another one. The drawback of 3D simulations is the large computational cost. In fact, in a 2D simulation, the dopant atoms are cylindrical and the pounding fluctuation of the potential can block or enhance the cement across the whole device width in the third dimension. In a 3D case, the current could flow around the impurity in the third dimension and the impact of the individual dopant atoms would be less. In order to reduce the overall computational cost, a two-dimensional implementation was chosen for the numerical results presented here. A three-dimensional implementation would, of course, be a more faithful idealization of the three-dimensional reality, not leading to a constant, infinite extension of the two dimensions into three. In other words, in order to demonstrate the computational properties of the method a 2D test is sufficient.

In order to solve the system of equations, we use Scharfetter-Gummel iteration. In spite of the quadratic convergence of Newton's method for the system, Scharfetter-Gummel iteration has advantages for the problem at hand. First of all, Scharfetter-Gummel iteration is much less sensitive to the choice of the initial guess than Newton's method. Another important feature is the reduced computational effort and memory requirement, since in each iteration, it requires the successive solution of three much smaller elliptic problems.

The calculations are performed using MATLAB version 2015a on an Intel Core i5-4430 3.00 GHz 4-core processor with 8 GB of main memory.

As the first step, we calculate the coefficients in the expressions (3.25) for the computational work. To that end, we solve the system for various mesh sizes and measure elapsed wall-clock time spent on matrix assembly and solving the resulting system, both for the Poisson equation and the drift-diffusion equations. Figure 3.2 shows the results for the coefficients in the expressions for the computational work.

The coefficients α and C_1 in the FE discretization error

$$\|\mathbb{E}[V - \hat{V}_h]\|_X + \|\mathbb{E}[u - \hat{u}_h]\|_X + \|\mathbb{E}[v - \hat{v}_h]\|_X \leq C_1 h^\alpha$$

of the system are given in Figure 3.3. The exponent $\alpha = 1.926$ found here agrees very well with the order of the discretization used here, i.e., P_1 finite elements.

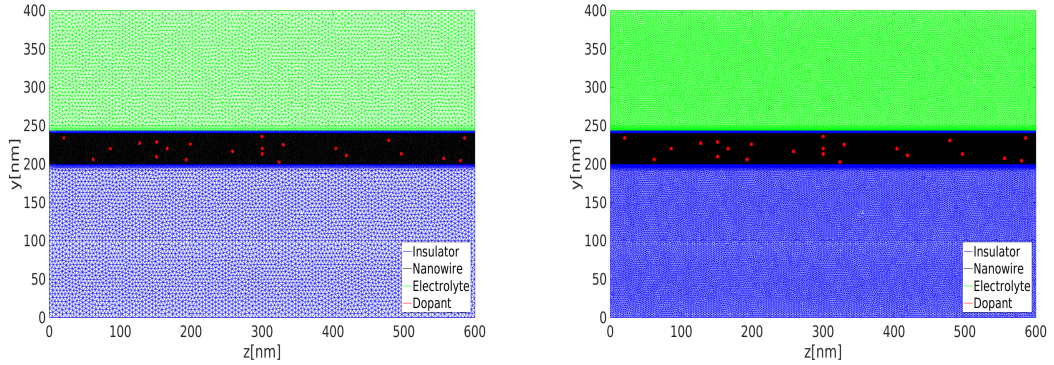


FIGURE 3.1: Meshes for the random distribution of impurity atoms (red circles) in a nanowire field-effect sensor for levels $\ell = 0$ (left) and $\ell = 1$ (right), where $h_0 = 4.02$, $r = 2$, and $C_{\text{dop}} = 4 \times 10^{16}\,\text{cm}^{-3}$. Additionally, oxide ($D_{\text{ox}}$), transducer ($D_{\text{Si}}$) and the electrolyte ($D_{\text{liq}}$) subdomains are depicted with blue, black and green meshes, respectively.

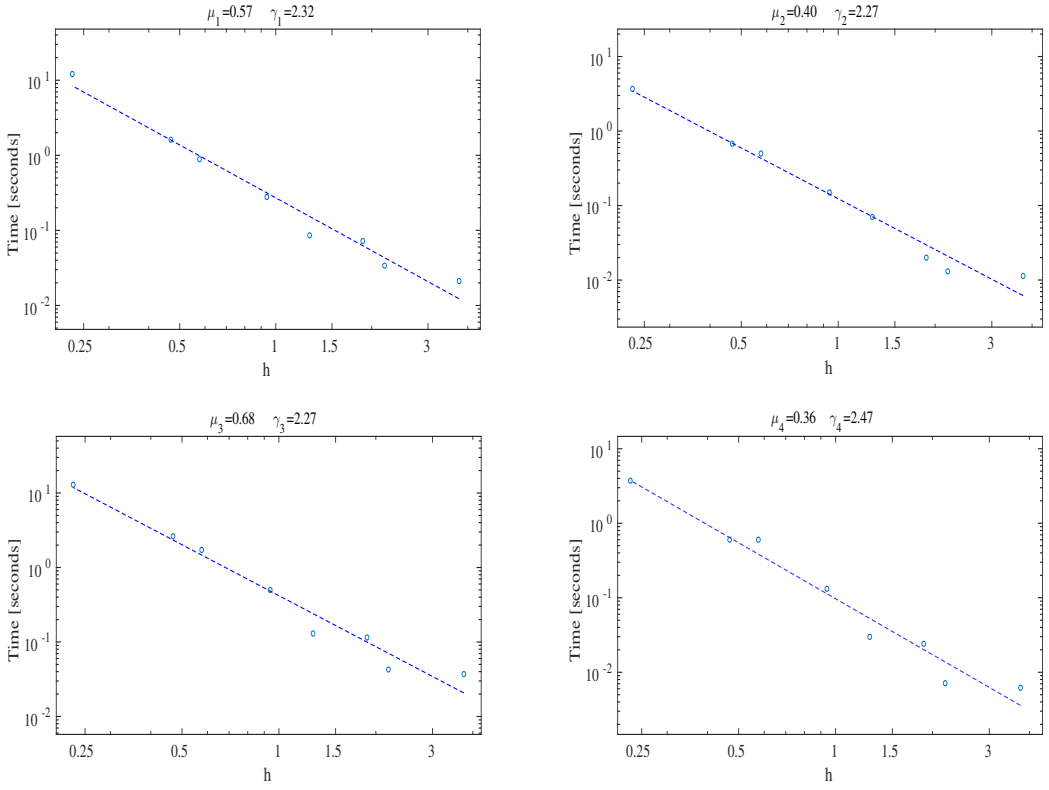


FIGURE 3.2: Computational work for matrix assembly (top) and solving the system (bottom), both for the Poisson equation (left) and the drift-diffusion-equations (right).

For the statistical error, we determine the coefficients in the inequality

$$(\sigma[\Delta V_{h_0}] + \sigma[\Delta V_{h_\ell}]) + (\sigma[\Delta u_{h_0}] + \sigma[\Delta u_{h_\ell}]) + (\sigma[\Delta v_{h_0}] + \sigma[\Delta v_{h_\ell}]) \leq C_{00} + C_0 h_{\ell-1}^{\beta}.$$

Here $C_{00} = 0.07$ and the rest of the coefficients are shown in Figure 3.3.

Having determined the coefficients in the expressions for the computational work, it is

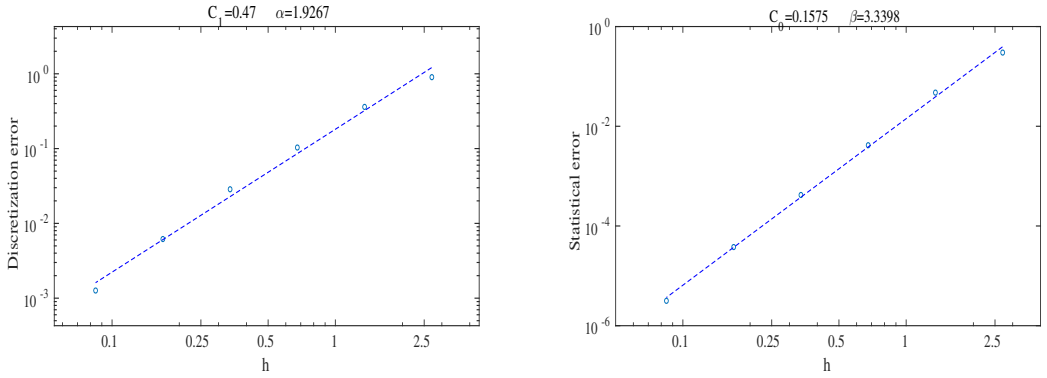


FIGURE 3.3: Discretization error (left) and statistical (right) error as a function of h.

now possible to numerically solve the optimization problems. As described in Section 3.3, we apply an iterative interior-point method to optimize both the number of samples and mesh sizes.

First of all, we solve the optimization problem (3.28) for the MC-FE method. Because there is only one level, it is straightforward to solve. The optimal values for the MC FE method are summarized in Table (3.1) for given ε.

ε	0.1	0.05	0.02	0.01	0.005	0.002	0.001
h	0.348	0.243	0.151	0.105	0.074	0.046	0.032
M	12	46	282	1 130	4 519	28 268	113 130

TABLE 3.1: Optimal MC FE method parameters for various given error tolerances.

In the MLMC-FE method, determining the optimal number of levels is an important part of the calculation. This is achieved here by solving the optimization problem for several levels starting with a single level and noting that the computational work increases above a certain number of levels. More precisely, we solve the optimization problem (3.33) for $0 \leq L \leq 7$ levels as well as for various given error bounds.

Since the number of samples in each level is a continuous variable in the optimization problem, the optimal number of samples is – in general – not an integer and hence we choose $\lceil M_\ell \rceil$, $\ell = 0, \ldots, L$, as the final numbers of levels.

The results of the optimization problems provide insight into the MLMC procedure. Figure 3.4 shows the minimized computational work as a function of the number of levels and as a function of the given tolerance. It shows that for smaller tolerances ε, a larger L is required.In other words, for smaller errors, using more levels leads to a better distribution of the mesh sizes and number of samples among the levels. This fact can be seen in the figure where in order to obtain lower computational complexity the minima is shifted to higher levels. Also, in [27], indicated that in MLMC-FEM the computational work is $O(\varepsilon^{-2-\gamma/\alpha})$ which agrees well with the left and right plots.

In Figure 3.5, the two approaches to multilevel Monte Carlo are compared, namely choosing the h_ℓ as a geometric progressions or freely. Due to generality of the second

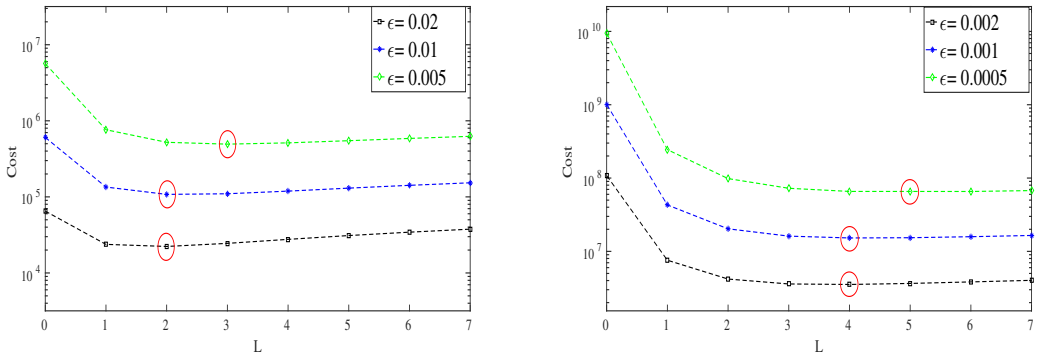


FIGURE 3.4: The minimized computational work for the MLMC-FE method as a function of the number of levels and as a function of the given error tolerance. The results for a geometric progression for h (left) and general h (right) are shown. The number of levels yielding the minimal overall computational work is indicated by red circles.

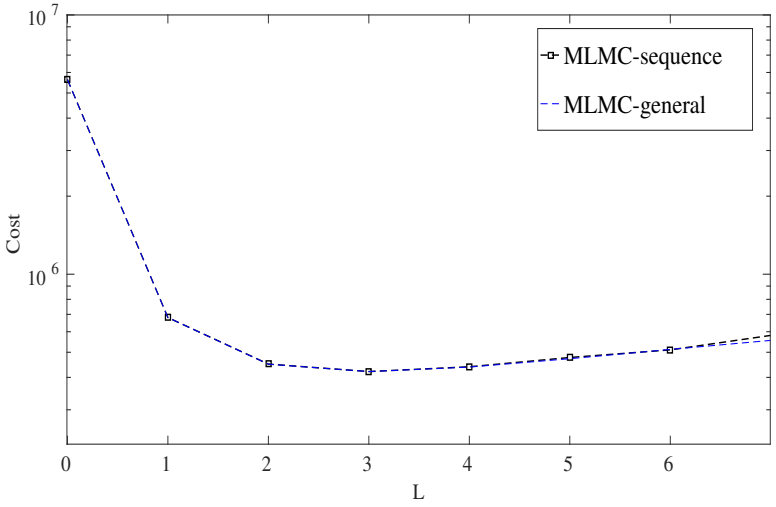


FIGURE 3.5: Comparison between the two different approaches to MLMC FE method for $\varepsilon = 0.015$.

option, compared to the first option, choosing the h_ℓ freely gives rise to less computational work. However, only a small reduction in computational cost is achieved by the choosing meshes freely. The results for both approaches to MLMC-FEM are summarized in Tables 3.2 and 3.3 for various given error tolerances. Both figures show additionally that more than two levels (i.e., $L > 2$) only yield a relatively small reduction in computational cost even for small tolerance levels. In practice, it should hence be considered that the interior-point method requires more time as the number of levels increases.

Finally, as Figure 3.6 shows, the computational work for the multilevel Monte Carlo method is approximately two times lower than the one for the Monte Carlo method for larger tolerance levels such as $\varepsilon = 0.1$. The effectiveness of the MLMC-FE method is more pronounced for smaller error bounds; for $\varepsilon = 0.001$, the computational work is about a factor 10^2 lower than the Monte Carlo work. The results agree with Giles'

ε	h_0	r	M_0	M_1	M_2	M_3	M_4
0.1	0.5171	1.7381	16	4	–	–	–
0.05	0.4433	2.1319	63	9	–	–	–
0.02	0.4620	2.0079	471	70	11	–	–
0.01	0.4222	2.2940	1 882	207	22	–	–
0.005	0.4515	2.0765	8 534	1 167	161	23	–
0.002	0.4549	2.0033	58 203	8 536	1296	197	30
0.001	0.4407	2.1669	232 299	29 141	3 575	438	54

TABLE 3.2: Optimal levels for the MLMC-FE method with h_ℓ chosen as a geometric progression for given error tolerances ε.

ε	h_0	r_1	r_2	r_3	r_4
0.1	0.5171	1.738	–	–	–
0.05	0.4433	2.131	–	–	–
0.02	0.4618	2.020	1.990	–	–
0.01	0.4201	2.270	2.320	–	–
0.005	0.4507	2.080	2.070	2.060	–
0.002	0.4587	2.038	2.017	1.990	1.950
0.001	0.4412	2.140	2.157	2.170	2.196

ε	M_0	M_1	M_2	M_3	M_4
0.1	16	4	–	–	–
0.05	63	9	–	–	–
0.02	471	69	11	–	–
0.01	1 884	210	22	–	–
0.005	8 531	1 162	160	22	–
0.002	58 100	8 327	1 221	185	29
0.001	232 539	29 564	3701	455	55

TABLE 3.3: Optimal levels for the MLMC-FE method with general h_ℓ for given error tolerances ε.

standard complexity theorem [33] in the sense that the estimated exponents α, β, and γ satisfy the assumption of the theorem, i.e., $\alpha \geq \frac{1}{2}\min(\beta, \gamma)$. Therefore, according to the theorem, the computational cost of the MLMC-FEM is $O(\varepsilon^{-2})$. Additionally, according to Figure 3.6, the total cost of the MC-FEM is $O(\varepsilon^{-2-\gamma/\alpha})$, which agrees with [27]. The optimal distribution of the samples among the levels in the multilevel method leads to more evaluations in the first levels (which are cheaper) and to fewer evaluations in the higher levels. On the other hand, to satisfy the first constraint of (3.28), the Monte Carlo method needs a smaller mesh size compared to the multilevel method, which greatly increases the total computational work although the total number of samples is lower.

3.4 Optimal multilevel randomized quasi-Monte Carlo

One approach to accelerate the convergence rate of Monte Carlo method has been to construct variance reduction methods. An alternative approach to this end is to change

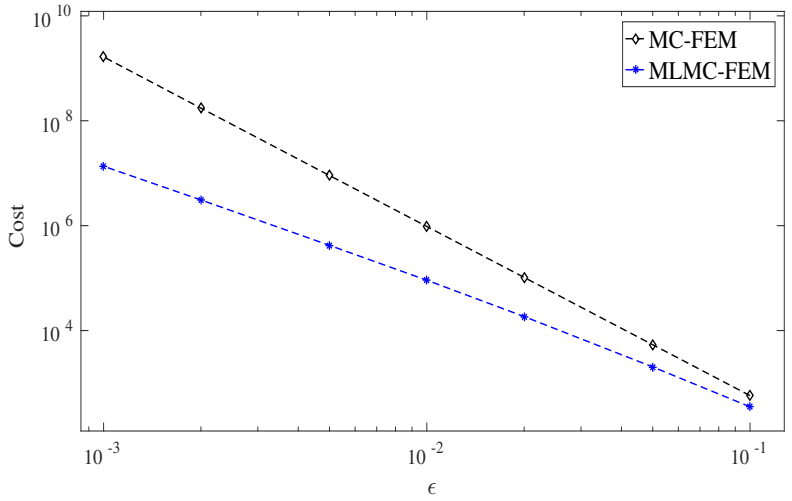


FIGURE 3.6: Comparison of total computational work for MC-FEM and the two approaches to MLMC-FEM for various given tolerances.

the choice of used sequence. In the quasi-Monte Carlo method, instead of a random sequence, a quasi-random sequence is used. In this method, correlation between the points to provide greater uniformity speeds up the computation and therefore its convergence rate is of better order than Monte Carlo method. Uniformity of a sequence is measured in terms of its discrepancy and thus quasi-random sequences are also called low-discrepancy sequences. The problem for uniformity and consequently accuracy of Monte Carlo method is the clumping as well as regions that have no points, which can be seen in the random points used in this method. About $\sqrt{N}$ out of N points lie in clumps [24]. The reason of the clumping issue in the Monte Carlo method is the independence of random points while in quasi-Monte Carlo method, the points are correlated and this avoids clumping. Vanilla Monte Carlo methods provide a convergence rate of $O(N^{-1/2})$ for N samples or points, while quasi-Monte Carlo methods use quasi-random sequences, which are deterministic with correlation between the points to eliminate clumping. The resulting convergence rate of this method is $O((\log N)^d N^{-1})$, where d is the dimension of the sequence. Therefore, quasi-Monte Carlo method has a smaller error and a faster convergence than Monte Carlo method. However, high dimensionality can limit the effectiveness of quasi-Monte Carlo sequences [24, 96].

There are different kinds of sequences used as quasi-random sequences to make the desired point sets. For instance, the simplest quasi-random sequence is the Van der Corput sequence in one dimension which was introduced by Niederreiter in 1992. Halton and Sobol sequences are also other examples of quasi-random sequences. A sequence $\{\omega_j\}_{j=1}^N$ is quasi-random if it has a discrepancy bound of the form

$$D_N \leq c_d (\log N)^d N^{-1}, \tag{3.40}$$

where c_d is a constant depending on the dimension of the sequence d. The more recent sequences, of course, have much better constants c_d. Formulating a quantitative measure of uniformity is an important step in studying sequences. Uniformity of a sequence of

points is measured in terms of its discrepancy which shows the variability of the sequence (the nodes) from the ideal distribution. The constant c_d plays an important role to make much better sequences in the sense of low-discrepancy sequences [24].

It is convenient to describe quasi-Monte Carlo methods in the context of numerical quadrature rules. QMC methods approximate an integral on a high-dimensional hypercube with an N-point equal-weight quadrature rule of the form

$$\int_{[0,1]^d} f(\boldsymbol{\omega})\mathrm{d}\boldsymbol{\omega} \approx \frac{1}{N}\sum_{j=1}^{N} f(\omega_j). \tag{3.41}$$

This is the same form which is used in the Monte Carlo method. However, rather than choosing the d-dimensional points ω_j uniformly from the unit cube, as is the case with the Monte Carlo method, QMC methods choose the points in some deterministic manner; these points are the jth terms of a d-dimensional low-discrepancy sequence in the quasi-Monte Carlo method.
The basis for analyzing quasi-Monte Carlo quadrature error is the Koksma–Hlawka inequality [24]:

Theorem 3.7 (Koksma–Hlawka theorem)**.** *For any sequence* $\{\omega_j\}_{j\geq 1}$ *and any function* f *with bounded variation, the integration error due to* (3.41) *is bounded by*

$$\left|\frac{1}{N}\sum_{j=1}^{N} f(\omega_j) - \int_{[0,1]^d} f(\boldsymbol{\omega})\mathrm{d}\boldsymbol{\omega}\right| \leq V_{\mathrm{HK}}(f)D_N^*(\omega), \tag{3.42}$$

where $V_{\mathrm{HK}}(f)$ *is the Hardy-Krause variation of* f *defined by*

$$V_{\mathrm{HK}}(f) := \int_{[0,1]^d} \left|\frac{\partial^d f}{\partial\omega^1\cdots\partial\omega^d}\right|\mathrm{d}\boldsymbol{\omega} \tag{3.43}$$

for sufficiently differentiable f*.*

The first term, $V_{HK}(f)$, is the variation of f in the sense of Hardy and Krause [116]. This term measures the variability in the function values, whereas the discrepancy term $D_N^*(\omega_j)$ measures the variability of the underlying sequence (the nodes) from the ideal distribution.

The quasi-Monte Carlo method (using the quasi-random sequences) has some drawbacks; if the dimension d is high, the order of convergence of the quasi-Monte Carlo method i.e. $O((\log N)^d N^{-1})$ will be less than that of Monte Carlo method i.e. $O(N^{-1/2})$. To avoid this, we need d to be small and N to be large. Furthermore, $V_{HK}(f)$ and D_N^* are difficult to compute. In order to overcome these difficulties, we can use a *randomized quasi-Monte Carlo method* [149].

In practice, when the dimension d is too large, the calculation of the integral in (3.41) is computationally extremely expensive. In other words, for large d, the number of samples N has to be considerably large for $(\log N)^d N^{-1}$ to be smaller than $N^{-1/2}$. In [139], it is proved that their exist lattice rules such that with the parameter $\alpha > 1$, the optimal

rate of convergence for QMC rules is $\mathcal{O}(N^{-\alpha/2+\delta})$ for any $\delta > 0$. This convergence rate is independent of the dimension d. In [94], Kuo showed that their exist shifted rank-1 lattice rules (constructed by the CBC algorithm) that achieve the optimal convergence of $\mathcal{O}(N^{-1+\delta})$ for any $\delta > 0$. The value of δ depends on the implementation and in Section 4.3.2 it will be estimated.

The accuracy of a quasi-Monte Carlo method can be improved by rewriting the function so that the variation term is reduced [117], or by constructing sequences that have smaller discrepancy [118]. Using randomized quasi-Monte Carlo method with very low discrepancy sequences such as *rank-1 lattice rules* helps us to increase the accuracy of the method.

3.4.1 Randomized quasi-Monte Carlo finite element methods

In order to analyze and estimate the variance to get a better estimate of the error, we can randomize the method. This method is called the *randomized quasi-Monte Carlo (RQMC) method* and can be also considered as a variance reduction technique for the standard Monte Carlo method. The simplest method of randomizing is to use a d-dimensional random shift $\mathbf{\Delta} \sim U[0,1)^d$, which is a uniformly distributed vector.

In particular, a randomized rank-1 lattice rule [38] can be constructed as

$$\omega_j^{(i)} := \frac{j}{N}\lambda + \Delta^{(i)} \mod 1, \quad j \in \{1,\dots,N\}, \quad i \in \{1,\dots,M\}, \tag{3.44}$$

where N is the number of quasi-random points, $\Delta \in [0,1]^d$ is the random shift, which is uniformly distributed over $[0,1]^d$, M is the number of random shifts, and $\lambda \in \mathbb{R}^d$ is a d-dimensional deterministic generating vector. Choosing λ carefully is important in order to achieve uniformity. The quality of a randomly shifted lattice rule is determined by the choice of the generating vector λ. This essential question is addressed, e.g., in [67, Section 4]. Particularly, it is called *randomized rank-1 lattice rule*, if the rank-1 lattice rule as the low-discrepancy sequence is applied. Here, again N is the number of quasi-random points or number of quasi-random points realizations or samples. In this method, choosing $\lambda_1,\dots,\lambda_d$ carefully is important in order to achieve uniformity. We take the fractional part of each component of the argument and disregard the integer part so that ω_j lies within the half-open unit cube. In this method, we choose a number of different random offsets $\Delta_1,\dots,\Delta_M$ and consider a family of d-dimensional sequences. Then, we calculate the estimate (3.41) for each family of sequences (which is made using different random shifts $\Delta_i,\ i = 1,\dots,M$) and take sample mean over the number of shift realizations M.

If the system (2.23) has a solution (V,u,v), we denote finite-element numerical approximations by $(V_h(x,\omega),u_h(x,\omega),v_h(x,\omega))$ for a given $\omega \in \Omega$. Since all three components of the solution are in $H^1(D)$ for a given $\omega \in \Omega$, the variable u may denote any of the three components from now on to simplify notation.

The RQMC estimator to approximate $\mathbb{E}[u_h]$ is then defined by

$$Q_{N,M}(u_h) := \frac{1}{M}\sum_{i=1}^{M}\frac{1}{N}\sum_{j=1}^{N} u_h(x,\omega_j^{(i)}) \tag{3.45}$$

using the quasi-random points defined in (3.44).

3.4.2 Error bound for RQMC-FEM

As aforementioned, in order to overcome the difficulty of finding an error bound for the QMC approach, we use an RQMC method. In this method, the standard assumption is that u_h has bounded variation $V_{\mathrm{HK}}(u_h)$ in the sense of Hardy and Krause, and behaves like the variance [59]. Therefore, we assume that

$$V_{\mathrm{HK}}(u_h) \le C_0, \tag{3.46}$$

where ν_0 is a positive constant. Similar to the standard MC method, the mean square error (MSE) can be written as the sum of the variance of the estimator plus the square of the discretization error [145]. As in [145], a prescribed accuracy is to be achieved, i.e., $\mathrm{MSE} \le \varepsilon^2$.

Using the Koksma-Hlawka inequality (3.42), we estimate the variance of the RQMC estimator (3.45) by calculating

$$\begin{aligned}
\sigma^2[Q_{N,M}(u_h)] &= \sigma^2\left[\frac{1}{M}\sum_{i=1}^{M}\frac{1}{N}\sum_{j=1}^{N} u_h(x,\omega_j^{(i)})\right] \\
&= \frac{1}{M}\sigma^2\left[\frac{1}{N}\sum_{j=1}^{N} u_h(x,\omega_j)\right] \\
&= \frac{1}{M}\int_{[0,1]^d}\left(\frac{1}{N}\sum_{j=1}^{N} u_h(x,\omega_j) - \mathbb{E}[u_h]\right)^2 \mathrm{d}\boldsymbol{\omega} \\
&\le \frac{1}{M}\int_{[0,1]^d}\left(V_{\mathrm{HK}}(u_h)D_N^*(\omega_j)\right)^2 \mathrm{d}\boldsymbol{\omega} \\
&= \mathcal{O}(V_{\mathrm{HK}}^2(u_h)N^{-2+\delta}) \qquad \forall\delta>0.
\end{aligned} \tag{3.47}$$

variance of the RQMC estimator (3.45). In fact, in rank-1 lattice rules, the discrepancy satisfies

$$D_N^*(\omega_j) = \mathcal{O}(N^{-1+\delta}) \qquad \forall\delta>0 \tag{3.48}$$

for any number of points $N > 1$, any shift of the lattice, and for any dimension $d \ge 1$ [138]. The above result is obtained by using component-by-component (CBC) construction, i.e., the components of the generating vector λ are constructed one at a time to minimize the worst-case error in certain weighted function spaces [38].

Using the boundedness assumption (3.46) for $V_{\mathrm{HK}}(u_h)$ in (3.47), we obtain the estimate

$$\sigma^2[Q_N(u_h)] \leq C_0 M^{-1} N^{-2+\delta} \qquad \forall \delta > 0 \tag{3.49}$$

for the variance of the RQMC method, where C_0 is estimated using (3.46). Furthermore, δ will be estimated in the numerical results (see Figure 4.36). The inequality (3.49) will be used later for an error estimate.

We recall that the variable u may represent any of the three components of the solution (V, u, v) of the system (2.23) in order to simplify notation, since all three components are in $H^1(D)$ for a given $\omega \in \Omega$.

Proposition 3.8. *Suppose that $Q_{N,M}(u_h)$ is the RQMC estimator to approximate the expectation $\mathbb{E}[u]$ of the solution $u(x,\omega) \in X$ of (2.23). Assume further that the spatial discretization error converges with order α, i.e.,*

$$\|\mathbb{E}[u - u_h]\|_{L^2(\Omega;X)} \leq C_1 h^\alpha \qquad \exists C_1 \in \mathbb{R}^+, \tag{3.50}$$

where $u_h(x,\omega) \in X_h$ is the FE approximation with mesh size h and it has bounded variation. Then the mean square error of the RQMC estimator $Q_{N,M}$ satisfies

$$\|Q_{N,M}(u_h) - \mathbb{E}[u]\|^2_{L^2(\Omega;X)} = \mathcal{O}(M^{-1}N^{-2+\delta}) + \mathcal{O}(h^{2\alpha}) \qquad \forall \delta > 0. \tag{3.51}$$

Proof. We estimate the mean square error (MSE). Using inequality (3.49) and assumption (3.50), we find that

$$\begin{aligned}
\mathrm{MSE} &:= \|Q_{N,M}(u_h) - \mathbb{E}[u]\|^2_{L^2(\Omega;X)} \\
&= \|Q_{N,M}(u_h) - \mathbb{E}[Q_{N,M}(u_h)]\|^2_{L^2(\Omega;X)} + \|\mathbb{E}[Q_{N,M}(u_h)] - \mathbb{E}[u]\|^2_{L^2(\Omega;X)} \\
&= \sigma^2[Q_{N,M}(u_h)] + \|\mathbb{E}[u - u_h]\|^2_{L^2(\Omega;X)} \\
&\leq C_0 M^{-1} N^{-2+\delta} + C_1 h^{2\alpha} \\
&= \mathcal{O}(M^{-1}N^{-2+\delta}) + \mathcal{O}(h^{2\alpha})
\end{aligned} \tag{3.52}$$

for every $\delta > 0$. □

3.5 Multilevel randomized quasi-Monte Carlo finite element method (MLRQMC-FEM)

Based on the RQMC method in the previous part, a multilevel version of these ideas is developed now.

The finite element approximation at level L can be written as the telescoping sum

$$u_{h_L} = u_{h_0} + \sum_{\ell=1}^{L} (u_{h_\ell} - u_{h_{\ell-1}}),$$

where u_{h_ℓ} is the approximation on the mesh τ_{h_ℓ} at level ℓ. Furthermore, $\mathbb{E}[u_{h_\ell} - u_{h_{\ell-1}}]$ can be estimated using N_ℓ quasi-random points and M_ℓ random shifts on each level ℓ. Therefore the multilevel RQMC FE estimator with respect to one or more random shift is defined as

$$Q_{L,N_\ell,M_\ell}(u_{h_L}) := \frac{1}{M_0}\sum_{i=1}^{M_0}\frac{1}{N_0}\sum_{j=1}^{N_0} u_{h_0}(x,\omega_j^{(i)}) + \sum_{\ell=1}^{L}\frac{1}{M_\ell}\sum_{i=1}^{M_\ell}\frac{1}{N_\ell}\sum_{j=1}^{N_\ell}\left(u_{h_\ell}(x,\omega_j^{(i)}) - u_{h_{\ell-1}}(x,\omega_j^{(i)})\right). \tag{3.53}$$

The sample points $\omega_j^{(i)}$ are obtained using (3.44), for example, and their total number is $M_\ell N_\ell$.

Here again the standard assumption is that V_{HK} is bounded. It is expected that the strong convergence of the discretization method effects the variation. By using the multilevel approach, for higher levels the difference between u_{h_ℓ} and $u_{h_{\ell-1}}$ decreases and therefore V_{HK} reduces. Hence, it seems to be a decent assumption that the Hardy-Krause variation works similar to the variance of $u_{h_\ell} - u_{h_{\ell-1}}$, which gives rise to the following necessary assumptions.

Assumptions 1. The assumptions on the boundedness of the variations of the FEM approximation and on the convergence order of the discretization error are

1. $V_{\mathrm{HK}}(u_{h_0}) \le C_{00} \quad \exists C_{00} \in \mathbb{R}^+$,
2. $V_{\mathrm{HK}}(u_{h_\ell} - u_{h_{\ell-1}}) \le C_0 h_{\ell-1}^{\beta} \quad \exists C_0, \beta \in \mathbb{R}^+$,
3. $\|\mathbb{E}[u - u_{h_\ell}]\|_{L^2(\Omega;X)} \le C_1 h_\ell^{\alpha} \quad \exists C_1, \alpha \in \mathbb{R}^+$,

Proposition 3.9. *Suppose Assumptions 1 hold and $Q_{L,N_\ell,M}(u_{h_L})$ is the multilevel randomized quasi-Monte Carlo estimator with $N_\ell M_\ell$ sample points in level ℓ, $\ell \in \{0,1,2,\dots,L\}$, to approximate the expectation $\mathbb{E}[u]$ of the solution $u(\cdot,\boldsymbol{\omega}) \in X$ of (2.23) using FEM approximations $u_{h_\ell}(\cdot,\boldsymbol{\omega}) \in X_{h_\ell}$ with mesh size h_ℓ.*

Then the mean square error of the multilevel RQMC estimator satisfies

$$\|\mathbb{E}[u] - Q_{L,N_\ell,M_\ell}(u_{h_L})\|^2_{L^2(\Omega;X)} = \mathcal{O}(h_L^{2\alpha}) + \mathcal{O}(M_0^{-1}N_0^{-2+\delta}) + \sum_{\ell=1}^{L}\mathcal{O}(h_{\ell-1}^{2\beta}M_\ell^{-1}N_\ell^{-2+\delta}) \qquad \forall \delta > 0. \tag{3.54}$$

Proof. We first estimate the variance of the multilevel RQMC estimator using inequality (3.42) by calculating

$$\begin{aligned}
\sigma^2[Q_{L,N_\ell,M_\ell}(u_{h_L})] &= \sigma^2\Big[\frac{1}{M_0}\sum_{i=1}^{M_0}\frac{1}{N_0}\sum_{j=1}^{N_0}u_{h_0}(x,\omega_j^{(i)}) + \sum_{\ell=1}^{L}\frac{1}{M_\ell}\sum_{i=1}^{M_\ell}\frac{1}{N_\ell}\sum_{j=1}^{N_\ell}\big(u_{h_\ell}(x,\omega_j^{(i)}) - u_{h_{\ell-1}}(\omega_j^{(i)})\big)\Big] \\
&= \frac{1}{M_0}\sigma^2\Big[\frac{1}{N_0}\sum_{j=1}^{N_0}u_{h_0}(x,\omega_j)\Big] + \sum_{\ell=1}^{L}\frac{1}{M_\ell}\sigma^2\Big[\frac{1}{N_\ell}\sum_{j=1}^{N_\ell}\big(u_{h_\ell}(x,\omega_j) - u_{h_{\ell-1}}(x,\omega_j)\big)\Big] \\
&= \frac{1}{M_0}\int_{[0,1]^d}\Big(\frac{1}{N_0}\sum_{j=1}^{N_0}u_{h_0}(x,\omega_j) - \mathbb{E}[u_{h_0}]\Big)^2\mathrm{d}\boldsymbol{\omega} \\
&\quad + \sum_{\ell=1}^{L}\frac{1}{M_\ell}\int_{[0,1]^d}\left(\frac{1}{N_\ell}\sum_{j=1}^{N_\ell}\big(u_{h_\ell}(x,\omega_j) - u_{h_{\ell-1}}(x,\omega_j)\big) - \mathbb{E}[u_{h_\ell}(x,\omega_j) - u_{h_{\ell-1}}(x,\omega_j)]\right) \\
&\le \frac{1}{M_0}\int_{[0,1]^d}\Big(V_{HK}(u_{h_0})D^*_{N_0}(\omega_j)\Big)^2\mathrm{d}\omega \\
&\quad + \sum_{\ell=1}^{L}\frac{1}{M_\ell}\int_{[0,1]^d}\Big(V_{HK}\big(u_{h_\ell}(x,\omega_j) - u_{h_{\ell-1}}(x,\omega_j)\big)D^*_{N_\ell}(\omega_j)\Big)^2\mathrm{d}\omega \\
&= \mathcal{O}(V^2_{HK}(u_{h_0})N_0^{-2+\delta}) + \mathcal{O}(V^2_{HK}\big(u_{h_\ell}(x,\omega_j) - u_{h_{\ell-1}}(x,\omega_j)\big)N_\ell^{-2+\delta}),
\end{aligned} \tag{3.55}$$

where we used the estimate (3.48).

Therefore, we have

$$\sigma^2[Q_{L,N_\ell,M_\ell}(u_{h_L})] \le C_{00}M_0^{-1}N_0^{-2+\delta} + C_0\sum_{\ell=1}^{L}h_{\ell-1}^{2\beta}M_\ell^{-1}N_\ell^{-2+\delta}, \tag{3.56}$$

using the assumptions of bounded variations, i.e., Assumptions 1.1 and 1.2. This estimate shows that how the error of the method behaves in terms of number of samples, as we will see in the following.

Similarly to the RQMC estimator, the MSE assesses the accuracy of the MLRQMC-FE estimator. Using Assumptions 1.3 and the variance estimate (3.55), we find

$$\begin{aligned}
\mathrm{MSE} &:= \|Q_{L,N_\ell,M_\ell}(u_{h_L}) - \mathbb{E}[u]\|^2_{L^2(\Omega;X)} \\
&= \|Q_{L,N_\ell,M_\ell}(u_{h_L}) - \mathbb{E}[Q_{L,N_\ell,M_\ell}(u_{h_L})]\|^2_{L^2(\Omega;X)} + \|\mathbb{E}[Q_{L,N_\ell,M_\ell}(u_{h_L})] - \mathbb{E}[u]\|^2_{L^2(\Omega;X)} \\
&= \sigma^2[Q_{L,N_\ell,M_\ell}(u_{h_L})] + \|\mathbb{E}[u - u_{h_L}]\|^2_{L^2(\Omega;X)} \\
&\le C_{00}M_0^{-1}N_0^{-2+\delta} + C_0\sum_{\ell=1}^{L}h_{\ell-1}^{2\beta}M_\ell^{-1}N_\ell^{-2+\delta} + (C_1h_L^\alpha)^2 \\
&= \mathcal{O}(M_0^{-1}N_0^{-2+\delta}) + \sum_{\ell=1}^{L}\mathcal{O}(h_{\ell-1}^{2\beta})\mathcal{O}(M_\ell^{-1}N_\ell^{-2+\delta}) + \mathcal{O}(h_L^{2\alpha})
\end{aligned} \tag{3.57}$$

for every $\delta > 0$. □

3.5.1 Optimal multilevel randomized quasi-Monte Carlo

Having modeled the computational work, we can now state the optimization problem in the sense that we want to minimize the total computational work for a prescribed error tolerance ε [88]. The minimization problem is

$$\begin{aligned} &\underset{M_\ell, N_\ell, h_0, r}{\text{minimize}} \quad f(M_\ell, N_\ell, h_0, r, L) := \sum_{\ell=0}^{L} M_\ell N_\ell \sum_{k=1}^{4} \mu_k h_0^{-\gamma_k} r^{\gamma_k} \\ &\text{subject to} \quad g(N_\ell, h_0, r, L) := C_{00} M_0^{-1} N_0^{-2+\delta} + C_0 \sum_{\ell=1}^{L} h_{\ell-1}^{2\beta} M_\ell^{-1} N_\ell^{-2+\delta} + (C_1 h_L^{\alpha})^2 \leq \varepsilon^2 \end{aligned} \tag{3.58}$$

for every $\delta > 0$, where $h_0 > 0$, $r > 1$, N_ℓ, and $N_\ell \geq 1$. The given maximal total error ε^2 is an upper bound for (3.57), i.e., MSE $\leq \varepsilon^2$. The goal is to determine optimal values h_ℓ (by calculating optimal values for h_0 and r and using their relation (3.1)) and N_ℓ, $\ell \in \{0, 1, \ldots, L\}$. For all levels, the number M_ℓ of shift realizations is an integer, i.e., $M_\ell \in \mathbb{N}$.

The nonlinear constraint problem can be solved numerically with iterative optimization numerical techniques. In fact, the nonlinearity of the constraint (g) and the objective function (f) due to the exponents motivates us to we use sequential quadratic programming (SQP) [18] as a generalization of Newton's method for unconstrained optimization. The method generates steps by solving quadratic subproblems; it can be used both in line search and trust-region frameworks. The SQP is appropriate for small and large problems and it is well-suited to solving problems with significant nonlinearities. The methods relies on a profound theoretical foundation and provides powerful algorithmic tools for the solution of large-scale technologically relevant problems. Let the vector χ denotes (N_ℓ, h_0, r, L), the SQP as an iterative procedure can be used to optimize the problem (3.58) for a given iterate χ^s, $s \in \mathbb{N}_0$ by a quadratic programming (QP) subproblem, solves that QP subproblem, and then uses the solution to construct a new iterate χ. This construction is done in such a way that the sequence χ^s for $s \in \mathbb{N}_0$ converges to a local minimum χ as $s \to \infty$. Here, (3.58) resembles the Newton and quasi-Newton methods for the numerical solution of nonlinear algebraic systems of equations. To this end, the principal idea is the formulation of a QP subproblem based on a quadratic approximation of the Lagrangian function:

$$\mathcal{L}(\chi, \zeta) := f(\chi) + \sum_{i=1}^{m} \zeta^T g_i(\chi), \tag{3.59}$$

where ζ ate the Lagrange multipliers. In order to solve the optimization problem (3.58) because of the nonlinearity of the work function i.e.,the exponents γ_k, we replace the objective function by its local quadratic approximation as

$$f(\chi) \approx f(\chi^s) + \nabla f(\chi^s)(\chi - \chi^s) + \frac{1}{2}(\chi - \chi^s) H f(\chi^s)(\chi - \chi^s), \tag{3.60}$$

where H is the Hessian matrix (the symmetric matrix of second derivatives). We should note that the term $(f(\chi^s))$ in the expression above can be eliminated for the minimization problem, since it is constant. The nonlinearity of the first constraint (g), i.e., the convergence order of discretization error and convergence order of variance function motivate us to replaces the constraint by its linear approximations. Therefore, the nonlinear constraint function should be replaced by its local affine approximations as

$$g(\chi) \approx g(\chi^s) + \nabla g(\chi^s)(\chi - \chi^s). \tag{3.61}$$

The optimization problem (3.58) can be rewritten to the following form of QP subproble

$$\begin{aligned} \text{minimize} \quad & \frac{1}{2}\nu(\chi)^T H f(\chi^s)\nu(\chi) + \nabla f(\chi^s)^T \nu(\chi) \\ \text{subject to} \quad & \nabla g\,(\chi^s)^T\,\nu(\chi) + g(\chi^s) \leq 0, \end{aligned} \tag{3.62}$$

where $\nu(\chi) = \chi - \chi^s$. Here, to take nonlinearities of the constraints into account the SQP method uses a quadratic model of the Lagrangian function as the objective. Therefore, (3.62) is related to a local quadratic model of the Lagrangian $\mathcal{L}$ as the objective functional which leads to the QP subproblem

$$\begin{aligned} \text{minimize} \quad & \frac{1}{2}\nu(\chi)^T H \mathcal{L}(\chi^s, \zeta^s)\nu(\chi) + \nabla f(\chi^s)^T \nu(\chi) \\ \text{subject to} \quad & \nabla g\,(\chi^s)^T\,\nu(\chi) + g(\chi^s) \leq 0. \end{aligned} \tag{3.63}$$

The solution is used to form a new iterate

$$\chi^{s+1} = \chi^s + \alpha^s \nu^s, \tag{3.64}$$

where ν_s is obtained by (3.62). The step length parameter α^s is determined by an appropriate line search procedure [115] i.e., choosing a step length that approximately minimizes f along the search direction and H can be updated by any of the quasi-Newton method, e.g., BFGS method [101].

Finally, as a summary of the simulation strategy (for MLMC-FEM) is given in the subsequent algorithm. The simpler procedure can be implemented for Monte Carlo by dropping the levels, i.e., using optimal (h, M).

Algorithm 3.1 The algorithm for solving stochastic DDP system using MLMC-FEM

1. Solve the optimization problem (3.33) by estimated coefficient and exponents (see 3.3.3 as an example) and calculate the optimal hierarchies of $(h_0,\, r,\, M_\ell, L)$.
2. For $\ell = 0, \ldots, L$:
   (a) Produce the independent random samples (Monte Carlo) or quasi-points (rank-1 lattice rule). It is a $d \times M_\ell$ dimensional matrix where d is the dimension of randomness (e.g., number of dopants).
   (b) For $i = 1, \ldots, M_\ell$
      i. Construct the device geometry considering h_ℓ and the random variables.
      ii. Use the initial guess $(V_0, u_0, v_0, \alpha_0, \gamma_0)$.
      iii. Solve the coupled system of equations (2.23) using Scharfetter-Gummel iteration (2.2.6)
      iv. Estimate $(V_{h_\ell}^{(i)}, v_{h_\ell}^{(i)}, u_{h_\ell}^{(i)})$.
3. Estimate the expected value of $(V_{h_L}, v_{h_L}, u_{h_L})$ using the telescopic sum (3.16) and the variance.
4. Calculate the current statistics.

3.6 Basis adaptation

In this section, a basis-adaptation method based on polynomial chaos expansion is applied to the stochastic nonlinear Poisson-Boltzmann equation. The method is based on using the polynomial chaos expansion. Here we use the Hermite polynomials as the bias functions and transfer random variables from uncorrelated to correlated variables. The advantages of the method, i.e., exactness of the solution compared with the full dimensional solution will be shown in Section (4.1).

3.6.1 Polynomial chaos expansion (PCE)

Generalized polynomial chaos (GPC) seeks to represent an approximation of a random function by a set of random variables and orthogonal polynomials. It estimates coefficients for known orthogonal polynomial basis functions based on a set of response-function evaluations using sampling, tensor-product quadrature, or Smolyak sparse-grid approaches [53].

The general idea of the expansion is to transfer randomness to the basis functions and to use Hermite polynomials as basis functions. A stochastic function like $u \in L^2(D, \Omega)$ can be explained as its Wiener–Hermite polynomial chaos expansion [165] as

$$u(\boldsymbol{x}, \boldsymbol{\omega}) := \sum_{\boldsymbol{\beta}} u_{\boldsymbol{\beta}}(\boldsymbol{x}) \Phi_{\boldsymbol{\beta}}(\boldsymbol{\omega}). \tag{3.65}$$

Here, $\Phi_{\boldsymbol{\beta}}$ is an orthonormal Hermit polynomials, $\boldsymbol{\beta} = (\beta_1, \beta_2, \cdots, \beta_n)$ is a vector of n nonnegative integers describes the order of polynomials, $\boldsymbol{x} \in D$ and $\boldsymbol{\omega}$ is a vector of uncorrelated Gaussian random variables. In order to approximate the series (3.65), we truncate it to a finite number of terms for the sake of computation

$$u(\boldsymbol{x}, \boldsymbol{\omega}) := \sum_{\boldsymbol{\beta} \in M_k} u_{\boldsymbol{\beta}}(\boldsymbol{x}) \Phi_{\boldsymbol{\beta}}(\boldsymbol{\omega}), \tag{3.66}$$

where the truncated index set

$$M_k = \{\boldsymbol{\beta} = (\beta_i, i \geq 1 \mid \beta_i \in \{0, 1, \cdots, k\}\}$$

is used for the series. The function can be characterized by its expected value with respect to the probability space as

$$\mathbb{E}(u(\boldsymbol{x}, \boldsymbol{\omega})) = \int_{\Omega} u(\boldsymbol{x}, \boldsymbol{\omega}) \mu(\boldsymbol{\omega}) \mathrm{d}\boldsymbol{\omega}, \tag{3.67}$$

where $\mu(\boldsymbol{\omega})$ is the probability density function (PDF) corresponding to random variable $\boldsymbol{\omega}$. By the Cameron-Martin theorem [165], GPC approximation of (3.66) is fully converged in L^2 norm if

$$\lim_{k \to \infty} \int_{\Omega} \left(\sum_{\boldsymbol{\beta} \in M_k} u_{\boldsymbol{\beta}}(\boldsymbol{x}) \Phi_{\boldsymbol{\beta}}(\boldsymbol{\omega}) - u(\boldsymbol{x}, \boldsymbol{\omega}) \right) \mu(\boldsymbol{\omega}) \mathrm{d}\boldsymbol{\omega} = 0. \tag{3.68}$$

The general idea of our basis adaptation is rotating random variables and transferring them from uncorrelated to correlated random variables. To this end, we define an isometry $\boldsymbol{\mathcal{L}} : \mathbb{R}^n \to \mathbb{R}^n$ to define new basis. Therefore, the rotated random variables are defined as

$$\boldsymbol{\gamma} := \boldsymbol{\mathcal{L}} \boldsymbol{\omega}. \tag{3.69}$$

The solution of (2.23) under this isometry can be obtained by

$$u(\boldsymbol{x}, \boldsymbol{\gamma}) = \sum_{\boldsymbol{\beta} \in M_k} u_{\boldsymbol{\beta}}^{\boldsymbol{\mathcal{L}}}(\boldsymbol{x}) \Phi_{\boldsymbol{\beta}}(\boldsymbol{\mathcal{L}} \boldsymbol{\omega}). \tag{3.70}$$

The calculation of the coefficients of the series is the main point which can be defined as [86]

$$u_{\boldsymbol{\beta}}^{\boldsymbol{\mathcal{L}}}(\boldsymbol{x}) = \sum_{\boldsymbol{\beta}, \boldsymbol{\delta} \in M_k} u_{\boldsymbol{\delta}}(\boldsymbol{x}) \langle \Phi_{\boldsymbol{\beta}}(\boldsymbol{\omega}), \Phi_{\boldsymbol{\delta}}^{\boldsymbol{\mathcal{L}}}(\boldsymbol{\omega}) \rangle = \sum_{\boldsymbol{\beta}, \boldsymbol{\delta} \in M_k} u_{\boldsymbol{\delta}}(\boldsymbol{x}) \langle \Phi_{\boldsymbol{\beta}}(\boldsymbol{\omega}), \Phi_{\boldsymbol{\delta}}(\boldsymbol{\gamma}) \rangle. \tag{3.71}$$

The inner product in the Hilbert space is characterized by weight function as the probability density function relative to the Gaussian measure [165]. An important property of the polynomials which will be used in the following estimations is their orthogonality with respect to the Gaussian probability measure. Therefore, the orthogonality of

polynomial basis can be used to simplify (3.71) as

$$u_{\boldsymbol{\beta}}^{\boldsymbol{\mathcal{L}}}(\boldsymbol{x}) = \sum_{\boldsymbol{\beta}\in M_k} u_{\boldsymbol{\beta}}(\boldsymbol{x})\langle\Phi_{\boldsymbol{\beta}}(\boldsymbol{\omega}), \Phi_{\boldsymbol{\beta}}(\boldsymbol{\gamma})\rangle. \tag{3.72}$$

The isometry $\boldsymbol{\mathcal{L}}$ still needs to be constructed in a suitable manner to transfer one basis ($\boldsymbol{\omega}$) to other basis ($\boldsymbol{\gamma}$). To construct the isometry $\boldsymbol{\mathcal{L}}$, we use quadratic adaptation [148]. As the first step, we define a multi-index $\boldsymbol{q}_i = (0, \ldots, 0, 1, 0, \ldots, 0)$ where only the ith point is 1 and other elements are zero. The matrix $\boldsymbol{\mathcal{L}}$ is given by

$$\boldsymbol{\mathcal{L}}^T \boldsymbol{D} \boldsymbol{\mathcal{L}} = \boldsymbol{B}, \tag{3.73}$$

where the diagonal elements of $\boldsymbol{B}$ are $b_{ii} = \frac{u_{2\boldsymbol{q}_i}}{\sqrt{2}}$ and the rest of entries are $b_{ij} = \frac{u_{\boldsymbol{q}_{ij}}}{\sqrt{2}}$. After this calculation, $\boldsymbol{\mathcal{L}}$ and $\boldsymbol{D}$ which are respectively eigenvectors and eigenvalues matrices of matrix $\boldsymbol{B}$ can be calculated.

3.6.2 Application to the stochastic nonlinear Poisson-Boltzmann equation

In the application considered here, the random process is localized near the manifold that describes the surface of the sensor. Physically speaking, the free ions in the aqueous solution screen the effect of the charges of the biomolecules, whose movement is random. The distance where the field effect is still significant is given by (a multiple of) the Debye length. Mathematically speaking, the semilinear term in (2.23) results in an exponential decay of the solution away from a point charge. Therefore the important uncertainty area of biomolecules is at the surface [86].

In Monte Carlo sampling the coefficients of (3.66) are estimated as

$$u_{\boldsymbol{\beta}}(\boldsymbol{x}) = \frac{1}{M}\sum_{j=1}^{M} u(\boldsymbol{x}, \boldsymbol{\omega}^{(j)})\Phi_{\boldsymbol{\beta}}(\boldsymbol{\omega}^{(j)}), \tag{3.74}$$

where M is the number of evaluations and $\boldsymbol{\beta} \in M_k$. For the fluctuation of n target molecules at the surface, we calculate (3.70) as an approximation of (2.23) by

$$u^{\boldsymbol{\mathcal{L}}}(\boldsymbol{x}, \boldsymbol{\gamma}) = u_0^{\boldsymbol{\mathcal{L}}}(\boldsymbol{x}) + \sum_{i=1}^{n} u_i^{\boldsymbol{\mathcal{L}}}(\boldsymbol{x})\gamma_i + \sum_{i=1}^{n} u_{ii}^{\boldsymbol{\mathcal{L}}}(\boldsymbol{x})\frac{\gamma_i^2 - 1}{\sqrt{2}} + \sum_{\substack{\boldsymbol{\beta}\in M_k \\ k\geq 3}} \sum_{i=1}^{n} u_{\beta_i}^{\boldsymbol{\mathcal{L}}}\Phi_{\boldsymbol{\beta}}(\gamma_i), \tag{3.75}$$

where the rotated random variables are from (3.69) and the coefficients are calculated by (3.72) and (3.74). The main advantage of the basis adaptation compared to full-dimensional variables ($\boldsymbol{\omega}$) is that with transformation of the chaos to Gaussian process cost of calculation decreases dramatically. In fact, in spite of a truncation of (3.75) e.g. 2nd order adapted series, very good estimation of (2.23) can be achieved. In this work, the main goal is the calculation of electrical current (quantity of interest). Hence, with respect to the transformation, it can finally be obtained by the equation

$$I(\boldsymbol{\gamma}) = f(u_{\boldsymbol{\beta}}^{\boldsymbol{\mathcal{L}}}(\boldsymbol{x}, \boldsymbol{\gamma})). \tag{3.76}$$

3.7 Conclusions

We balanced the various parameters in the numerical methods by viewing this problem as a global optimization problem. The goal is to determine the numerical parameters such that the computational work to achieve a total error, i.e., discretization error plus statistical error, less than or equal to a given error tolerance is minimized. Although the exponential terms in the constraints make the optimization problems nonlinear, the optimization problems can be solved by an interior-point method with sufficient iterations. We applied the system of equation to a leading example, i.e., random dopant fluctuation in the sensors and used MC-FEM and MLMC-FEM approach to obtain the solution. The solution of the constrained optimization problem leads to optimal $(M,\ h)$ in the case of the standard MC method and to hierarchies consisting of $(L, \{M_\ell\}_{\ell=0}^{L}, h_0, r)$ in the case of the MLMC method.

We investigated two different options to the mesh refinement in the multilevel method. Although the less computational effort is needed by choosing the mesh sizes freely, the difference is negligible. In the comparison of the MC with the MLMC method, the MLMC method was found to decrease the total computational effort by four orders of magnitude for small error tolerances. The speed-up becomes better as the error tolerance decreases.

We also developed optimal multilevel randomized quasi-Monte Carlo to model the fluctuation in the microelectronic device. Using quasi-random points instead of Gaussian random points gives rise to faster convergence rate. In order to obtain the hierarchies i.e., solving the optimization problem, we exploited SQP method as a generalization of Newton's method and linearized the nonlinear objective function by its local quadratic approximation.

Chapter 4

Application of UQ in nanotechnology

Uncertainty quantification (UQ) has become an important task and an emerging topic in many engineering fields. Uncertainties can be caused by many factors, e.g., the random nature of some design parameters, external environmental fluctuations, measurement noise. Therefore, in order to enable robust engineering design and optimal decision making, efficient stochastic solvers are highly desired to quantify the effects of uncertainties on the performance of complex engineering designs.

As regards the main field of investigation of thesis, while previous mathematical modeling [13, 14, 76, 153] has focused on the deterministic problem and stochastic surface reactions, the current work describes how various stochastic processes propagate through a PDE model and result in noise and fluctuations in a transport model. Quantifying noise and fluctuations in sensors is important, since they determine the detection limit and the signal-to-noise ratio. In this chapter, we also use the introduced PDE models in Chapter 2 and the developed stochastic numerical techniques in Chapter 3 to quantify noise and fluctuations in the introduced silicon nanowire sensors.

Nowadays, quantification of uncertainty due to noise and fluctuations is of great importance especially in nanometer-scale devices, as any random effect becomes proportionally more important as devices dimensions are shrunk and power supply voltage is reduced. Randomness due to the number and the location of impurity atomsis one of the most important effects that all together limit the design of integrated circuits. Hence, introducing a stochastic model to quantify the randomness in the transistors is significantly important. We should note that the popular methods e.g., Monte Carlo are computationally expensive (suffer from slow convergence rate). Therefore, the main aim of this chapter is applying the introduced advanced stochastic numerical techniques in previous chapters to model the randomness (the RDF effect) in field-effect transistors.

Finally, this chapter is a summary of the numerical results that are explained in [85–89, 145].

4.1 Silicon nanowire field-effect sensors

The concept of nanowire field-effect sensors is very general and has been applied to the detection of DNA, proteins like tumor markers, and toxic gases such as carbon monoxide [14, 86, 87, 151]. The sensors offer advantages like miniaturization, high sensitivity, fast response, and low power consumption [50, 122, 142]. In this device, the target molecules be labeled in contrast to the commonly used fluorescent or radioactive markers in other detection methods.

As regards noise and fluctuation in such devices, there are various sources of randomness to be considered. The distribution of the receptor molecules at the surface is random and determined at the time of surface functionalization. In other words, in field-effect sensors, target molecules bind to randomly placed probe molecules in a stochastic process so that the detection mechanism is inherently stochastic. The Brownian motion of the target molecules also results in changes in charge concentration and permittivity. This randomness on the sensor surface propagates through the self-consistent transport equations and finally results in noise in the sensor output. Also, diffusion in the liquid and association and dissociation at the surface receptors are stochastic processes and occur at the time of usage. The random distribution of the dopant atoms in the semiconductor is determined at fabrication time and leads to important device variation, while charge transport obviously occurs at the time of usage.

4.1.1 Noise quantification in nanowire field-effect sensors

Biological macromolecules [86, 87, 89], such as proteins and nucleic acids are typically charged in aqueous solution, as such, can be detected readily by nanowire sensors when appropriate receptors are linked to the nanowire active sensor [120]. In this part, we apply the already developed basis adaptation approach (3.6) to model the random distribution of DNA molecules in the electrolyte. We use a 2D cross-section of the device (see Figure 4.1), the stochastic nonlinear Poisson-Boltzmann equation (2.11) to model the electrostatic potential and drift-diffusion equations (2.15) to model the charge transport.

When quantifying noise and fluctuations in sensors, various situations with different types of molecules are relevant. Probe molecules are functionalized at the sensor surface [125] when the sensor is manufactured and they are responsible for selectivity. In the case of DNA sensors, the probe molecules may be single-stranded peptide-nucleic-acid (PNA) oligomers, which are uncharged, or ssDNA oligomers, which are highly charged. The probe molecules move randomly, although there are preferred orientations, which have been calculated [72]. Target molecules bind to the probe molecules and are detected by the field effect modeled here. In the case of a DNA sensor, ssDNA oligomers bind to ssDNA or PNA oligomers. Binding and unbinding are stochastic processes [153]. Here we consider the leading example of a DNA sensor with ssDNA oligomers as probe molecules and ssDNA oligomers as target molecules. The double-stranded probe-target complex carries twice the charge of a single strand. These considerations give the stochastic coefficients in (2.11).

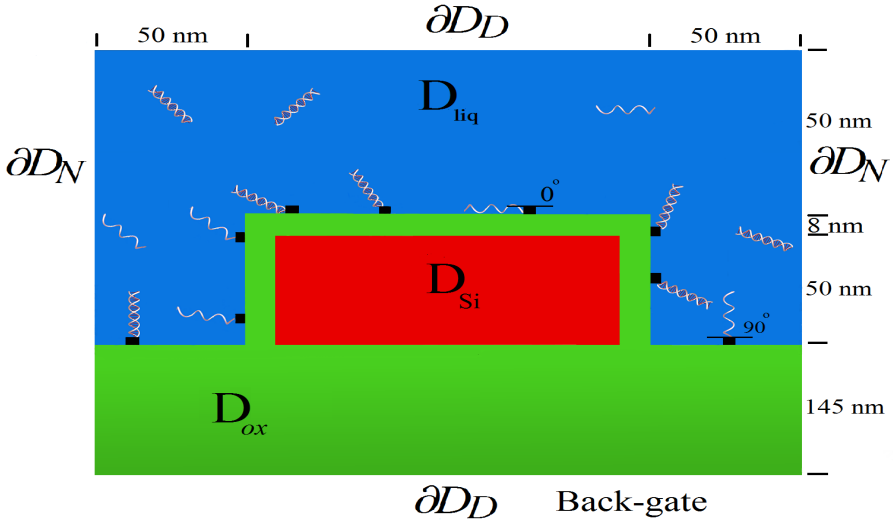


FIGURE 4.1: Cross section through a field-effect nanowire sensor, showing subdomains and boundary conditions. In the electrolyte (D_{liq}), the random binding of target molecules to immobilized receptor molecules at the surface defines molecule subdomain (D_M).

The biological noise, i.e., the random movement of probe and target molecules at or near the surface of any affinity based sensor, propagates through a PDE model of the sensor and results in noise in the sensor output. Biological noise is one of the major sources of noise and fluctuations in field-effect sensors; it is due to two effects: the random association of target molecules to probe molecules functionalized at the sensor surface and their random dissociation from the probe molecules as well as randomness in the orientation of any molecule bound to a surface. In order to quantify biological noise, the association and dissociation processes were modeled in [153], where the expected number and variance of the number of target molecules bound to probe molecules were calculated. The random orientations were modeled in [72], where the probabilities of the orientations were determined.

When any affinity based sensor is manufactured, the probe molecules are functionalized at the sensor surface [125] at random, but fixed locations. In other words, each probe molecule is a binding site that is occupied by a target molecule with a certain probability that can be determined [153]. Unspecific binding of target molecules to the sensor surface in the absence of probe molecules is also possible. Since this effect is not important in a well-designed sensor, it is not included here, although it can be taken into account in the model in a straightforward manner.

The orientation of a charged molecule with respect to a charged surface is determined by the electrostatic free energy of the system. A method for determining the free energies of charged molecules as functions of various parameters was presented in [72]. First, the electrostatic free energy $E(\eta)$ is calculated as a function of the angle $\eta := (\eta_1, \eta_2)$, which represents the orientation of the molecule with respect to the surface. In general, each molecule has two degrees of freedom, although in the case of DNA oligomers their structure leads to a simplification and one angle $\eta := \eta_1 \in [0, \pi/2]$ is sufficient. Then a Boltzmann distribution is used to find the probability of a configuration as a function

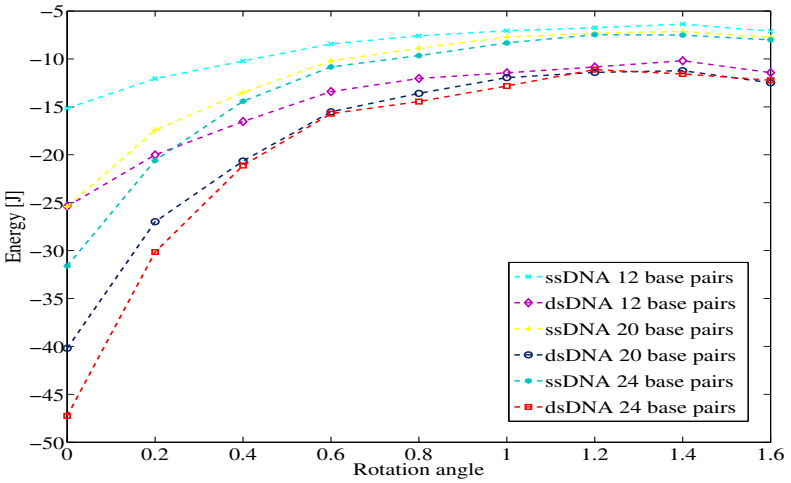


FIGURE 4.2: The electrostatic free energies of various ssDNA and dsDNA oligomers as a function of angle for a surface charge of $-0.5\,\mathrm{q/nm^2}$ in a liquid with an ionic concentration of 30 mM. The angles are defined with respect to the surface, where 0 means a molecule parallel to the surface and $\pi/2$ means a molecule perpendicular to the surface (as indicated in Figure 4.1). Data from [72].

of the angle η. It is given by

$$P(\eta) = \frac{\exp(-E(\eta)/(k_B T))}{\int \exp(-E(\eta)/(k_B T))\mathrm{d}\eta} \propto \exp\left(-\frac{E(\eta)}{k_B T}\right). \tag{4.1}$$

Figure 4.2 shows a concrete example and the data used in the numerical examples in this paper. Electrostatic free energies for single- and double-stranded DNA oligomers of different lengths are shown. Due to their twice as large intrinsic charges, the binding energies of double-stranded DNA (dsDNA) oligomers are higher than their single-stranded (ssDNA) counterparts. The length of the oligomers decreases the free energy mostly for lower angles, i.e., for horizontal configurations, where electrostatic interactions with the surface are stronger. The orientations also depend on the ionic concentration of the liquid, as the effect of Debye screening is significant. Figure 4.3 shows the probability density function (PDF) and cumulative distribution function (CDF) of random orientation of various DNA oligomers bound to the nanowire surface. The figure indicates the Gaussian distribution of random variables. In summary, the coefficients $A(x, y, .)$, $\rho(x, y, .)$ and $\varphi(x, y, .)$ in (2.23) are random variables, i.e., $A(x, y, \boldsymbol{\omega})$, $\rho(x, y, \boldsymbol{\omega})$ and $\varphi(x, y, \boldsymbol{\omega})$ depend on an element $\boldsymbol{\omega} = (\omega_1, \omega_2, \ldots, \omega_n)$ of the underlying probability space (Ω, Σ, P). The sample space Ω describes the locations of the probe molecules, the state of the probe molecules (bound to the target molecules or not), and the orientations of the probe molecules and probe-target complexes. The modeling and simulation results in [72, 153] yield the probability measure P.

We assume that the number of probe molecules per unit area follows a Poisson distribution. Once the number N of probe molecules or binding sites and their positions are fixed, the sample space is

$$\Omega = \big(\{0, 1\} \times [0, \pi/2]\big)^N,$$

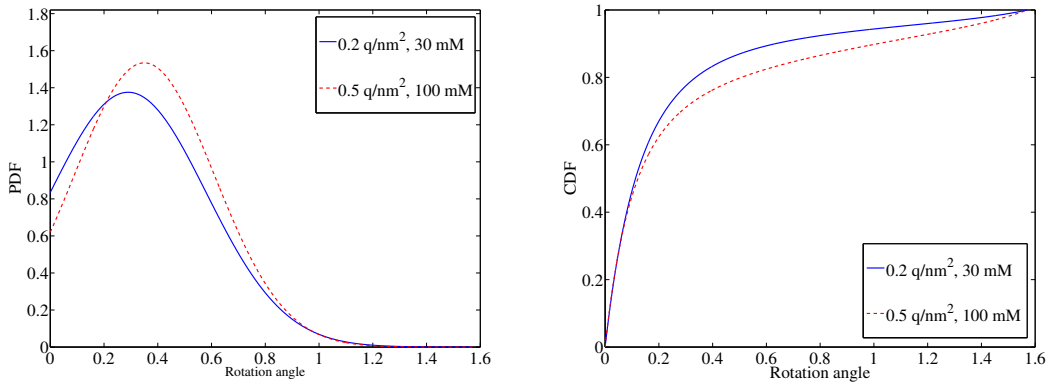


FIGURE 4.3: Probability density function (left) and cumulative distribution function (right) of random orientation of 12 base pairs ssDNA oligomers in an aqueous solution with different ionic concentration and surface charge. The proteins rotate between 0 (horizontal) and $\pi/2$ (vertical) degrees at the surface.

where 0 denotes the absence of any target molecule, 1 the presence of a target molecule, and $\eta \in [0, \pi/2]$ is the angle of molecule.

The sizes in the various subdomains in Figure 4.1 were determined by the following considerations. As found in [14], the optimal width of the silicon transducer is certainly smaller than 100 nm, while its precise value depends on other parameters such as the applied back-gate voltage. Smaller geometries were found to have higher sensitivity.

In order to validate the basis-adaptation approach, several comparisons for two nanowires with different widths are shown in Figure 4.4. The geometry of the sensor is shown in Figure 4.1, where the thickness of oxide layer is 8 nm and the thickness of the nanowire is 50 nm. For the simulations, we define a reference structure, where the back-gate voltage (V_{BG}) is -3 V, the solution voltage is 0 V, $V_S - V_D$ is 0.2 V, the length of the nanowire is 1000 nm, the ionic concentration is 30 mM, the surface charge is $-0.5\,\mathrm{q}\cdot\mathrm{nm}^{-2}$ [72], the doping concentration is $10^{16}\,\mathrm{cm}^{-3}$, the oligomers consist of 12 base pairs and the thermal voltage is 0.021 V. The length of each base pair is 0.34 nm. Furthermore, the electron mobility in silicon is 1000 $\mathrm{cm}^2\mathrm{V}^{-1}\mathrm{s}^{-1}$, the hole mobility is 100 $\mathrm{cm}^2\mathrm{V}^{-1}\mathrm{s}^{-1}$. The model is validated by comparison with experimental data (using the same data as in [14]).

The good agreement shows that the current calculated by the graded-channel approximation works very well for this kind of device due to its long length and small V_{DS}. Secondly, the solutions obtained by basis adaptation are compared with full-dimensional solutions.

The basis-adaptation approximation is obtained using a 2nd order polynomial chaos expansion of (3.75). The full-dimensional solution is the benchmark and actually results from Hermite polynomial chaos expansion up to order 2. Here the simulation are for fluctuation of 10 target molecules ($n = 10$) and 1000 Monte Carlo replications ($M = 1000$). The agreement suggests that the implementation is correct. The differences between the full dimensional solutions and the solutions obtained by basis adaptation

become larger as the absolute value of the back-gate voltage increases; this is due to the fact that small differences are amplified by the large applied potential. The results are shown in Figure 4.4. In basis adaptation the difference between 2nd-order and 3rd-order of PCE for both 60nm and 100nm wide nanowires were negligible so that 2nd order is used for all expected value and noise calculation in subsequent simulations. The results indicate the efficiency and the exactness of the basis adaptation against the full solution. The agreement with experimental data is very good and again justifies the model equations.

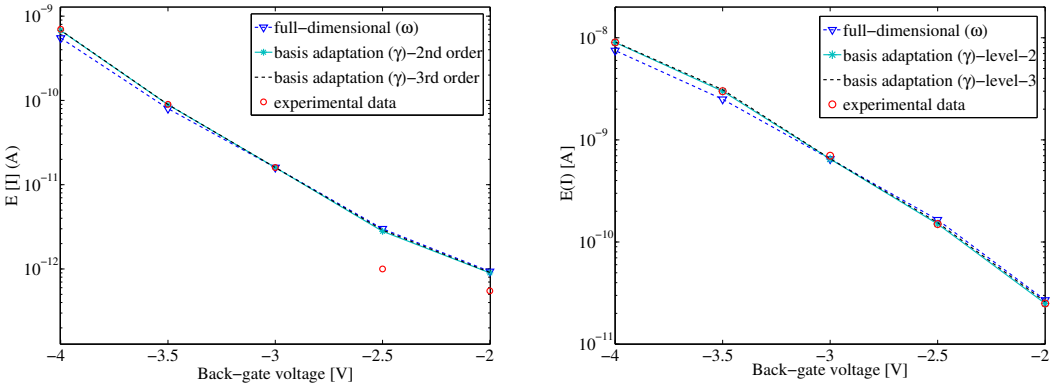


FIGURE 4.4: The comparison of measured and simulated currents (expected value) in respect of different back-gate voltages for 60 nm (left) and 100 nm (right) width of transducer. The simulations are performed for the reference structure, where the back-gate voltage was varied. Here, $V_{SD} = 0.2\,\mathrm{V}$ and for both devices the same threshold voltage is used.

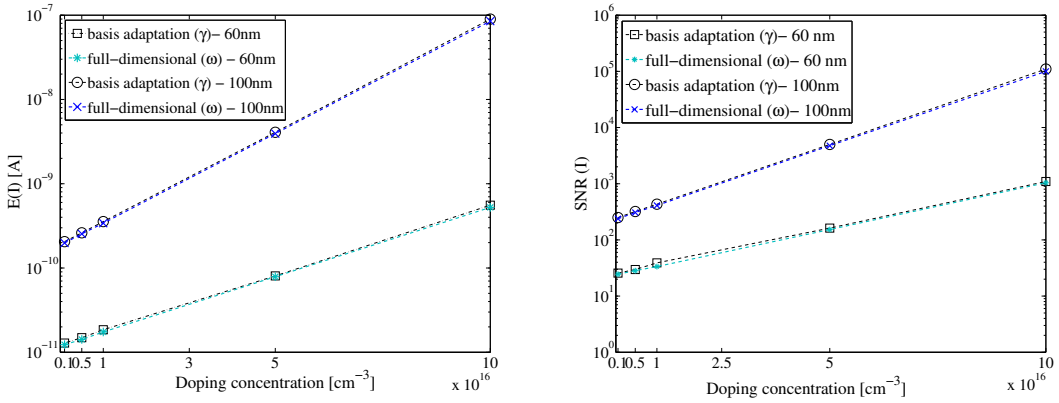


FIGURE 4.5: Expected value of current and its signal-to-noise ratio as functions of doping concentration for 60 nm and 100 nm wide devices. Here, the ionic concentration is 30 mM, the surface charge is $-0.5\,\mathrm{q/nm^2}$ [72], the oligomer length is 12 base pairs, $V_{BG} = -3\,\mathrm{V}$, and the thermal voltage is 0.021 V.

The stochastic equation (2.23) makes it possible to calculate higher-order moments and in particular the signal-to-noise ratio, an important characteristic value. In the following, we discuss how various important device parameters influence the quantity of interest, i.e., the current, and the signal-to-noise ratio. These simulations cover a large part of the

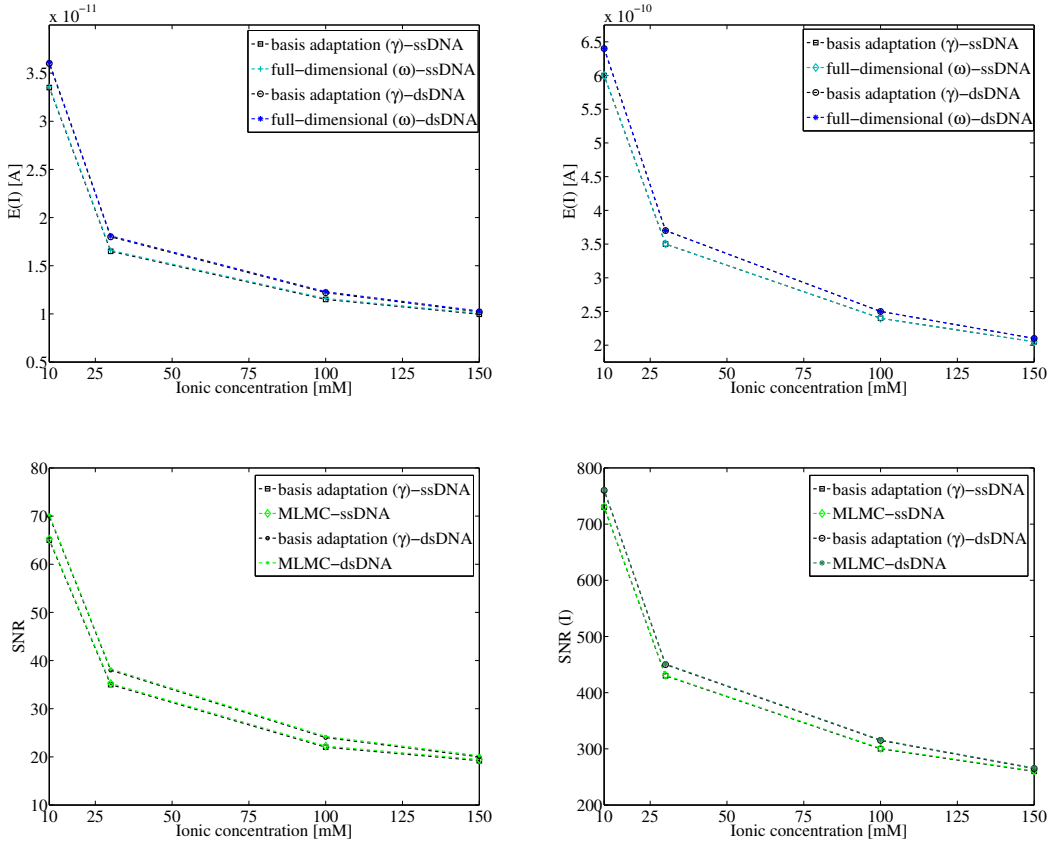


FIGURE 4.6: The comparison of expected value (top) and signal-to-noise ratio of current (bottom) for 60 nm (left) and 100 nm (right) width as functions of ionic concentration. Here, the doping concentration is $10^{16}\,\mathrm{cm}^{-3}$, the surface charge is $-0.5\,\mathrm{q/nm}^2$ [72], the oligomer length is 12 base pairs, $V_{BG} = -3\,\mathrm{V}$, and the thermal voltage is 0.021 V.

parameter space and hence answer the question whether basis adaptation is generally useful or only for the choice of parameters in the previous figures.

The first parameter investigated here is doping concentration. Currents were calculated for doping concentrations between $10^{15}\,\mathrm{cm}^{-3}$ and $10^{17}\,\mathrm{cm}^{-3}$ and are shown in Figure 4.5. The results show that both the current and the signal-to-noise ratio increase for 60 nm and 100 nm wide transducers as the doping concentration increases. This means that higher doping concentrations not only increase the total current, but they also improve the signal compared to the noise, yielding a better sensor.

The second parameter considered here is the ionic concentration. It plays a crucial role, since a higher ionic concentration leads to higher screening and thus reduces the effectiveness of field-effect sensing. On the other hand, a certain ionic concentration (at least about 10 mM) is usually necessary – especially in the case of DNA – to enable probe-target binding. A Monte-Carlo algorithm to find the concentration of (counter) ions around biomolecules was developed in [22], and the ramifications of screening and how to overcome them were discussed in [93, 102]. For a typical salt concentration of 100 mM, the Debye length is approximately 1 nm and any charge is completely screened at a distance of only a few nanometers. The numerical results in Figure 4.10 show

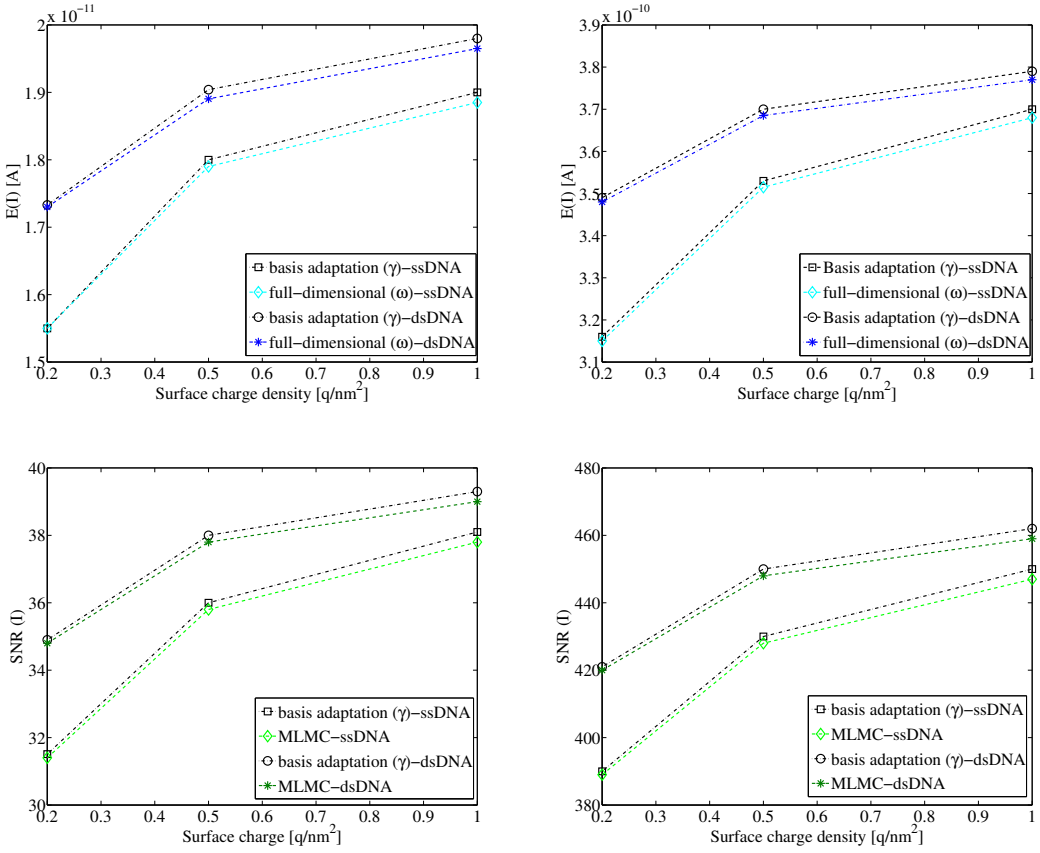


FIGURE 4.7: The comparison of expected value (top) and the signal-to-noise ratio of the current (bottom) for 60 nm (left) and 100 nm (right) wide sensors as functions of surface charge density. Here, the doping concentration is $10^{16}\,\mathrm{cm}^{-3}$, the ionic concentration is 30 nm, the oligomer length is 12 base pairs, $V_{BG} = -3\,\mathrm{V}$, and the thermal voltage is 0.021 V.

that the effect of the intrinsic charges of the target molecules on charge transport in the transducer is still measurable. Furthermore, the wider nanowire is more affected by screening within the semiconductor. Additionally, the signal-to-noise ratio in the 100 nm wide transducer is increased by a factor of 10 compared to the 60 nm wide device. Here, the ionic concentration varies between 10 mM and 150 mM.

The third parameter investigated here is the surface (fixed) charge of molecules. The surface charge is important since it determines the operating point of the sensor, which has a crucial influence on the sensitivity of the sensor [14]. Furthermore, a more negative surface charge repels target DNA oligomers, again emphasizing the necessity of considering the system in a self-consistent manner. In Figure 4.7, the difference between ssDNA and dsDNA oligomers is clearly seen in both 60 nm and 100 nm wide devices, as expected. The width of the device has a strong influence on current and signal-to-noise ratio. The current is about twenty times as large in the larger device, while the signal-to-noise ratio is approximately twelve times as large.

The fourth and final parameter varied here is the length (and hence charge) of the DNA oligomers. The oligomers in the reference structure considered here are 12 base

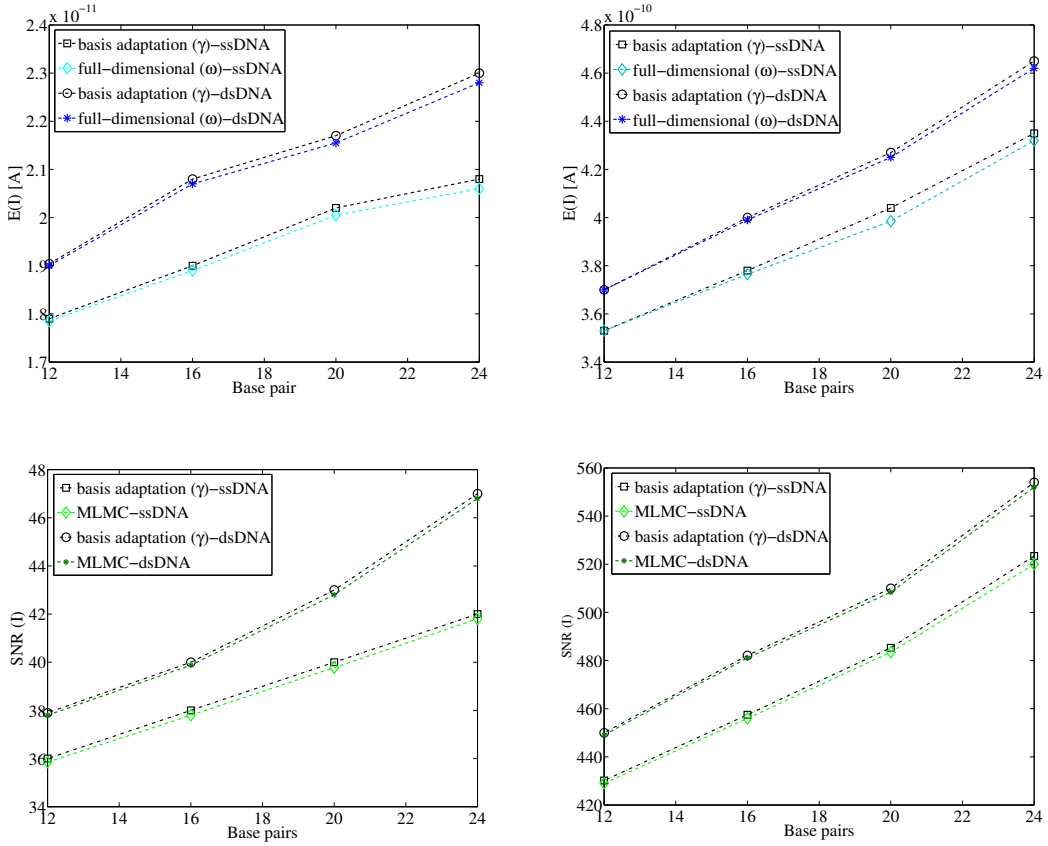


FIGURE 4.8: The comparison of mean value (top) through the transducer and the signal-to-noise ratio of the current (bottom) for 60 nm (left) and 100 nm (right) as functions of oligomer length. Here, the doping concentration is $10^{16}\,\mathrm{cm}^{-3}$, the ionic concentration is 30 mM, the surface charge is $-0.5\,\mathrm{q/nm}^2$, $V_{BG} = -3\,\mathrm{V}$, and the thermal voltage is 0.021 V.

pairs long. However, depending on the application, the length of the probe and target oligomers may be varied. Figure 4.8 illustrates that increasing the oligomer length increases the current as well as the signal-to-noise ratio.

4.1.2 Three-dimensional simulation of SiNW-FETs

The simulation capability developed here is general enough to include many situations where charge transport occurs in a random environment. In the case of field-effect sensors, understanding noise and fluctuations is essential to calculate detection limits and signal-to-noise ratios. The main numerical challenge here is a large number of stochastic dimensions. Each dopant and each receptor for target molecules result in some stochastic dimensions. Therefore, the number of stochastic dimensions is at least in the dozens but can be in the hundreds or thousands for larger devices. Here, the three-dimensional stochastic drift-diffusion-Poisson system is used to model charge transport through nanoscale devices in a random environment. The whole algorithm is optimal in the sense that the total computational cost is minimized for prescribed total errors. This comprehensive and efficient model makes it possible to study the effect of design

parameters such as applied voltages and the geometry of the devices on the expected value of the current [89].

The source of randomness inside the transducer is the random motion of dopant atoms through the semiconductor during the fabrication steps of implantation and annealing, resulting in their random locations.

Various models such as nearest-grid-point (NGP), cloud-in-cell (CIC) [78], and the Sano method [136] may be used to describe randomly placed dopants in semiconducting devices. In the simplest model, the charge concentration due to N ionized atoms is given by

$$\xi_1(x) := C_j \sum_{j=1}^{N} \delta(x - x_j), \tag{4.2}$$

where C_j is the charge of the jth dopant atom, N is the number of dopant atoms, x_j is the position of jth dopant, and δ is the Dirac delta distribution.

In [80], Gaussian distributions for the individual dopant atoms were placed at random positions. In [28], the standard deviation σ of the Gaussian or normal distributions was used to adjust the size of the dopant atoms yielding the charge concentration

$$\xi_2(x) := \sum_j \frac{C_j}{(2\pi\sigma^2)^{3/2}} \exp\left(-\frac{(x - x_j)^2}{2\sigma^2}\right). \tag{4.3}$$

Here, $\sigma := 0.25\,\text{nm}$ is used to represent a dopant; the results are not very sensitive to the value of σ.

To make the results comparable between continuous and discrete doping models, the total doping must match. In other words, the integrals over a continuous doping concentration C_{dop} and over a discrete doping concentration must agree, i.e.,

$$\int_{D_{\text{Si}}} C_{\text{dop}}(x)\mathrm{d}x = \int_{D_{\text{Si}}} \xi_1(x)\mathrm{d}x = \int_{D_{\text{Si}}} \xi_2(x)\mathrm{d}x.$$

The association and dissociation processes of target molecules at the surface can be described by the reaction equations (2.41). In [153], in order to optimize the sensor design, a random-walk based model for diffusive transport to the association-dissociation processes at the sensor surface was used. It was found in [153] that the number **PT** of probe-target complexes satisfies the stochastic ordinary differential equation (2.46).

In the simulation, the reaction parameters are taken from [151]. The simulation was performed for a receptor density of $3 \times 10^{12}\,\text{cm}^{-2}$ and 40 target molecules in the liquid for a nanowire with 80 nm diameter. The surface was partitioned into three different regions, called edge, middle, and corner regions as illustrated in Figure 4.9. In addition, the average probe-target concentration at the surface is called the overall concentration. Table 4.6 gives the equilibrium values of **PT** in these regions and Figure 4.10 shows the probability density distributions; these values are used in the numerical experiments.

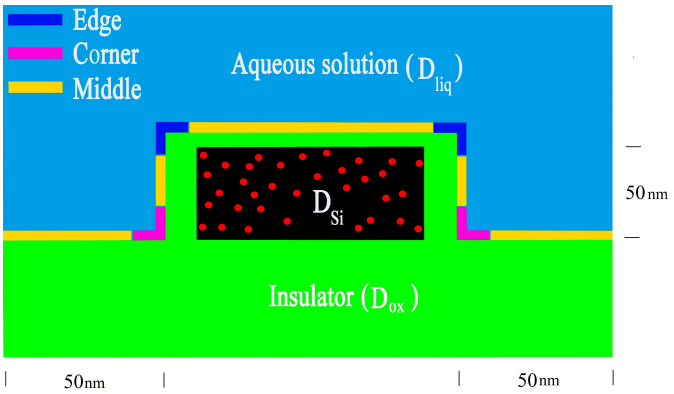


FIGURE 4.9: A cross section of the field effect sensor indicating the three different regions of the surface.

Region	Mean	Variance
Edge	1.3089	0.5816
Middle	0.9817	0.4732
Corner	0.6061	0.4743
Overall	1.0180	0.0862

TABLE 4.1: The expected values and variances of the probe-target concentration **PT** at the nanowire sensor surface. All values are in the unit $10^{12}\,\mathrm{cm}^{-2}$.

μ_1	γ_1	μ_2	γ_2	μ_3	γ_3	μ_4	γ_4
0.611	3.11	0.76	3.09	0.42	3.08	0.35	3.07

TABLE 4.2: The measured constants in (3.27).

The geometry of the device is shown in Figure 1.2 and the random binding of the molecules at different regions of the device is illustrated in Figure 4.9. The corresponding 3D meshes for a nanowire sensor 50 nm thick, 60 nm wide, 500 nm long, and containing 15 dopants are depicted in Figure 4.11.

As aforementioned, solving the optimization problem (3.33) with respect to a given error bound yields h_ℓ and M_ℓ on each level ℓ. The optimization problem depends on the constants μ_k and γ_k, $k \in \{1, \ldots, 4\}$. They are measured by running three-dimensional simulations and saving the CPU time needed for assembling the system matrices and solving the three elliptic equations that constitute (2.23). The values are shown in Table 4.2 and depend on the implementation and hardware used.

If there is only one level ($L = 0$), then the multi-level Monte-Carlo method simplifies to the standard Monte-Carlo method. A comparison between the optimized Monte-Carlo and the optimized multi-level Monte-Carlo methods is drawn in Figure 4.38. The effectiveness of the MLMC method is more pronounced for smaller tolerance levels. At the smallest error tolerance in this figure, the MLMC method is more efficient by more than two orders of magnitude. The coefficients and the exponents, i.e., α and β in (3.22), are shown in Figure 4.12, where $C_{00} = 2.95$. The estimated exponents (here $\gamma \approx 3.0875$) also agree well with the three-dimensional simulations. The optimal number of samples and the mesh sizes for the optimized Monte Carlo and multilevel Monte-Carlo

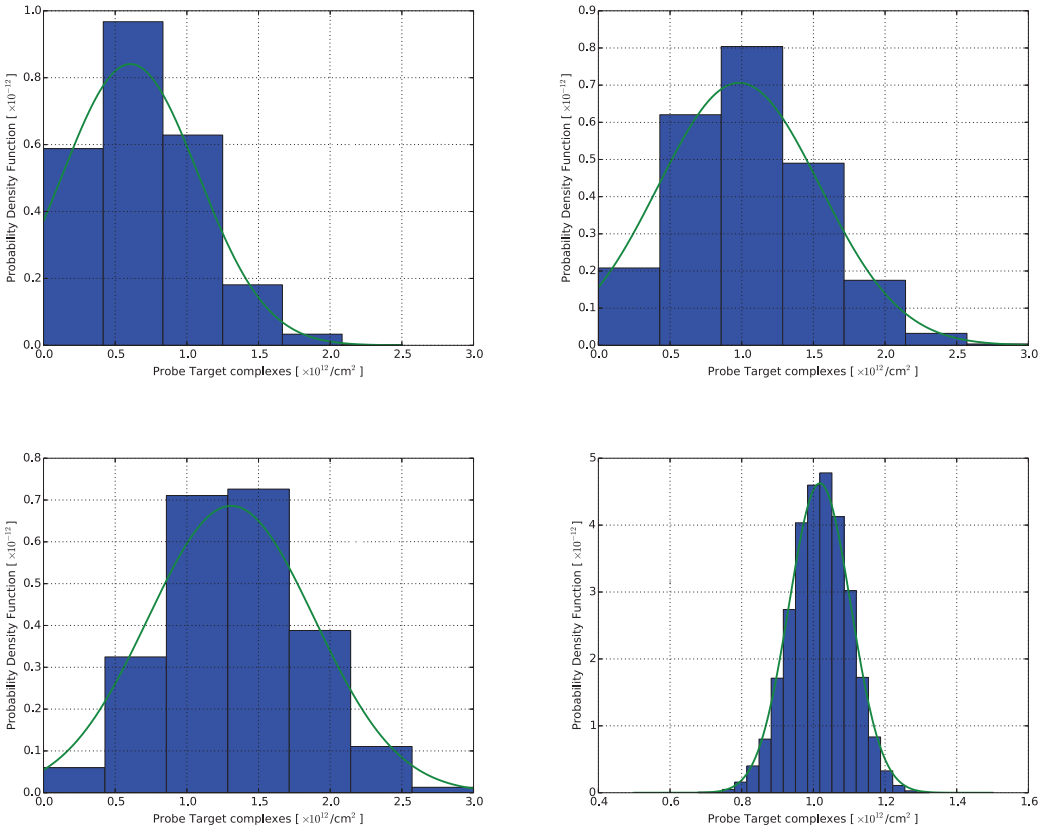


FIGURE 4.10: Histograms of the **PT**-complex density in equilibrium at the corners (top left), in the middle (top right), at the edges (bottom left), and overall (bottom right). The green lines show a Gaussian distribution with the parameters in Table 4.6.

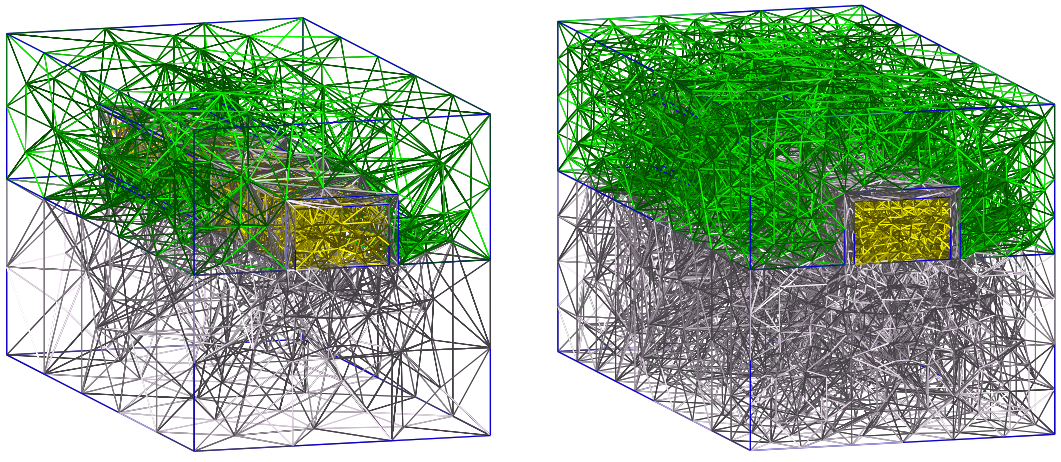


FIGURE 4.11: The meshes for the nanowire field-effect sensor for $\ell = 0$ (left) and $\ell = 1$ (right). The subdomains are depicted with gray (substrate), golden (nanowire), and green (electrolyte) meshes. The randomly distributed molecules and the dopants are inside the electrolyte and the nanowire, respectively.

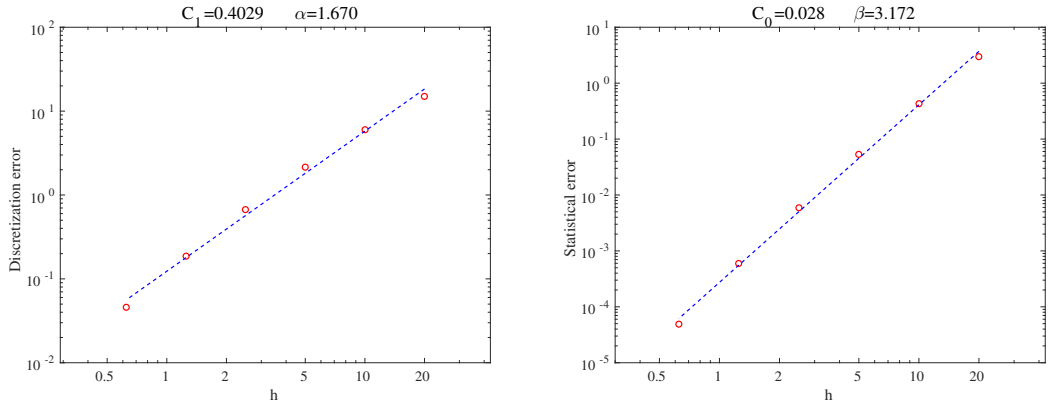


FIGURE 4.12: Statistical and discretization errors for different mesh sizes. The coefficients α and β behave according to Assumption 1.

ε	0.100	0.050	0.020	0.010	0.005
h	0.918	0.600	0.350	0.231	0.153
M	578	2 309	14 431	57 725	230 902

TABLE 4.3: Optimal parameters for the Monte-Carlo method.

ε	h_0	r	M_0	M_1	M_2	M_3	M_4	M_5	M_6
0.100	1.526	1.802	941	149	24	4	–	–	–
0.050	1.382	2.001	3 761	431	49	6	–	–	–
0.020	1.405	1.967	27 894	3 366	405	49	6	–	–
0.010	1.608	1.749	146 482	26 249	792	156	27	5	–
0.005	1.608	1.749	584 957	87 555	12 603	1 814	296	42	6

TABLE 4.4: Optimal parameters for the MLMC method.

are summarized in Table 4.3 and 4.4, respectively. Finally, a comparison between MC-FEM and MLMC-FEM is given in Figure 4.13. It points out the noticeable advantage of the multilevel method where for the lowest tolerance ($\epsilon = 0.005$); the work is reduced by more than two orders of magnitude. The measured constants satisfy the assumptions of the standard complexity theorem [33], i.e., $\alpha \geq \frac{1}{2}\min(\beta, \gamma)$. According to this theorem, the computational cost of the MLMC method is $\mathcal{O}(\varepsilon^{-2})$ agreeing with the numerical results. Furthermore, the total cost of the Monte-Carlo method is $\mathcal{O}(\varepsilon^{-3.5})$ according to the figure, which agrees with [27].

As already mentioned, only the biological noise (random movement and random orientation) is taken into account in the continuum model, whereas the effect of random dopants is also included in the discrete model. Figure 4.14 shows the expected value of the electrical current as a function of different gate voltages for two devices that are 60 nm and 100 nm wide. The results are compared with experimental data [14]. In the simulation, the thermal voltage U_T is 21 mV. In the continuum model $C_{\text{dop}} = 1 \times 10^{16}\text{cm}^{-3}$, the thickness of the oxide layer is 8 nm, the source-to-drain voltage is $V_{SD} = 0.2$ V, the salt concentration is 30 mM, and the molecule surface charge is $-0.8\,\text{q} \cdot \text{nm}^{-2}$ (fitting parameter).

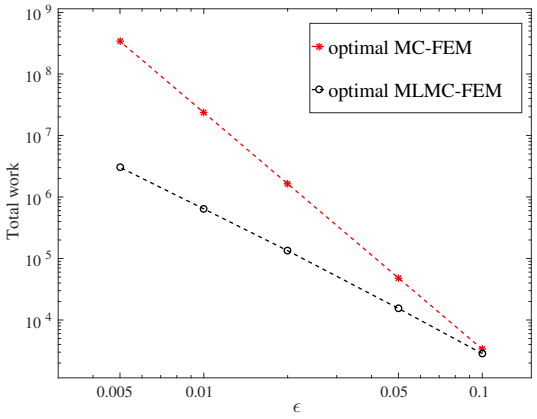


FIGURE 4.13: A comparison of the total computational work necessary in the MC and MLMC methods as a function of the prescribed total error.

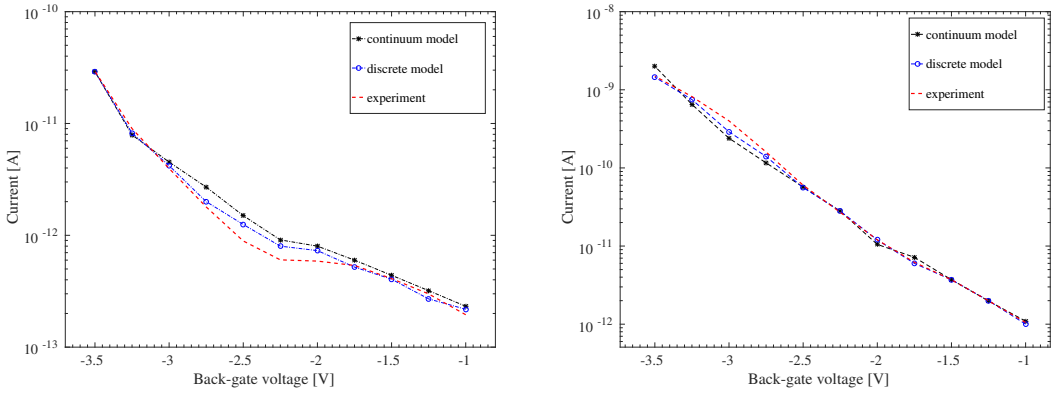


FIGURE 4.14: The expected value of the electrical current as a function of back-gate voltage for 60 nm width (left) and 100 nm width (right) for continuum and discrete models. Here, the discrete model points out the biological noise in addition to the RDF and in continuum model only the RDF is considered. In the simulation, the results are with the experimental data [14] with the same main parameters i.e., $t_{\text{ox}} = 8\,\text{nm}$, $C_{\text{dop}} = 1\times10^{16}\text{cm}^{-3}$, $V_{SD} = 0.2\,\text{V}$, the nanowire thickness of 50 nm and $\mu_p = 100\ \text{cm}^{-2}\text{V}^{-1}\text{s}^{-1}$.

Very good agreement between the experiments and the simulations was found for both the discrete and the continuum model. The results show that the discrete model agrees better with the experiments than the continuum model. This is probably due to the fact that including the effect of the random dopants is a better model for the current compared to just taking the average doping as in the continuum model.

Figure 4.15 depicts the fluctuation of the current in the discrete model for two doping concentrations, namely $C_{\text{dop}} = 1\times10^{16}\text{cm}^{-3}$ and $C_{\text{dop}} = 1\times10^{17}\text{cm}^{-3}$. Here, the effects of random molecules and random dopants on the current are taken into account. For the lower doping concentration, the expected value of the current is $\mathbb{E}(I) = 2.17\times10^{-13}\,\text{A}$ and its standard deviation is $\sigma(I) = 2.38\times10^{-14}\,\text{A}$. The simulation indicate that more than 95% of the obtained currents are between $2\times10^{-13}\,\text{A}$ and $2.5\times10^{-13}\,\text{A}$. The expected value relatively agrees with the experiments [14] ($I = 1.5\times10^{-13}\,\text{A}$). Also, for the higher doping concentration, the values are $\mathbb{E}(I) = 2.34\times10^{-12}\,\text{A}$ and $\sigma(I) = 2.90\times$

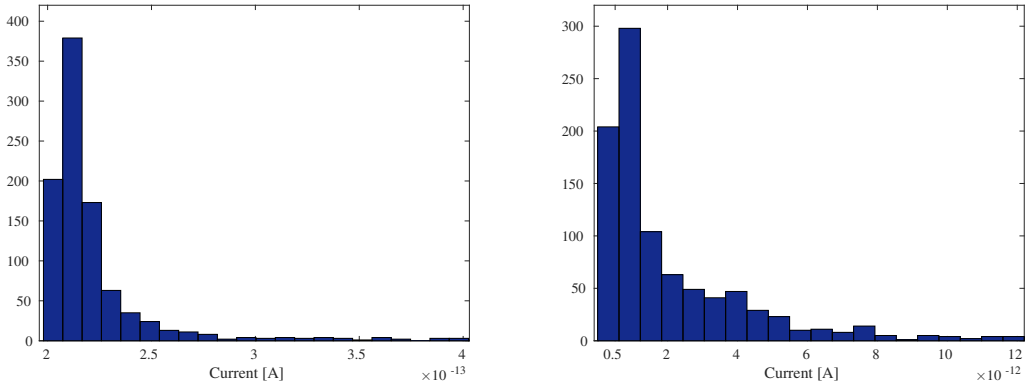


FIGURE 4.15: Histograms of the electrical current calculated by the discrete model (biological and RDF fluctuation) with 941 simulations for a doping concentration of $1 \times 10^{16}\,\mathrm{cm}^{-3}$ (left) and for a doping concentration of $1 \times 10^{17}\,\mathrm{cm}^{-3}$ (right).

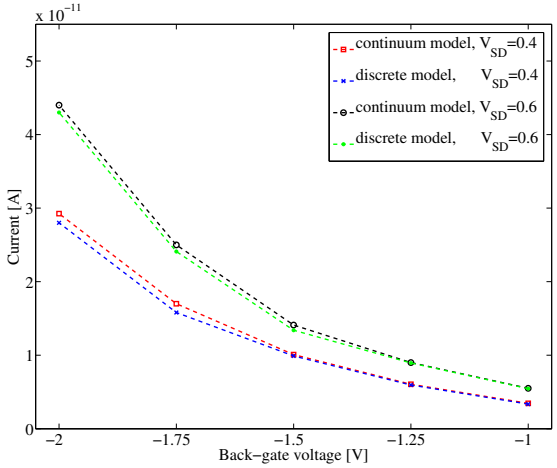


FIGURE 4.16: The expected value of the current for $V_{SD} = 0.4\,\mathrm{V}$ and $V_{SD} = 0.6\,\mathrm{V}$ for both the continuum and discrete models where $V_T = -0.98\,\mathrm{V}$ (threshold voltage).

$10^{-12}\,\mathrm{A}$. The simulations show that more dopants increase the variance of the current. The figure shows that for $C_{\mathrm{dop}} = 1 \times 10^{16}\mathrm{cm}^{-3}$ approximately 95% of the simulated currents are between $2 \times 10^{-13}\,\mathrm{A}$ and $2.4 \times 10^{-13}\,\mathrm{A}$, resulting in a small fluctuation. On the other hand, the results obtained for the higher doping concentration fluctuate between $1.80 \times 10^{-13}\,\mathrm{A}$ and $1.08 \times 10^{-11}\,\mathrm{A}$, indicating a larger variation. Using the p-type semiconductor (as well as negatively charged molecules) increase the conductivity of the device and therefore, its variation. It is expected that positively charged molecules decreases the fluctuations slightly.

Generally, applying a source-to-drain voltage V_{SD} results in a low-resistance conducting path between the source and drain contacts. Figure 4.16 shows the current for different the source-to-drain voltages. Here, both models are used and the back-gate voltage varies between $V_G = -1\,\mathrm{V}$ and $V_G = -2\,\mathrm{V}$.

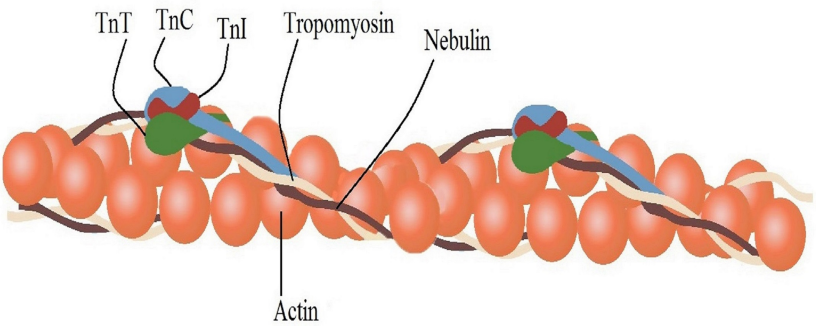


FIGURE 4.17: The four principal regulatory components of the skeletal muscle, i.e., actin, tropomyosin, nebulin and the troponin complex [55].

4.2 Cardiac troponin sensitive sensors

The purpose of this section is the development and quantitative understanding of biological sensors for the detection of cardiac troponin in blood [87] starting just from its known structure (PDB code 1MXL [99]). We determine the effective parameters to design and fabricate more sensitive nanowire field-effect sensors to detect different ranges of cTn. Here, the sensitivity indicates the response of the sensor to the binding of target molecules (cTn) to the immobilized probe molecules (anti-troponin receptors) at the sensor surface.

As for every sensor, a crucial question is how to achieve the best response of the SiNW-FET. There are several substantial parameters which are effective in the conductivity of the device. In other words, the sensor response is influenced by different physical and geometric device properties. Here, we propose an array of silicon nanowire field-effect biosensors optimized with regard to parameters such as length, width, doping concentration, dopant type, type of the nanowire, backgate voltage, and the number of parallel nanowires. Thus, by changing influential parameters, it is made possible to optimize the electrical characteristics of devices and to fabricate the optimal field-effect sensor to detect cTn concentration more accurately. Noise and fluctuations of the device conductivity due to the random binding of cTn to the receptors are also taken into account. The random binding of troponin molecules (target molecules) to the anti-troponin molecules (antigens) is shown in Figure 4.18.

The troponin complex regulates the contraction of striated muscles. It consists of three subunits, i.e., cTnC, cTnT, and cTnI (Figure 4.17). These protein subunits along with tropomyosin are located on the actin filament and are essential for the calcium-mediated regulation of skeletal and cardiac muscle contraction [146]. Cardiac TnT binds the troponin components to tropomyosin and TnI inhibits the interaction of myosin with actin [110, 164]. Cardiac TnC contains the binding sites for Ca^{2+} and its interaction with cTnI and cTnT is central to the regulation of skeletal and cardiac muscle contraction [66]. TnT and TnI have been found to have excellent sensitivity and specificity, and are superior to CK-MB as indicators of myocardial necrosis [109]. For the last twenty-five

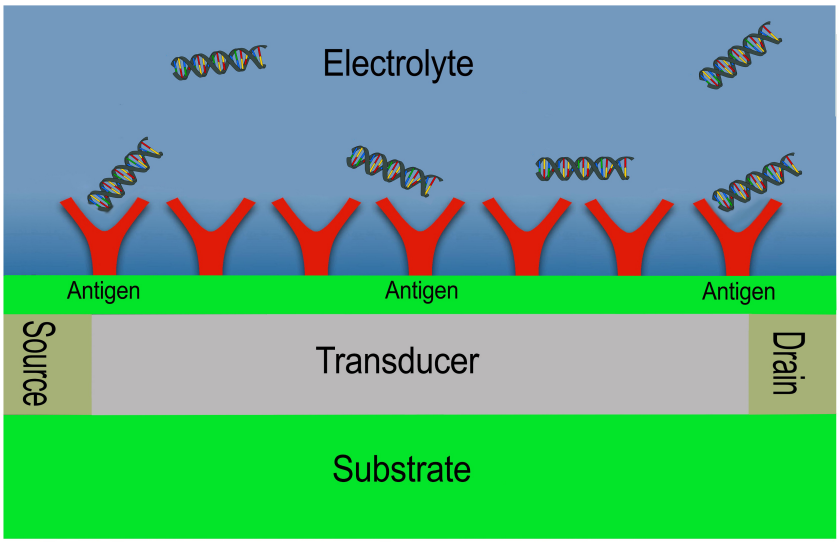


FIGURE 4.18: A longitudinal cross section of a troponin sensitive SiNW-FET. The random binding of troponin molecules to the probe molecules (antigens) is depicted as well.

years, isoforms of troponin I and T have been widely used for immunochemical diagnostics of pathologies associated with cardiomyocyte death, e.g. AMI, unstable angina, post-surgery myocardial trauma, and other diseases related to cardiac muscle injury [82].

Cardiac TnI and TnT are released after AMI or other cardiacs disease [164] and their clinical sensitivity and specificity improve with time. More precisely, for both troponins, sensitivity raises from 10% to 45% within 1 hour of the onset of pain to more than 90% after 8 or more hours [52]. Specificity does not change noticeably over time. It decreases from 87% to 80% from 1 to 12 hours after the onset of chest pain for troponin T and is approximately 95% for troponin I [52]. The diagnostic performance/accuracy of TnI and TnT has been observed similarly and is very high [131].

Few studies have reported the 99th percentile of high-sensitive cardiac troponin I (hscTnI) among different age groups and genders. Since 1995, the diagnostic cutoff has been decreased from 1500 pg/mL to 10 pg/mL [107, 158]. As in [158], the 99th percentile concentration of TnI was greater than 19 pg/mL for individuals older than 60 years and 10 pg/mL for individuals younger than 60 years. Therefore, concentrations greater than 10 pg/mL have been shown to have prognostic value. In other words, the upper limit for a normal individual is 10 pg/mL, and for patients who have acute coronary syndromes or AMI, rising troponin values greater than or equal to the diagnostic cutoff value result in the diagnosis of cardiac injury. Also, decreasing values are indicative of recent cardiac injury. We also consider that patients with low-level elevations (smaller than 20 pg/mL) of TnI and diagnostic uncertainty for acute coronary syndrome should be evaluated by repeated measurements.

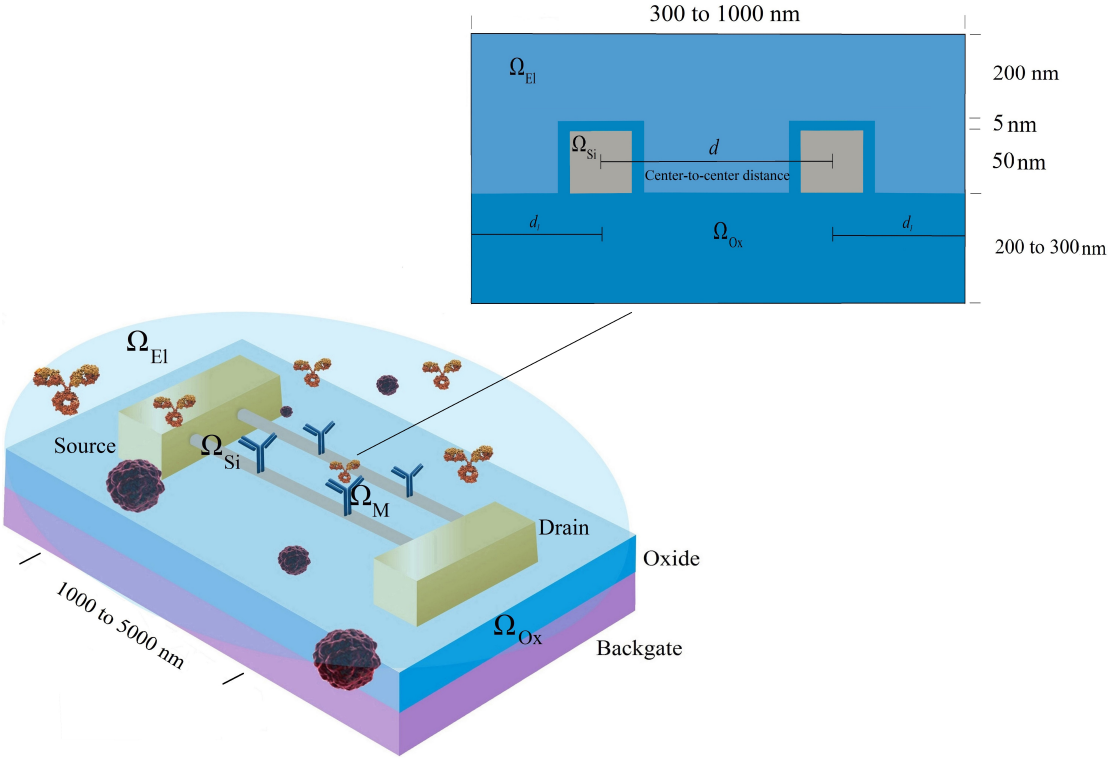


FIGURE 4.19: Schematic diagram of the nanowire field-effect sensor showing receptor and target molecules. The subdomains, i.e., silicon nanowire Ω_{Si}, insulator Ω_{Ox}, the specific binding of target to probe molecules Ω_M, and the electrolyte Ω_{El} are illustrated with their dimensions and ranges. Additionally, d indicates the center-to-center distance between the nanowires and d_1 is the distance between a nanowire and the boundary.

Over the last fifteen years, new techniques and strategies for rapid detection of biomarkers, including cardiac troponin, have been utilized to shorten the diagnostic time and increase the reliability of tests [120]. Quick determination of the concentration of biomarkers in the body has drawn attention in the past decade. New techniques are being incorporated into products [126]. As the medical diagnostic methods progress, therapies with high specificity according to biomarkers determined in tests are continuously being targeted. High-throughput sensors and systems for the ultrasensitive detection of biomolecular interactions are in high demand [90].

Here the main aim of the SiNW-FET is the detection of cardiac troponin in blood. For this reason, the sensor must be able to determine the target protein concentration in the meaningful range. In other words, the dynamic range of the sensor is to designed. The range of cardiac troponin in human blood is between 3.4 pg/mL and 10 000 pg/mL as the concentration rises from almost 20 pg/mL within one hour of myocardial infarction to 10 000 pg/mL after 32 hours from the incidence [107, 134].

The basic structure of the device including its dimensions is shown in Figure 4.19. Here, we consider four shapes or types of nanowires: rectangular, trapezoidal, radial, and triangular, all with a cross-sectional area of 2500 nm^2, a doping concentration (C_{dop}) of 10^{17} cm^{-3} (p-type transducer), protected by a 5 nm thick silicon oxide (Ω_{Ox}), and a

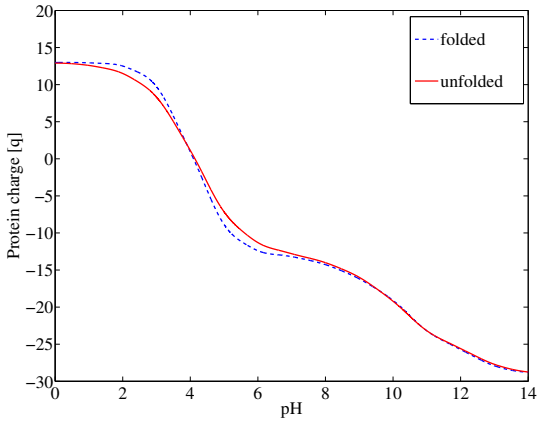


FIGURE 4.20: The net charge of the folded and unfolded states of protein 1MXL for different pH values. The results are obtained by PDB2PQR simulation.

thermal voltage of 26 mV. The applied voltages are $V_G = 1\,\mathrm{V}$ at the back-gate contact and $V_{SD} = 0.2\,\mathrm{V}$ as the source-to-drain voltage.

4.2.1 The charge of biomolecules

The most common and well-established continuum model for the description of ionic concentrations and the electrostatic interactions of the biomolecules is the Poisson-Boltzmann equation [104]. It can be used to calculate ionic concentrations around molecules and the effect of the charged target molecules (cTn) on the transducer.

The modeling of the electrostatics of biomolecules is essential for the simulation of nanowire field-effect sensors. The surface of dielectric materials such as SiO_2, Si_3N_4, Al_2O_3, and Ta_2O_5 is charged when it is in contact with an electrolyte and it is neutral only at the isoelectric point. This surface charge provides an important baseline value regarding the operating regime of the sensor since the surface charge is a function of pH value [15]. There are several methods to describe the effect of charged molecules: the atomistic approach, i.e., Monte-Carlo simulations [22], the continuum approach, i.e., the Poisson-Boltzmann equation [104, 119], and the empirical PROPKA model [98].

The pK_a values of the ionizable residues are the negative logarithm of the ratio of dissociated acid and conjugated base over the concentration of the associated chemical. They are the basis for understanding the pH-dependent characteristics of proteins and catalytic mechanisms of many enzymes. Here, the program PDB2PQR [47] is used to compute the charge distributions of proteins of known structure. Given a protein structure, it computes the pK_a value of each ionizable amino acid. Based on the computed pK_a value, it is possible to determine the protonation state of each ionizable amino acid based on pH value [47].

Figure 4.20 shows the troponin (PDB code 1MXL) charge of the folded and unfolded states as a function of pH values between 0 and 14. Here the folded molecule carries no net electrical charge at a pH value of 4.13, while for unfolded proteins the isoelectric

point is a pH value of 4.08. Blood is normally slightly basic in a pH range of 7.35 to 7.45. According to the simulation, the protein total charge is $-13.58\,\mathrm{q}$ at blood pH (7.4 in this work). The net charges of the target molecules are negative since the protein isoelectric values are lower than pH 7.4. Finally, the negative charges of the target protein (cTn) result in a carrier accumulation on the p-type silicon nanowire and consequently an increase of conductance.

4.2.2 Troponin sensor response

By solving the system of stochastic drift-diffusion-Poisson equations (2.15), the current-voltage characteristics and the sensor response are determined as functions of the target molecule concentration. Hence the behavior of the nanowire sensors can be studied by varying all influential device parameters [87].

In field-effect biosensors, the target molecules (cTn) carry negative (due to blood pH value) charges and act as a negative gate voltage. Since we use a p-type (boron-doped) semiconductor as the transducer, the accumulation of charge carriers increases the conductance as well. The critical issue for the modeling of the sensitivity of nanowire field-effect sensors is the screening of the partial charges of the target molecules by the free ions.

Definition 1. The sensor response (sensitivity) is defined as

$$\frac{I_{\mathrm{mol}} - I_0}{I_0}, \tag{4.4}$$

where I_{mol} and I_0 are the currents through the device with and without molecules, respectively.

In the subsequent simulations, we consider I_{mol} as the signal. The difference $(I_{\mathrm{mol}} - I_0)$ can be interpreted as the response of the sensor to the specific binding of cTn to the anti-troponin receptors.

The limit of detection (LOD) of an individual analytical procedure is the lowest amount of analyte in a sample which can be detected, but not necessarily quantified. In field-effect sensors, surface reactions at the oxide surface depending on the pH value and the binding of charged target molecules result in changes in the charge concentration at and near the surface, and subsequently in changes in the electrostatic potential, which then modulate the current through the transducer. In other words, the PROPKA algorithm [12, 98, 119] is used to estimate the charge of biomolecule in the liquid. Also, the LOD is defined as the minimum troponin concentration that induces a measurable difference in output current. A signal-to-noise ratio larger than 5 is generally considered acceptable for determining the detection limit.

First, we calculate the statistics of the **PT**-complex by solving the Langevin equation. As mentioned already, the dynamic TnI range is between $3.4\,\mathrm{pg/mL}$ and $10\,000\,\mathrm{pg/mL}$. To convert the troponin concentration to a number of molecules, the protein weight of $24\,000\,\mathrm{Da}$ is used. In the simulations, we also used $C_P := 2 \times 10^{12}\,\mathrm{cm}^{-2}$ as the probe

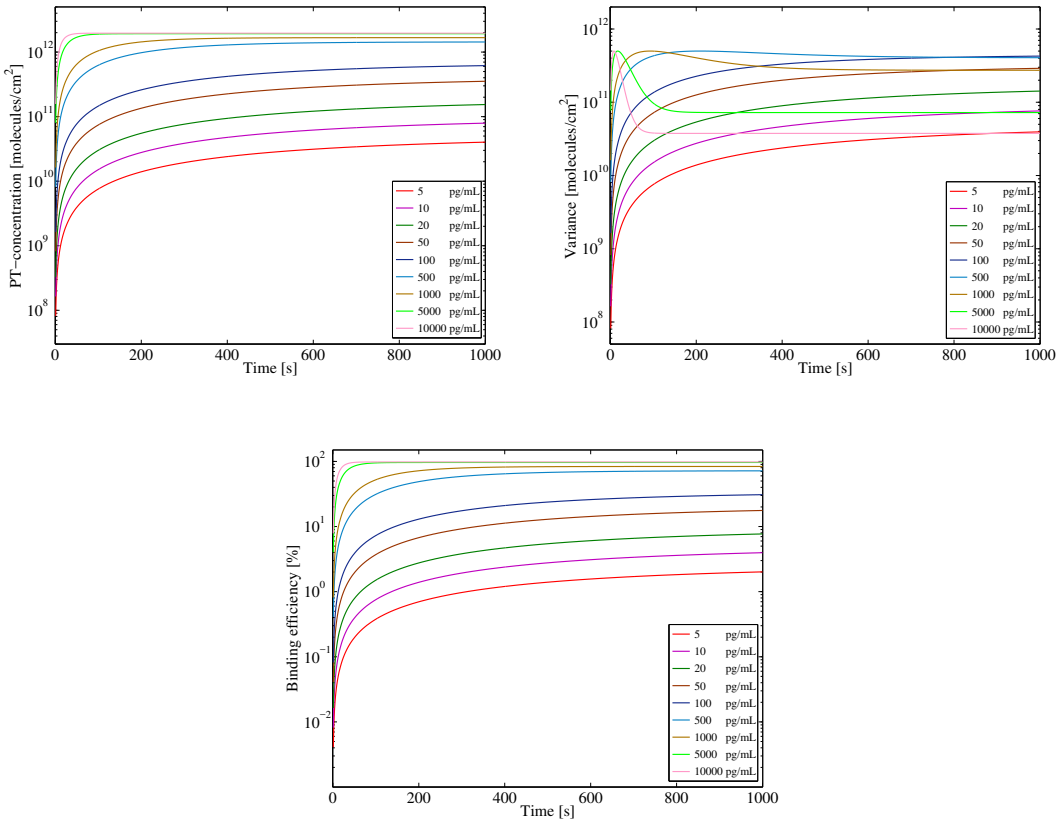


FIGURE 4.21: The expected value (top left), variance (top right), and binding efficiency (bottom) of **PT**-complexes for different troponin concentrations.

density, and the association and dissociation constants $r_a = 3933$ and $r_d = 0.0016$ are taken from [123, 152].

Figure 4.21 shows the results of the simulation for different concentrations of target molecules. For the lower concentrations (less than 10 pg/mL), the ratio of hybridized complexes at the surface to the total number of probe molecules is less than 10%. In this range, the equilibrium time is also considerably larger than for higher concentrations. On the other hand, for concentrations higher than 500 pg/mL, the binding efficiency attains a very good value of nearly 100% and the equilibrium time is less than 200 s. Moreover, a remarkable feature of such a field-effect sensors is that even if the binding efficiency is lower for certain probe and target concentrations, the surface charge density can be larger and therefore result in better detection by a field-effect sensor. Finally, for all troponin concentrations, the binding time (of cTn to the antibodies) shows the very fast response of the sensor. This reaction time indicates the significance of using SiNW-FETs compared to traditional methods such as ELISA.

Here, we consider four shapes or types of nanowires: rectangular, trapezoidal, radial, and triangular, all with a cross-sectional area of 2500 nm^2, a doping concentration (C_{dop}) of 10^{17} cm^{-3}, protected by a 5 nm thick silicon oxide (Ω_{Ox}), and a thermal voltage of 26 mV. The applied voltages are $V_G = 1$ V at the back-gate contact and $V_{SD} = 0.2$ V as the source-to-drain voltage. Also, all devices have aluminum gate (work function is

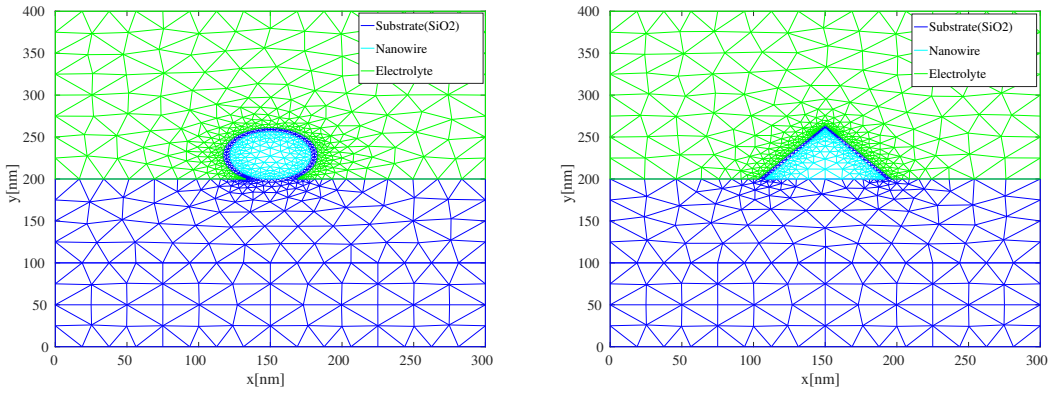


FIGURE 4.22: Cross-section of radial (left) and triangular (left) nanowires with nanowire area of 2500 nm. In the triangular device, the sidewall angels are $\approx 54.7°$.

4.1 V) and for all simulated devices same threshold voltage is employed. This structure is used for all devices unless a parameter is changed. In order to compute the current, a 2D simulation in addition to the graded channel approximation are used.

Using the 99th percentile among different age groups and genders, cTnI assay values are more than 19 pg/mL in individuals older than 60 years and 10 pg/mL in the rest of the individuals [135]. A sharp increase in the troponin concentration is observed after two to three hours after the onset of symptoms, e.g., chest pain. For example, in [107], the value raised from 60 pg/mL to 6.3 ng/mL six hours after the medical examination.

According to these concentrations mentioned in the literature, we define three different concentration ranges and design three sensors, one for each concentration range.

For the first concentration range (low risk or healthy patients), the device is designed for a concentration between 5 pg/mL and 50 pg/mL. The sensor is 300 nm wide and is characterized by a 200 nm thick bulk oxide; the length of the nanowire is 1000 nm. A schematic of the cross-section of the device is given in Figure 4.22.

In acute coronary syndrome, the concentration reaches 500 pg/mL after three hours [107]. Therefore, the second concentration range is defined to be 50 pg/mL to 500 pg/mL. Here, the width of this device is 1 μm, the length of the nanowire is 5 μm, the height of the bulk oxide is 5 nm and the substrate is 300 nm. To consider the situation when many molecules may bind, two parallel nanowires are used.

The cTnI value rises to its peak value of 10 ng/mL within twenty hours and then it decreases gradually [107]. The third and highest concentration range is thus from 500 pg/mL to 10 ng/mL. For this range, the sensor is an array of four nanowires for improved detection of high concentrations.

The first comparison discusses the effect of the four different cross sections of nanowires in the first device. Figure 4.23 shows the results for the first device, the one for healthy or low-risk concentration, for different cross sections, all with a cross-sectional area of 2500 nm^2 and a length of 1000 nm (see Figure 4.22).

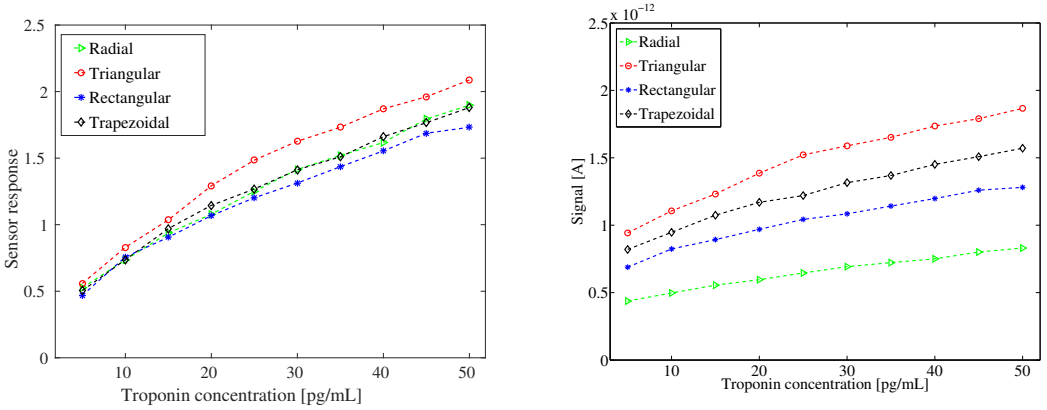


FIGURE 4.23: Sensor response (left) and signal (right) as a function of troponin concentration varying from 5 pg/ml and 50 pg/ml for different nanowire cross sections. The sensors are 300 nm wide and the bulk oxide is 200 nm thick. Each sensor has one 1000 nm long nanowire, a cross-sectional area of 2500 nm^2, a doping concentration of 10^{17} cm^{-3}, and they are protected by a 5 nm thick silicon oxide layer.

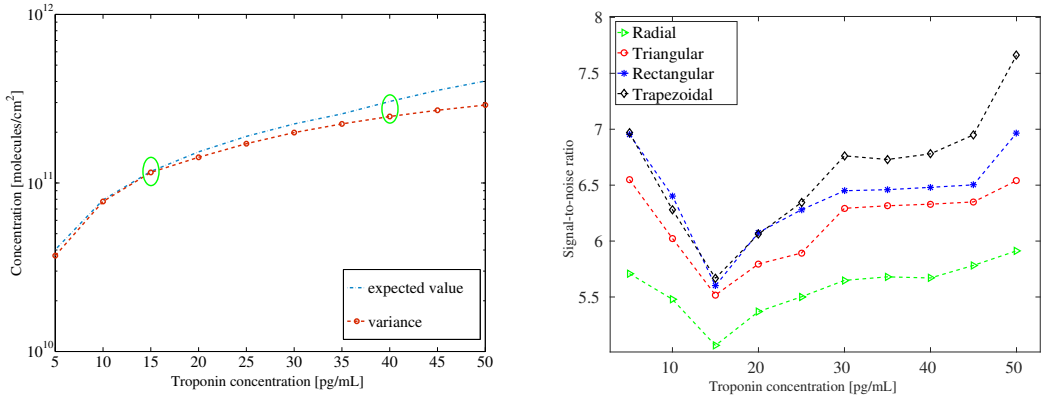


FIGURE 4.24: Expected value and standard deviation of **PT**-complexes (left) and signal-to-noise ratio (right) as a function of troponin concentration varying from 5 pg/ml and 50 pg/ml for different nanowire cross sections. The sensors are 300 nm wide and the bulk oxide is 200 nm thick. Each sensor has one 1000 nm long nanowire, a cross-sectional area of 2500 nm^2, a doping concentration of 10^{17} cm^{-3}, and they are protected by a 5 nm thick silicon oxide layer.

The figure shows that the triangular nanowire performs considerably better than the other transducers, especially for concentrations higher than 10 pg/mL. The radial and trapezoidal nanowires show approximately the same sensor response for most of the concentrations and perform better than the rectangular shape. However, the sensitivity of the rectangular transducer at the diagnostic cutoff is slightly better than the trapezoidal and radial ones.

The radial nanowire (see Figure 4.22) yields the lowest signal compared to the others, while the triangular cross section again yields the highest current. As already mentioned, the device conductivity depends on the density of bound analytes. Figure 4.24 illustrates the variation in the number of probe-target complexes for cTn concentration between 5 pg/mL and 50 pg/mL. The results indicate that from 5 pg/mL to 15 pg/mL

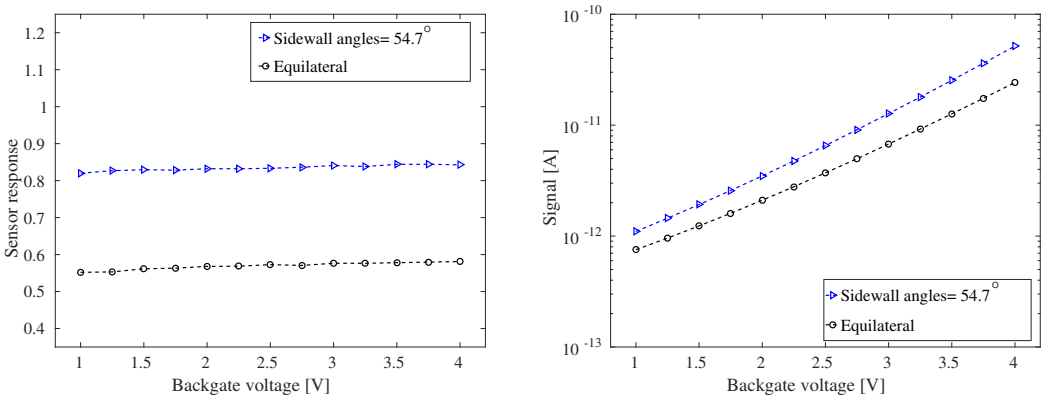


FIGURE 4.25: Sensor response (left) and signal (right) of two triangular nanowires for different backgate voltages at 10 pg/mL troponin concentration. The sensors are 300 nm wide and the bulk oxide is 200 nm thick. Each sensor has one 1000 nm long nanowire, a cross-sectional area of 2500 nm^2, a doping concentration of 10^{17} cm^{-3}, and they are protected by a 5 nm thick silicon oxide layer.

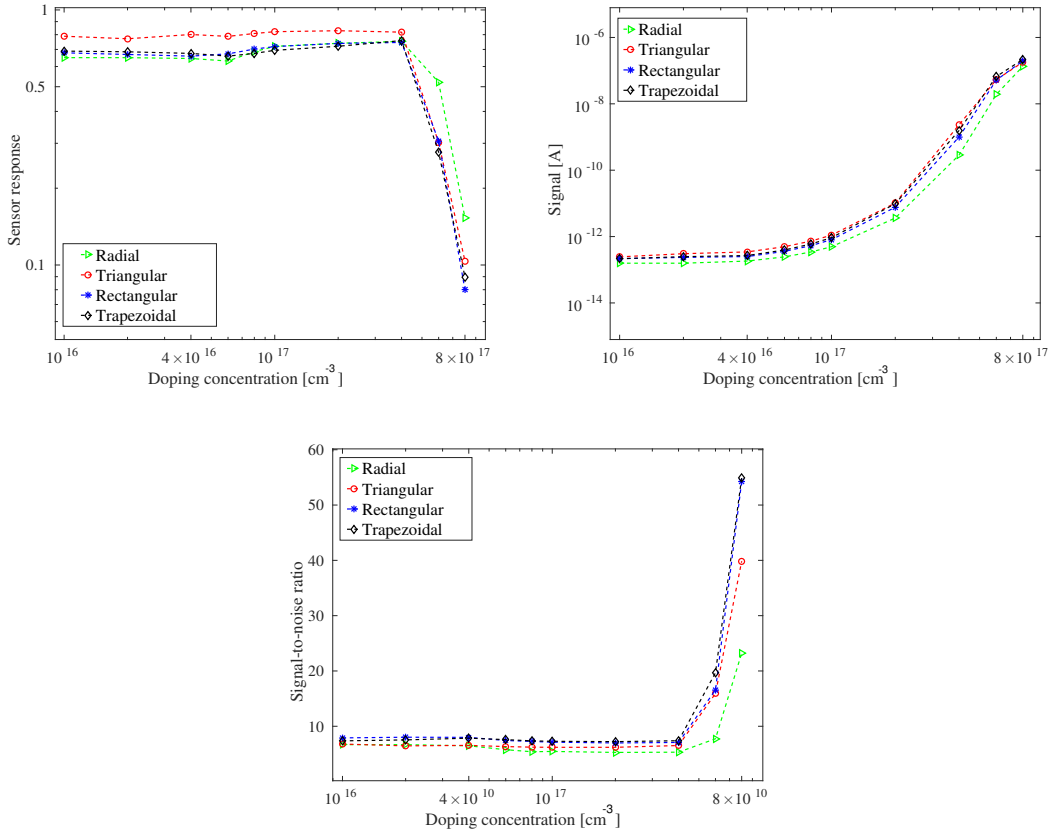


FIGURE 4.26: Sensor response (top left), signal (top right), and SNR (bottom) as a function of doping concentration for different nanowire cross sections. The sensors are 300 nm wide and the bulk oxide is 200 nm thick. Each sensor has one 1000 nm long nanowire, a cross-sectional area of 2500 nm^2 and they are protected by a 5 nm thick silicon oxide layer.

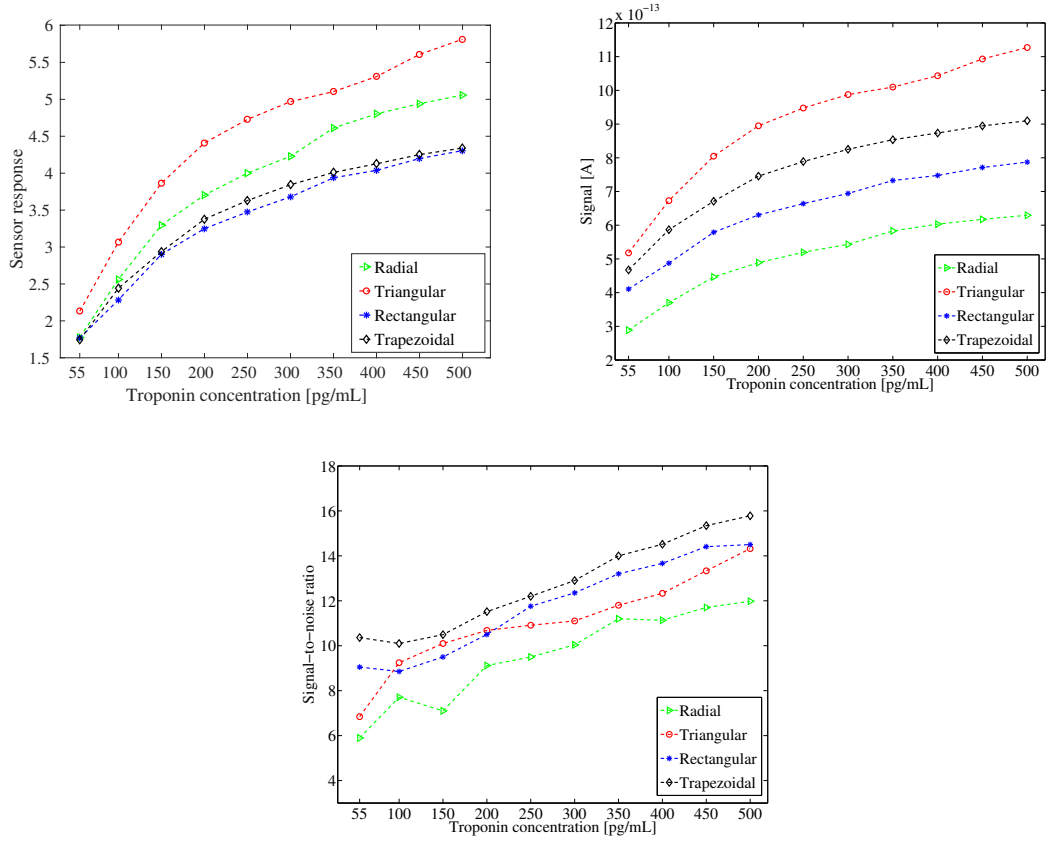


FIGURE 4.27: Sensor response (top left), signal (top right), and SNR (bottom) as a function of troponin concentration varying from 5 pg/ml and 50 pg/ml for different nanowire cross sections. The sensors are 1000 nm wide and the bulk oxide is 300 nm thick. Each sensor has two parallel 5000 nm long nanowires, a cross-sectional area of 2500 nm^2, a doping concentration of 10^{17} cm^{-3}, and they are protected by a 5 nm thick silicon oxide layer.

the variance increases sharper than the expected value. As a consequence, as shown in Figure 4.24, for this range the SNR is sloped downward since the current variance is sloped upward. For higher concentrations, more **PT**-complexes increase the signal, which counteracts the increase in noise. Therefore, in all sensors, the SNR shows a gradual upward trend. Furthermore, in spite of the fact that the triangular nanowire yields a higher signal, the higher noise in this device compared to the rectangular and trapezoidal devices decreases the ratio. Again, due to a lower signal, the SNR for the radial nanowire is significantly lower than the rest of the devices. For more than 40 pg/mL, the **PT**-complex increase is pronounced compared to the variance. Therefore, as an inflection point, again the SNR shows an upward trend for the higher concentrations. Finally, we should note that the variation in the density of bound analytes leads to threshold voltage fluctuations since the threshold voltage variation depends only on the number of absorbed molecules.

A higher sensor response of SiNW-FETs depends considerably on the size of the device [54]. In [129, 166], SiNW-FETs were fabricated by using commercially available (100) silicon-on-insulator wafers and anisotropic tetramethylammonium hydroxide (TMAH).

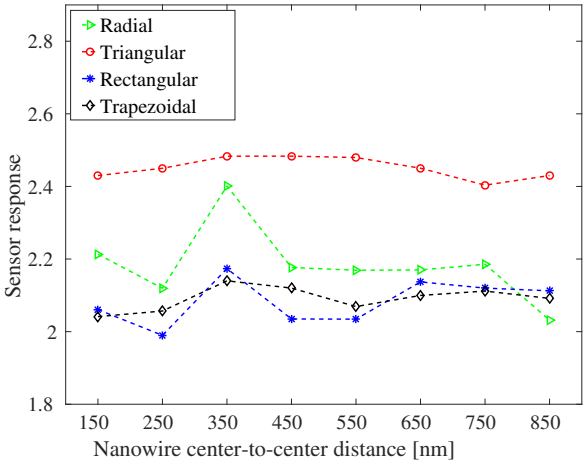


FIGURE 4.28: The sensor response of different devices as a function of the nanowire center-to-center distance at 75 pg/ml cTn concentration. The sensors are 1000 nm ($d = d_1 = 333$ nm) wide and the bulk oxide is 300 nm thick. Each sensor has two parallel 5000 nm long nanowires, a cross-sectional area of 2500 nm^2, a doping concentration of 10^{17} cm^{-3}, and they are protected by a 5 nm thick silicon oxide layer.

Thus, a smooth triangular SiNW-FET is produced with a sidewall angle of $\approx 54.7°$ to the horizontal surface (see Figure 4.22) and (111) silicon sidewall plane. Again, the cross-section of the device indicating the nanowire side angles and the area exposed to the liquid are shown in Figure 4.22. In Figure 4.25, the sensor response for the mentioned triangular device and for an equilateral cross section are given. The figure shows the sensitivity and the signal for both triangular cross sections as functions of different backgate voltages. The device performance, i.e., signal and the sensitivity of the (111) planes compared to the equilateral transducer is noticeably better. Also, due to higher obtained signal, the SNR is expected to be higher in the (111) sensor. Concerning the voltage, the figure shows that the sensitivity is not considerably affected by the gate voltage, although a slight increase is observed. On the other hand, the signal in both devices rise noticeably as the backgate voltage increases.

The optimal doping concentration is a crucial design parameter. Figure 4.26 shows the effect of the doping concentration varying between 1×10^{16} cm^{-3} and 8×10^{17} cm^{-3}. According to the simulation results, although the sensor response shows a small fluctuation from 1×10^{16} cm^{-3} to 4×10^{17} cm^{-3}, the change in the sensitivity is negligible. This fact indicates that this interval is a suitable range for the sensor. For higher doping concentrations, the sensitivity decreases considerably for all devices, since the nanowires are mostly affected by the doping and the effect of charged molecules on the signal decreases. As is seen, the doping concentration affects noticeably the sensitivity only at high doping levels (decreasing it). Thus, lower concentrations (i.e., less than 4×10^{17} cm^{-3}) are more suitable for achieving a higher sensor response. This fact is shown by the signal curve, where the increment is approximately five orders of magnitude. Regarding the noise, it decreases when the doping concentration increases as already indicated since the nanowires are not affected as much by the fluctuation of the molecules. This effect causes a dramatic increase in SNR.

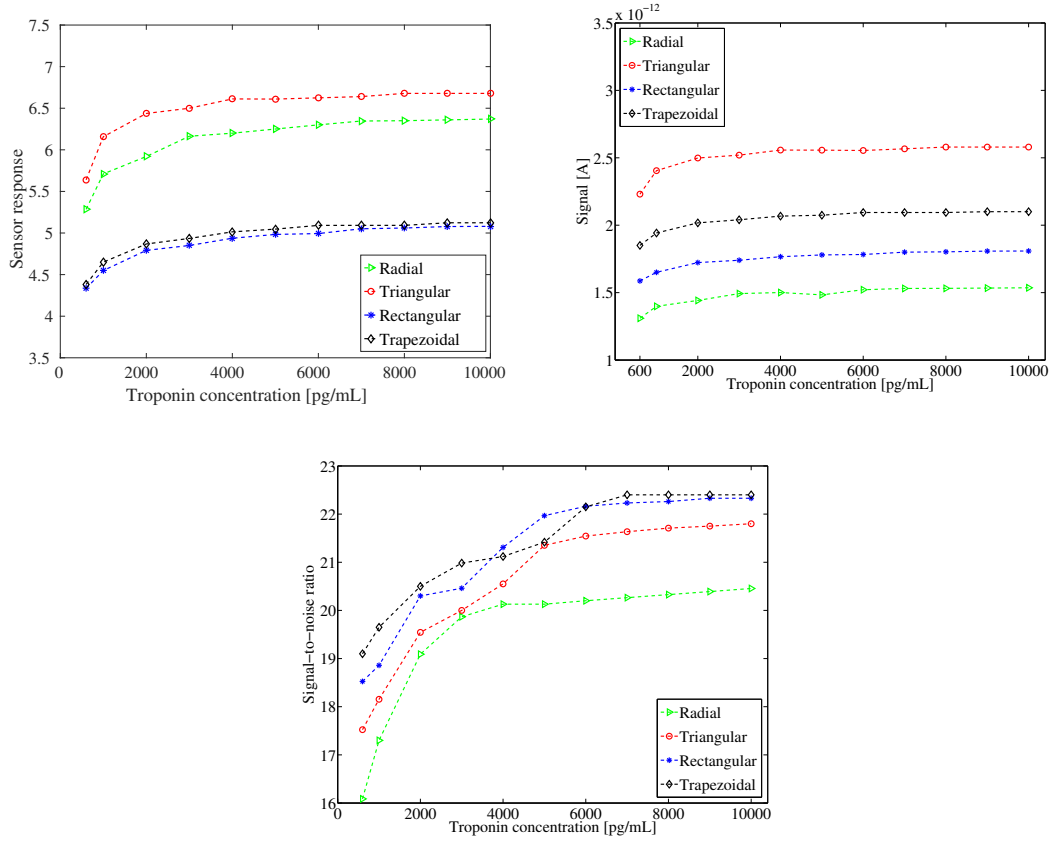


FIGURE 4.29: Sensitivity (top left), signal (top right), and SNR (bottom) as a function of troponin concentration varying from 500 pg/mL and 10 ng/mL for different nanowires cross sections. The sensor is 1000 nm wide and the bulk oxide is 300 nm thick. Each sensor has four parallel 5000 nm long nanowires, a cross-sectional area of 2500 nm^2, a doping concentration of 10^{17} cm^{-3}, and they are protected by a 5 nm thick silicon oxide layer.

Although absolute cTn elevations are seen in multiple chronic cardiac and noncardiac conditions, a rise in serial cTn levels strongly support an acutely evolving cardiac injury such as most commonly, acute myocardial infarction. As aforementioned, larger sensors are used for higher concentrations. As Figure 4.27 shows, the triangular nanowire is again the most sensitive device and the rectangular and trapezoidal show the same performance. Also, higher concentration increases the sensitivity of the device. The same holds for the signal, which doubles from 50 pg/ml to 500 pg/ml. The SNR increases with higher concentrations, while the devices show small fluctuations. The peak SNR is reached at 500 pg/ml.

This simulation capability makes it possible to study the arrangement of the nanowires. More precisely, the distance between the nanowires is an important parameter for increasing the sensitivity. Figure 4.19 depicts the arrangement of the nanowires indicating the center-to-center distance d between the nanowires and the distance d_1 between a nanowire and the boundary. Figure 4.28 shows the sensitivity of sensors with two nanowires whose distance d varies between 150 nm and 850 nm. The sensor width $d+2d_1$ is 1000 nm. For larger distances, i.e., $d > 750$ nm, the effect of charged molecules on the

transducers decreases since the nanowires are closer to the boundaries. For distances less than 250 nm, the competition between the transducers to bind the target molecules gives rise to a decrease in the sensitivity. The simulations show that the maximum sensitivity for all transducer shapes is obtained for a center-to-center distance of 350 nm (symmetric arrangement).

In high-risk myocardial infarction patients, the cTn concentration reaches its peak approximately after six hours. In this time interval, the concentration rises sharply. For the concentration range from 500 pg/mL to 10 ng/mL, we use a sensor with four parallel nanowires. The results are shown in Figure 4.29. Similar to the previous ranges, the triangular nanowire performs more efficiently. Due to the noticeably higher number of target molecules, the sensitivity is considerably higher than in the first range. Most of the receptors are bound to target molecules. This fact is more pronounced in the SNR since the simultaneously high **PT**-concentration (close to C_P) and small variance decrease the noise significantly.

4.3 Current variation in FinFETs

The scaling of conventional planar MOSFETs has been facing problems such as subthreshold swing degradation, significant drain-induced barrier lowering (DIBL), fluctuation of device characteristics, and current leakage [8, 25, 35]. To solve the problems, 3-D device structures have been studied. Fin field-effect transistors (FinFETs) among 3-D devices are very promising candidate for future nano-scale CMOS technology and high-density memory application [31, 36, 56]. In these devices, the current variation due to statistical fluctuations in the number and position of dopant atoms becomes a serious problem when they are scaled to sub 0.1 micron dimensions. In fact, the randomness of the dopant position and number in the device makes the fluctuation of device characteristics difficult to model and mitigate [100].

The basic structure of FinFET is a channel controlled by more than one side of the channel. Modern FinFETs are 3D structures as shown in Figure 1.4 and also called tri-gate transistor. FinFETs can be implemented either on bulk silicon or SOI wafer. This FinFET structure consists of a thin (vertical) fin of silicon body on a substrate. The gate is wrapped around the channel providing excellent control from three sides of the channel. This structure is called the FinFET because its silicon body resembles the back fin of a fish.

The numerical example discussed here is a realistic one: the dopant atoms in nanoscale transistors are distributed randomly resulting in unavoidable device variations between the many transistors in an integrated circuit. These random-dopant effects are of great importance in nanoscale devices. We apply the stochastic method to a realistic numerical example, i.e., random position/number of dopants in source/drain regions of FinFETs and demonstrate its usefulness by comparing its computational effort to other methods.

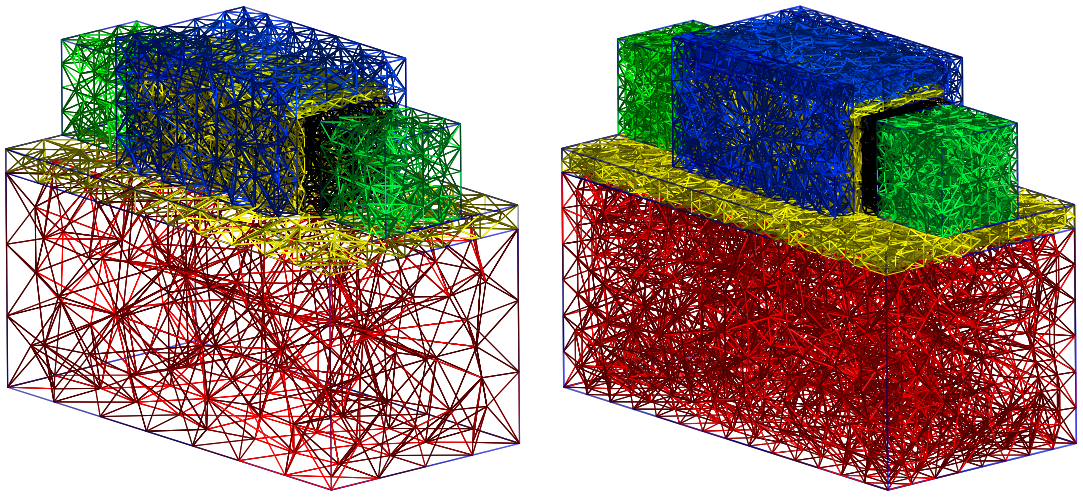


FIGURE 4.30: The three-dimensional meshes for the SOI FinFET in Figure 1.4 for levels $\ell = 0$ (left) and $\ell = 1$ (right). The subdomains are indicated by red for the substrate, by yellow for the insulator, by black for the channel, by green for the source and drain regions, and blue gate.

4.3.1 Three-dimensional simulation of SOI-FinFETs

In our simulations, as the first step, we use the optimal multilevel Monte Carlo to quantify current variation in a Silicon on insulator (SOI)-FinFET (Figure 1.4). As the next step, the developed randomized quasi-Monte Carlo will be implemented to model the current fluctuations.

We consider a three-gate FinFET structure with a 20 nm thick and 20 nm high silicon fin. In the simulations, we use $V_{SD} = 0.1\,\mathrm{V}$ and $U_T = 26\,\mathrm{mV}$. The channel length is 50 nm with a doping concentration of $10^{16}\,\mathrm{cm}^{-3}$. We assume that the acceptors and donors are distributed identically and independently in source and drain regions. The number of donors and acceptors is constant. In the continuum version of the model, a doping concentration of $10^{19}\,\mathrm{cm}^{-3}$ is used for these regions.

The silicon-on-insulator (SOI) FinFET considered here and its subdomains are shown in Figure 1.4. Corresponding three-dimensional meshes for two different levels are shown in Figure 4.30. The channel is surrounded by a 1 nm thick layer of silicon dioxide.

Here we simulate the subthreshold current. In the subthreshold regime, the gate voltage is below the threshold voltage so that no inversion channel is formed. In this regime, the diffusion component of the current is more pronounced than the drift component. The number N_{dop} of dopants and the doping concentration C_{dop} are related by $N_{\mathrm{dop}} = V \cdot C_{\mathrm{dop}}$ of course, where V is the volume of the subdomain. The occupation probability follows a Poisson distribution with the parameter $\lambda = \sqrt{N_{\mathrm{dop}}}$.

In the continuum model, both the doping in the source and drain regions and the doping in the channel are uniform. In the discrete model, the random locations of the dopants in the source and drain regions as well as randomness in the number of dopants result

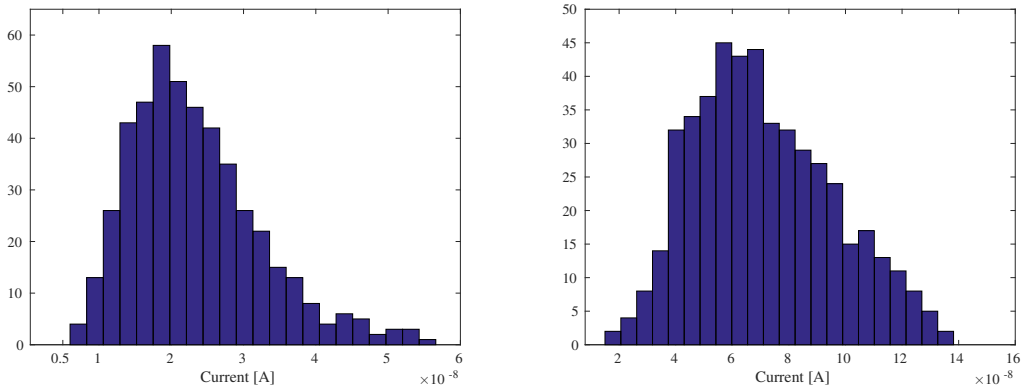


FIGURE 4.31: Histogram of the current in the discrete model with 482 simulations for $V_g = 0.1\,\mathrm{V}$ (left) and $V_g = 0.2\,\mathrm{V}$ (right). The number of dopants is $N_{\mathrm{dop}} = 80$.

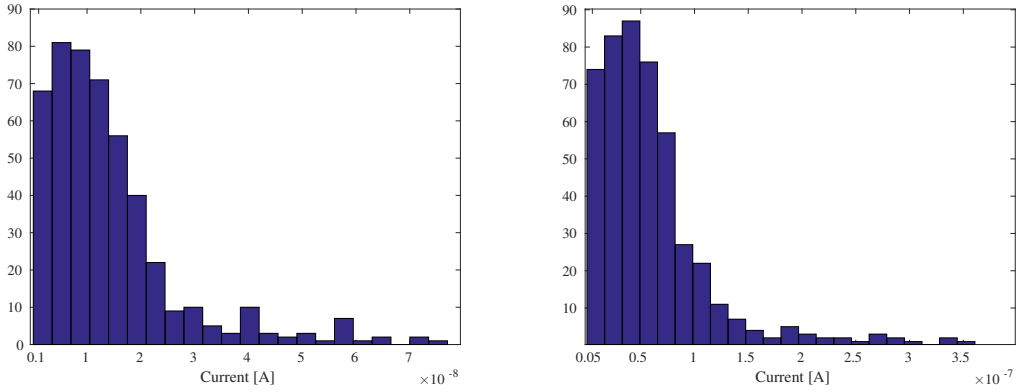


FIGURE 4.32: Histogram of the current in the discrete model with 482 simulations for $V_g = 0.1\,\mathrm{V}$ (left) and $V_g = 0.2\,\mathrm{V}$ (right). The number of dopants is $N_{\mathrm{dop}} = 20$.

in device variations. For $V_g = 0.1\,\mathrm{V}$ and $V_g = 0.2\,\mathrm{V}$, these variations are shown in Figure 4.31 and Figure 4.32, respectively, for $N_{\mathrm{dop}} = 20$ and $N_{\mathrm{dop}} = 80$ (number of dopants the in source and drain regions). The results indicate that in the discrete model, the higher number of dopants decreases current fluctuation. As an example, for the lower gate voltage, the simulation for $N_{\mathrm{dop}} = 80$ yields $\sigma(I) = 8.99 \times 10^{-9}\,\mathrm{A}$, while the simulation for $N_{\mathrm{dop}} = 20$ yields $\sigma(I) = 1.27 \times 10^{-8}\,\mathrm{A}$.

Figure 4.33 depicts the subthreshold current obtained by both models for different gate voltages varying from $V_g = -0.1\,\mathrm{V}$ to $V_g = 0.4\,\mathrm{V}$ for three different numbers of dopants (in the source/drain regions), namely $N_{\mathrm{dop}} = 20$, $N_{\mathrm{dop}} = 40$, and $N_{\mathrm{dop}} = 80$. The results show that for different gate voltages, the difference between the higher number of dopants and the continuum model is not significant. However, a noticeable discrepancy is obtained with $N_{\mathrm{dop}} = 20$.

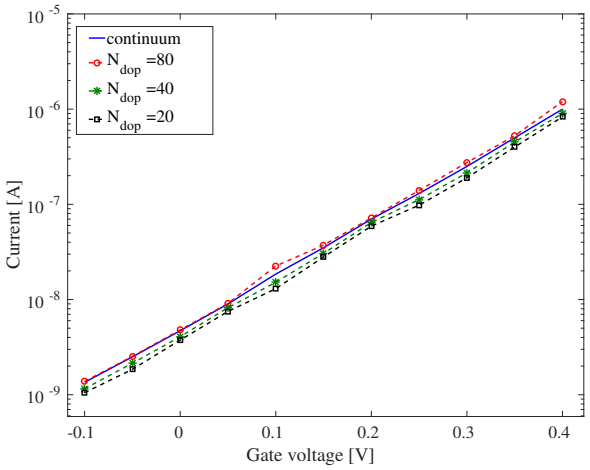


FIGURE 4.33: The expected value of the current as a function of different gate voltages calculated using the continuum and discrete models.

4.3.2 MLRQMC-FEM for FinFETs current variations

In this section, we implement the developed optimal MLRQMC finite element method (3.5.1) to model the current variations in FinFETs. We calculate the computational cost of the MLRQMC approach applied to drift-diffusion-Poisson system of equations. In optimal point of view, the function modeling the computational work is minimized such that the estimated total error of the procedure is less than or equal to a prescribed error tolerance. By solving this optimization problem, optimal values for parameters such as the mesh sizes in the spatial discretization and the optimal number of quasi-points are obtained in a natural manner.

The FinFET device is shown in Figure 4.34 and the 3D corresponding meshes for two different levels are illustrated in Figure 4.35. This FinFET structure consists of a thin (vertical) silicon fin on a substrate. In the device, the gate length is 60 nm, and it is separated from the silicon channel by a 1.2 nm thick oxide layer. This channel is connected to the n-type doped source and drain regions of lengths $L_{\mathrm{SD}} = 15$ nm. Regarding the boundary conditions in (2.23), Dirichlet boundary conditions are employed at the gate, source, and drain contacts. Zero Neumann boundary condition are applied everywhere else. The main source of randomness inside the device is the random motion of dopant atoms through the semiconductor during the fabrication steps of implantation and annealing resulting in their random locations.

The electron and hole mobilities have a similar dependence on doping. For low doping concentrations, the mobility is almost constant and is primarily limited by phonon scattering. At higher doping concentrations the mobility decreases due to ionized impurity scattering with the ionized doping atoms. The actual mobility also depends on the type

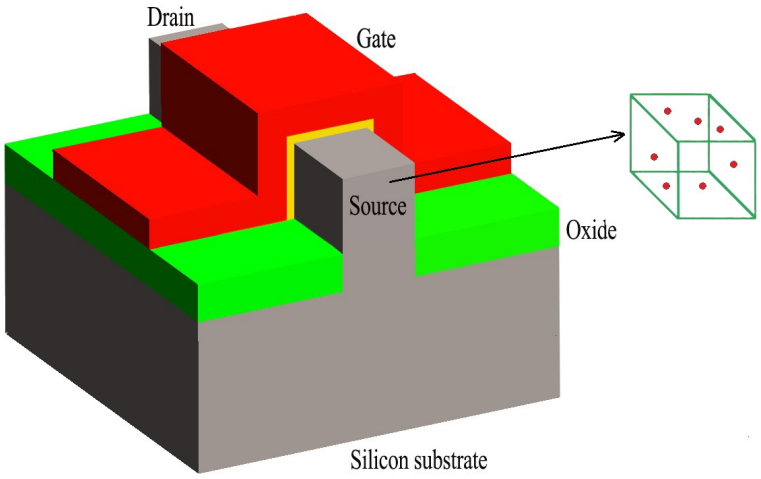


FIGURE 4.34: Schematic structure of a three-dimensional FinFET. The random dopants are distributed in the source and drain regions.

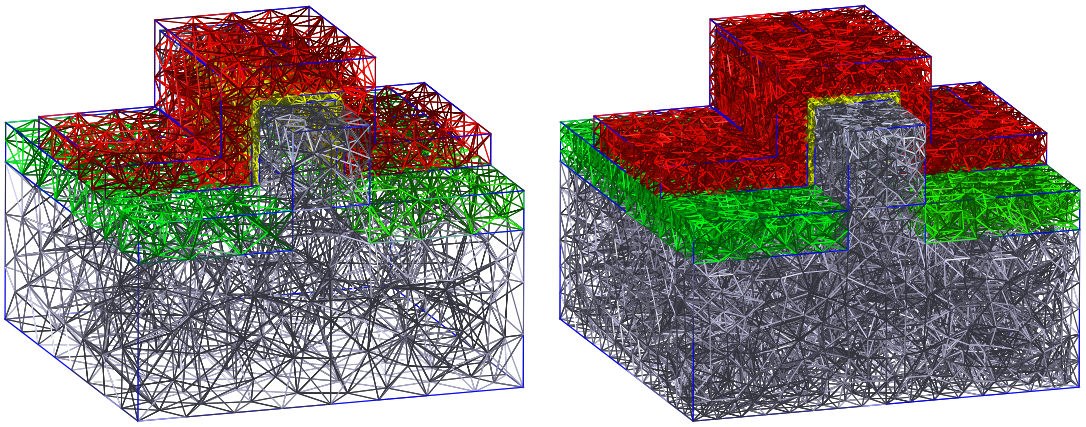


FIGURE 4.35: The 3D meshes corresponding to the FinFET for $\ell = 0$ (left) and $\ell = 1$ (right).

of dopant. Here we use the expressions

$$\mu_p := 54.3T_1^{-0.57} + \frac{1.36 \cdot 10^8 T^{-2.33}}{1 + \left(\frac{C_{\text{dop}}}{2.35 \cdot 10^{17} T_1^{2.546}}\right) 0.88 T_1^{-0.146}}, \tag{4.5}$$

$$\mu_n := 88T_1^{-0.57} + \frac{7.4 \cdot 10^8 T^{-2.33}}{1 + \left(\frac{C_{\text{dop}}}{1.26 \cdot 10^{17} T_1^{2.4}}\right) 0.88 T_1^{-0.146}}, \tag{4.6}$$

where $T_1 = T/300$ and T is the temperature to model the electron and hole mobility in silicon as a function of temperature and net doping concentration [7].

As discussed in Section 3.3.2, the optimal parameters are found by solving the minimization problem that minimizes the computational work for a prescribed total error. This procedure yields the mesh sizes and numbers of samples in the multilevel approach. Before the minimization problem can be solved, the constants and the exponents in (3.58)

Coefficient	μ_1	γ_1	μ_2	γ_2	μ_3	γ_3	μ_4	γ_4
Value	0.51	3.07	0.63	3.06	0.38	2.98	0.34	2.93

TABLE 4.5: The estimated coefficients and exponents in (3.27).

must be measured.

As we already mentioned, the statistical error depends on the mesh size (h) and number of samples (N). Figure 4.36 (left) depicts the error for different mesh sizes ($h_0 = 5$, $r = 2$ and $N = 100$) with decay of variance of order $\beta = 1.652$. We assumed that applying shifted rank-1 lattice rules gives rise to the rate of convergence $\mathcal{O}(N^{-2+\delta})$, for any $\delta > 0$. However, the estimation of δ is crucial to solve the optimization problem. As seen in the figure, the variance of MLRQMC-FEM decays with $\mathcal{O}(N^{-1.88})$ (i.e., $\delta = 0.12$), while for MC-FEM the rate of $\mathcal{O}(N^{-1})$ is achieved. These values are obtained using $h = 5$ with respect of differenet number of quasi points. Additionally, Figure 4.37 illustrates the discretization error for different mesh sizes. where the parameters were estimated using 100 samples by comparing the variance of the multilevel estimator (3.53) for different mesh sizes. The numerically determined exponent $\alpha = 1.731$ agrees very well with the order of the P_1 FE discretization used here. The coefficients in the model for the computational work were also found numerically. For matrix assembly and solving the system, we recorded the CPU time used as a function of different mesh sizes, and hence the values of μ_k and γ_k are found. A summary of the coefficients and exponents is given in Table 4.5.

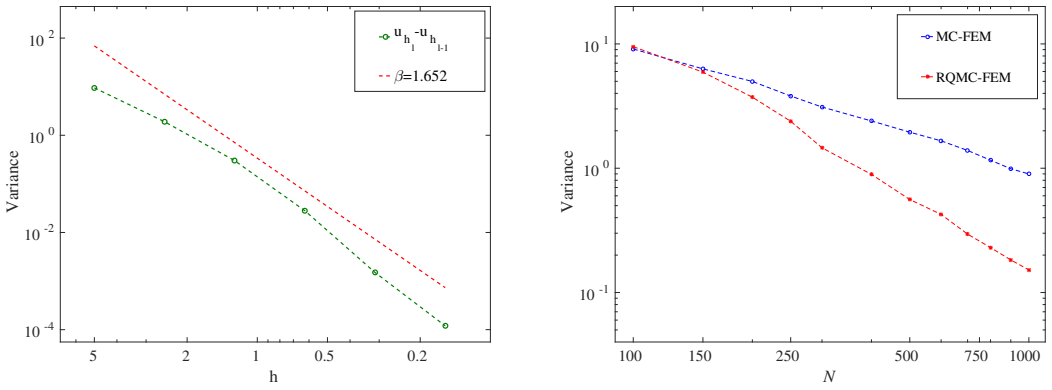


FIGURE 4.36: The decay of variance of the solution as a function of different mesh sizes (left) and number of samples (right). The values $C_{00} = 9.45$, $C_0 = 0.338$, and $\delta = 0.06$ are found additionally.

Since (3.58) is a continuous optimization problem, the solutions N_ℓ are generally no integers. We therefore round the values N_ℓ up to the next integer. Regarding the number of shift realizations, the value $M_\ell = 10$ is used in all the QMC estimators. Summaries of the optimal parameter values (h, N), (h_0, r, N_ℓ) and (h_0, r, M_ℓ) for the QMC-FE and MLRQMC-FE and MLMC-FE methods are given in Table 4.6, Table 4.7 and Table 4.8 respectively.

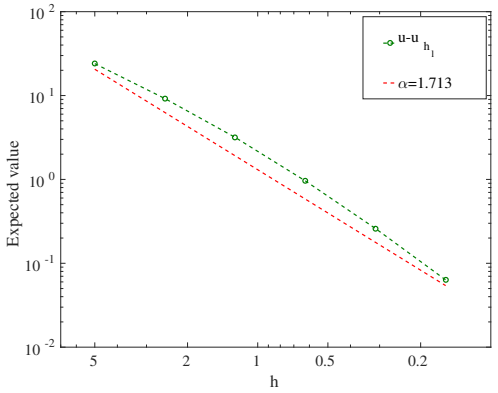


FIGURE 4.37: The expected value of the solution as a function of different mesh sizes with $C_1 = 1.304$.

ε	0.100	0.050	0.030	0.020	0.010	0.005	0.003	0.001
h	0.427	0.208	0.154	0.122	0.081	0.054	0.071	0.041
N	65	135	231	356	744	1 554	3 844	9 913

TABLE 4.6: Optimal mesh size h and number N of samples for the QMC-FE method for different prescribed total errors ε.

ε	h_0	r	N_0	N_1	N_2	N_3	N_4	N_5	N_6
0.100	2.192	2.270	209	31	6	2	–	–	–
0.050	2.651	2.144	633	124	24	5	2	–	–
0.030	2.174	2.204	1 015	154	28	5	2	–	–
0.020	2.943	2.094	2 363	534	106	21	5	2	–
0.010	2.213	2.149	4 395	697	131	25	5	2	–
0.005	2.899	2.115	14 139	3 107	603	117	25	5	2

TABLE 4.7: Optimal hierarchies in the MLRQMC-FE method for different prescribed total errors ε.

ε	h_0	r	M_0	M_1	M_2	M_3	M_4	M_5	M_6
0.100	1.303	2.151	3 920	363	33	3	–	–	–
0.050	1.370	2.020	18 046	1 993	215	24	3	–	–
0.030	1.430	1.908	56 136	7 344	957	125	17	3	–
0.020	1.390	1.987	126 266	14 749	1 688	193	23	3	–
0.010	1.459	1.9829	545 840	73 009	9 182	1 154	165	21	3

TABLE 4.8: Optimal hierarchies in the MLMC-FE method for different prescribed total errors ε.

We compare a previously developed optimal MLMC-FE method [145] with the optimal MLRQMC-FE method developed in Section 3.3.2. Figure 4.38 shows the computational work for the optimal quasi-Monte-Carlo method and the multilevel methods. It shows that $\mathcal{O}(\varepsilon^{-2.75})$ is roughly constant for the standard QMC method. In the MLMC-FE method, the assumptions of the standard complexity theorem [33] are satisfied, i.e., $\alpha \geq \frac{1}{2}\min(\beta, \gamma)$, so that the computational cost is $\mathcal{O}(\varepsilon^{-2.2})$. The faster convergence rate of the RQMC points results in less computational work for a given total error. In the MLRQMC-FE method, the RQMC aspect yields a computational complexity of

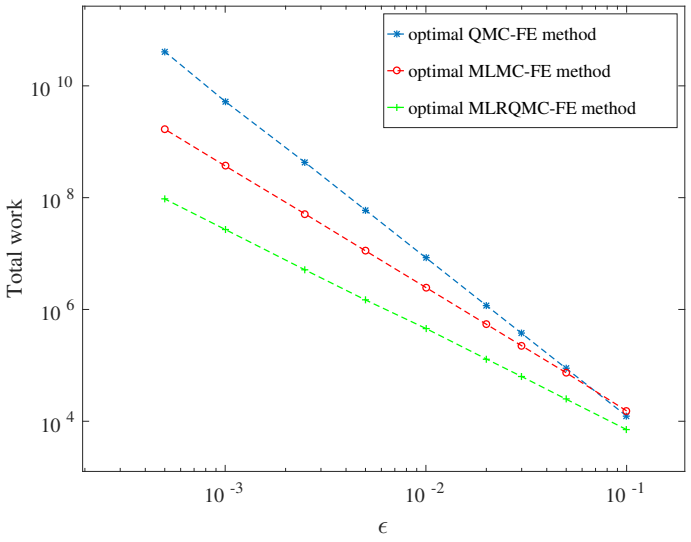


FIGURE 4.38: Comparison of the total computational work required for the optimal MLRQMC and MLMC methods. For smaller total errors, the effectiveness of the randomized method is more pronounced.

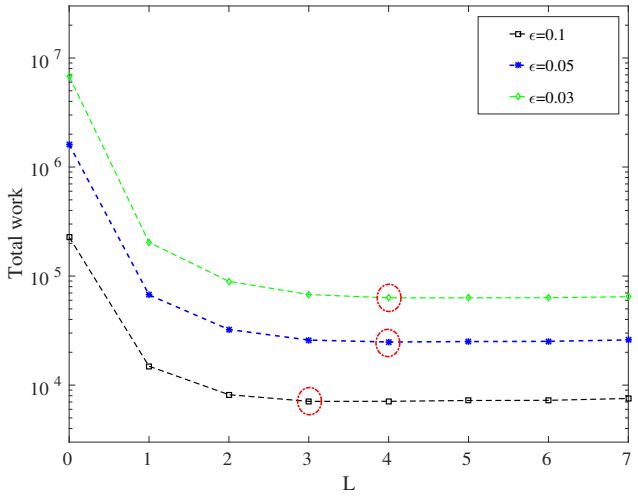


FIGURE 4.39: The comparison of the total work of MLRQMC for different levels (between $L = 0$ and $L = 7$) for three different total errors $\varepsilon = 0.1$, $\varepsilon = 0.05$, and $\varepsilon = 0.03$. For each prescribed total error, the optimal number of levels is indicated by a red circle.

$\mathcal{O}(\varepsilon^{-1.82})$, which results in additional savings of a factor between 2 and 17 (relative to MLMC) and 2 and 500 (relative to QMC) Therefore, the efficiency increase of the multilevel RQMC method is more pronounced for smaller prescribed total errors [88].

Additionally, choosing the optimal number L of levels is another important consideration. Figure 4.39 depicts the optimal number of levels for three different prescribed total errors. Using only one level ($L := 0$) results in the standard Monte-Carlo method. Distributing the samples among several levels $\ell \in \{0, \ldots, L\}$ results in significant savings

in computational cost. For smaller error bounds, a larger number of levels is necessary to obtain the minimum of computational cost.

Now, we focus on the simulation of the device using the above obtained computational results. We use the subthreshold current, where the diffusion component of the current is larger than the drift component. First of all, we study the effect of randomness in the position of the dopants, whose number is constant. Figure 4.40 shows the comparison between the expected value of the current calculated using the discrete model (obtained for $\epsilon = 0.05$) and the continuum model for different gate voltages varying between $V_g = -0.1\,\mathrm{V}$ and $V_g = 0.3\,\mathrm{V}$. The fluctuation of the current in the discrete model for $V_g = 0.1\,\mathrm{V}$ and $V_g = 0.2\,\mathrm{V}$ is also shown in Figure 4.41. The results show approximately 10% of difference between the models.

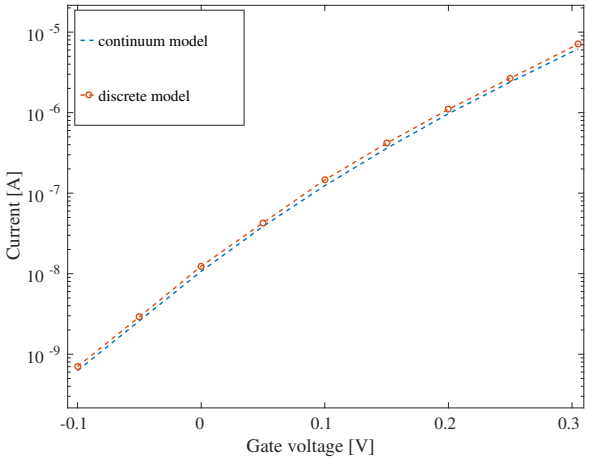


FIGURE 4.40: The expected value of current as a function of different gate voltages calculated using continuum and discrete models with $V_{SD} = 0.1\,\mathrm{V}$.

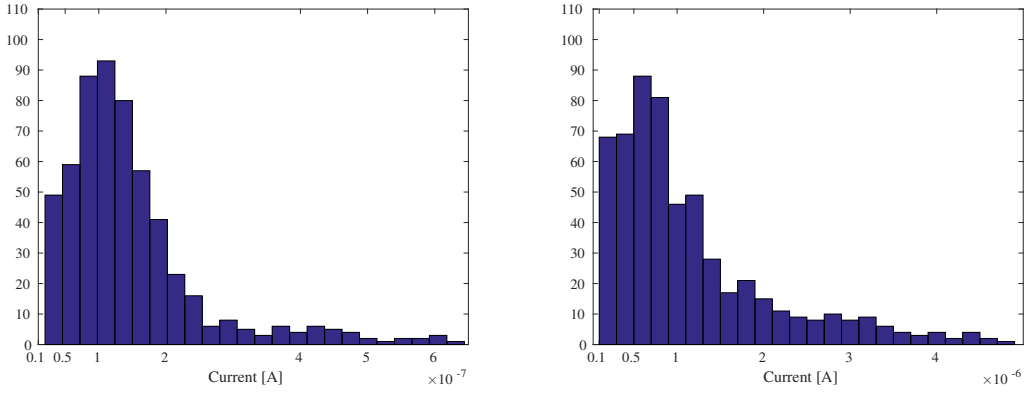


FIGURE 4.41: Histogram of the current for $V_g = 0.1\,\mathrm{V}$ (left) and $V_g = 0.2\,\mathrm{V}$ (right) and 563 simulations. Here $\mathbb{E}(I) = 1.49 \cdot 10^{-7}\,\mathrm{A}$ for the lower gate voltage and $\mathbb{E}(I) = 1.14 \cdot 10^{-6}\,\mathrm{A}$ for the higher gate voltage.

Next, we compare the expected value of the current for different numbers N_{dop} of dopants with the continuum model. Figure 4.42 shows the expected value of the current for different numbers of dopants, varying from 5 to 50, for various gate voltages. The total

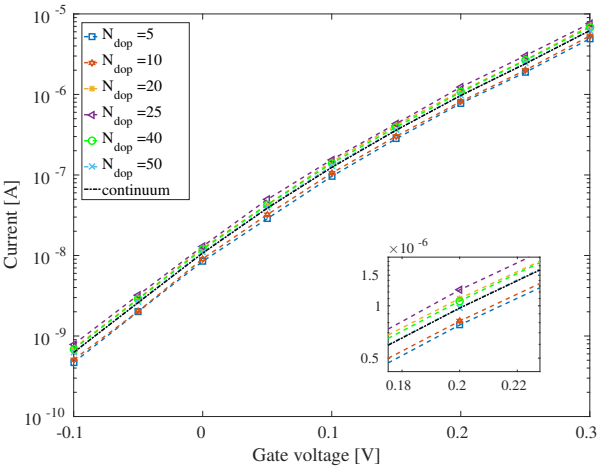


FIGURE 4.42: The I-V characteristics for different numbers of dopants. The results for the continuum model are shown as well.

charge of the dopants is kept constant to allow the comparison. According to the figure, the presence of more than 10 atoms in the regions results in a higher current compared to the deterministic model at same gate voltage.

An interesting result of the simulations is that considering the discrete nature of the dopants in the devices results in a decrease of the threshold voltage. It is also seen that the fluctuation due to the number of dopants is more significant than the effect of random positions. The variations decrease gradually when there are more dopants in the region, which is consistent with convergence to the continuum model as the number of dopants tends to infinity.

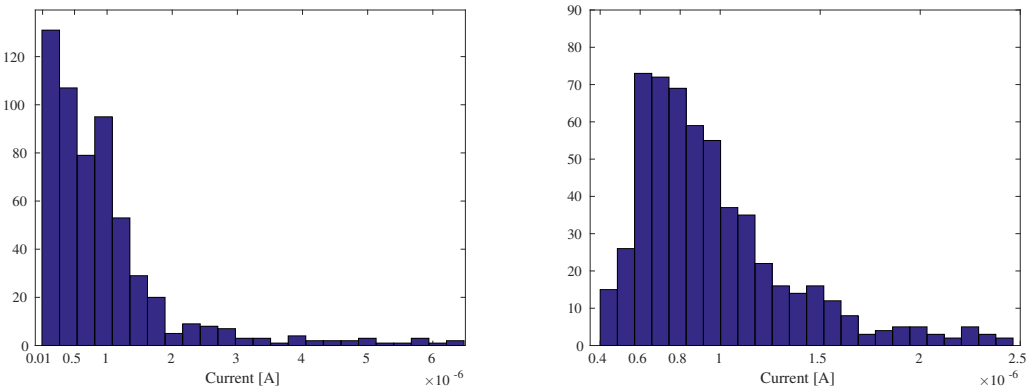


FIGURE 4.43: Histogram of the current for $V_g = 0.2\,\mathrm{V}$ and for 563 simulations. Left: $N_{\mathrm{dop}} = 5$ resulting in $\mathbb{E}(I) = 9.22 \cdot 10^{-7}\,\mathrm{A}$. Right: $N_{\mathrm{dop}} = 50$, resulting in $\mathbb{E}(I) = 9.66 \cdot 10^{-7}\,\mathrm{A}$. The current obtained by the continuum model is $I = 9.66 \cdot 10^{-7}\,\mathrm{A}$.

4.4 Confined structure applied to the ion channels

Ion channels are of essential physiological importance, since they manage the concentration gradients of ions across cell membranes [75, 85]. They are located in cells membranes and manage the concentration gradients of ions across the membranes. Hence, they are the fundamental regulators, amplifiers, and transducers of the nervous system. Ion channels are small enough that interactions between the ions and the channel protein are important for their operation, while they are large enough that it is impossible to calculate all such interactions at the atomistic level on realistic time scales where ionic conductance occurs. Ion channels conduct electrical signals inside neurons, muscles, and touch receptor cells, and they generate the electrical impulses underlying information transfer in the nervous system.
All organisms have ion channels for Na^+, K^+ and Cl^-. These are significant in osmoregulation and the transmission of signals via the transmembrane potential between the inside (potassium) and the outside (sodium and chlorine) of the cell. Because of their important role in physiology, we simulate currents through three different ion channels. The channels considered are the phosphate selective OprP channel, the Gramicidin A channel, and the Streptomyces lividans KcsA channel. In each case, the calculated currents are compared with measurements. We also discuss virtual KcsA channels in order to elucidate if and how the structure of the natural channels is optimal with respect to its selectivity [85].

4.4.1 Determination of the confinement potential

The confinement potential enters the transport model via equations 2.35 and 2.37. For each channel type and each ionic species, the potential of mean force (PMF) and the channel width completely determine the confinement potential, i.e., the PMF and the channel width determine the functions V_0, b and B in the confinement potential V in 2.35. In other words, the microscopic structure of the channel as it is experienced by each ionic species is fully described by the PMF and the channel width.

Harmonic confinement potentials can always be constructed by calculating the best approximation from given forces according to [74, Section 5.1]. Here the channels are considered to be straight for simplicity so that $b_1(x) = b_2(x) = 0$ holds for all x. The minimum energy, i.e., the minimum of each parabola, at each x along the channel is then given by $V(x, (0,0)^\top) = V_0(x)$. These energies are taken from the literature for each structure considered here, e.g., they are potentials of mean force (PMF) [45]. Applied potentials can be added to V_0.

Finally, the coefficient function B is determined from the known width of the structure. For simplicity, we assume that the channels have a rotational symmetry so that $B := B_1 = B_2$. The width r of the structure at x for the present purposes is the distance $r(x)$ in y-direction from the center of the cross section where the confinement force reaches a constant value F that may depend on channel type. In order to determine the coefficient B from the known width $r(x)$ i.e., the channel radius (distance from the

center), we first calculate the gradient as

$$\nabla_y V(x,y) = \nabla_y\big(V_0(x) + \frac{1}{2}B(x)(y_1^2+y_2^2)\big) = \begin{pmatrix} B(x)y_1 \\ B(x)y_2 \end{pmatrix}.$$

Therefore, the confinement force F at x is

$$|F| = |\nabla_y V(x,y)| = |B(x)|\sqrt{y_1^2+y_2^2} = B(x)r(x)$$

so that the sought coefficient is

$$B(x) = \frac{|F|}{r(x)}.$$

This procedure is used to determine the functions V_0, b, and B in 2.35 and 2.37 from the given structure in all of the following simulations. The channel width is known from structures in the Protein Data Bank and the energy landscape along the channel from data in the literature for the potential of mean force, where it has been calculated, e.g., from molecular-dynamics simulations.

4.4.2 Simulation of phosphate specific OprP channels

Pseudomonas aeruginosa is a versatile gram-negative outer membrane bacterium, which can live in various environments and leads to diseases in humans and animals such as pneumonia, osteomyelitis, and meningitis. OprP is a transmembrane beta-barrel protein of this bacterium and forms a highly selective phosphate channel (see Figure 4.44). The selectivity of the pore for molecular interactions and the permeability of OprP for small anions or antibiotics in the absence of phosphate were studied in [111, 113].

We simulate the passage of potassium and chlorine ions through the OprP channel. The potentials of mean force as well as the width of the channel were determined in [112]. The potentials of mean forces are shown in 4.45. Figure illustrates that the potential barriers have their extrema in the middle of the pore, between R226 and K121 for chlorine and R59 and D94 for potassium, whereas the barriers are smaller and the pore is wider near R220, K30, and K322. These areas are entrance funnels to OprP allowing chlorine and potassium ions to move easily [112].

In 4.46, the measured and simulated K^+ and Cl^- conductance (I/V) are shown as functions of the applied voltage for an ionic bath concentration of 0.1M. The simulations indicate that the conductance is fairly constant up to 100mV; however, the increases show exponential behavior for larger applied voltages meaning that the currents become voltage driven in this regime. Furthermore, the considerable difference between the conductivities shows that the current in OprP is mostly chlorine. The simulations show good agreement with the experimental data points in 4.46, although the potassium current is overestimated.

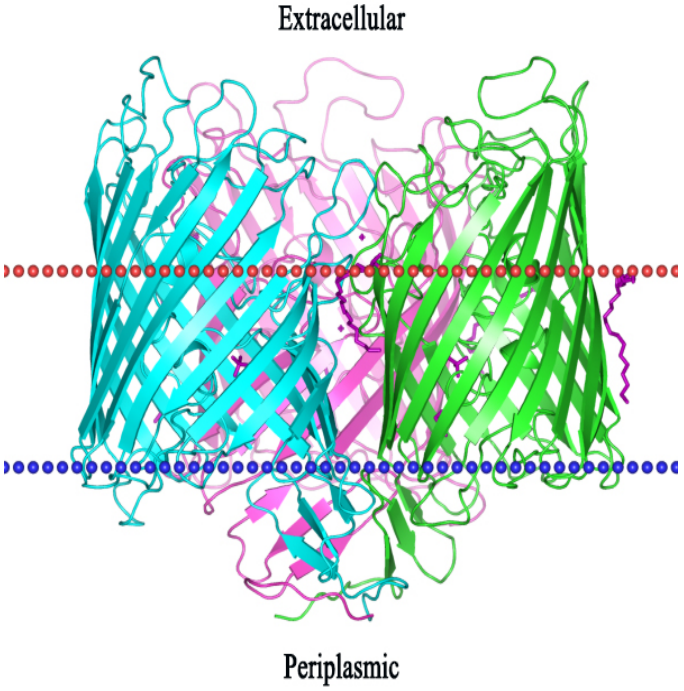


FIGURE 4.44: X-ray crystallography of Oprp phosphate channel. Periplasmic and extracellular are shown.

4.4.3 Simulation of Gramicidin A Channels

More measurements are available for Gramicidin A channels. Gramicidin channels are polypeptide antibiotics active against gram-positive bacteria such as, e.g., *Escherichia coli, Shigella,* and *Stenotrophomonas.* They are selective for monovalent cations [5]. Their effect is to increase the cation flow through the target bacterial membrane due to the formation of bilayer spanning channels. 4.47 shows the Gramicidin A channel from the side with its alternating L-D amino-acid sequence. The structure of the bilayer spanning channel is well known (Figure 4.49) and the ion permeability can be modulated by defined chemical modifications whose influence on the structure can be specified experimentally.

In order to validate the simulation approach, we compare the simulated sodium current as a function of applied voltage and bath concentration with measurements [4, 105]. 4.48 shows the results for various ionic concentrations from 10mM to 1000mM, and 4.50 shows the results for positive and negative applied voltages. In both figures, very good agreement between the simulated and measured Na^+ currents is observed.

The selectivity of Gramicidin channels with respect to different ion species is also an important property. In order to investigate this effect, we calculated the potassium current and compared the results with experimental data [4]. Very good agreement was found and is shown in Figure 4.51. The potential barrier inside the channel leads to higher selectivity for K^+ ions compared to Na^+ ions, and the current ratio varies between 2.5 and 3 depending on applied potential. The similar results are obtained for

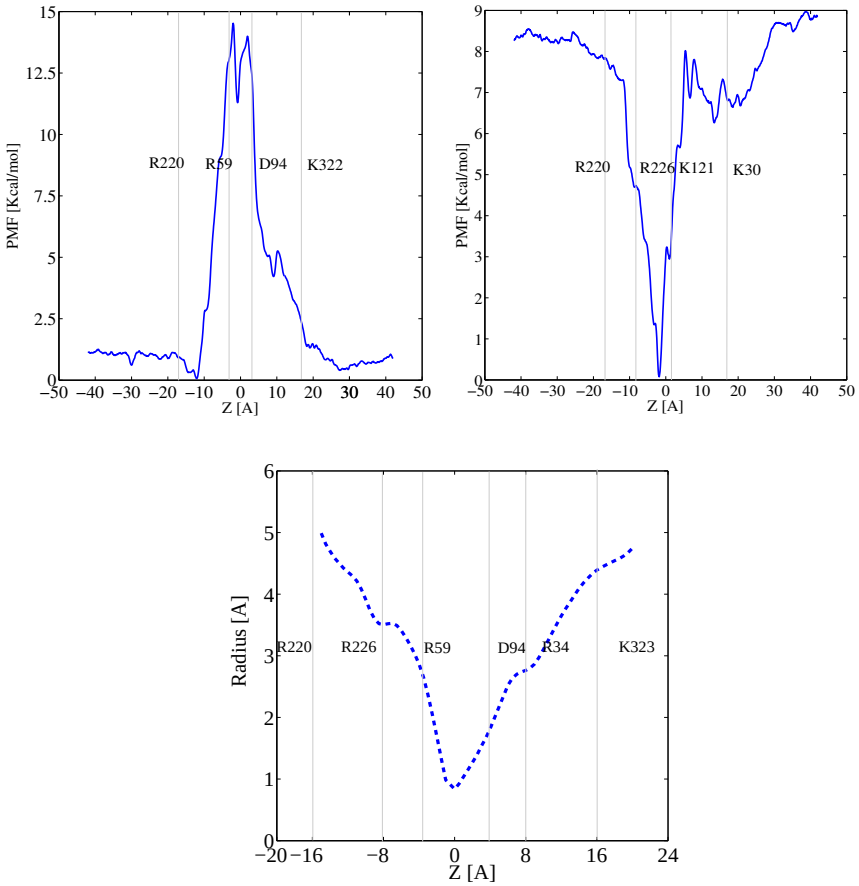


FIGURE 4.45: Potentials of mean force (top) of potassium (left) and chlorine (right) in the OprP phosphate channel. At the bottom figure, the corresponding channel radius ($r(x)$) are shown as the distance from the center. Arginine ladders are additionally shown.

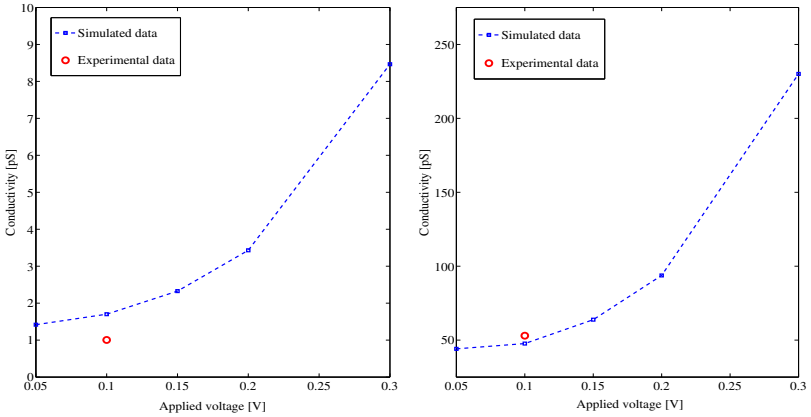


FIGURE 4.46: The simulated potassium (left) and chlorine (right) conductivities versus experimental data as functions of applied voltage for one of the monomers of the porin.

a salt concentration of 500mM as is depicted in 4.52 [84]. The PMFs are from [2] and [103], respectively.

In order to model the transport of anions, we used the PMF of Cl^- in Gramicidin A from

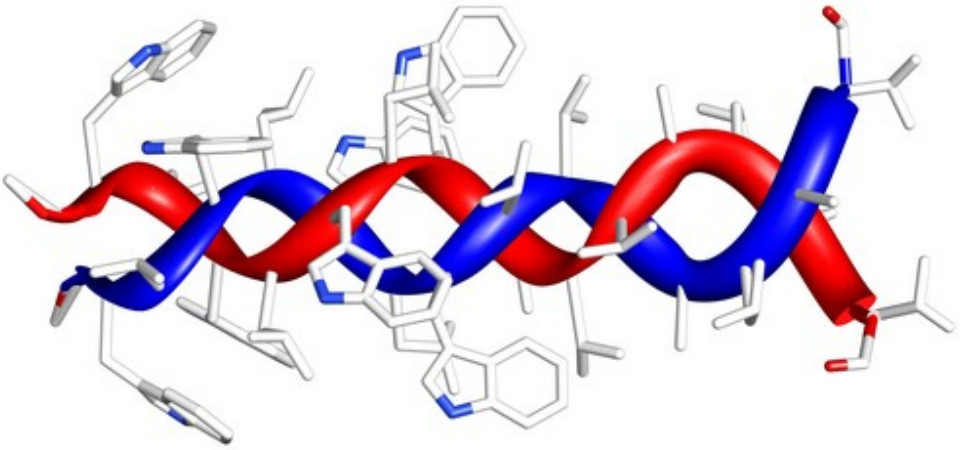


FIGURE 4.47: Structure of the Gramicidin A channel (PDB code 1MIC).

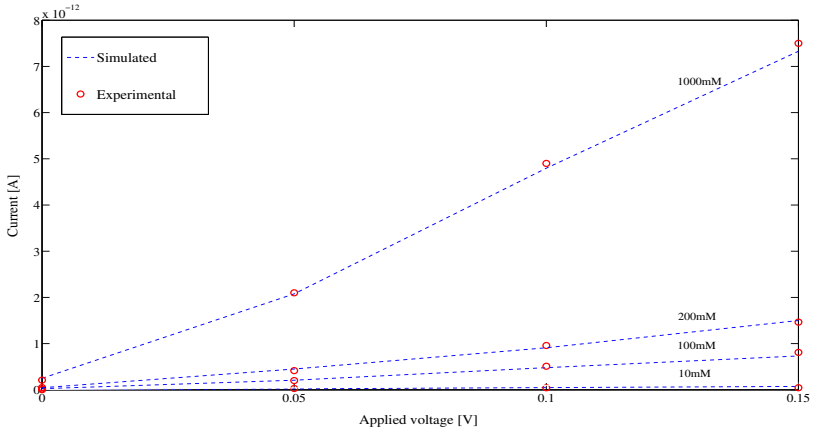


FIGURE 4.48: Comparison of experimental [105] and simulated Na^+ currents through the Gramicidin A channel as functions of applied potential for different bath concentrations.

[48, Figure 3]. The PMF in the channel is approximately two times larger than the PMF of potassium, which greatly reduces the Cl^- current. Using an ionic concentration of 0.1mM and an applied voltage of 0.1mV yields a negligible Cl^- current of $1.5577 \cdot 10^{-7}$pA, which agrees well experimental data [48].

4.4.4 Simulation of KcsA channels

The transduction of potassium ions through transmembrane channels plays an important role in cell metabolism. In contrast to sodium, potassium is intracellular. Potassium channels enable and control the flux of potassium ions across cell membranes and are found in most cell types. They regulate a wide variety of cell functions; for example, the high selectivity of the KcsA channel with respect to potassium is fundamental for signal conduction in nerve cells.

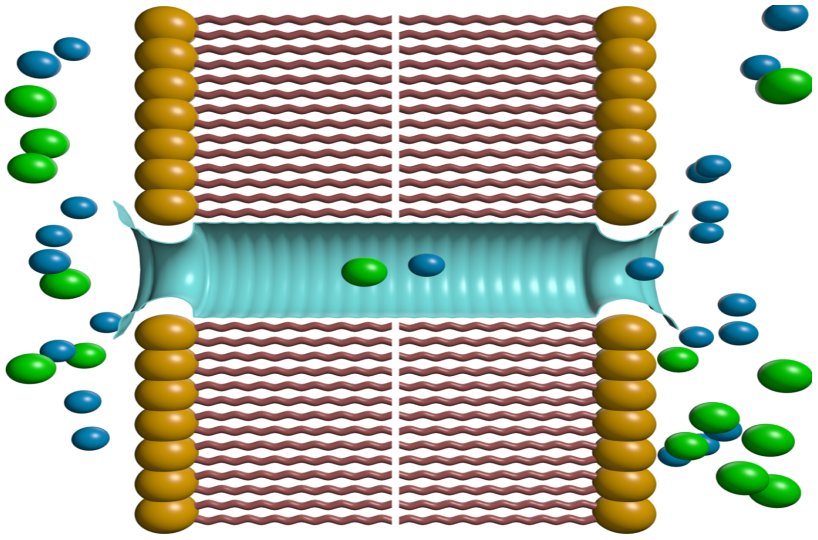


FIGURE 4.49: Diffusion of ions through the Gramicidin A channel

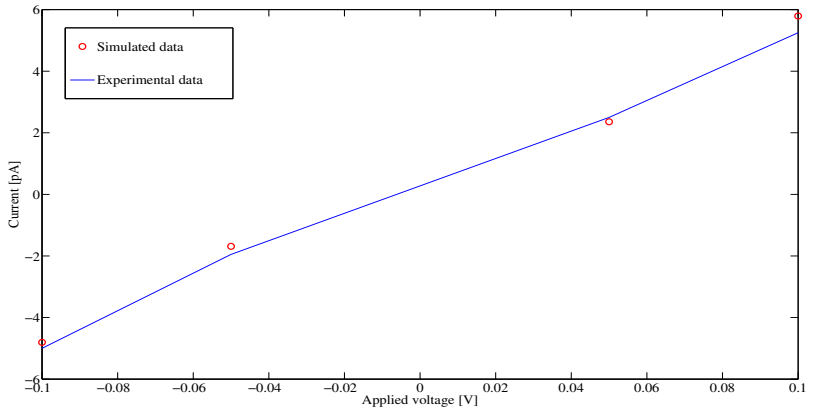


FIGURE 4.50: The measured [105] and simulated Na^+ currents through the Gramicidin A channel for positive and negative applied voltages at1 M bath concentration.

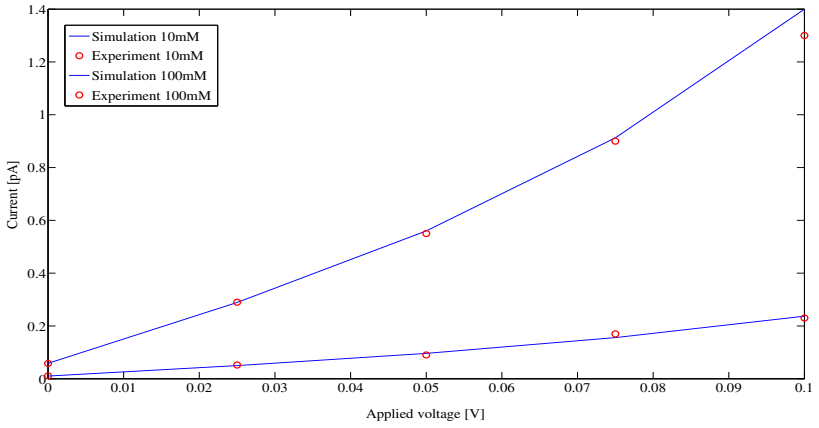


FIGURE 4.51: The simulated versus the experimental [4] K^+ current for different applied voltages.

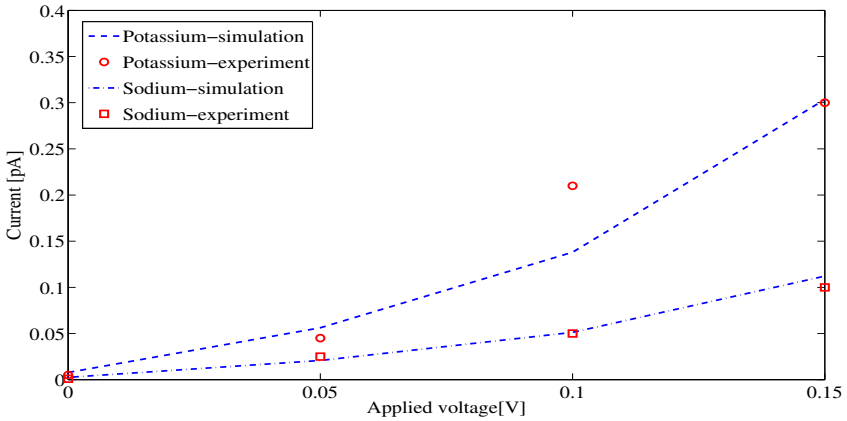


FIGURE 4.52: The simulated versus the experimental [4] sodium and potassium currents for different applied voltages through the Gramicidin A channel at 2 M salt concentration.

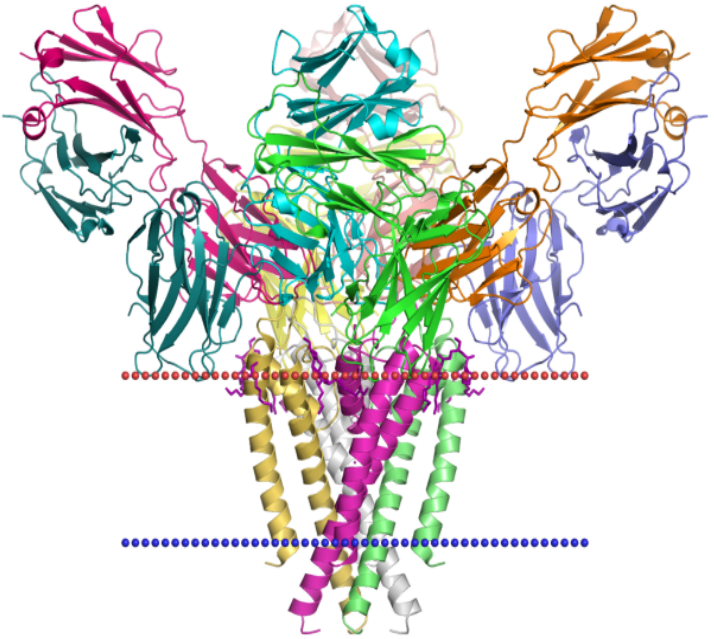


FIGURE 4.53: The 1K4C potassium channel KcsA with a radius of 0.28nm and a length of 12.4nm. The extracellular and cytoplasmic are illustrated with red and blue dotted lines respectively.

The potassium channel of *Streptomyces lividans,* KcsA (PDB id 1K4C), is a membrane protein with sequence similarity to all known potassium channels, implying that the selectivity filter is highly conserved. The KcsA channel consists of four identical subunits that form an inverted pyramid surrounding a large central cavity and leading to a narrow pore at the extracellular end. The pore region consists of an inner pore, a large cavity near the middle of the pore, and the selectivity filter that separates the

cavity from the extracellular liquid (see 4.53) [23, 49]. The inner pore and the internal cavity are hydrophobic, while the selectivity filter is lined exclusively by chain atoms belonging to the conserved sequence. Mutation experiments demonstrated that this signature sequence is responsible for potassium selectivity. The selectivity filter has four binding sites which can be occupied by monovalent cations or water molecules. Geometry of the KcsA channel is much more complicated than other transmembrane pores. The coefficient functions were again determined as described in 4.4.1 according to the geometry of the protein. Numerical investigations show that the current as a function

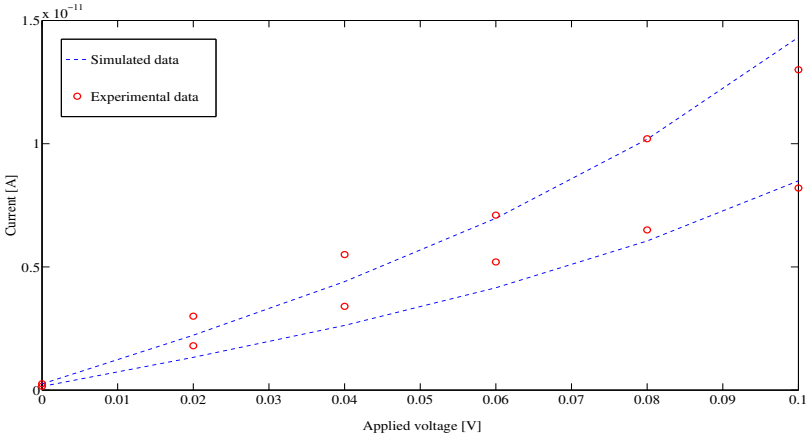


FIGURE 4.54: Comparison of simulated and measured [17] K^+ current through a KcsA channel for bath concentrations of 100mM and 200mM.

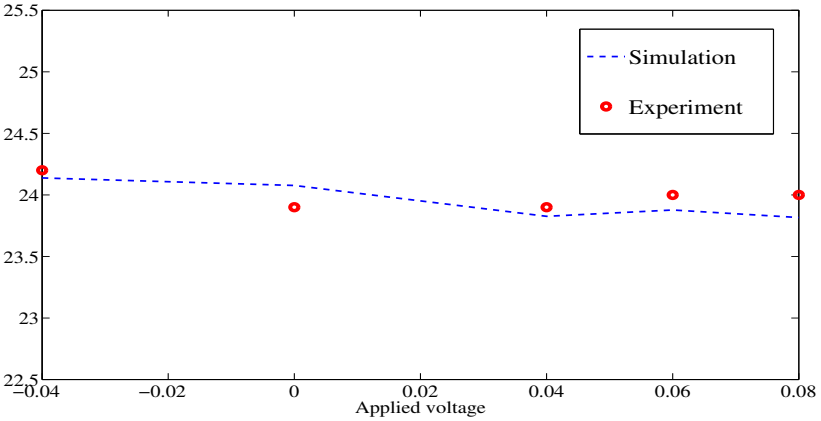


FIGURE 4.55: Current ratio of potassium over sodium for simulated and measured [41] current through a KcsA channel for a bath concentration of 500mM.

of applied voltage is larger compared to the other pores underlining the selectivity of the channel for potassium (see 4.54). In the next step, we simulate the transduction of sodium ions through the channel. As is well-known, their conductivity is much smaller and the sodium current is much lower even at high sodium concentrations. As Figure 4.55 shows, current ratio of potassium over sodium for both negative and positive applied voltages is more than 24, although there is a slight fluctuation in it. This is also seen in the simulations in Figure 4.56 using the correct potential barrier for sodium ions

[157]. Moreover, in order to simulate the transport of the ions, we used the experimental data in [17] and the potential of mean force in [157].

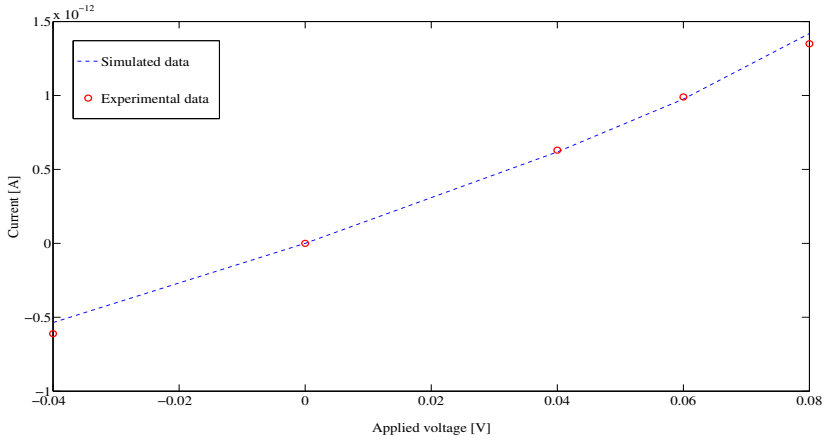


FIGURE 4.56: Comparison of simulated and measured [41] Na+ current through a KcsA channel at 500 mM bath concentration.

Having validated the simulations in this manner, we can now discuss the selectivity of the KcsA channel. We pose the question why the rings of oxygen atoms in the selectivity filter are repeated four times. The oxygen atoms in the selectivity filter provide binding sites for the cations and they imitate the hydration shells of cations in bulk water. In the natural protein, the oxygen atoms are arranged in four rings with the coordination distance varying from 0.27nm to 0.308nm [169]. The length of the selectivity filter in the continuum model corresponds, of course, to the number of binding sites in the filter.

The natural selectivity filter is approximately 1.2nm long [23]. Since the length of the natural selectivity filter cannot be changed in experiments (huge modifications of the protein would be necessary) but can be changed quite easily in simulations, we have investigated the effect of filter length here. In other words, we have simulated virtual channels that have shorter and longer selectivity filters. An applied voltage of 100mV is applied across the channel for bath concentration of 100mM and 200mM. The numerical results for the ratio of potassium to sodium current, used here as a measure of selectivity, are shown in Figure 4.58.

If there is only a selectivity filter shorter than the natural one, the selectivity decreases. On the other hand, for filters longer than four oxygen rings, the selectivity remains essentially constant. This behavior is observed independent of bath concentration. Because of the selectivity for potassium, the Na^+ current is more than 20 times smaller than the K^+ current.

These results mean that a filter length of four oxygen rings is the optimal filter length: Longer filters would not be advantageous compared to the natural selectivity filter, but they would be harder to assemble and stabilize in a lipid bilayer and would be generally wasteful, while shorter filters would have the disadvantage of allowing larger sodium currents and reducing selectivity, diminishing the physiological purpose of the KcsA channel.

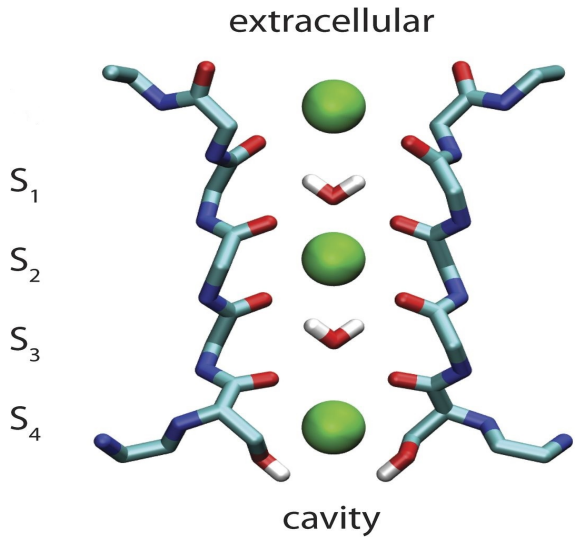


FIGURE 4.57: The Selectivity filter of the KcsA channels, four oxygen rings are illustrated in the figure.

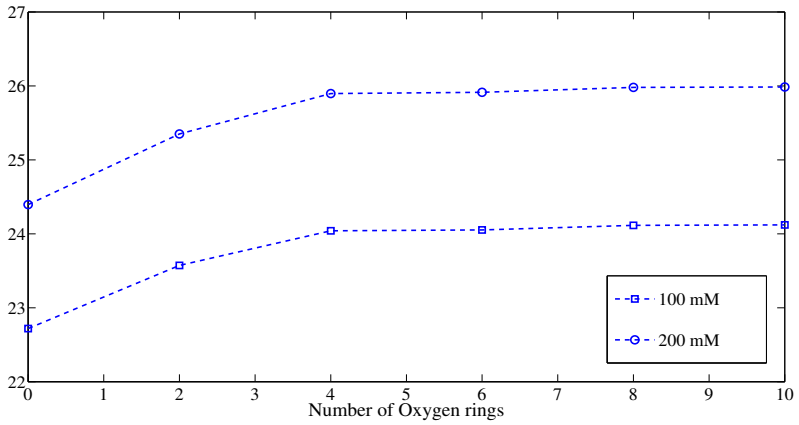


FIGURE 4.58: The ratio of potassium to sodium currents as a function of the length of the selectivity filter. For filters longer than four oxygen rings, the ratio is constant, while it decreases as the filter length decreases below this length.

4.5 Conclusions

First, we used the stochastic Poisson-Boltzmann equation to quantify the biological noise in nanowire field effect sensors. Here, we applied the drift-diffusion system to model the charge transport of the carriers. The basis adaptation base on the polynomial chaos expansion we implemented for noise quantification. In all the numerical results, very good agreement between basis adaptation and the full solution was found. This is true for a wide range of parameter values: doping concentration, ionic concentration, surface charge, and size and charge of molecules were varied over large intervals. These numerical results show the effectiveness of basis adaptation for the stochastic nonlinear Poisson-Boltzmann equation.

The effectiveness of basis adaptation is due to the choice of uncertainty domain and the

properties of solutions of the (stochastic) Poisson-Boltzmann equation. In particular, it is known that pointwise estimates hold for this type of semilinear problem [108], [13, Lemma 3.2], justifying the choice of uncertainty domain as a vicinity of the support of the stochastic process.

Basis adaptation was compared to the multi-level Monte-Carlo method as an example of another modern numerical approach for computing expected values of solutions of stochastic partial differential equations. Multi-level Monte Carlo performs much better than Monte Carlo, but not as well as basis adaptation. This is mainly due to the fact that the particular multi-level Monte-Carlo method used here does not take into account the special structure of the model equation, whereas the combination of basis adaptation and suitable uncertainty domain does. Ideas from the multilevel Monte Carlo approach adapted to the problem at hand may increase performance considerably.

Regarding the application of field-effect sensors, where the stochastic Poisson-Boltzmann equation plays an important role as a fundamental model equation, very good agreement of the basis-adaptation method with measurements was found. The stochastic Poisson-Boltzmann equation makes it possible to include noise and fluctuations in the modeling, and the numerical results show how the various parameters affect the signal-to-noise ratio, an important characteristic value of sensors.

Second, we have developed an efficient three-dimensional multilevel Monte Carlo finite-element method for the stochastic drift-diffusion-Poisson system to simulate randomness and process variations due to target molecules (in biosensors) and dopant atoms (in FinFET devices). The most noticeable advantage of this method compared to classical methods such as Monte Carlo is the much reduced computational expense. An optimization problem is solved for a given tolerance level to find the optimal parameters (M_ℓ, h_ℓ, L).

We studied the effect of random-dopant fluctuation as a concrete example. In the (classical) continuum model, the doping concentration is considered as a macroscopic quantity and the effect of the dopants is averaged out. In the discrete model, the dopant atoms have microscopic structure and the device variation due to the individual dopants was quantified. We calculated the fluctuation of the current in the subthreshold regime in a FinFET for different gate voltages and compared the results with the continuum model. In another example, namely in nanowire field-effect sensors, we used a fully three-dimensional system of stochastic PDE, namely the stochastic drift-diffusion-Poisson system, to model the effects of random DNA oligomers in a liquid on a semiconductor. We first compared the simulation results with experimental data, where a very good agreement was found. The results obtained by the discrete model, i.e., the stochastic PDE, agree better with the experiments than the (classical, deterministic) continuum model. The distributions of the molecules were obtained from a physical model, namely from a random-walk based stochastic method to simulate the association/dissociation processes of the molecules in three specific surface regions of the nanowire.

Third, the troponin sensitive sensors have shown recently their efficiencies to shorten heart disease diagnostic time and increase the reliability of tests. We considered the cardiac troponin dynamic range for healthy and risky individuals. To calculate the

charge of molecules in the blood we used the PROPKA algorithm as well. Also, we calculated the statistics i.e., expected value and the variance of the **PT**-concentration of binding cTnI molecules to the receptors. The sensitivity of the device with respect to the troponin molecules has been a crucial parameter in this paper. To that end, we studied the effect of parameter e.g., doping concentration, the back-gate voltage, etc. on the device sensing.

In the fabrication process of nanowire field effect sensors, the geometry of nanowire is very important. We simulated the device with four types of the transducers. The simulations were done for the three different ranges of the troponin concentrations. The triangular nanowires performed more efficient than other devices in the sense of sensitivity and the signal. Furthermore, we obtained that the triangular transducers with a sidewall angle of $\approx 54.7^\circ$ to the horizontal surface and (111) silicon sidewall plane performs better than the equilateral device. Finally, the arrangement of parallel nanowires was studied in this work. According to the simulations, the symmetric arrangement i.e., the equal distance between the nanowires (center-to-center distance) and the boundaries gives rise to the maximum of device sensing.

Fourth, we have developed an optimal multilevel randomized quasi-Monte Carlo method to calculate the expected value of the solution. We have compared the new method with the optimal multilevel Monte Carlo method, where a reduction in the computational cost of the new method by more than one order of magnitude is found. In order to obtain the parameters of the numerical method and to solve the resulting optimization problem, we have used an SQP method as a generalization of Newton's method and approximated the nonlinear objective function by its local quadratic approximation. In summary, a computational complexity of $\mathcal{O}(\varepsilon^{-1.82})$ is achieved.

The numerical method developed here has also been applied to a realistic problem, namely the effects of random dopants in a state-of-the-art transistor. Variations due to the location and the number of dopants have been considered and compared to the continuum model. As the number of dopants in the discrete model goes to infinity, the continuum model is obtained as the limit as expected. The variations are significant for a realistically small number of dopants, which is consistent with random dopants being the main limiting factor in today's transistor technology.

Finally, we have used a continuum transport model for confined structures to investigate three kinds of transmembrane channels. The main feature of this diffusion-type transport equation is that the geometry of the confining protein directly determines the transport coefficients in the equation. Its great advantage as a continuum model is the fact that the currents are obtained immediately from the 2D numerical solution by integration over local energy; the numerical solutions of this 2D equation can be calculated quickly. The model was validated by the application to three kinds of channels. In all cases, very good agreement between simulation and experiments was found, implying that the potential barriers (PMFs) inside the channel and the widths of the channels already capture the essential features of their functioning. In the case of the OprP porin and Gramicidin A, this simulation capability can be used to further our quantitative understanding of antibiotics. For example, mutations can be investigated by first calculating the potential

barrier that ions experience and then calculating ionic currents through the proteins. The KcsA channel was considered as the third example. The main physiological function of the KcsA potassium channel is its selectivity between sodium and potassium ions. Here the geometry of the protein is much more complicated than the geometry of other pores. Nevertheless, the simulated sodium and potassium currents match the measured data very well. The optimal selectivity filter length was determined by simulating virtual channels and agrees well with the natural filter length. Hence it is possible to explain why the KcsA channel has this particular geometry.

Chapter 5

Conclusions

The main objective of this dissertation was the development of advanced numerical techniques and physical models to quantify noise in nanoelectronic devices.

First, we considered the stochastic drift–diffusion-Poisson equations as the main model equation for describing transport in random environments with many applications. We presented existence and local uniqueness theorems for the weak solution of the system. Afterward, we define a global optimization problem which minimizes the computational complexity such that the error bound is less than or equal to a given tolerance level. MLMC-FE method was found to decrease the total computational effort by four orders of magnitude for small error tolerances. The speed-up becomes better as the error tolerance decreases. To further improve the computational efficiency, a randomized low-discrepancy sequence such as a randomly shifted lattice were applied as well. Again, compared with the optimal multilevel Monte Carlo method, a reduction in the computational cost of the new method by more than one order of magnitude is found. We used a continuum transport model for confined structures to investigate three kinds of transmembrane channels.

The methods developed here were applied to a realistic transport problem, namely the calculation of random-dopant effects in nanoscale field-effect transistors. As another example, namely, in SiNW-FETs, we used the fully three-dimensional system of the stochastic drift-diffusion-Poisson system, to model the effects of random DNA oligomers in a liquid on a semiconductor. We compared the simulation results with experimental data, where a very good agreement was found. In ion channels, in spite of computational advantages of the transport model, the verification with the experiments shows its exactness. These examples proved the efficiency of the developed models/techniques for modeling the randomness in different nanoelectronic devices.

We used the PDE-based models to develop the cardiac troponin sensors. The efficiency of SiNW-FETs compared with traditional methods such as ECG and popular tools e.g., ELISA discussed in this dissertation in details. We proposed a design strategy for affinity-based biosensors using nanowires for sensing and measuring biomarker concentration in biological samples. In other words, we explained the effect of influential parameters, like sensor length, width, doping concentration, dopant type, type of the

nanowire, backgate voltage, and the number of parallel nanowires on the sensor response. Therefore, by varying the substantial parameters, it has been made possible to optimize the electrical characteristics of devices and to fabricate the optimal field-effect sensor to detect cTn concentration more accurately.

List of Figures

1.1 Schematic diagram of a nanowire field-effect sensor showing metal source and drain electrodes with the NW and contacts on the surface of SiO_2/Si substrate. 5
1.2 A longitudinal cross section of nanowire field effect sensor indicating the random binding of the target molecules to the receptors. Here, the Dirichlet boundary conditions (V_g, V_{solution}, V_S and V_D) and zeros Neumann boundary condition (on left and right) are depicted. The geometry of the device is shown additionally. 6
1.3 The orientation of a molecule in respect of oxide layer. The reference axes are shown additionally. 6
1.4 The 3D structure of the simulation geometry where the dopant atoms are distributed in source and drain regions. 10
1.5 Schematic representation of the valence of silicon lattice where the phosphorous and boron atoms create an extra electron and hole, respectively. . 11

3.1 Meshes for the random distribution of impurity atoms (red circles) in a nanowire field-effect sensor for levels $\ell = 0$ (left) and $\ell = 1$ (right), where $h_0 = 4.02$, $r = 2$, and $C_{\text{dop}} = 4 \times 10^{16}\,\text{cm}^{-3}$. Additionally, oxide ($D_{\text{ox}}$), transducer ($D_{\text{Si}}$) and the electrolyte ($D_{\text{liq}}$) subdomains are depicted with blue, black and green meshes, respectively. 53
3.2 Computational work for matrix assembly (top) and solving the system (bottom), both for the Poisson equation (left) and the drift-diffusion-equations (right). 53
3.3 Discretization error (left) and statistical (right) error as a function of h. . 54
3.4 The minimized computational work for the MLMC-FE method as a function of the number of levels and as a function of the given error tolerance. The results for a geometric progression for h (left) and general h (right) are shown. The number of levels yielding the minimal overall computational work is indicated by red circles. 55
3.5 Comparison between the two different approaches to MLMC FE method for $\varepsilon = 0.015$. 55
3.6 Comparison of total computational work for MC-FEM and the two approaches to MLMC-FEM for various given tolerances. 57

4.1 Cross section through a field-effect nanowire sensor, showing subdomains and boundary conditions. In the electrolyte (D_{liq}), the random binding of target molecules to immobilized receptor molecules at the surface defines molecule subdomain (D_{M}). 72

4.2 The electrostatic free energies of various ssDNA and dsDNA oligomers as a function of angle for a surface charge of $-0.5\,\mathrm{q/nm^2}$ in a liquid with an ionic concentration of 30 mM. The angles are defined with respect to the surface, where 0 means a molecule parallel to the surface and $\pi/2$ means a molecule perpendicular to the surface (as indicated in Figure 4.1). Data from [72]. 73
4.3 Probability density function (left) and cumulative distribution function (right) of random orientation of 12 base pairs ssDNA oligomers in an aqueous solution with different ionic concentration and surface charge. The proteins rotate between 0 (horizontal) and $\pi/2$ (vertical) degrees at the surface. 74
4.4 The comparison of measured and simulated currents (expected value) in respect of different back-gate voltages for 60 nm (left) and 100 nm (right) width of transducer. The simulations are performed for the reference structure, where the back-gate voltage was varied. Here, $V_{SD} = 0.2\,\mathrm{V}$ and for both devices the same threshold voltage is used. 75
4.5 Expected value of current and its signal-to-noise ratio as functions of doping concentration for 60 nm and 100 nm wide devices. Here, the ionic concentration is 30 mM, the surface charge is $-0.5\,\mathrm{q/nm^2}$ [72], the oligomer length is 12 base pairs, $V_{BG} = -3\,\mathrm{V}$, and the thermal voltage is 0.021 V. 75
4.6 The comparison of expected value (top) and signal-to-noise ratio of current (bottom) for 60 nm (left) and 100 nm (right) width as functions of ionic concentration. Here, the doping concentration is $10^{16}\,\mathrm{cm^{-3}}$, the surface charge is $-0.5\,\mathrm{q/nm^2}$ [72], the oligomer length is 12 base pairs, $V_{BG} = -3\,\mathrm{V}$, and the thermal voltage is 0.021 V. 76
4.7 The comparison of expected value (top) and the signal-to-noise ratio of the current (bottom) for 60 nm (left) and 100 nm (right) wide sensors as functions of surface charge density. Here, the doping concentration is $10^{16}\,\mathrm{cm^{-3}}$, the ionic concentration is 30 nm, the oligomer length is 12 base pairs, $V_{BG} = -3\,\mathrm{V}$, and the thermal voltage is 0.021 V. 77
4.8 The comparison of mean value (top) through the transducer and the signal-to-noise ratio of the current (bottom) for 60 nm (left) and 100 nm (right) as functions of oligomer length. Here, the doping concentration is $10^{16}\,\mathrm{cm^{-3}}$, the ionic concentration is 30 mM, the surface charge is $-0.5\,\mathrm{q/nm^2}$, $V_{BG} = -3\,\mathrm{V}$, and the thermal voltage is 0.021 V. 78
4.9 A cross section of the field effect sensor indicating the three different regions of the surface. 80
4.10 Histograms of the **PT**-complex density in equilibrium at the corners (top left), in the middle (top right), at the edges (bottom left), and overall (bottom right). The green lines show a Gaussian distribution with the parameters in Table 4.6. 81
4.11 The meshes for the nanowire field-effect sensor for $\ell = 0$ (left) and $\ell = 1$ (right). The subdomains are depicted with gray (substrate), golden (nanowire), and green (electrolyte) meshes. The randomly distributed molecules and the dopants are inside the electrolyte and the nanowire, respectively. 81
4.12 Statistical and discretization errors for different mesh sizes. The coefficients α and β behave according to Assumption 1. 82

4.13 A comparison of the total computational work necessary in the MC and MLMC methods as a function of the prescribed total error. 83
4.14 The expected value of the electrical current as a function of back-gate voltage for 60 nm width (left) and 100 nm width (right) for continuum and discrete models. Here, the discrete model points out the biological noise in addition to the RDF and in continuum model only the RDF is considered. In the simulation, the results are with the experimental data [14] with the same main parameters i.e., $t_{\text{ox}} = 8\,\text{nm}$, $C_{\text{dop}} = 1 \times 10^{16}\text{cm}^{-3}$, $V_{SD} = 0.2\,\text{V}$, the nanowire thickness of 50 nm and $\mu_p = 100\ \text{cm}^{-2}\text{V}^{-1}\text{s}^{-1}$. 83
4.15 Histograms of the electrical current calculated by the discrete model (biological and RDF fluctuation) with 941 simulations for a doping concentration of $1 \times 10^{16}\,\text{cm}^{-3}$ (left) and for a doping concentration of $1 \times 10^{17}\,\text{cm}^{-3}$ (right). 84
4.16 The expected value of the current for $V_{SD} = 0.4\,\text{V}$ and $V_{SD} = 0.6\,\text{V}$ for both the continuum and discrete models where $V_T = -0.98\,\text{V}$ (threshold voltage). 84
4.17 The four principal regulatory components of the skeletal muscle, i.e., actin, tropomyosin, nebulin and the troponin complex [55]. 85
4.18 A longitudinal cross section of a troponin sensitive SiNW-FET. The random binding of troponin molecules to the probe molecules (antigens) is depicted as well. 86
4.19 Schematic diagram of the nanowire field-effect sensor showing receptor and target molecules. The subdomains, i.e., silicon nanowire Ω_{Si}, insulator Ω_{Ox}, the specific binding of target to probe molecules Ω_{M}, and the electrolyte Ω_{El} are illustrated with their dimensions and ranges. Additionally, d indicates the center-to-center distance between the nanowires and d_1 is the distance between a nanowire and the boundary. 87
4.20 The net charge of the folded and unfolded states of protein 1MXL for different pH values. The results are obtained by PDB2PQR simulation. . 88
4.21 The expected value (top left), variance (top right), and binding efficiency (bottom) of **PT**-complexes for different troponin concentrations. 90
4.22 Cross-section of radial (left) and triangular (left) nanowires with nanowire area of 2500 nm. In the triangular device, the sidewall angels are $\approx 54.7°$. 91
4.23 Sensor response (left) and signal (right) as a function of troponin concentration varying from 5 pg/ml and 50 pg/ml for different nanowire cross sections. The sensors are 300 nm wide and the bulk oxide is 200 nm thick. Each sensor has one 1000 nm long nanowire, a cross-sectional area of $2500\,\text{nm}^2$, a doping concentration of $10^{17}\,\text{cm}^{-3}$, and they are protected by a 5 nm thick silicon oxide layer. 92
4.24 Expected value and standard deviation of **PT**-complexes (left) and signal-to-noise ratio (right) as a function of troponin concentration varying from 5 pg/ml and 50 pg/ml for different nanowire cross sections. The sensors are 300 nm wide and the bulk oxide is 200 nm thick. Each sensor has one 1000 nm long nanowire, a cross-sectional area of $2500\,\text{nm}^2$, a doping concentration of $10^{17}\,\text{cm}^{-3}$, and they are protected by a 5 nm thick silicon oxide layer. 92

4.25 Sensor response (left) and signal (right) of two triangular nanowires for different backgate voltages at 10 pg/mL troponin concentration. The sensors are 300 nm wide and the bulk oxide is 200 nm thick. Each sensor has one 1000 nm long nanowire, a cross-sectional area of 2500 nm^2, a doping concentration of 10^{17} cm^{-3}, and they are protected by a 5 nm thick silicon oxide layer. 93
4.26 Sensor response (top left), signal (top right), and SNR (bottom) as a function of doping concentration for different nanowire cross sections. The sensors are 300 nm wide and the bulk oxide is 200 nm thick. Each sensor has one 1000 nm long nanowire, a cross-sectional area of 2500 nm^2 and they are protected by a 5 nm thick silicon oxide layer. 93
4.27 Sensor response (top left), signal (top right), and SNR (bottom) as a function of troponin concentration varying from 5 pg/ml and 50 pg/ml for different nanowire cross sections. The sensors are 1000 nm wide and the bulk oxide is 300 nm thick. Each sensor has two parallel 5000 nm long nanowires, a cross-sectional area of 2500 nm^2, a doping concentration of 10^{17} cm^{-3}, and they are protected by a 5 nm thick silicon oxide layer. . . . 94
4.28 The sensor response of different devices as a function of the nanowire center-to-center distance at 75 pg/ml cTn concentration. The sensors are 1000 nm ($d = d_1 = 333$ nm) wide and the bulk oxide is 300 nm thick. Each sensor has two parallel 5000 nm long nanowires, a cross-sectional area of 2500 nm^2, a doping concentration of 10^{17} cm^{-3}, and they are protected by a 5 nm thick silicon oxide layer. 95
4.29 Sensitivity (top left), signal (top right), and SNR (bottom) as a function of troponin concentration varying from 500 pg/mL and 10 ng/mL for different nanowires cross sections. The sensor is 1000 nm wide and the bulk oxide is 300 nm thick. Each sensor has four parallel 5000 nm long nanowires, a cross-sectional area of 2500 nm^2, a doping concentration of 10^{17} cm^{-3}, and they are protected by a 5 nm thick silicon oxide layer. . . . 96
4.30 The three-dimensional meshes for the SOI FinFET in Figure 1.4 for levels $\ell = 0$ (left) and $\ell = 1$ (right). The subdomains are indicated by red for the substrate, by yellow for the insulator, by black for the channel, by green for the source and drain regions, and blue gate. 98
4.31 Histogram of the current in the discrete model with 482 simulations for $V_g = 0.1$ V (left) and $V_g = 0.2$ V (right). The number of dopants is $N_{\text{dop}} = 80$. 99
4.32 Histogram of the current in the discrete model with 482 simulations for $V_g = 0.1$ V (left) and $V_g = 0.2$ V (right). The number of dopants is $N_{\text{dop}} = 20$. 99
4.33 The expected value of the current as a function of different gate voltages calculated using the continuum and discrete models. 100
4.34 Schematic structure of a three-dimensional FinFET. The random dopants are distributed in the source and drain regions. 101
4.35 The 3D meshes corresponding to the FinFET for $\ell = 0$ (left) and $\ell = 1$ (right). 101
4.36 The decay of variance of the solution as a function of different mesh sizes (left) and number of samples (right). The values $C_{00} = 9.45$, $C_0 = 0.338$, and $\delta = 0.06$ are found additionally. 102

4.37 The expected value of the solution as a function of different mesh sizes with $C_1 = 1.304$. . . . 103
4.38 Comparison of the total computational work required for the optimal MLRQMC and MLMC methods. For smaller total errors, the effectiveness of the randomized method is more pronounced. . . . 104
4.39 The comparison of the total work of MLRQMC for different levels (between $L = 0$ and $L = 7$) for three different total errors $\varepsilon = 0.1$, $\varepsilon = 0.05$, and $\varepsilon = 0.03$. For each prescribed total error, the optimal number of levels is indicated by a red circle. . . . 104
4.40 The expected value of current as a function of different gate voltages calculated using continuum and discrete models with $V_{SD} = 0.1\,\mathrm{V}$. . . . 105
4.41 Histogram of the current for $V_g = 0.1\,\mathrm{V}$ (left) and $V_g = 0.2\,\mathrm{V}$ (right) and 563 simulations. Here $\mathbb{E}(I) = 1.49 \cdot 10^{-7}\,\mathrm{A}$ for the lower gate voltage and $\mathbb{E}(I) = 1.14 \cdot 10^{-6}\,\mathrm{A}$ for the higher gate voltage. . . . 105
4.42 The I-V characteristics for different numbers of dopants. The results for the continuum model are shown as well. . . . 106
4.43 Histogram of the current for $V_g = 0.2\,\mathrm{V}$ and for 563 simulations. Left: $N_{\mathrm{dop}} = 5$ resulting in $\mathbb{E}(I) = 9.22 \cdot 10^{-7}\,\mathrm{A}$. Right: $N_{\mathrm{dop}} = 50$, resulting in $\mathbb{E}(I) = 9.66 \cdot 10^{-7}\,\mathrm{A}$. The current obtained by the continuum model is $I = 9.66 \cdot 10^{-7}\,\mathrm{A}$. . . . 106
4.44 X-ray crystallography of Oprp phosphate channel. Periplasmic and extracellular are shown. . . . 109
4.45 Potentials of mean force (top) of potassium (left) and chlorine (right) in the OprP phosphate channel. At the bottom figure, the corresponding channel radius ($r(x)$) are shown as the distance from the center. Arginine ladders are additionally shown. . . . 110
4.46 The simulated potassium (left) and chlorine (right) conductivities versus experimental data as functions of applied voltage for one of the monomers of the porin. . . . 110
4.47 Structure of the Gramicidin A channel (PDB code 1MIC). . . . 111
4.48 Comparison of experimental [105] and simulated Na^+ currents through the Gramicidin A channel as functions of applied potential for different bath concentrations. . . . 111
4.49 Diffusion of ions through the Gramicidin A channel . . . 112
4.50 The measured [105] and simulated Na^+ currents through the Gramicidin A channel for positive and negative applied voltages at1 M bath concentration. . . . 112
4.51 The simulated versus the experimental [4] K^+ current for different applied voltages. . . . 112
4.52 The simulated versus the experimental [4] sodium and potassium currents for different applied voltages through the Gramicidin A channel at 2 M salt concentration. . . . 113
4.53 The 1K4C potassium channel KcsA with a radius of 0.28nm and a length of 12.4nm. The extracellular and cytoplasmic are illustrated with red and blue dotted lines respectively. . . . 113
4.54 Comparison of simulated and measured [17] K^+ current through a KcsA channel for bath concentrations of 100mM and 200mM. . . . 114
4.55 Current ratio of potassium over sodium for simulated and measured [41] current through a KcsA channel for a bath concentration of 500mM. . . . 114

4.56 Comparison of simulated and measured [41] Na+ current through a KcsA channel at 500 mM bath concentration. 115
4.57 The Selectivity filter of the KcsA channels, four oxygen rings are illustrated in the figure. 116
4.58 The ratio of potassium to sodium currents as a function of the length of the selectivity filter. For filters longer than four oxygen rings, the ratio is constant, while it decreases as the filter length decreases below this length. 116

Bibliography

[1] Edward Allen. *Modeling with Itô Stochastic Differential Equations*, volume 22. Springer Science & Business Media, 2007.

[2] Toby W Allen, Olaf Sparre Andersen, and Benoit Roux. Ion permeation through a narrow channel: using Gramicidin to ascertain all-atom molecular dynamics potential of mean force methodology and biomolecular force fields. *Biophysical Journal*, 90(10):3447–3468, 2006.

[3] Steven Allender, Peter Scarborough, Vito Peto, Mike Rayner, Jose Leal, Ramon Luengo-Fernandez, and Alastair Gray. European cardiovascular disease statistics. 2008.

[4] Olaf Sparre Andersen. Ion movement through Gramicidin A channels: single-channel measurements at very high potentials. *Biophysical Journal*, 41(2):119–133, 1983.

[5] Olaf Sparre Andersen, RE Koeppe, B Roux, et al. Gramicidin channels. *IEEE Transactions on NanoBioscience*, 4(1):10–20, 2005.

[6] Jeffrey L Anderson, Cynthia D Adams, Elliott M Antman, Charles R Bridges, Robert M Califf, Donald E Casey, William E Chavey, Francis M Fesmire, Judith S Hochman, Thomas N Levin, et al. ACC/AHA 2007 guidelines for the management of patients with unstable angina/non–ST-elevation myocardial infarction: a report of the American College of Cardiology/American Heart Association Task Force on Practice Guidelines (Writing Committee to Revise the 2002 Guidelines for the Management of Patients With Unstable Angina/Non–ST-Elevation Myocardial Infarction) developed in collaboration with the American College of Emergency Physicians, the Society for Cardiovascular Angiography and Interventions, and the Society of Thoracic Surgeons endorsed by the American Association of Cardiovascular and Pulmonary Rehabilitation and the Society for Academic Emergency Medicine. *Journal of the American College of Cardiology*, 50(7):e1–e157, 2007.

[7] Narain D Arora, John R Hauser, and David J Roulston. Electron and hole mobilities in silicon as a function of concentration and temperature. *IEEE Transactions on Electron Devices*, 29(2):292–295, 1982.

[8] Asen Asenov, Andrew R Brown, John H Davies, Savas Kaya, and Gabriela Slavcheva. Simulation of intrinsic parameter fluctuations in decananometer and

nanometer-scale MOSFETs. *IEEE transactions on electron devices*, 50(9):1837–1852, 2003.

[9] Luciano Babuin and Allan S Jaffe. Troponin: the biomarker of choice for the detection of cardiac injury. *Canadian Medical Association Journal*, 173(10):1191–1202, 2005.

[10] AJ Bakker, R Smits, FDM Hagen, JPMC Gorgels, B van Vlies, MJW Koelemay, and JGP Tijssen. Failure of new biochemical markers to exclude acute myocardial infarction at admission. *The Lancet*, 342(8881):1220–1222, 1993.

[11] Andrea Barth, Christoph Schwab, and Nathaniel Zollinger. Multi-level Monte Carlo finite element method for elliptic PDEs with stochastic coefficients. *Numerische Mathematik*, 119(1):123–161, 2011.

[12] Delphine C Bas, David M Rogers, and Jan H Jensen. Very fast prediction and rationalization of pka values for protein–ligand complexes. *Proteins: Structure, Function, and Bioinformatics*, 73(3):765–783, 2008.

[13] Stefan Baumgartner and Clemens Heitzinger. Existence and local uniqueness for 3D self-consistent multiscale models for field-effect sensors. *Commun. Math. Sci*, 10(2):693–716, 2012.

[14] Stefan Baumgartner, Clemens Heitzinger, Aleksandar Vacic, and Mark A Reed. Predictive simulations and optimization of nanowire field-effect PSA sensors including screening. *Nanotechnology*, 24(22):225503, 2013.

[15] Stefan Baumgartner, Martin Vasicek, and Clemens Heitzinger. Modeling and simulation of nanowire based field-effect biosensors. *Chemical Sensors: Simulation and Modeling*, 2:447–469, 2012.

[16] Hande Y Benson, David F Shanno, and Robert J Vanderbei. Interior-point methods for nonconvex nonlinear programming: Jamming and comparative numerical testing. *Operations Research and Financial Engineering, Princeton University, ORFE-00-02*, 2000.

[17] C Berti, S Furini, S Cavalcanti, E Sangiorgi, and C Fiegna. Particle-based simulation of conductance of solid-state nanopores and ion channels. In *Proc. International Conference on Simulation of Semiconductor Processes and Devices 2009 (SISPAD 2009)*, pages 1–4. IEEE, 2009.

[18] Paul T Boggs and Jon W Tolle. Sequential quadratic programming. *Acta Numerica*, 4:1–51, 1995.

[19] Brian Bohunicky and Shaker A Mousa. Biosensors: the new wave in cancer diagnosis. *Nanotechnology, science and applications*, 4:1, 2011.

[20] M Bruel. Silicon on insulator material technology. *Electronics Letters*, 31(14):1201–1202, 1995.

[21] E Brunet, T Maier, GC Mutinati, S Steinhauer, A Köck, C Gspan, and W Grogger. Comparison of the gas sensing performance of SnO2 thin film and SnO2 nanowire sensors. *Sensors and Actuators B: Chemical*, 165(1):110–118, 2012.

[22] Alena Bulyha and Clemens Heitzinger. An algorithm for three-dimensional Monte-Carlo simulation of charge distribution at biofunctionalized surfaces. *Nanoscale*, 3(4):1608–1617, 2011.

[23] A Burykin, CN Schutz, J Villa, and A Warshel. Simulations of ion current in realistic models of ion channels: the KcsA potassium channel. *Proteins: Structure, Function, and Bioinformatics*, 47(3):265–280, 2002.

[24] Russel E Caflisch. Monte Carlo and quasi-Monte Carlo methods. *Acta Numerica*, 7:1–49, 1998.

[25] Leland Chang, Kevin J Yang, Yee-Chia Yeo, Igor Polishchuk, Tsu-Jae King, and Chenming Hu. Direct-tunneling gate leakage current in double-gate and ultrathin body mosfets. *IEEE Transactions on Electron Devices*, 49(12):2288–2295, 2002.

[26] Lingqian Chang, Jiaming Hu, Feng Chen, Zhou Chen, Junfeng Shi, Zhaogang Yang, Yiwen Li, and Ly James Lee. Nanoscale bio-platforms for living cell interrogation: current status and future perspectives. *Nanoscale*, 8(6):3181–3206, 2016.

[27] Julia Charrier, Robert Scheichl, and Aretha L Teckentrup. Finite element error analysis of elliptic PDEs with random coefficients and its application to multilevel Monte Carlo methods. *SIAM Journal on Numerical Analysis*, 51(1):322–352, 2013.

[28] Duan Chen and Guo-Wei Wei. Modeling and simulation of electronic structure, material interface and random doping in nano-electronic devices. *Journal of Computational Physics*, 229(12):4431–4460, 2010.

[29] Kuan-I Chen, Bor-Ran Li, and Yit-Tsong Chen. Silicon nanowire field-effect transistor-based biosensors for biomedical diagnosis and cellular recording investigation. *Nano Today*, 6(2):131–154, 2011.

[30] Meng-Hsueh Chiang, Jeng-Nan Lin, Keunwoo Kim, and Ching-Te Chuang. Random dopant fluctuation in limited-width FinFET technologies. *Electron Devices, IEEE Transactions on*, 54(8):2055–2060, 2007.

[31] Yang-Kyu Choi, Tsu-Jae King, and Chenming Hu. Nanoscale CMOS spacer FinFET for the terabit era. *IEEE Electron Device Letters*, 23(1):25–27, 2002.

[32] Jay Huiyi Chua, Ru-Ern Chee, Ajay Agarwal, She Mein Wong, and Guo-Jun Zhang. Label-free electrical detection of cardiac biomarker with complementary metal-oxide semiconductor-compatible silicon nanowire sensor arrays. *Analytical Chemistry*, 81(15):6266–6271, 2009.

[33] KA Cliffe, MB Giles, Robert Scheichl, and Aretha L Teckentrup. Multilevel Monte Carlo methods and applications to elliptic PDEs with random coefficients. *Computing and Visualization in Science*, 14(1):3–15, 2011.

[34] J-P Colinge. *Silicon-on-Insulator Technology: Materials to VLSI: Materials to Vlsi*. Springer Science & Business Media, 2004.

[35] Jean-Pierre Colinge. Multiple-gate SOI MOSFETs. *Solid-State Electronics*, 48(6):897–905, 2004.

[36] Jean-Pierre Colinge et al. *FinFETs and other multi-gate transistors*. Springer, 2008.

[37] Jean-Pierre Colinge, MH Gao, A Romano-Rodriguez, H Maes, and C Claeys. Silicon-on-insulator"gate-all-around device". In *Electron Devices Meeting, 1990. IEDM'90. Technical Digest., International*, pages 595–598. IEEE, 1990.

[38] Ronald Cools, Frances Y Kuo, and Dirk Nuyens. Constructing embedded lattice rules for multivariate integration. *SIAM Journal on Scientific Computing*, 28(6):2162–2188, 2006.

[39] Julio F Cordero-Morales, Luis G Cuello, Yanxiang Zhao, Vishwanath Jogini, D Marien Cortes, Benoît Roux, and Eduardo Perozo. Molecular determinants of gating at the potassium-channel selectivity filter. *Nature Structural & Molecular Biology*, 13(4):311–318, 2006.

[40] R Cranley and TNL Patterson. Randomization of number theoretic methods for multiple integration. *SIAM Journal on Numerical Analysis*, 13(6):904–914, 1976.

[41] Nora B Cronin, Andrias O'Reilly, Hervé Duclohier, and BA Wallace. Binding of the anticonvulsant drug lamotrigine and the neurotoxin batrachotoxin to voltage-gated sodium channels induces conformational changes associated with block and steady-state activation. *Journal of Biological Chemistry*, 278(12):10675–10682, 2003.

[42] Yi Cui, Xiangfeng Duan, Jiangtao Hu, and Charles M Lieber. Doping and electrical transport in silicon nanowires. *The Journal of Physical Chemistry B*, 104(22):5213–5216, 2000.

[43] Yi Cui, Qingqiao Wei, Hongkun Park, and Charles M Lieber. Nanowire nanosensors for highly sensitive and selective detection of biological and chemical species. *Science*, 293(5533):1289–1292, 2001.

[44] F. Cuvelier, C. Japhet, and G. Scarella. An efficient way to perform the assembly of finite element matrices in Matlab and Octave. Technical Report 8305, Université Paris 13 and INRIA Paris-Rocquencourt, May 2013.

[45] Eric Darve and Andrew Pohorille. Calculating free energies using average force. *The Journal of Chemical Physics*, 115(20):9169–9183, 2001.

[46] Roberto De La Rica and Molly M Stevens. Plasmonic ELISA for the ultrasensitive detection of disease biomarkers with the naked eye. *Nature Nanotechnology*, 7(12):821–824, 2012.

[47] Todd J Dolinsky, Paul Czodrowski, Hui Li, Jens E Nielsen, Jan H Jensen, Gerhard Klebe, and Nathan A Baker. PDB2PQR: expanding and upgrading automated preparation of biomolecular structures for molecular simulations. *Nucleic Acids Research*, 35(suppl 2):W522–W525, 2007.

[48] Vladimir L Dorman and Peter C Jordan. Ionic permeation free energy in Gramicidin: a semimicroscopic perspective. *Biophysical Journal*, 86(6):3529–3541, 2004.

[49] Declan A Doyle, Joao Morais Cabral, Richard A Pfuetzner, Anling Kuo, Jacqueline M Gulbis, Steven L Cohen, Brian T Chait, and Roderick MacKinnon. The structure of the potassium channel: molecular basis of K+ conduction and selectivity. *Science*, 280(5360):69–77, 1998.

[50] Xuexin Duan, Yue Li, Nitin K Rajan, David A Routenberg, Yorgo Modis, and Mark A Reed. Quantification of the affinities and kinetics of protein interactions using silicon nanowire biosensors. *Nature Nanotechnology*, 7(6):401–407, 2012.

[51] FC Ebeling, UM Schmitt, M Untch, D Nagel, A Fateh-Moghadam, P Stieber, and D Seidel. Tumour markers cea and ca 15-3 as prognostic factors in breast cancer–univariate and multivariate analysis. *Anticancer Research*, 19(4A):2545–2550, 1998.

[52] Mark H Ebell, Dan Flewelling, and Cheryl A Flynn. A systematic review of troponin T and I for diagnosing acute myocardial infarction. *Journal of Family Practice*, 49(6):550–550, 2000.

[53] MS Eldred and John Burkardt. Comparison of non-intrusive polynomial chaos and stochastic collocation methods for uncertainty quantification. In *Proc. 47th AIAA Aerospace Sciences Meeting*, volume 976, pages 1–20, 2009.

[54] Niklas Elfström, Robert Juhasz, Ilya Sychugov, Torun Engfeldt, Amelie Eriksson Karlström, and Jan Linnros. Surface charge sensitivity of silicon nanowires: Size dependence. *Nano Letters*, 7(9):2608–2612, 2007.

[55] CS Farah and FC Reinach. The troponin complex and regulation of muscle contraction. *The FASEB Journal*, 9(9):755–767, 1995.

[56] Isabelle Ferain, Cynthia A Colinge, and Jean-Pierre Colinge. Multigate transistors as the future of classical metal-oxide-semiconductor field-effect transistors. *Nature*, 479(7373):310–316, 2011.

[57] Anders Forsgren, Philip E Gill, and Margaret H Wright. Interior methods for nonlinear optimization. *SIAM Review*, 44(4):525–597, 2002.

[58] Daniel Gallego-Perez, Lingqian Chang, Junfeng Shi, Junyu Ma, Sung-Hak Kim, Xi Zhao, Veysi Malkoc, Xinmei Wang, Mutsuko Minata, Kwang J Kwak, et al. On-chip clonal analysis of glioma-stem-cell motility and therapy resistance. *Nano Letters*, 16(9):5326–5332, 2016.

[59] Thomas Gerstner and Marco Noll. Randomized multilevel quasi-Monte Carlo path simulation. In *Recent Developments in Computational Finance: Foundations, Algorithms and Applications*, pages 349–369. World Scientific, 2013.

[60] Roger G Ghanem and Pol D Spanos. *Stochastic Finite Element: a Spectral Approach*.

[61] Michael B Giles. Multilevel Monte Carlo path simulation. *Operations Research*, 56(3):607–617, 2008.

[62] Michael B Giles and Ben J Waterhouse. Multilevel quasi-Monte Carlo path simulation. *Advanced Financial Modelling, Radon Series on Computational and Applied Mathematics*, pages 165–181, 2009.

[63] Mike Giles. Improved multilevel Monte Carlo convergence using the Milstein scheme. In *Monte Carlo and quasi-Monte Carlo methods 2006*, pages 343–358. Springer, 2008.

[64] Daniel T Gillespie. The chemical Langevin equation. *The Journal of Chemical Physics*, 113(1):297–306, 2000.

[65] Alan S Go, Dariush Mozaffarian, Véronique L Roger, Emelia J Benjamin, Jarett D Berry, Michael J Blaha, Shifan Dai, Earl S Ford, Caroline S Fox, Sheila Franco, et al. Heart disease and stroke statistics-2014 update. *Circulation*, 129(3), 2014.

[66] Aldrin V Gomes, James D Potter, and Danuta Szczesna-Cordary. The role of troponins in muscle contraction. *IUBMB life*, 54(6):323–333, 2002.

[67] Ivan G Graham, Frances Y Kuo, James A Nichols, Robert Scheichl, Ch Schwab, and Ian H Sloan. Quasi-Monte Carlo finite element methods for elliptic PDEs with lognormal random coefficients. *Numerische Mathematik*, 131(2):329–368, 2015.

[68] HK Gummel. A self-consistent iterative scheme for one-dimensional steady state transistor calculations. *Electron Devices, IEEE Transactions on*, 11(10):455–465, 1964.

[69] Jong-in Hahm and Charles M Lieber. Direct ultrasensitive electrical detection of DNA and DNA sequence variations using nanowire nanosensors. *Nano Letters*, 4(1):51–54, 2004.

[70] Abdul-Lateef Haji-Ali, Fabio Nobile, Erik von Schwerin, and Raúl Tempone. Optimization of mesh hierarchies in multilevel Monte Carlo samplers. *Stochastics and Partial Differential Equations Analysis and Computations*, 4(1):76–112, 2016.

[71] Stefan Heinrich. Multilevel Monte Carlo methods. In *Large-scale scientific computing*, pages 58–67. Springer, 2001.

[72] Clemens Heitzinger, Yang Liu, Norbert J Mauser, Christian Ringhofer, and Robert W Dutton. Calculation of fluctuations in boundary layers of nanowire field-effect biosensors. *Journal of Computational and Theoretical Nanoscience*, 7(12):2574–2580, 2010.

[73] Clemens Heitzinger, Norbert J Mauser, and Christian Ringhofer. Multiscale modeling of planar and nanowire field-effect biosensors. *SIAM Journal on Applied Mathematics*, 70(5):1634–1654, 2010.

[74] Clemens Heitzinger and Christian Ringhofer. A transport equation for confined structures derived from the Boltzmann equation. *Comm. Math. Sci.*, 9(3):829–857, 2011.

[75] Clemens Heitzinger and Christian Ringhofer. Hierarchies of transport equations for nanopores. *Journal of Computational Electronics*, 13(4):801–817, 2014.

[76] Clemens Heitzinger and Christian Ringhofer. Multiscale modeling of fluctuations in stochastic elliptic PDE models of nanosensors. *Commun. Math. Sci*, 12(3):401–421, 2014.

[77] Desmond J Higham. Modeling and simulating chemical reactions. *SIAM Review*, 50(2):347–368, 2008.

[78] Roger W Hockney and James W Eastwood. *Computer simulation using particles*. CRC Press, 1988.

[79] Matthew Hoyles, Vikram Krishnamurthy, May Siksik, and Shin-Ho Chung. Brownian dynamics theory for predicting internal and external blockages of tetraethylammonium in the KcsA potassium channel. *Biophysical Journal*, 94(2):366–378, 2008.

[80] Xiang-Wei Jiang, Hui-Xiong Deng, Jun-Wei Luo, Shu-Shen Li, and Lin-Wang Wang. A fully three-dimensional atomistic quantum mechanical study on random dopant-induced effects in 25-nm MOSFETs. *Electron Devices, IEEE Transactions on*, 55(7):1720–1726, 2008.

[81] Stephen Joe. Randomization of lattice rules for numerical multiple integration. *Journal of Computational and Applied Mathematics*, 31(2):299–304, 1990.

[82] IA Katrukha. Human cardiac troponin complex. structure and functions. *Biochemistry (Moscow)*, 78(13):1447–1465, 2013.

[83] Mahin Keshavarz, Mohsen Behpour, and Hossain-Ali Rafiee-pour. Recent trends in electrochemical microrna biosensors for early detection of cancer. *RSC Advances*, 5(45):35651–35660, 2015.

[84] Amirreza Khodadadian and Clemens Heitzinger. Ionic currents through transmembrane proteins calculated by a transport equation for confined structures. In *Proc. 4th International Conference on Computational and Mathematical Biomedical Engineering (CMBE 2015)*, Cachan, France, 29 June – 1 July 2015.

[85] Amirreza Khodadadian and Clemens Heitzinger. A transport equation for confined structures applied to the OprP, Gramicidin A, and KcsA channels. *Journal of Computational Electronics*, 14(2):524–532, 2015.

[86] Amirreza Khodadadian and Clemens Heitzinger. Basis adaptation for the stochastic nonlinear Poisson–Boltzmann equation. *Journal of Computational Electronics*, 15(4):1393–1406, 2016.

[87] Amirreza Khodadadian, Kiarash Hosseini, Ali Manzour-ol Ajdad, Marjan Hedayati, Reza Kalantarinejad, and Clemens Heitzinger. Optimal design of nanowire field-effect troponin sensors. *Computers in Biology and Medicine*, 87:46–56, 2017.

[88] Amirreza Khodadadian, Leila Taghizadeh, and Clemens Heitzinger. Optimal multilevel randomized quasi-Monte-Carlo method for the stochastic drift-diffusion-Poisson system. *Computer Methods in Applied Mechanics and Engineering (CMAME)*, pages 1–22, 2017. *in print.*

[89] Amirreza Khodadadian, Leila Taghizadeh, and Clemens Heitzinger. Three-dimensional optimal multi-level Monte-Carlo approximation of the stochastic drift-diffusion-Poisson system. *Journal of Computational Electronics*, pages 1–18, 2017. *in print.*

[90] Kihyun Kim, Chanoh Park, Donghoon Kwon, Donghoon Kim, M Meyyappan, Sangmin Jeon, and Jeong-Soo Lee. Silicon nanowire biosensors for detection of cardiac troponin I (ctni) with high sensitivity. *Biosensors and Bioelectronics*, 77:695–701, 2016.

[91] Anton Köck, Alexandra Tischner, Thomas Maier, Michael Kast, Christian Edtmaier, Christian Gspan, and Gerald Kothleitner. Atmospheric pressure fabrication of SnO2-nanowires for highly sensitive CO and CH4 detection. *Sensors and Actuators B: Chemical*, 138(1):160–167, 2009.

[92] Tairong Kuang, Lingqian Chang, Xiangfang Peng, Xianglong Hu, and Daniel Gallego-Perez. Molecular beacon nano-sensors for probing living cancer cells. *Trends in Biotechnology*, 2016.

[93] Girish S Kulkarni and Zhaohui Zhong. Detection beyond the Debye screening length in a high-frequency nanoelectronic biosensor. *Nano Letters*, 12(2):719–723, 2012.

[94] Frances Y Kuo. Component-by-component constructions achieve the optimal rate of convergence for multivariate integration in weighted korobov and sobolev spaces. *Journal of Complexity*, 19(3):301–320, 2003.

[95] Frances Y Kuo, Christoph Schwab, and Ian H Sloan. Quasi-Monte Carlo finite element methods for a class of elliptic partial differential equations with random coefficients. *SIAM Journal on Numerical Analysis*, 50(6):3351–3374, 2012.

[96] Frances Y Kuo, Christoph Schwab, and Ian H Sloan. Multi-level quasi-Monte Carlo finite element methods for a class of elliptic PDEs with random coefficients. *Foundations of Computational Mathematics*, 15(2):411–449, 2015.

[97] Wing-Cheung Law, Ken-Tye Yong, Alexander Baev, and Paras N Prasad. Sensitivity improved surface plasmon resonance biosensor for cancer biomarker detection based on plasmonic enhancement. *ACS Nano*, 5(6):4858–4864, 2011.

[98] Hui Li, Andrew D Robertson, and Jan H Jensen. Very fast empirical prediction and rationalization of protein pka values. *Proteins: Structure, Function, and Bioinformatics*, 61(4):704–721, 2005.

[99] Monica X Li, Leo Spyracopoulos, and Brian D Sykes. Binding of cardiac troponin-i147-163 induces a structural opening in human cardiac troponin-c. *Biochemistry*, 38(26):8289–8298, 1999.

[100] Yiming Li, Chih-Hong Hwang, and Tien-Yeh Li. Random-dopant-induced variability in nano-CMOS devices and digital circuits. *IEEE Transactions on Electron Devices*, 56(8):1588–1597, 2009.

[101] Dong C Liu and Jorge Nocedal. On the limited memory BFGS method for large scale optimization. *Mathematical Programming*, 45(1):503–528, 1989.

[102] Yang Liu, Klas Lilja, Clemens Heitzinger, and Robert W. Dutton. Overcoming the screening-induced performance limits of nanowire biosensors: a simulation study on the effect of electro-diffusion flow. In *IEDM 2008 Technical Digest*, pages 491–494, San Francisco, CA, USA, December 2008.

[103] Zhanwu Liu, Yan Xu, and Pei Tang. Steered molecular dynamics simulations of Na^+ permeation across the Gramicidin A channel. *The Journal of Physical Chemistry B*, 110(25):12789–12795, 2006.

[104] BZ Lu, YC Zhou, MJ Holst, and JA McCammon. Recent progress in numerical methods for the Poisson-Boltzmann equation in biophysical applications. *Commun Comput Phys*, 3(5):973–1009, 2008.

[105] DG Luchinsky, R Tindjong, I Kaufman, PVE McClintock, and RS Eisenberg. Self-consistent analytic solution for the current and the access resistance in open ion channels. *Physical Review E*, 80(2):021925, 2009.

[106] Roderick MacKinnon. Potassium channels and the atomic basis of selective ion conduction (Nobel Lecture). *Angewandte Chemie International Edition*, 43(33):4265–4277, 2004.

[107] Vinay S Mahajan and Petr Jarolim. How to interpret elevated cardiac troponin levels. *Circulation*, 124(21):2350–2354, 2011.

[108] P.A. Markowich, C.A. Ringhofer, and C. Schmeiser. *Semiconductor Equations*. Springer, 1990.

[109] SJ Maynard, IBA Menown, and AAJ Adgey. Troponin T or troponin I as cardiac markers in ischaemic heart disease, 2000.

[110] Jason L McDonough and Jennifer E Van Eyk. Developing the next generation of cardiac markers: disease-induced modifications of troponin I. *Progress in Cardiovascular Diseases*, 47(3):207–216, 2004.

[111] Niraj Modi, Ivan Barcena-Uribarri, Manjeet Bains, Roland Benz, Robert EW Hancock, and Ulrich Kleinekathöfer. Role of the central arginine R133 toward the ion selectivity of the phosphate specific channel OprP: Effects of charge and solvation. *Biochemistry*, 52(33):5522–5532, 2013.

[112] Niraj Modi, Roland Benz, Robert EW Hancock, and Ulrich Kleinekathöfer. Modeling the ion selectivity of the phosphate specific channel OprP. *The Journal of Physical Chemistry Letters*, 3(23):3639–3645, 2012.

[113] Trevor F Moraes, Manjeet Bains, Robert EW Hancock, and Natalie CJ Strynadka. An arginine ladder in OprP mediates phosphate-specific transfer across the outer membrane. *Nature Structural & Molecular Biology*, 14(1):85–87, 2007.

[114] Margit Müller-Bardorff, Klaus Hallermayer, Angelika Schröder, Christoph Ebert, Anneliese Borgya, Willie Gerhardt, Andrew Remppis, Jörg Zehelein, and Hugo A Katus. Improved troponin T ELISA specific for cardiac troponin T isoform: assay development and analytical and clinical validation. *Clinical Chemistry*, 43(3):458–466, 1997.

[115] Pu-yan Nie. An SQP approach with line search for a system of nonlinear equations. *Mathematical and Computer Modelling*, 43(3):368–373, 2006.

[116] Harald Niederreiter and NSF-CBMS Regional Conference on Random Number Generation. *Random number generation and quasi-Monte Carlo methods*, volume 63. SIAM, 1992.

[117] Giray Ökten. Error reduction techniques in quasi-Monte Carlo integration. *Mathematical and Computer Modelling*, 30(7):61–69, 1999.

[118] Giray Ökten and Warren Eastman. Randomized quasi-Monte Carlo methods in pricing securities. *Journal of Economic Dynamics and Control*, 28(12):2399–2426, 2004.

[119] Mats HM Olsson, Chresten R Søndergaard, Michal Rostkowski, and Jan H Jensen. PROPKA3: consistent treatment of internal and surface residues in empirical pKa predictions. *Journal of Chemical Theory and Computation*, 7(2):525–537, 2011.

[120] Fernando Patolsky and Charles M Lieber. Nanowire nanosensors. *Materials Today*, 8(4):20–28, 2005.

[121] Fernando Patolsky, Brian P Timko, Guihua Yu, Ying Fang, Andrew B Greytak, Gengfeng Zheng, and Charles M Lieber. Detection, stimulation, and inhibition of neuronal signals with high-density nanowire transistor arrays. *Science*, 313(5790):1100–1104, 2006.

[122] Fernando Patolsky, Gengfeng Zheng, and Charles M Lieber. Fabrication of silicon nanowire devices for ultrasensitive, label-free, real-time detection of biological and chemical species. *Nature Protocols*, 1(4):1711–1724, 2006.

[123] Alexander W Peterson, Richard J Heaton, and Rosina M Georgiadis. The effect of surface probe density on DNA hybridization. *Nucleic Acids Research*, 29(24):5163–5168, 2001.

[124] T Poiroux, M Vinet, O Faynot, J Widiez, J Lolivier, T Ernst, B Previtali, and S Deleonibus. Multiple gate devices: advantages and challenges. *Microelectronic Engineering*, 80:378–385, 2005.

[125] Manuel Punzet, Dieter Baurecht, Franz Varga, Heidrun Karlic, and Clemens Heitzinger. Determination of surface concentrations of individual molecule-layers used in nanoscale biosensors by in situ atr-ftir spectroscopy. *Nanoscale*, 4(7):2431–2438, 2012.

[126] Anjum Qureshi, Yasar Gurbuz, and Javed H Niazi. Biosensors for cardiac biomarkers detection: A review. *Sensors and Actuators B: Chemical*, 171:62–76, 2012.

[127] Nitin K Rajan, Xuexin Duan, and Mark A Reed. Performance limitations for nanowire/nanoribbon biosensors. *Wiley Interdisciplinary Reviews: Nanomedicine and Nanobiotechnology*, 5(6):629–645, 2013.

[128] Nitin K Rajan, David A Routenberg, and Mark A Reed. Optimal signal-to-noise ratio for silicon nanowire biochemical sensors. *Applied Physics Letters*, 98(26):264107, 2011.

[129] Sami Ramadan, Kelvin Kwa, Peter King, and Anthony O'Neill. Reliable fabrication of sub-10 nm silicon nanowires by optical lithography. *Nanotechnology*, 27(42):425302, 2016.

[130] Subinoy Rana, Arvind K Singla, Avinash Bajaj, S Gokhan Elci, Oscar R Miranda, Rubul Mout, Bo Yan, Frank R Jirik, and Vincent M Rotello. Array-based sensing of metastatic cells and tissues using nanoparticle-fluorescent protein conjugates. *ACS Nano*, 6(9):8233, 2012.

[131] Tobias Reichlin, Willibald Hochholzer, Stefano Bassetti, Stephan Steuer, Claudia Stelzig, Sabine Hartwiger, Stefan Biedert, Nora Schaub, Christine Buerge, Mihael Potocki, et al. Early diagnosis of myocardial infarction with sensitive cardiac troponin assays. *New England Journal of Medicine*, 361(9):858–867, 2009.

[132] Kim R Rogers. Principles of affinity-based biosensors. *Molecular Biotechnology*, 14(2):109–129, 2000.

[133] Scott Roy and Asen Asenov. Where do the dopants go? *Science*, 309(5733):388–390, 2005.

[134] AK Saenger, R Beyrau, S Braun, Ruby Cooray, A Dolci, H Freidank, E Giannitsis, S Gustafson, B Handy, H Katus, et al. Multicenter analytical evaluation of a high-sensitivity troponin T assay. *Clinica Chimica Acta*, 412(9):748–754, 2011.

[135] Yader Sandoval and Fred S Apple. The global need to define normality: the 99th percentile value of cardiac troponin. *Clinical Chemistry*, 60(3):455–462, 2014.

[136] Nobuyuki Sano, Kazuya Matsuzawa, Mikio Mukai, and Noriaki Nakayama. On discrete random dopant modeling in drift-diffusion simulations: physical meaning of datomistic'dopants. *Microelectronics Reliability*, 42(2):189–199, 2002.

[137] Wen Shen, Dayong Tian, Hua Cui, Di Yang, and Zhiping Bian. Nanoparticle-based electrochemiluminescence immunosensor with enhanced sensitivity for cardiac troponin I using N-(aminobutyl)-N-(ethylisoluminol)-functionalized gold nanoparticles as labels. *Biosensors and Bioelectronics*, 27(1):18–24, 2011.

[138] Vasile Sinescu and Pierre L'Ecuyer. Existence and construction of shifted lattice rules with an arbitrary number of points and bounded weighted star discrepancy for general decreasing weights. *Journal of Complexity*, 27(5):449–465, 2011.

[139] Ian H Sloan and Henryk Woźniakowski. Tractability of multivariate integration for weighted korobov classes. *Journal of Complexity*, 17(4):697–721, 2001.

[140] Eric Stern, James F Klemic, David A Routenberg, Pauline N Wyrembak, Daniel B Turner-Evans, Andrew D Hamilton, David A LaVan, Tarek M Fahmy, and Mark A Reed. Label-free immunodetection with CMOS-compatible semiconducting nanowires. *Nature*, 445(7127):519–522, 2007.

[141] Eric Stern, Aleksandar Vacic, Nitin K Rajan, Jason M Criscione, Jason Park, Bojan R Ilic, David J Mooney, Mark A Reed, and Tarek M Fahmy. Label-free biomarker detection from whole blood. *Nature Nanotechnology*, 5(2):138–142, 2010.

[142] Eric Stern, Aleksandar Vacic, Nitin K Rajan, Jason M Criscione, Jason Park, Bojan R Ilic, David J Mooney, Mark A Reed, and Tarek M Fahmy. Label-free biomarker detection from whole blood. *Nature Nanotechnology*, 5(2):138–142, 2010.

[143] Peter Stubbs and Paul O Collinson. Point-of-care testing: a cardiologist's view. *Clinica Chimica Acta*, 311(1):57–61, 2001.

[144] Simon M Sze and Kwok K Ng. *Physics of Semiconductor Devices*. John Wiley & Sons, 2006.

[145] Leila Taghizadeh, Amirreza Khodadadian, and Clemens Heitzinger. The optimal multilevel monte-carlo approximation of the stochastic drift–diffusion-poisson system. *Computer Methods in Applied Mechanics and Engineering*, 318:739–761, 2017.

[146] Soichi Takeda, Atsuko Yamashita, Kayo Maeda, and Yuichiro Maeda. Structure of the core domain of human cardiac troponin in the Ca2+-saturated form. *Nature*, 424(6944):35–41, 2003.

[147] AL Teckentrup, R Scheichl, MB Giles, and E Ullmann. Further analysis of multilevel Monte Carlo methods for elliptic PDEs with random coefficients. *Numerische Mathematik*, 125(3):569–600, 2013.

[148] Ramakrishna Tipireddy and Roger Ghanem. Basis adaptation in homogeneous chaos spaces. *Journal of Computational Physics*, 259:304–317, 2014.

[149] Bruno Tuffin. Randomization of quasi-Monte Carlo methods for error estimation: Survey and normal approximation. *Monte Carlo Methods and Applications MCMA*, 10(3-4):617–628, 2004.

[150] Bruno Tuffin et al. On the use of low discrepancy sequences in Monte Carlo methods. *Monte Carlo Methods and Applications*, 2:295–320, 1996.

[151] Gerhard Tulzer, Stefan Baumgartner, Elise Brunet, Giorgio C Mutinati, Stephan Steinhauer, Anton Köck, Paolo E Barbano, and Clemens Heitzinger. Kinetic parameter estimation and fluctuation analysis of co at SnO2 single nanowires. *Nanotechnology*, 24(31):315501, 2013.

[152] Gerhard Tulzer and Clemens Heitzinger. Fluctuations due to association and dissociation processes at nanowire-biosensor surfaces and their optimal design. *Nanotechnology*, 26(2):025502, 2014.

[153] Gerhard Tulzer and Clemens Heitzinger. Fluctuations due to association and dissociation processes at nanowire-biosensor surfaces and their optimal design. *Nanotechnology*, 26(2):025502, 2015.

[154] Gerhard Tulzer and Clemens Heitzinger. Brownian-motion based simulation of stochastic reaction–diffusion systems for affinity based sensors. *Nanotechnology*, 27(16):165501, 2016.

[155] Aleksandar Vacic, Jason M Criscione, Nitin K Rajan, Eric Stern, Tarek M Fahmy, and Mark A Reed. Determination of molecular configuration by debye length modulation. *Journal of the American Chemical Society*, 133(35):13886–13889, 2011.

[156] Bart Van Zeghbroeck. Principles of semiconductor devices. *Colarado University*, 2004.

[157] Sameer Varma and Susan B Rempe. Structural transitions in ion coordination driven by changes in competition for ligand binding. *Journal of the American Chemical Society*, 130(46):15405–15419, 2008.

[158] Per Venge, Nina Johnston, Bertil Lindahl, and Stefan James. Normal plasma levels of cardiac troponin I measured by the high-sensitivity cardiac troponin I access prototype assay and the impact on the diagnosis of myocardial ischemia. *Journal of the American College of Cardiology*, 54(13):1165–1172, 2009.

[159] Joseph Wang. Electrochemical glucose biosensors. *Chemical Reviews*, 108(2):814–825, 2008.

[160] Kyuhyun Wang, Richard W Asinger, and Henry JL Marriott. St-segment elevation in conditions other than acute myocardial infarction. *New England Journal of Medicine*, 349(22):2128–2135, 2003.

[161] Fang Wei, Dongping Yang, Ronny Straube, and Jianwei Shuai. Brownian diffusion of ion channels in different membrane patch geometries. *Physical Review E*, 83(2):021919, 2011.

[162] Norbert Wiener. The homogeneous chaos. *American Journal of Mathematics*, 60(4):897–936, 1938.

[163] Margaret Wright. The interior-point revolution in optimization: history, recent developments, and lasting consequences. *Bulletin of the American mathematical Society*, 42(1):39–56, 2005.

[164] Alan HB Wu. The role of cardiac troponin in the recent redefinition of acute myocardial infarction. *Clinical Laboratory Science*, 17(1):50, 2004.

[165] Dongbin Xiu and George Em Karniadakis. The Wiener–Askey polynomial chaos for stochastic differential equations. *SIAM Journal on Scientific Computing*, 24(2):619–644, 2002.

[166] Nor F Za'bah, Kelvin SK Kwa, Leon Bowen, Budhika Mendis, and Anthony O'Neill. Top-down fabrication of single crystal silicon nanowire using optical lithography. *Journal of Applied Physics*, 112(2):024309, 2012.

[167] Bailin Zhang, Andres W Morales, Ralph Peterson, Liang Tang, and Jing Yong Ye. Label-free detection of cardiac troponin I with a photonic crystal biosensor. *Biosensors and Bioelectronics*, 58:107–113, 2014.

[168] Guo-Jun Zhang, Jay Huiyi Chua, Ru-Ern Chee, Ajay Agarwal, and She Mein Wong. Label-free direct detection of MiRNAs with silicon nanowire biosensors. *Biosensors and Bioelectronics*, 24(8):2504–2508, 2009.

[169] Yufeng Zhou, Joao H Morais-Cabral, Amelia Kaufman, and Roderick MacKinnon. Chemistry of ion coordination and hydration revealed by a K^+ channel-fab complex at 2.0 Å resolution. *Nature*, 414(6859):43–48, 2001.

Curriculum Vitae

Personal Information

Name	Amirreza Khodadadian
Date of Birth	28.08.1984
Place of Birth	Tehran, Iran
Nationality	Iran

Education

Since 10/2012	**University of Vienna**
	Doctoral studies in mathematics
08/2009-12/2010	**Military Service**
09/2006-10/2008	**University of Isfahan**
	Master studies in mathematics
09/2002-09/2006	**Shahid Chamran University of Ahvaz**
	Bachelor studies in mathematics
09/1995-09/2002	**NODET (Iranian exceptionally talented students schools)**
	High school
	Middle school

Academic Employment

Since 11/2013	**Vienna University of Technology**
	FWF (Austrian Science Fund) START prize project No. Y660 PDE models for Nanotechnology
11/2012-10/2013	**AIT Austrian Institute of Technology**
	WWTF (Viennese Science and Technology Fund) project No. MA09-028

Visiting Program

03/2014-04/2014 **Arizona State University**

School of Mathematical and Statistical Sciences

Journal Publications

1. Amirreza Khodadadian and Clemens Heitzinger. A transport equation for confined structures applied to the OprP, Gramicidin A, and KcsA channels. *Journal of Computational Electronics.*, 14(2):524–532, 2015.

2. Amirreza Khodadadian and Clemens Heitzinger, Basis adaptation for the stochastic nonlinear Poisson-Boltzmann equation. *Journal of Computational Electronics.* 2016, 15(4):1393–1406, 2016.

3. Leila Taghizadeh, Amirreza Khodadadian, and Clemens Heitzinger. The optimal multilevel Monte-Carlo approximation of the stochastic drift-diffusion-Poisson system. *Computer Methods in Applied Mechanics and Engineering (CMAME)*, 318:739–761, 2017.

4. Amirreza Khodadadian, Kiarash Hosseini, Ali Manzour ol Ajdad, Marjan Hedayati, Reza Kalantarinjead, and Clemens Heitzinger. Optimal design of nanowire field-effect troponin sensors, *Computers in Biology and Medicine* (2017), 87: 46–56, 2017, DOI: 10.1016/j.compbiomed.2017.05.008.

5. Amirreza Khodadadian, Leila Taghizadeh, and Clemens Heitzinger. Three-dimensional optimal multi-level Monte-Carlo approximation of the stochastic drift-diffusion-Poisson system, *Computer Methods in Applied Mechanics and Engineering (CMAME)*, 2017 *in print.*

6. Amirreza Khodadadian, Leila Taghizadeh, and Clemens Heitzinger. Optimal multi-level randomized quasi-Monte Carlo method for the stochastic drift-diffusion-Poisson system, *Journal of Computational Electronics*, 2017, *in print.*

7. Amirreza Khodadadian, Maryam Parvizi, and Clemens Heitzinger. An Adaptive multilevel Monte Carlo Algorithm for Stochastic Drift-Diffusion-Poisson System, 2017, *in preparation.*

8. Amirreza Khodadadian, Leila Taghizadeh, and Clemens Heitzinger. The Stochastic Drift-Diffusion-Poisson System and Applications in Nanoscale Sensors, Biosensors, 2017, *invited review paper*, *in preparation.*

Contributions to Conferences and Proceeding

1. Amirreza Khodadadian and Clemens Heitzinger. Simulation of nanowire sensors using the stochastic Poisson-Boltzmann equation. In *Proceeding of 2nd International Conference on Mathematical Modeling in Physical Sciences (IC-MSQUARE 2013)*, Prague, Czech Republic, 1–5 September 2013.

2. Amirreza Khodadadian and Clemens Heitzinger. Uncertainty quantification in nanowire sensors using the stochastic nonlinear Poisson-Boltzmann equation. In *Proceeding of SIAM Conference on Uncertainty Quantification*, Savannah, Georgia, USA, 31 March – 3 April 2014.

3. Amirreza Khodadadian and Clemens Heitzinger. Uncertainty quantification in nanowire sensors using the stochastic nonlinear Poisson-Boltzmann equation. In *Proceeding of 11th International Conference on Monte Carlo and Quasi-Monte Carlo Methods in Scientific Computing (MCQMC2014)*, Leuven, Belgium, 6–11 April 2014.

4. Amirreza Khodadadian and Clemens Heitzinger. Using the stochastic Poisson-Boltzmann equation to quantify noise in nanowire bio- and gas sensors. In *Proceeding of 11th World Congress on Computational Mechanics*, Barcelona, Spain, 20–25 July 2014.

5. Amirreza Khodadadian and Clemens Heitzinger. Ionic currents through transmembrane proteins calculated by a transport equation for confined structure. In *Proceeding of 4th International Conference on Computational and Mathematical Biomedical Engineering (CMBE 2015)*, Cachan, France, 29 June–1 July 2015.

6. Amirreza Khodadadian and Clemens Heitzinger. The signal-to-noise ratio due to biological noise in field-effect sensor. calculated using the stochastic Poisson equation and polynomial-chaos expansion. In *Proceeding of 13th U.S national congress on computational mechanics*, San Diego, California, July 26–30, 2015.

7. Leila Taghizadeh, Amirreza Khodadadian, Caroline Geiersbach, and Clemens Heitzinger. Optimal multi-level Monte-Carlo method for a system of stochastic PDEs. *SIAM Conference on the Analysis of Partial Differential Equations (SIAM PD15)*, Scottsdale, AZ, USA, 7–10 December 2015.

8. Amirreza Khodadadian, Leila Taghizadeh and Clemens Heitzinger. Stochastic modeling of dopant atoms in nanowire sensors with multi-level Monte Carlo *SIAM conference on uncertainty quantification*, Lausanne, Switzerland, April 8–10, 2016.

9. Clemens Heitzinger, Amirreza Khodadadian, Gudmund Pammer, Leila Taghizadeh, Gerhard Tulzer. Stochastic partial differential equations for the modeling of nanowire and nanopore sensors, *19th European Conference on Mathematics for Industry*, Santiago de Compostela, June 13–17 2016.

10. Clemens Heitzinger , Amirreza Khodadadian, Stefan Rigger, and Leila Taghizadeh. Optimal multi-level Monte-Carlo methods for the stochastic drift-diffusion-Poisson System and for stochastic homogenization, *USNCMM 14 th U.S. National Congress on Computational Mechanics*, Canada, 17–20 July 2017.

11. Leila Taghizadeh, Amirreza Khodadadian, and Clemens Heitzinger. Optimal multi-level randomized-quasi-Monte-Carlo methods for the stochastic drift-diffusion-poisson system and for stochastic homogenization. In Proc. International Conference on Scientific Computation and Differential Equations 2017 (SciCADE 2017), Bath, UK, 11–15 Sep 2017.